Probing the Atmospheric Boundary Layer Using Remotely Piloted Aircraft With Special Regard to the Morning Transition and Wind Energy Research

Dissertation

der Mathematisch-Naturwissenschaftlichen Fakultät

der Eberhard Karls Universität Tübingen

zur Erlangung des Grades eines

Doktors der Naturwissenschaften

(Dr. rer. nat.)

vorgelegt von

Dipl. Ing (BA), M.Sc. Norman Wildmann

aus Mainz

Tübingen

20*15*

Tag der mündlichen Qualifikation:	27.08.2015
Dekan:	Prof. Dr. Wolfgang Rosenstiel
1. Berichterstatter:	Prof. Dr. habil. Jens Bange
2. Berichterstatter:	Prof. Dr. Burkhard Wrenger
3. Berichterstatter:	Prof. Dr. Phillip B. Chilson

Contents

Abbreviations

μC	microcontroller
5HP	five-hole probe
ABL	atmospheric boundary layer
AMOC	airborne meteorological on-board computer
agl	above ground level
asc	ascent
CAA	civil aviation authority
CAP	constant-altitude profiling
CBL	convective boundary layer
CFD	computational fluid dynamics
DAQ	data acquiring systems
den	denominator
des	descent
DPM	dew-point mirror hygrometer
DWD	Deutscher Wetterdienst
EC	eddy-covariance
EKF	extended kalman filter
EUR	Euro
EZ	entrainment zone
FCC	free convection conditions
FPGA	field programmable gate array
FWPRT	fine wire platinum resistance thermometer
GPS	global positioning system
HP	high pressure port
HS-OWL	Hochschule Ostwestfalen-Lippe (University of Applied Sciences Ostwestfalen-Lippe)
IAG	Institute of Aero- and Gasdynamics (University Stuttgart)

IEC	International Electrotechnical Commission
IFR	Institute of Flight Mechanics and Control (University Stuttgart)
IMU	inertial measurement unit
ISM	Institute for Fluid Dynamics (Technical University Braunschweig)
IST	Innovative Sensor Technologies AG
LES	large-eddy simulation
Lidar	light detection and ranging
LP	low pressure port
M^{2}AV	meteorological mini aerial vehicle
MASC	multi-purpose airborne sensor carrier
MEMS	micro-electromechanical system
MHP	multi-hole probe
ML	mixed layer
MSLP	mean sea level pressure
NCAR	National Center for Atmospheric Research
NIL	nightly inversion layer
NIST	National Institute of Standards and Technology
num	numerator
P0-P4, Ps	pressure ports of a 5HP
PCB	printed circuit board
PVC	polyvinyl chloride
Radar	radio detection and ranging
RASS	radio acoustic sounding system
RC (low pass)	resistor capacitor (low pass)
RH	relative humidity
RL	residual layer
RMS	root mean square
ROCS	Research Onboard Computer System
RPA	remotely piloted aircraft

RPAS	remotely piloted aircraft system
TC	thermocouple
TDLAS	tunable diode laser absorption hygrometer
TKE	turbulent kinetic energy
SCBL	shallow convective boundary layer
SD	secure digital
Sodar	sound/sonic detection and ranging
SUMO	small unmanned meteorological observer
SWE	Stuttgard Wind Energy (University Stuttgart)
UAV	unmanned aerial vehicle
UTC	coordinated universal time
VP	vertical profile
WEC	wind-energy converter

Symbols

α	heat transfer coefficient
α	angle of attack
α	polarizability
β	angle of sideslip
ΔT_{sh}	self-heating temperature
ΔP	reference pressure for 5HP calibration
ε_0	vacuum permittivity
ε_{r}	relative permittivity
$\varepsilon_{\mathrm{r}}^{\mathrm{H_2O}}$	relative permittivity of water
$\varepsilon_{\mathrm{r}}^{\mathrm{Poly}}$	relative permittivity of the polymer
κ	Poisson constant
μ	electrical dipole moment
ω	angular frequency
$\mathbf{\Omega}$	angular rotation rate vector
ϕ	wind direction
ϕ, φ	phase shift
Φ	roll angle
ρ	air density
ϱ	density
ϱ	cross-correlation function
σ	standard deviation
τ	time lag
θ	potential temperature
θ_v	virtual potential temperature
θ_*	convective velocity scale
ζ	scaled measurement height
A	surface area

B	ratio between h_0 and h_i
$\mathbf{c}_\alpha, \mathbf{c}_\beta, \mathbf{c_s}, \mathbf{c_q}$	coefficients of the 5HP calibration polynomial
c	concentration
c_m	measured average water concentration in polymer
c_s	surface water concentration on the polymer
C	capacitance
C_0	capacitance of vacuum between capacitor plates
$C_{\mathrm{H_2O}}$	capacitance of absorbed water in polymer
C_p, c_p	specific heat of dry air at constant pressure
d	distance
D	diffusion coefficient
D	length of a time series
D	WEC rotor diameter
D_Φ	structure function of variable Φ
E	latent heat flux
$\mathbf{E}$	unity matrix
f_x	polynomial functions for 5HP calibration
g	acceleration due to gravity
G**,**H	transfer function
H	sensible heat flux
H_0	surface sensible heat flux
h_0	heat flux zero crossing height
h_i	thermal inversion height
I	electrical current
$\mathbf{J}$	diffusion flux
$k_\alpha, k_\beta, k_p, k_q$	5HP calibration coefficients
k_B	Boltzmann constant
$\mathbf{K}$	5HP calibration matrix
L_v	latent heat for vaporization at 20 $^\circ C$

m	mixing ratio
M	molecular mass
$\mathbf{M}_{\mathrm{mf}}$	Rotation matrix between meteorological coordinate system and aircraft body fixed coordinate system
N	number of modelled layers in polymer
N_A	Avogadro constant
P	power
P_i	measure pressure at 5HP pressure ports
dP_{i}	pressure difference between 5HP pressure port and reference pressure
dP_{ij}	pressure differences between 5HP pressure ports
P_{c}	convective power loss
P_{m}	molar polarisation
P_{l}	electrical power
P_{s}, p	static pressure
P_{t}	total pressure
q	dynamic pressure
q	specific humidity
Q	electrical charge
r	water vapour mixing ratio
r	recovery factor
R	electrical resistance
R_{d}	specific gas constant of dry air
Re	Reynolds number
RH	Relative humidity
$\mathbf{s_p}$	lever arm vector
S	Minimization criteria for solution of overestimated set of linear equations
S_m	Signal artefact due to phase shift between 5HP pressure ports
S	Surface
t	time

T	temperature
T_{s}	static temperature
T_{m}	measured temperature
T_{tot}	total temperature
T_{v}	virtual temperature
u_h	horizontal wind speed
u_*	friction velocity
U	voltage
$\mathbf{v}$	meteorological wind vector
$\mathbf{v}_{\mathrm{gs}}$	ground speed velocity vector
$\mathbf{v}_{\mathrm{tas}}$	true airspeed velocity vector
V	volume
w	vertical wind component
w_*	convection velocity scale
$\langle w'\theta' \rangle_0$	surface kinematic heat flux
$\mathbf{Y}$	system matrix of humidity sensor model
z_i	boundary layer scaling height
z_{NIL}	boundary layer scaling height
Z	particle density

Acknowledgements

I want to thank all the people who have contributed to the work in this thesis. In particular I would like to acknowledge:

- My supervisor Prof. Dr. Jens Bange, for making this work possible, providing the necessary infrastructure, contacts, and advise in manifold ways.
- Prof. Dr. Jens Bange and Prof. Dr. Burkhard Wrenger for acting as reviewers of this thesis and participating in the doctoral graduation procedure.
- All my colleagues in the Umphy-team: Torsten Auerswald, Christian Behrens, Yvonne Breitenbach, Asmae El-Bahlouli, Milad Kiaee, Aline van den Kroonenberg, Daniel Martinez Villagrasa, Bastian Paas, Andreas Platis, Uwe Putze, Sridhar Ravi, Joe Smith and David-James Tupman
- All the students that helped me with maintenance of MASC, teaching tasks, data analysis and research. Thank you Albrecht, Andreas, Fabian, Florian, Germar, Gerrit, Kirsten, Maren, Martin, Marvin, Moritz, Sarah and Timm
- Christoph, Jürgen, Henrik, Max, Markus and Philipp for acting as safety pilot for MASC.
- Roland Kern (Roke-Modelle) for his great job with the design and building of the MASC airframe.
- Prof. Dr.-Ing. Walter Fichter and his team members Florian Weimer, Alexander Joos, and Michael Frangenberg at the Institute for Flight Mechanics and Control at the University of Stuttgart for the provision and support with the ROCS autopilot.
- Jens Dünnermann for his work on the AMOC data acquisition system.
- Frank Beyrich and the DWD for allowing us to take measurements at the Richard-Aßmann-Observatory in Lindenberg.
- The model aircraft clubs in Kusterdingen and Kirchentellinsfurt for allowing the operation of MASC on their airfields.
- My parents for their support and advice!

The Project Lidar complex is funded by the German Federal Ministry for Economic Affairs and Energy (BMWi) on the basis of a resolution of the German Bundestag.

Abstract

The thesis at hand is a work in the field of atmospheric physics. It deals with the experimental study of physical processes in the so-called atmospheric boundary layer. The atmospheric boundary layer is the lowest part of the earth's atmosphere, which is in direct contact with the earth surface. It is important to have considerable knowledge about the processes in the boundary layer to understand the concepts of weather and climate. Two scientific problems have been addressed in this dissertation. An experimental study of the morning transition of the atmospheric boundary layer was conducted to assess the applicability of a theoretical model of the convective boundary layer at all times during the transition period. Limited evidence was found for such a uniform description based on the used parameters. It has been found that the entrainment layer is far from homogeneous, and single events of entrainment and convection have a strong influence on the local boundary layer's thermal stratification. A further experiment was conducted within striking distance of wind-energy converters (WEC). In-situ measurements of meteorological quantities were taken in the wake of a WEC to quantify its extension and intensity.

The measuring instrument described and used in this thesis is a small unmanned aircraft. Aircraft of this kind are frequently used in all types of civil applications and are of great benefit for airborne meteorology in particular. A significant part of this thesis describes the development of sensors for the unmanned aircraft MASC, developed at the University of Tübingen, and their test and first measurement results. Two fast, lightweight temperature sensors of different types were developed and validated against established instrumentation at the Richard-Aßmann-Observatory of the German Meteorological Service in Lindenberg. The common method of measuring the airflow vector with multi-hole probes was scrutinised with regard to its applicability in turbulence measurement and optimized for integration into the MASC system. It was made possible to resolve small-scale turbulent motions of temperature and wind in the sub-meter range through this measures. Important improvements could also be accomplished in the field of water vapour measurement. With the help of a dynamic model of a capacitive humidity sensor, it was possible to reconstruct fast changes in humidity from the originally slow sensor readings.

Zusammenfassung

Die vorliegende Arbeit behandelt die experimentelle Untersuchung physikalischer Vorgänge in der sogenannten atmosphärischen Grenzschicht. Die atmosphärische Grenzschicht ist die unterste Schicht der Atmosphäre, welche sich in direktem Kontakt zur Erdoberfläche befindet. Eine genaue Kenntnis der hier vorherrschenden physikalischen Prozesse ist von entscheidender Bedeutung für das Verständnis von Wetter und Klima. Zwei unterschiedliche wissenschaftliche Fragestellungen werden in dieser Arbeit thematisiert. Eine experimentelle Untersuchung der morgendlichen Transition der atmosphärischen Grenzschicht wurde durchgeführt, um die Anwendbarkeit eines theoretischen Modells der konvektiven Grenzschicht auf jeden Zeitpunkt während der Transition, zu überprüfen. Es wurden eingeschränkt Hinweise gefunden, dass eine solche einheitliche Beschreibung, basierend auf den zur Hilfe genommenen Parametern, möglich ist. Es konnte gezeigte werden, dass die Entrainment-Zone starke horizontale Unebenheiten aufweist, und einzelne Entrainment- und Konvektionsereignisse starken Einfluss auf die lokale thermische Schichtung der Grenzschicht haben. Ein weiteres Experiment fand in unmittelbarer Nähe von Windenergieanlagen statt. Meteorologische In-situ-Messungen in den Wirbelschleppen der Anlagen wurden durchgeführt um deren Ausdehnung und Intensität zu quantifizieren.
Das Messinstrument, welches zur Gewinnung der Daten in dieser Arbeit genutzt wird, ist ein unbemanntes Kleinflugzeug. Solche Flugzeuge halten zunehmend Einzug in zivile Anwendungen und sind ein großer Gewinn für die fluggestützte Meteorologie. Weite Teile dieser Arbeit beschreiben die Entwicklung von Messinstrumenten für einen solchen Sensorträger, deren Erprobung und erste Messergebnisse. Zwei verschiedene, schnelle und leichte Temperatursensoren wurden entwickelt und gegen bewährte Instrumente validiert. Die verbreitete Methode zur Messung des Strömungsvektors mit Mehrlochsonden, wurde für die Anwendung zur Turbulenzmessung in Flugzeugen kritisch hinterfragt und optimiert. Mit Hilfe dieser Maßnahmen konnte erreicht werden, dass kleinskalige turbulente Schwankungen von Temperatur und Wind im Submeterbereich, im Flug aufgelöst werden können. Entscheidende Verbesserungen konnten auch im Bereich der Luftfeuchtemessung erreicht werden. Durch Modellierung des verwendeten kapazitiven Sensors, wurde die Rekonstruktion schneller Änderungen der Luftfeuchte aus den urpsrünglich langsamen Messungen des Sensors ermöglicht.

List Of Publications

This thesis is presented as an integrated accumulation of five publications. Four manuscripts have been published in peer-reviewed journals. The fifth manuscript has been submitted for publication to a peer-reviewed journal.

Published manuscripts

- **Wildmann, N.**, **Mauz, M.** and **Bange, J.**, **2013**: Two fast temperature sensors for probing of the atmospheric boundary layer using small remotely piloted aircraft (RPA). *Atmospheric Measurement Techniques*, **6**(8), 2101–2113.

- **Wildmann, N.**, **Ravi, S.** and **Bange, J.**, **2014**: Towards higher accuracy and better frequency response with standard multi-hole probes in turbulence measurement with remotely piloted aircraft (RPA). *Atmospheric Measurement Techniques*, **7**(4), 1027–1041.

- **Wildmann, N.**, **Kaufmann, F.** and **Bange, J.**, **2014**: An inverse-modelling approach for frequency response correction of capacitive humidity sensors in ABL research with small remotely piloted aircraft (RPA). *Atmospheric Measurement Techniques*, **7**(9), 3059–3069.

- **Wildmann, N.**, **Hofsäß, M.**, **Weimer, F.**, **Joos, A.** and **Bange, J.**, **2014**: MASC - a small Remotely Piloted Aircraft (RPA) for wind energy research. *Advances in Science and Research*, **11**, 55–61.

- **Wildmann, N.**, **Rau, G**. and **Bange, J.**, **2015**: Observations of the Early Morning Boundary-Layer Transition with Small Remotely-Piloted Aircraft. *Boundary-Layer Meteorology*, Online First, 1–29.

Other publications not included in the thesis

- **Platis, A.**, **Altstädter, B.**, **Wehner, B.**, **Wildmann, N.**, **Lampert, A.**, **Hermann, M.**, **Birmilli, W.** and **Bange, J.**, **2015**: Case study of an airborne measured new particle formation event in the atmospheric boundary layer. *Boundary-Layer Meteorology*, *accepted for publication*.

- **Altstädter, B.**, **Platis, A.**, **Wehner, B.**, **Scholtz, A.**, **Wildmann, N.**, **Hermann, M.**, **Käthner, R.**, **Baars, H.**, **Bange, J.** and **Lampert, A.**, **2015**: ALADINA – an unmanned research aircraft for observing vertical and horizontal distributions of ultrafine particles within the atmospheric boundary layer. *Atmospheric Measurement Techniques*, **8**(4), 1627–1639.

- **Lothon, M.**, **Lohou, F.**, **Pino, D.**, **Couvreux, F.**, **Pardyjak, E. R.**, **Reuder, J.**, **Vilà-Guerau de Arellano, J.**, **Durand, P.**, **Hartogensis, O.**, **Legain, D.**, **Augustin, P.**, **Gioli, B.**, **Lenschow, D. H.**, **Faloona, I.**, **Yagüe, C.**, **Alexander, D. C.**, **Angevine, W. M.**, **Bargain, E.**, **Barrié, J.**, **Bazile, E.**, **Bezombes, Y.**, **Blay-Carreras, E.**, **van de Boer, A.**, **Boichard, J. L.**, **Bourdon, A.**, **Butet, A.**, **Campistron, B.**, **de Coster, O.**, **Cuxart, J.**, **Dabas, A.**, **Darbieu, C.**, **Deboudt, K.**, **Delbarre, H.**, **Derrien, S.**, **Flament, P.**, **Fourmentin, M.**, **Garai, A.**, **Gibert, F.**, **Graf, A.**, **Groebner, J.**, **Guichard, F.**, **Jiménez, M. A.**, **Jonassen, M.**, **van den Kroonenberg, A.**, **Magliulo, V.**, **Martin, S.**, **Martinez, D.**, **Mastrorillo, L.**, **Moene, A. F.**, **Molinos, F.**, **Moulin, E.**, **Pietersen, H. P.**, **Piguet, B.**, **Pique, E.**, **Román-Cascón, C.**, **Rufin-Soler, C.**, **Saïd, F.**, **Sastre-Marugán, M.**, **Seity, Y.**, **Steeneveld, G. J.**, **Toscano, P.**, **Traullé, O.**, **Tzanos, D.**, **Wacker, S.**, **Wildmann, N.** and **Zaldei, A.**, **2014**: The BLLAST field experiment: Boundary-Layer Late Afternoon and Sunset Turbulence. *Atmospheric Chemistry and Physics*, **14**(20), 10,931–10,960.

- **Jensen, A. M.**, **Wildmann, N.**, **Chen, Y.** and **Voos, H.**, **2010**: In-situ Unmanned Aerial Vehicle (UAV) Sensor Calibration to Improve Automatic Image Orthorectification. In: *Proc. IEEE Int. Geoscience and Remote Sensing Symp. (IGARSS)*, p. 596–599.

Conference contributions

- **Wildmann, N.**, **Bange, J.**, and **van den Kroonenberg, A.**. Airborne meteorological measurement unit for small uavs. In *EGU General Assembly 2011*, Vienna, Austria, 03 – 08 April **2011**. URL `http://meetingorganizer.copernicus.org/EGU2011/EGU2011-8278-1.pdf`. last access: 19.01.2015.

- **Wildmann, N.** and **Bange, J.**. Uncertainties in the measurement of temperature, humidity and pressure using small unmanned aerial vehicles (uavs). In *DMG METTOOLS VIII*, Leipzig,Germany, 20 – 22 March **2012**.

- **Wildmann, N.** and **Bange, J.**. Comparison of sensors for the measurement of temperature with (small) uav rpa. In *ISARRA 2013*, Palma de Mallorca, Spain, 18 – 20 February **2013**. URL `http://www.uibcongres.org/congresos/ponencia.en.html?cc=267&mes=2&ordpon=5`. last access: 19.01.2015.

- **Wildmann, N.** and **Bange, J.**. Description of the rpas "masc" as a measuring platform for thermodynamic processes in the abl. In *13th EMS Annual Meeting*, Reading, UK, 09 – 13 September **2013**. URL `http://meetingorganizer.copernicus.org/EMS2013/EMS2013-646.pdf`. last access: 19.01.2015.

- **Wildmann, N.**, **Bange, J.**, and **Hofsäß, M**. A "remotely piloted air system" (rpas) as complementary measurement tool for wind energy site evaluation, using the example of the project "lidar complex". In *13th EMS Annual Meeting*, Reading, UK, 09 – 13 September **2013**. URL `http://meetingorganizer.copernicus.org/EMS2013/EMS2013-486.pdf`. last access: 19.01.2015.

- **Wildmann, N.** and **Bange, J.**. Application of the remotely piloted aircraft (rpa) 'masc' in atmospheric boundary layer research. In *EGU General Assembly 2014*, Vienna, Austria, 27 April – 02 May **2014**. URL `http://meetingorganizer.copernicus.org/EGU2014/EGU2014-6354.pdf`. last access: 19.01.2015.

- **Wildmann, N.** and **Bange, J.**. A remotely piloted aircraft (rpa) as a measurement tool for wind-energy research. In *EGU General Assembly 2014*, Vienna, Austria, 27 April – 02 May **2014**. URL `http://meetingorganizer.copernicus.org/EGU2014/EGU2014-6300.pdf`. last access: 19.01.2015.

- **Wildmann, N.** and **Bange, J.**. Masc - a small remotely piloted aircraft (rpa) for atmospheric research. In *ISARRA 2014*, Odense, Denmark, 26 - 28 May **2014**. URL http://isarra.org/ISARRA2014_abstracts/ISARRA_2014_Abstract_Wildmann.pdf. last access: 19.01.2015.

- **Wildmann, N.** and **Bange, J.**. State of the art in-situ turbulence measurements with unmanned aerial systems (uas) in the abl. In *21st Symposium on Boundary Layers and Turbulence*, Leeds, UK, 09 - 13 June **2014**. URL https://ams.confex.com/ams/21BLT/webprogram/Paper248147.html. last access: 19.01.2015.

- **Wildmann, N.** and **Bange, J.**. Observation of wake and upstream turbulence of individual wind energy converters in a wind farm with unmanned aerial vehicles (uav). In *21st Symposium on Boundary Layers and Turbulence*, Leeds, UK, 09 - 13 June **2014**. URL https://ams.confex.com/ams/21BLT/webprogram/Paper248143.html. last access: 19.01.2015.

- **Wildmann, N.**, **Rau, G. A.**, **Platis, A.**, and **Bange, J.**. Towards a better understanding of the early morning boundary layer transition, using observations of small unmanned aerial vehicles (uav). In *21st Symposium on Boundary Layers and Turbulence*, Leeds, UK, 09 - 13 June **2014**. URL https://ams.confex.com/ams/21BLT/webprogram/Paper247503.html. last access: 19.01.2015.

- **Wildmann, N.** and **Bange, J.**. Unbemannte Flugzeuge als Messinstrument für die Windenergieforschung. In *ForWind Vortragsreihe*, Oldenburg, Germany, 21 November **2014**. URL http://www.forwind.de/forwind/index.php?article_id=671&clang=0. last access: 19.01.2015.

- **Wildmann, N.** and **Bange, J.**. Applications of the remotely piloted aircraft (RPA) 'MASC' in atmospheric boundary layer research. In *EGU General Assembly 2015*, Vienna, Austria, 13 April **2015**. URL http://meetingorganizer.copernicus.org/EGU2015/EGU2015-9658.pdf. last access: 30.08.2015.

1 Introduction

Theories and hypotheses about natural laws are permanently questioned and revisited in the natural sciences. Simplifications and assumptions have to be made in accordance with the possibilities that researchers are facing at the present state of the art. In order to improve their understanding and validate theories and hypotheses, which might have been postulated decades before, researchers are striving to get access to the newest technologies and most advanced tools in data acquisition and data processing. It is in this spirit that this thesis uses the modern tool of a remotely piloted aircraft (RPA) for atmospheric sciences. The main goal of science is to increase the knowledge and understanding of our environment by conducting fundamental research in a large diversity of fields. The work that has been done in this thesis towards a better understanding of the morning transition of the atmospheric boundary layer (ABL) can be seen as an example of this goal. Furthermore, whenever possible, scientists also have the task to apply their knowledge in support of social development for a better future. The energy evolution towards sustainable energy sources is one of these developments, which has been highly promoted by the German government at the beginning of the 21st century and is widely supported by the science community. One part of this thesis deals with atmospheric measurements in vicinities of wind energy converters (WEC), which can be a small contribution to the qualification and further development of the technology.

1.1 Boundary-Layer Meteorology

In atmospheric physics, the investigation of the processes in the ABL, i.e. the layer of the atmosphere that is directly influenced by the earth's surface, is of major concern (Garratt, 1992; Stull, 1988). Most of what is commonly referred to as 'weather' happens in the ABL and directly affects our everyday life. Pollutants, greenhouse gases, and other aerosols are transported from the ABL into the atmosphere aloft and thus can impact the climate in the long term. For weather forecast and climate prediction, the synoptic and mesoscale processes can be numerically resolved and modelled in modern computers, but micro-meteorological processes in the ABL still need to be parameterized. Erroneous parameterization can contribute large uncertainties to the models (Teixeira *et al.*, 2008). An understanding of turbulence is crucial to describe the

dynamics of the ABL, Since the ABL is always turbulent. While advection is important for horizontal transport, turbulence is a dominating factor for vertical transport. Air-sea or air-land interactions cannot be understood without considering turbulent transport. There are two main sources for turbulence in the ABL: shear and buoyancy. Over land surface, the ABL has a strong diurnal cycle. During the night, stable boundary layers are established because the surface temperature decreases and vertical motions are suppressed by negative buoyancy. Turbulence in the stable boundary layer is mostly weak and intermittent, with shear as the only considerable source for turbulence. In daytime, with radiation input, the surface heats up and a convective boundary layer (CBL) can develop in which buoyancy-generated turbulence can completely mix the atmosphere up to several hundred of metres. How fast the mixed layer (ML) develops and how high it grows depend primarily on the solar radiation input and the thermal stratification of the ABL of the day before, as well as on other factors such as water vapour content of the air, advection, wind shear, subsidence or soil moisture. Mathematical descriptions of the ML — the vertical distribution of thermodynamic scalars, fluxes, and turbulent kinetic energy (TKE) — have been derived from the Navier-Stokes equation (Kaimal *et al.*, 1976; Stull, 1988; Garratt, 1992; Deardorff, 1974). In order to compare the ABL evolution in different experiments, scaling parameters have been introduced. For the ML of a CBL, convection velocity scale w_* and convective temperature scale θ_*, both of which depend on the surface heat flux $\langle w'\theta' \rangle$, have been found to be adequate scaling parameters (also known as Deardorff scaling, Deardorff, 1970). Looking at vertical distributions, the measurement height is often scaled by the boundary layer height $\zeta = z/z_i$. While the ML physics is well described in the literature, and most parts of the theory could be validated satisfactorily by experiments, at least for homogeneous terrains, the transition phases in the morning and late afternoon are less well described.

Measurements in the morning transition from a night-time stable boundary layer to a day-time CBL is picked out as the field of research in this thesis. The prevailing physics during the morning transition is commonly acknowledged: After a short delay after sunrise, the surface starts to heat and surface heat flux changes sign from downward to upward transport of heat. From then on, a shallow convective boundary layer (SCBL) develops, which is not only fed by the increasing upward surface heat flux but also to a

large degree by entrainment from the residual layer (RL). This is the residual of the CBL from the day before and persists above the nightly inversion layer (NIL) (Angevine *et al.*, 2001; Lapworth, 2006; Beare, 2008). Figure 1 illustrates an idealized development in three steps. In most convective days, profiles of potential temperature similar to what is shown in Fig. 1 can be found. However, a general description of how fast the SCBL develops and grows is missing.

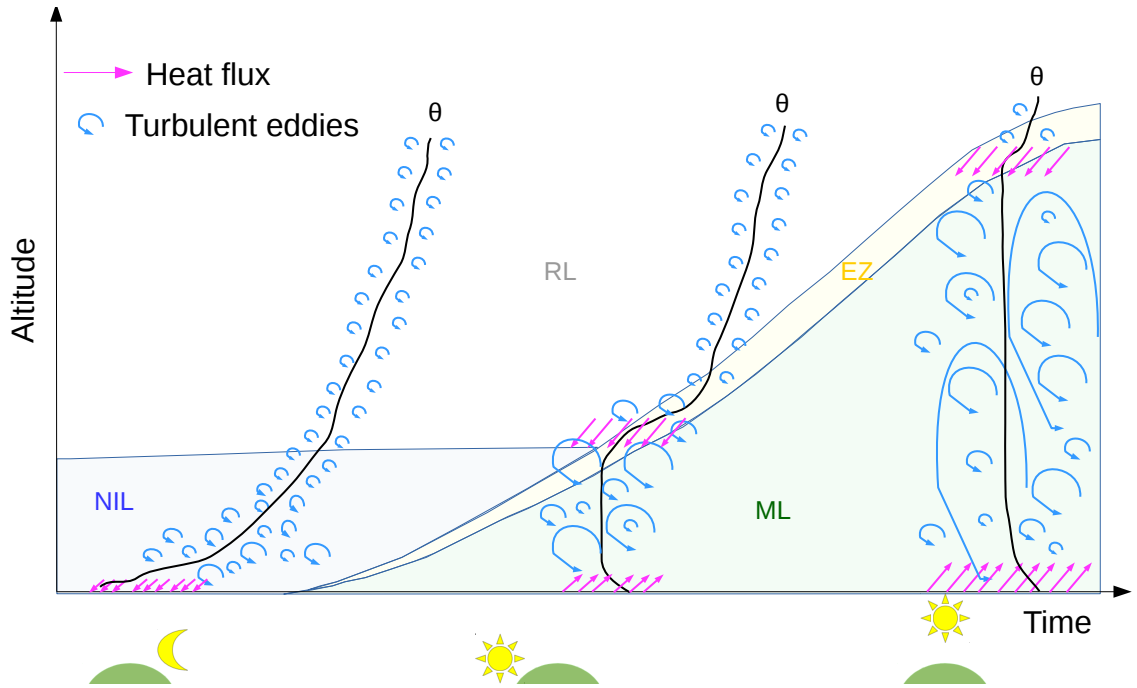

Figure 1: Sketch of the development of vertical profiles of potential temperature during the morning transition. The development of surface and entrainment heat flux (red), as well as the turbulence intensity and size of turbulent eddies (blue), is indicated by arrows.

The few articles that have been published on the morning transition focused on single aspects influencing the transition behaviour. Angevine *et al.* (2001) already found that shear has a strong influence on the speed of the growth of the SCBL and Beare (2008) could confirm these findings with LES simulations, stating that the SCBL growth is faster with higher wind shear. Edwards *et al.* (2014) investigated the effect of radiation effects in LES, while Bennett *et al.* (2010) put more focus on the development of thermals and moisture transport. As in ABL research in general, the influence of heterogeneous terrain and especially terrain with substantial orography is subject to the

ongoing research. Lenschow *et al.* (1979) already investigated the morning transition in a valley site. Brötz *et al.* (2014) and Eigenmann *et al.* (2009) have also conducted experiments in a mountain site to study coherent turbulent structures and free convection conditions, respectively, with a focus on the morning transition. Despite all the complexities, it would be desirable to be able to describe the processes of the morning transition for dedicated situations by means of ML theory. Bange *et al.* (2007) made an attempt in this direction by using airborne measurements by the helicopter probe Helipod. No conclusive evidence was found in this study because of a limited dataset and large scatter. It was however observed that in the early phase of the transition, the development of temperature, boundary layer height and fluxes are almost linear, which simplifies the modelling of the transition phase. The working hypothesis of this work is that Deardorff scaling can be used to describe the SCBL in the morning transition, when convection is the dominant forcing, even in heterogeneous terrains. Meteorological instrumentation that are used to investigate processes in the ABL are ground-based sensors (e.g., EC-stations), tower measurements, vertical soundings with radiosondes or tethered balloons, aircraft and helicopter measurements as well as remote sensing with radar, lidar, sodar and RASS — to mention only the most common instruments (Kaimal and Finnigan, 1994). Only recently, remotely piloted aircraft systems (RPAS) have started to become more popular in the field of ABL research. The role of RPAS as sensor carriers for ABL research is a central theme of this thesis.

1.2 Wind Energy Research

The evolution towards sustainable energy demands highly efficient renewable energy technologies that can also compete economically with nuclear and fossil-fuel energy resources. Wind energy is a primary branch of renewable energy, and high investments are being made in the field. Wind-energy converters (WEC) are placed within the ABL, and thus they are subject to the physics that is described by boundary-layer meteorology. The rotor tips of the modern WEC can be up to 200 m high and hence can touch all the regimes of the ABL. Wind shear, low-level jet, and turbulence are certain to have an impact on the loads, efficiency, and fatigue of the rotor blades. A better description of the meteorological boundary conditions at specific locations can help to optimize the design of a single WEC and entire wind farms (Emeis, 2013; Zhou

and Chow, 2012).
On the other hand, WEC also affect the ABL. The wakes of large WEC are still subject to intensive research. LES studies try to describe the precise extensions of such wakes (Wu and Porté-Agel, 2011). The thermal stratification of the atmosphere has an influence on the wake structure. Wakes spread out unequally and they decay unequally in different stability regimes (Smalikho *et al.*, 2013; Abkar and Porté-Agel, 2014; Wu and Porté-Agel, 2012). In wind park design, the descriptions of wakes are essential to determine the distance between individual WEC and calculate energy yields. But WEC wakes are also interesting for fundamental boundary layer research, since the wakes of large wind farms can even affect the micro-climate (Smith *et al.*, 2013).

1.3 RPA/UAV And Sensor Technology

Airborne in-situ measurements with manned aircraft have been a tool in atmospheric research for as long as aviation has prevailed. Lenschow (1986) provided a first general guideline for good practice in modern airborne boundary-layer meteorology. A wide variety of meteorological instruments has been utilized to be carried on large manned research aircraft. Wendisch and Brenguier (2013) gives an overview of the state of the art of instrumentation for this type of sensor carrier. A whole new class of sensor carriers are small, unmanned aircraft — the so-called RPA or UAV. The International Civil Aviation Organisation (ICAO) has introduced the term remotely piloted aircraft (RPA) or remotely piloted aircraft system (RPAS) as the official term, which will be used in this thesis from now on. These platforms have their benefit, in lower operational costs and more flexible operations even at low altitudes, within the lower boundary layer. The first outstanding meteorological RPA was the Aerosonde (Holland *et al.*, 2001). It carried standard radiosonde instrumentation for temperature and humidity measurements, and used a pitot static tube in combination with GPS ground speed measurements to estimate wind speed and direction. The M^2AV (Spieß *et al.*, 2007; Martin *et al.*, 2011) was the first UAV system with the capability to measure the three-dimensional wind vector (van den Kroonenberg *et al.*, 2008) and temperature with a resolution that was high enough to allow the calculation of sensible heat fluxes (Martin and Bange, 2014) and turbulent structure parameters (van den Kroonenberg *et al.*, 2011). Other applications were, e.g., the investigation of small-scale events in the ABL, such as entrainment

(Martin *et al.*, 2014). RPAS have appeared in ABL research in large numbers during the last decade. While some have started by focusing on mean measurement of thermodynamic scalars and their vertical profiles (Reuder *et al.*, 2009), others have followed the example of the M^{2}AV and equipped small RPA with flow probes — a development that paves the way to wind vector and turbulence measurement (Reineman *et al.*, 2013; Thomas *et al.*, 2012). Another approach is to only use fast temperature sensors to estimate the turbulent structure parameter of temperature (Lawrence and Balsley, 2013). Of late, an increased interest could be recognized in the field of wind energy research lately (Reuder and Jonassen, 2012; Subramanian *et al.*, 2012; Wildmann *et al.*, 2014a).

Since the M^{2}AV system was no longer developed and maintained, and thus not available to research groups outside the University of Braunschweig, the working group 'Environmental Physics' at the Eberhard-Karls-University of Tübingen (EKUT), under direction of Prof. Dr. Jens Bange, decided to plan a successor and advancement of the M^{2}AV, featuring an improved meteorological sensor unit and overall performance. The requirement specifications were postulated on the basis of the experience with the M^{2}AV and other RPAS in ABL research. The boundary conditions are: the RPA is operated by a small research group as a flexible tool to collect atmospheric data with accuracy and resolution, which allows to capture small-scale turbulence. The main points of these requirements are listed hereafter, and the key points are summarized in Tab. 1:

- The RPA should be small and lightweight to be operated under the regulations of the local CAA. In Germany, a weight of less than 25 kg is necessary to get special permissions under the regulations of the model aircraft and unmanned aerial systems. A weight of less than 5 kg is desired so that general permissions can be issued, which allow flight operations up to 100 m altitude at any suitable locations in the state of Baden-Württemberg. This is especially helpful for system testing and sensor development.
- It should be possible to transport all necessary equipment in one passenger vehicle. This implies that large take-off facilities like catapults are not practical.
- It should be possible to carry out operations in remote areas with poor infrastructure for general aviation (no runway etc.). This is especially critical for the take-off

and landing strategies. Bungee or hand launch and belly landing were seen to be adequate for this purpose in the past.

- Permissions are much easier to get if electrical propulsion is used in the RPA.
- It is important to measure small-scale features of the airflow; hence, the RPA itself should not disturb the airflow significantly in the length scales that are supposed to be measured.
- The propulsion system should in no way disturb the measurement.
- Long endurance of at least one hour is desired. This allows us to get better statistics for turbulence measurement and reduces the risk of a measurement campaign by reducing the necessary number of take offs and landings.
- The time in between flights should be small. This implies that the handling of the RPA is easy for the user and the exchange of batteries can be done quickly.
- Waypoint navigation is the desired mode of operation for the automatic flight of the RPA. It means that a list of spatial coordinates is programmed into an autopilot, which automatically guides the aircraft on straight lines between the waypoints. The possibility to change waypoints during the flight is necessary.
- Sensors will be calibrated for a defined flow speed. Thus, it is desirable that the autopilot should maintain airspeed to a precision of $\pm$ 1 m s^{-1}.
- It is desired to be able to fly in thin atmospheric layers. It is therefore required to maintain altitude with a precision of $\pm$ 5 m.
- The spatial resolution of measured data (i.e. temperature, humidity, barometric pressure, airflow, position, and orientation of the aircraft) should be in the sub-metre range to capture small-scale eddies in the inertial sub-range of turbulence. This has implications on the desired cruising speed, the sampling rate, and the necessary response times of the sensors. The initial target values are: 20 m s^{-1} cruising speed, 100 Hz sampling rate, and a time constant better than 0.05 s for all sensors.
- A possibility to monitor all sensor data during the flight is necessary.

aircraft	
weight	$<$5 kg
endurance	$>$ 1 hour
propulsion	electric
payload capability	$>$1 kg
take-off	bungee or hand launch
autopilot	
guidance	waypoint navigation
altitude precision	$\pm$ 5 m
airspeed precision	$\pm$ 1 m s^{-1}
measurement unit	
spatial resolution	$<$ 1 m
sampling rate	100 Hz
sensor response times	$<$ 0.05 s

Table 1: Requirement specification summary for a research RPA at the University of Tübingen.

- The sensor system and RPA should be independent.
- The payload capabilities should go beyond the necessary minimum for the thermodynamic sensor package, as used in the M^{2}AV, and leave space for additional sensors (e.g., camera, laser altimeter, etc.) up to 1 kg weight.
- Last but not least, the system ought to be affordable and not more expensive than a small passenger vehicle even after including all the sensors.

Till date, no commercially available RPA exists, which would meet all the requirements listed above, especially regarding the meteorological payload. This is merely because the application of RPA in atmospheric research is a niche that does not pay off for profit-oriented companies. In this thesis, the MASC RPA will be described as a sensor carrier platform that was developed in cooperation with other research institutes and a local model aircraft builder (see Sect. 2.1) to meet all requirements. In the past, results from RPA measurements were always subject to large uncertainties because the sensor system was neither well described nor systematically tested. One goal of

this thesis is to attend to this problem, and three of the articles that are included in this thesis are dedicated to design, qualification and testing of parts of the measurement system, namely the temperature measurement, the airflow measurement, and the humidity measurement. Especially the short response times that are necessary to capture small-scale turbulent motion with a moving platform is a problem, which has been tackled in these three articles. A main challenge is to reconcile the requirements of high accuracy and short response time with lightweight design, low power consumption, and small size. Further demands derived from the requirement list are robustness of the sensors in harsh environments, easy maintenance, and reliable calibration.

2 Results

This section will provide a summary of the most important results that are explained in detail in the articles attached to this thesis (Sect. A.1 to A.5).

2.1 The Multi-Purpose Airborne Sensor Carrier

All flight tests and atmospheric measurements that were carried out to collect the data presented in this thesis were done with an RPA that was specifically designed and build to meet the requirements described in Sect. 1.3. The airframe, equipped with RC-components, was build by the model aircraft company Roke-Modelle, based in Wannweil, Germany. The design with an electrical pusher propulsion system has the advantage of not disturbing the measurements in front of the fuselage. This was validated in a wind tunnel experiment with engine and measurement unit running. The drawback of this solution is an increased noise level compared with the twin-engine configuration of the M^2AV. Regarding the rudder configuration, a choice was made in favour of a V-tail, which is lightweight and can be assembled easily. Flaps and ailerons are placed on the trailing edge of the wings and can be controlled independently or in a combined air brake configuration to decelerate the aircraft during the landing approach.

A core part of the RPAS is the ROCS (Research Onboard Computer System) autopilot, developed and maintained by the Institute for Flight Mechanics and Control (IFR) at the University of Stuttgart. For the specific application in atmospheric research,

Figure 2: The MASC RPA in flight.

wing span	2.60 m, 3.00 m or 3.40 m
rudder configuration	ailerons, flaps, v-tail
weight	5 – 7.5 kg, depending on battery load
payload	max. 1.5 kg
endurance	15-60 min, depending on battery load
cruising speed	24 m s^{-1}
propulsion	electrical pusher motor
autopilot	ROCS, IFR Stuttgart
take-off	bungee launch

Table 2: Characteristics of the MASC RPA.

the ROCS was programmed to control the RPA at a constant airspeed of approximately 24 m s^{-1}. Waypoint navigation with the option to adjust waypoints during the flight constitutes the standard features of the autopilot. Automatic take off and landing are theoretically possible, but they are not used due to safety concerns. The combination of the ROKE-Modelle aircraft and the ROCS autopilot is operated at the EKUT under the name 'MASC' (multi-purpose airborne sensor carrier). Fig. 2 shows MASC during a landing approach. Table 2 summarizes the specifications of the RPA. Comparing the specifications with the requirements, it can be found that the desired weight limit is exceeded, if at the same time the target endurance should be held. Other than that, MASC turned out to fulfil the requirements adequately and has been deployed in 10 measurement campaigns since 2012 on more than 35 campaign days. The number of successful flights, including test flights, has recently exceeded 250.

The purpose of MASC is to carry sensors for boundary-layer research. In the first place, this means a thermodynamic sensor package is required, including tempera-

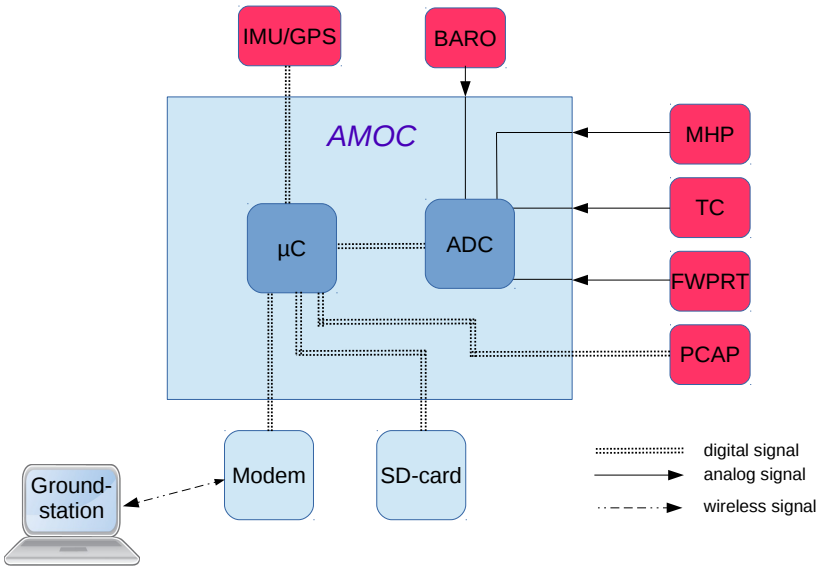

Figure 3: Schematic of the thermodynamic measurement unit.

ture, humidity, wind, and barometric pressure measurement. In cooperation with the University of Applied Sciences Ostwesfalen-Lippe (HS-OWL), the data acquisition system AMOC (Airborne Meteorological Onboard Computer) was developed as the central unit of the meteorological sensor system. It is based on two 32-bit microcontrollers and a 24-bit analog-to-digital converter. All sensors interface with AMOC and the data is stored in an SD-card with a sampling rate of 100 Hz. At the same time, a serial output that contains all sensor data is provided at 1 Hz. In MASC, this output is connected with a 2.4 GHz modem to establish a telemetry link to a groundstation software, which allows real-time monitoring. The temperature sensors are discussed in detail in Sect. 2.2.1 and Sect. A.1. The humidity sensor is presented in Sect. 2.2.3 and Sect. A.3. Sect. 2.2.2 and Sect. A.2 is focusing on wind measurement, in particular the airflow measurement with multi-hole probes (MHP). Sensors that are not further described in detail are the inertial measurement unit (IMU) and the barometric pressure transducer. The IMU measures the orientation angle of the RPA and its three-dimensional velocity vector in the earth's coordinate system, which are essential for wind measurement. A commercial system, the IG-500N by SBG Systems, is

used for this system, and it provides satisfactory results if the RPA is not subject to excessive dynamics (SBG Systems, 2014). A MEMS barometric pressure transducer of type HCA-BARO by Sensortechnics provides the measurement of air pressure. A representation of the measurement unit is given in Fig. 3.

2.2 Individual Sensor performance

Three of the papers that are part of this thesis were published in the peer-reviewed journal *'Atmospheric Measurement Techniques'* (Wildmann *et al.*, 2013, 2014b,c). The papers deal with design, improvement, qualification, and measurement performance of the sensor technology developed for the MASC.

2.2.1 Temperature

The design of the two temperature sensors and their optimization to be carried on the MASC RPA is described in detail in Sect. A.1. The two sensors operate on the basis of two different physical principles – both, however, are using fine wires in the range of 13-25 μm, which have a very low heat capacity and thus adapt to temperature changes very quickly. Fine-wire temperature sensors have a long tradition in meteorology in general (Foken, 1979), and in airborne meteorology in particular (Friehe and Khelif, 1992; Inverarity, 2000). One of the sensors is a fine-wire platinum resistance thermometer (FWPRT, see Fig. 4, left), inspired by Harrison and Pedder (2001), who designed a similar instrument for radiosonde applications. The resistance of the platinum wire is almost linear to temperature changes. A constant measuring current is passed through the fine wire and an electronic circuit, using two operational amplifiers, converts the voltage at the wire into a useful measurement voltage. The second sensor is a thermocouple (TC, see Fig. 4, right). The measurement principle of a TC is based on thermodiffusion, which is unequally strong in wires of different material. Soldering two metal wires together at a measurement tip makes it possible to measure the voltage (the so-called thermovoltage) between the open ends of the wires, which is linear to the temperature gradient between the tip and the open end (Pelster *et al.*, 2005). The TC measurement is always a relative measurement between the TC tip, which is in the flow, and the so-called cold junction, which is at the point where the open ends of the TC wires are attached to the amplifying electronic circuit. In order to achieve an abso-

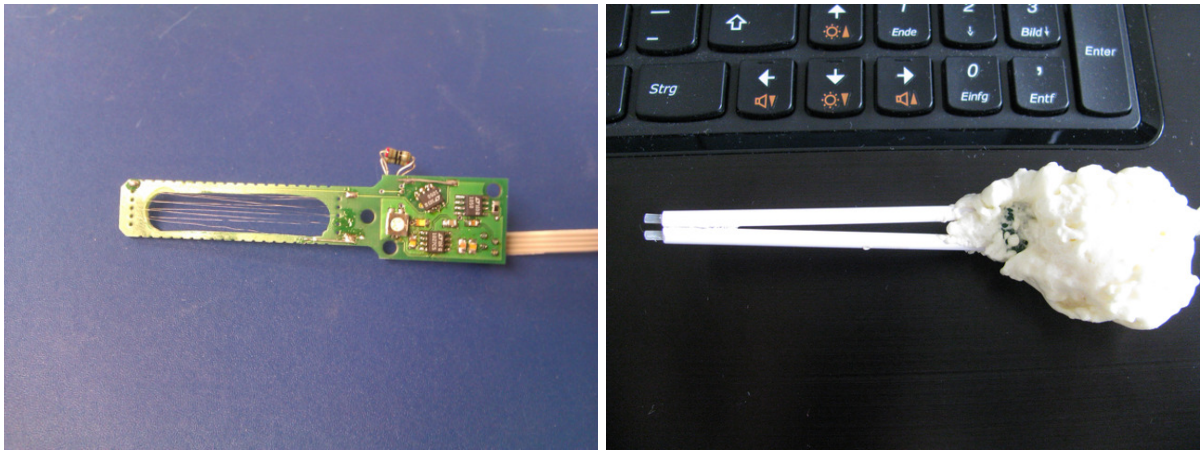

Figure 4: Picture of the FWPRT (left) and the TC (right).

lute reading, various scenarios exist: to measure the precise cold-junction temperature and add it to the differential measurement of the TC is the most straightforward approach. It is, however, crucial that there exists no temperature difference between the cold-junction temperature sensor and the cold-junction soldering spot. There are also ICs that automatically add a voltage to the TC voltage, proportional to the thermovoltage of the absolute temperature at the cold-junction. One of these ICs is the LTK001 and is described in A.1. It was found to be not accurate enough for decent meteorological measurements. The strategy that was finally pursued in the presented study is that the TC measurement is complementarily filtered with another slower sensor in the flow. For the presented setup, this second sensor was a PT1000, a very accurate platinum resistance thermometer with a resistance of 1000 Ω at 0 °C. Complementary filtering means that the PT1000 is low-pass filtered and the TC is high-pass filtered at the same frequency, and the two signals are added to each other. The filter frequency has to be chosen so that the PT1000 can still resolve signals at this frequency, and the cold-junction of the TC has to be protected from temperature changes faster than the filter frequency by some kind of insulation.

Although both measurement principles are well known, no inter-comparison exist, in the literature between thermocouples and resistance thermometers for airborne meteorology, and especially, for the application on RPA. Test flights in the vicinities of the Meteorological Observatory Lindenberg, operated by the DWD, were conducted with MASC to qualify the accuracy and precision of the new instruments. To estimate the to-

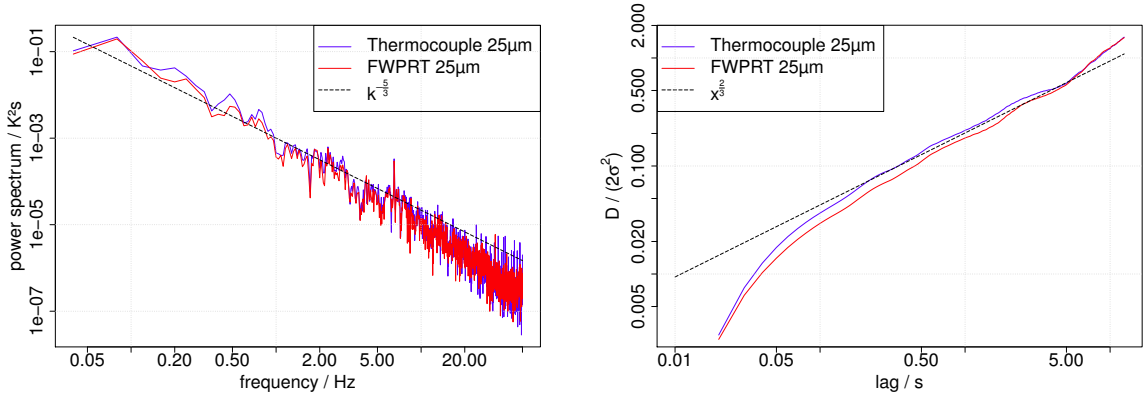

Figure 5: Variance spectrum (left) and structure function (right) of FWPRT (red) and TC (blue).

tal accuracy of the sensors, square flight patterns around a 99 m meteorological tower were performed at three heights where resistance thermometers are installed on the tower (60 m, 80 m and 98 m), maintaining each altitude for approximately the same time that is used as the averaging time for the stationary instruments (i.e. 10 minutes). A bias between the RPA sensors and the tower sensors was found, which showed to be persistent throughout the measurement campaign and was of the order of 0.5 K. Removing this bias, which is assumed to be a calibration error, a precision better than 0.1 K was found. Further validation of the sensor accuracy was done by vertical profile comparison flights with radiosondes and remote sensing instruments. The lapse rates, which have been measured, are in very good agreement, only the remote sensing instruments differ in altitudes where the signal-to-noise ratio of the soundings becomes too low. Unfortunately, in the described setup for the TC on the RPA, the cold-junction insulation was not good enough to prevent temperature changes faster than the response time of the PT1000. This shows in the vertical profiles, where temperature changes significantly within several seconds, as a hysteresis in ascent and descent.

Additional analysis of the sensor performance with regard to common error sources like radiation, adiabatic heating, or self-heating of the resistance thermometer was done in dedicated tests. Self-heating of the FWPRT was already minimized in the design process to be of the order of 10^{-4} K at the typical MASC cruising speed. Radiation effects only showed to have a significant impact on the complementary PT1000 measurement in the TC system. This is why a shield was designed to protect the cold junc-

tion of the TC from direct radiation input. Reverse heading manoeuvres with shadow on the sensor in one direction and direct sunlight in the other revealed that the shield provides the desired protection. In order to quantify the performance of the sensors with respect to response times, a spectral analysis of the temperature measurement in a turbulent flow (the daytime CBL) was done with the help of a variance spectrum and a structure function (see Fig. 5). Up to a frequency of 20 Hz (corresponding to a time lag of 0.05 s in the structure function), both sensors show equally good performance following the theoretically predicted slopes for a locally isotropic turbulent flow (Kolmogorov, 1941).

In conclusion, both sensors show similar good performances in the measurements of the average temperature and in the resolution of small-scale turbulence. Since the TC setup is more prone to design flaws, especially with regard to a proper cold-junction design, the inexperienced user might favour the FWPRT.

2.2.2 Airflow

Measuring the three-dimensional wind vector $\mathbf{v}$ with a moving platform requires the measurement of the true airspeed vector $\mathbf{v}_{\mathrm{tas}}$, the groundspeed vector $\mathbf{v}_{\mathrm{gs}}$, and the orientation of the aircraft to transform the airspeed vector to the meteorological coordinate system ($\mathbf{M}_{\mathrm{mf}}$, see Eq. 1).

$$\mathbf{v} = \mathbf{v}_{\mathrm{gs}} + \mathbf{M}_{\mathrm{mf}}\mathbf{v}_{\mathrm{tas}} \tag{1}$$

In the MASC thermodynamic sensor package, the commercial GPS/IMU unit IG500-N by the company SBG Systems is included (SBG Systems, 2014), which provides $\mathbf{v}_{\mathrm{gs}}$ and $\mathbf{M}_{\mathrm{mf}}$. For the measurement of the airflow vector with a high temporal resolution, commercial systems are rare and hence highly priced. Multi-hole probes (MHP) are a robust way to measure not only the true airspeed but also the airflow angles. The most popular field of application for MHP is mean airflow measurements in wind tunnel experiments (Telionis *et al.*, 2009; Treaster and Yocum, 1979; Sumner, 2000). The MASC thermodynamic sensor package features such an MHP, which was designed by the Institute for Fluid Dynamics (ISM) at the University of Braunschweig (see Fig. 6). The specific probe is a five-hole probe (5HP) with four additional holes perpendicular to the flow in front of a milled ring edge, merging into one common static pressure port. In order to achieve trustworthy turbulence measurement with this kind of instru-

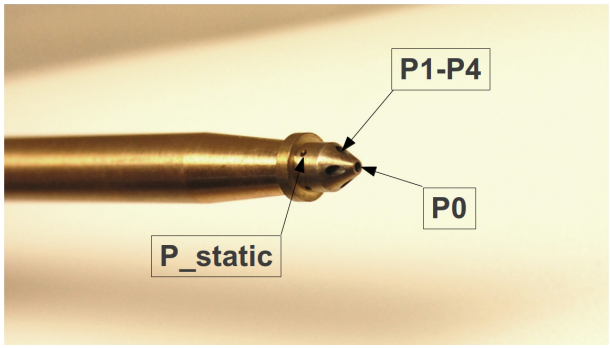

Figure 6: Picture of the 5HP, which is included in the measurement unit for MASC.

ment, a proper design and qualification of the whole measurement chain has to be done. In contrast to the predecessor system M^{2}AV, which contains the same probe, changes have been made to the airflow measurement with the 5HP in all parts of the measurement chain:

- The *mechanical design* with a milled ring edge behind the static pressure ports was questioned and found to be inappropriate for turbulence measurement because the ring induces increased turbulence at the static pressure ports at certain airflow angles. As a result, the *conversion of differential pressures at the probe to flow angles* was changed in such a manner that a flow angle estimation without using the static pressure holes is possible.

- An important part of the measurement system with MHP is the *pneumatic tubing system*, which connects the actual probe with pressure transducers. Key factors of a properly designed pneumatic system with little damping of the pressure signal are a suitable tubing material, the tubing length, and as little branching as possible. In the pneumatic connection of the M^{2}AV system, many branches were derived from the P0-hole of the 5HP. What did not seem to be a problem considering the amplitude response is shown in A.2 to be critical, in combination with the pneumatic connection of holes P1-P4. Different phase shifts in signals that are added in post-processing can lead to artefacts in the measured airflow vector. For the MASC 5HP system, the cut-off frequency of the pneumatics was theoretically designed to be far beyond 50 Hz and verified in an experiment. It was also made sure that the pneumatic response at all holes of the MHP is consistent and thus different phase-shifts that can lead to artificial signals are omitted.

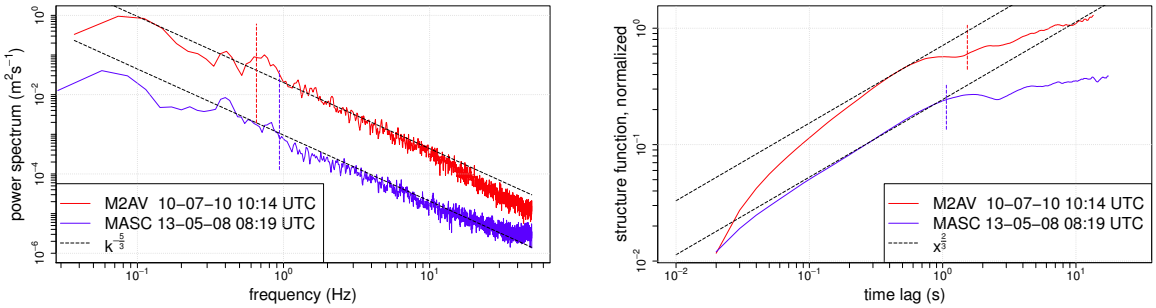

Figure 7: Comparison of variance spectrum (left) and structure function (right) of true airspeed measurement with MASC (blue) and M^{2}AV (red).

- To measure the dynamic pressures at the single holes of the probe, MEMS *pressure transducers* are connected to the probe via the pneumatic tubing. A new kind of pressure transducers that work on the basis of a thermal flow measurement is used in the MASC 5HP setup, which, unlike membrane-based pressure transducers, is insensitive to accelerations and vibrations.

- In the last step, the AMOC DAQ was optimized to guarantee a clean signal without aliasing effects up to at least 20 Hz. A combination of an analogue RC low pass filter and a digital moving average filter is implemented in AMOC and explained in detail in A.2.

To validate the fact that implemented actions to improve the MHP measurements are effective, flights with MASC were conducted and compared with previous measurements with the M^{2}AV. As can be seen in Fig. 7, MASC shows good agreement with the theoretical slopes of a locally isotropic turbulent flow, while the M^{2}AV measurement is strongly damped. The electronics of the M^{2}AV is not known to the author in detail, but it is assumed that a low-pass filter was applied to the MHP measurements in order to damp the noise level, which, according to the presented study, should be much higher.

2.2.3 Humidity

The most challenging thermodynamic quantity to measure in boundary-layer meteorology is water vapour content. A variety of measurement principles exist to measure humidity, and they are discussed in Sect. A.3. A review of the available sensors to

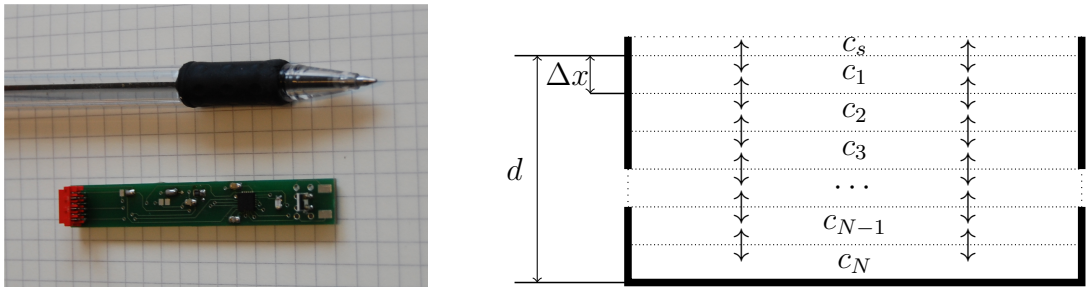

Figure 8: Picture of the humidity sensor (left) and a sketch of the sensor model (right).

measure water vapour content revealed that the typical instruments to capture turbulent fluctuations of humidity are optical instruments that are too heavy and large to be carried on the MASC platform. The type of sensor that is light enough and at the same time robust and small is a polymer-based capacitive humidity sensor. Typically designed for stationary room climate measurements, weather stations or radiosondes, the focus in the design of the sensors is not primarily on fast response times. There are attempts to design fast response versions of this type of sensors – for example, for medical applications or general purpose (Tetelin and Pellet, 2006), but they are still one order of magnitude slower than what is desired for turbulence measurement in the ABL. The goal for the meteorological measurement unit of MASC is to capture all thermodynamic quantities with at least 10 Hz. Eight different capacitive sensors, which have been advertised as fast response instruments by their manufacturers, were tested by the author to check for their accuracy and time response. The P14 Rapid by IST AG (IST AG, 2009) was chosen as the sensor with the best overall performance. In combination with a PCAP capacitance to digital converter chip, it is possible to read out the sensor value with a sampling rate of 100 Hz. The sensor plus electronics could be placed on a PCB smaller than a gum stick (see Fig. 8, left). The specified time constant of 1.5 s could be validated in an experiment. A model of the sensor physics, including the dynamic response, is proposed in A.3. The dynamic model is a diffusion model, which assumes vertical diffusion in the polymer as the main contributor to the sensor dynamics. The numerical model of the sensor divides the polymer into finite volumes, which is illustrated in Fig. 8 (right). To validate the model, a laboratory experiment was set up, which exposed the sensor to a quasi-instantaneous step from low water vapour content to high water vapour content and vice versa. The model performs very well if the diffusion coefficient is tuned to the best fit. The diffusion parameter is not known to

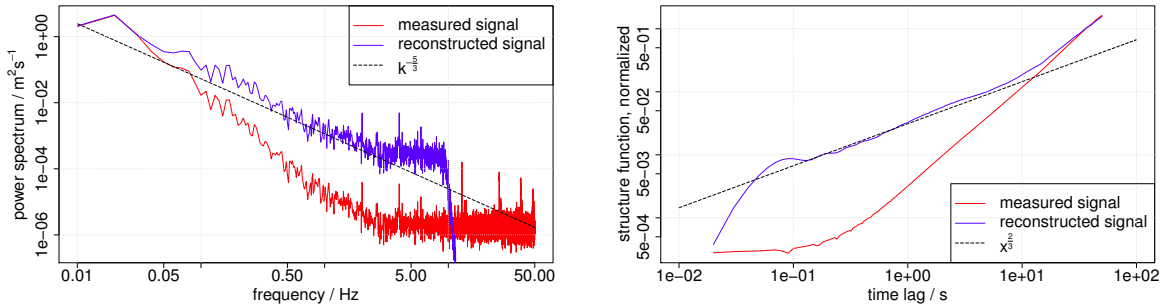

Figure 9: Comparison of variance spectrum (left) and structure function (right) of mixing ratio, before (red) and after (blue) the signal reconstruction with the inverse model.

the author and will not be revealed by the company due to trade secrets (Krogmann, 2012). No significant difference could be found between the rising and falling edge step responses. At low temperatures, the model characteristics change, which is assumed to be due to large changes in the diffusion coefficient under these conditions. It is obvious that thinner layers of the polymer or higher diffusion coefficients would help to decrease sensor response times. Since it is not possible for these parameters to be changed by the end user, other ways have to be found to get as much information from the sensor as possible.

Once a model is described and validated to predict the sensor output with high accuracy, it becomes possible to invert the model and apply it to measured data to restore a signal, which is closer to the original water vapour signal than the raw measured signal. Similar approaches have been followed in the field of temperature measurement with TC (Tagawa *et al.*, 2005), or airflow measurement with MHP (Rediniotis and Pathak, 1999). Previously, in airborne applications, time response corrections were carried out for temperature sensors (Inverarity, 2000) and humidity sensors (Leiterer *et al.*, 2005; Miloshevich *et al.*, 2004). A weakness of this approach is that small damages to the sensor surface, or low temperatures can change the diffusion coefficient and thus the sensor dynamics dramatically. It is therefore proposed to use vertical profiles at the beginning of a flight to tune the diffusion coefficient to the current environment. With a correctly tuned diffusion coefficient, no hysteresis between ascent and descent of the RPA should be visible in the vertical profile measurements of humidity.

To show the capabilities of the inverse model approach for turbulence measure-

ment, variance spectrum and structure function from a measurement flight are shown in Fig. 9. The results are opposed to raw measurements from the capacitive humidity sensor. While the raw measurements from a flight in a turbulent flow do not even show the predicted slope for the locally isotropic turbulence until the frequency of 0.05 Hz, the restored signal by the inverse model appears as a well-shaped turbulent signal until approximately 3 Hz. The noise level of the capacitance-to-digital converter chip limits better results because the inversion of a dynamical model naturally amplifies not only the physical signal but also noise. If the noise-level can be reduced by some more advanced electronic circuit, a restoration of the signal up to 10 Hz seems realistic.

2.3 Morning Transition Of The ABL

The main application of the MASC and its measurement system is to take in-situ measurements of features in the ABL. Measurements in the morning transition of the ABL were done with MASC on five days between May and September 2013 in the Neckar valley. The area is characterized by heterogeneous land use and some considerable orography. A more detailed description of the experiment is given in Sect. A.5. The goal of the measurements was to take systematic measurements of the transition phase from the NIL to a CBL on several days and to compare the measurements. As many as 36 flights with over seven hours of data were used for the analysis. The measurement strategy that was persistently pursued was a combination of vertical profiling (VP) and constant-altitude profiling (CAP) at 100 m above-ground level (agl). On two of the five days, a sonic anemometer of type *Young Model 81000* could be installed on site to capture wind and temperature data at 2 m agl along with the RPA measurements.

The flight pattern for the VP was a horizontal square with a constant climb rate. One VP consists of consecutive ascent and descent. The series of VPs of (virtual) potential temperature θ_v allows estimation of the instantaneous height of the SCBL z_i at the time of each flight and its development in the morning transition. The development of the distribution of water vapour content over altitude documents the transport of water vapour from the surface into the ABL, which was found on all days, with unequally strong occurrence. Horizontal wind speed and wind direction profiles visualize wind shear and wind veer. Crude smoothing had to be applied to the wind measurement because the flight pattern for the VP was not designed in favour of the wind measure-

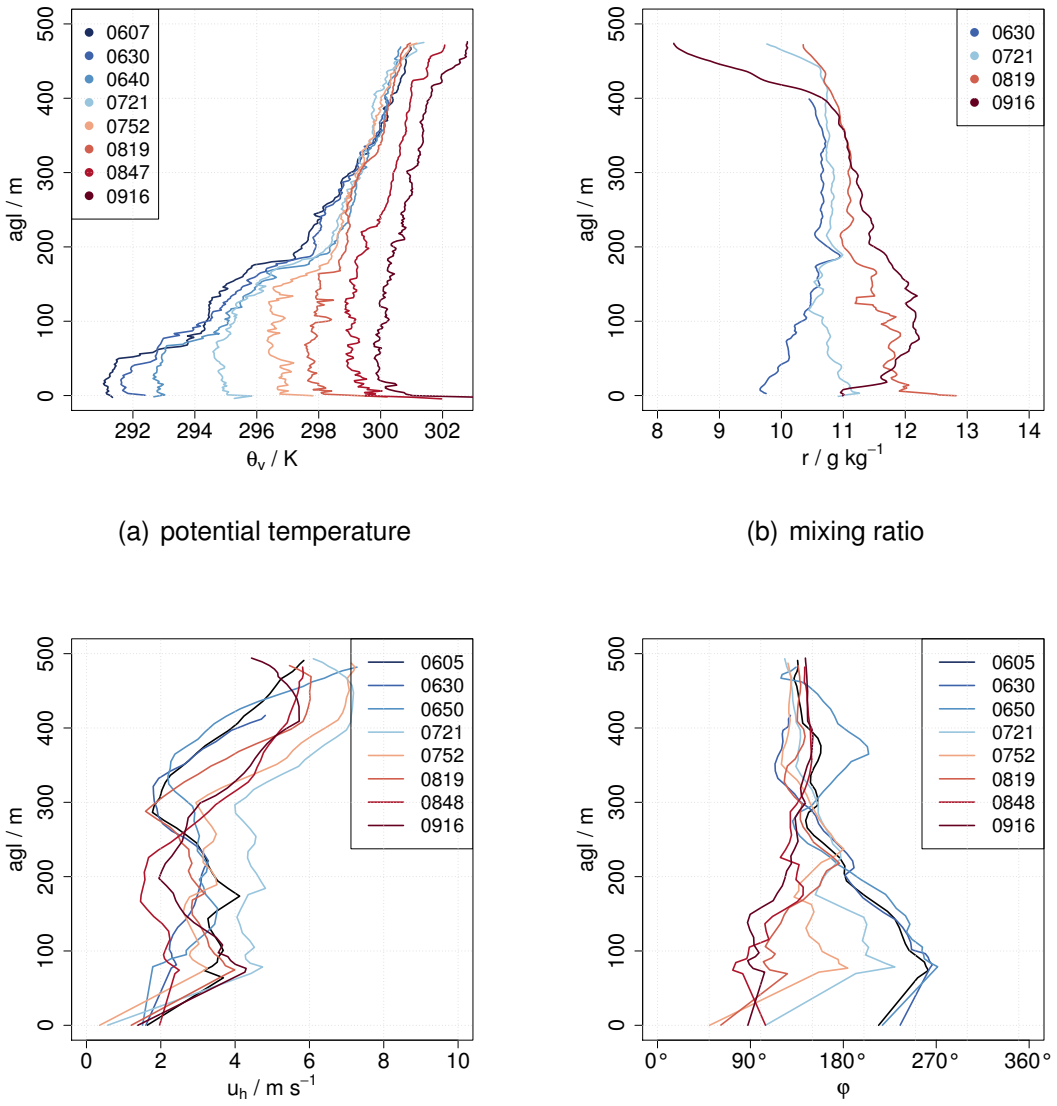

(a) potential temperature

(b) mixing ratio

(c) wind speed

(d) wind direction

Figure 10: The vertical profiles of virtual potential temperature θ_v (left) and mixing ratio r (right) for 5 September. For better readability, a few overlapping profiles of the mixing ratio were spared from the plot.

ment. The angle estimation of the IMU does not show good performance in turns of the RPA, but the VP pattern that was flown in the experiment was a rather small square pattern with only short straight legs in between the turns.

The CAP parts of the measurement flights are, on the one hand, used to calculate the average values of scalars and wind vector at 100 m agl. On the other hand, they serve to calculate the area averaged variances and fluxes of sensible and latent heat. Figure 10 shows an example of the VP measurements of all quantities measured on 5 September 2013. It is obvious how the NIL gets burned off until approximately 0820 UTC and the whole newly formed ML warms up afterwards. It is interesting in this case that a weak stability remains in the ML, which also prevents water vapour from being lifted further up than the original height of the NIL. Wind speeds are fairly constant and low during the transition, but wind direction changes with the growing SCBL towards geostrophic wind direction.
Since for Deardorff scaling, the kinematic surface heat flux is important but could only be measured with a sonic anemometer on two of the five days, the following equation was derived to estimate the surface sensible heat fluxes H_0 from the rate of temperature change in the SCBL and the boundary layer height z_i:

$$H_0 \approx B z_i \rho c_p \frac{\partial \theta}{\partial t} \tag{2}$$

with c_p as the specific heat capacity of dry air, ρ the air density and B the ratio between the height where heat flux crosses zero h_0, and the inversion base height h_i. A value of 0.75 can be found for B in the literature (Sorbjan, 1995). After analysing the data, the value for the given experiment was adjusted to 0.68 in an iterative process, which is elucidated in some more detail in Sect. A.5. It was found that this estimation is only good in the early stages of the morning transition, when the assumption is valid that the temperature in the SCBL changes linearly with time. In this case, however, the results compare fairly well to the sonic anemometer measurement at 2 m agl. The estimates of surface heat fluxes were computed for all measurement days by using the proposed method. With the help of the surface heat flux, ML scaling parameters w_* and θ_* could be calculated (Eq. 3) and heat fluxes measured by the RPA, as well as the variances of potential temperature σ_θ^2, horizontal wind speed σ_u^2 and vertical wind speed σ_w^2 could be scaled and compared for all days (see Fig. 11).

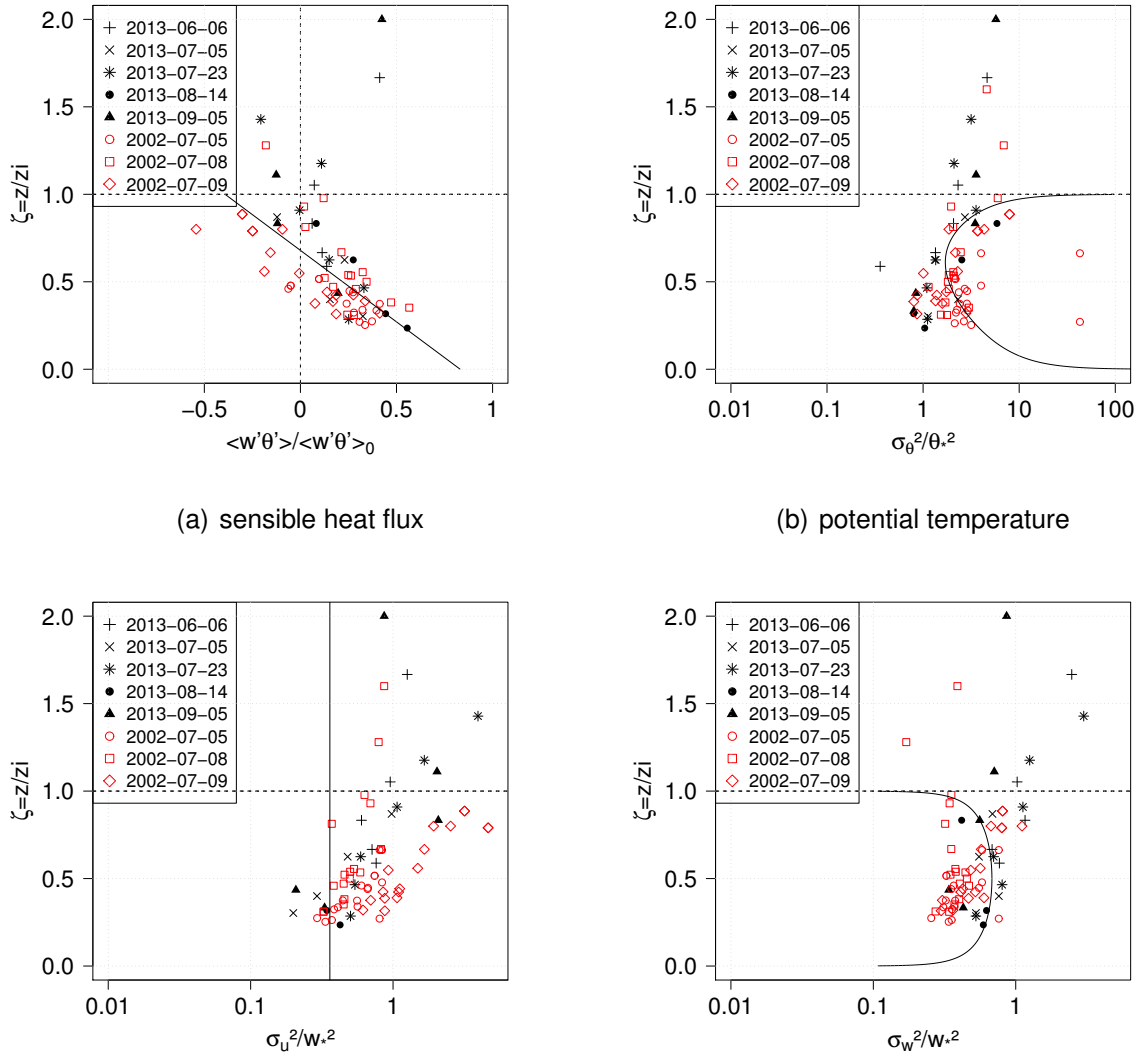

(a) sensible heat flux

(b) potential temperature

(c) horizontal wind

(d) vertical wind

Figure 11: Normalized sensible heat flux (a) and dimensionless variances of potential temperature (b), horizontal wind (c) and vertical wind (d). The dotted line shows the boundary layer top (ζ = 1). The solid line in (a) gives the linear regression of all measurement points below $\zeta = B$. The solid lines in (b), (c) and (d) are theoretical profiles that are found in literature for the ML (e.g. Garratt, 1992; Sorbjan, 1989). In red, data from Bange *et al.* (2007) is included in the graphs.

$$w_* = \left[\frac{g}{\overline{\theta}} z_i \langle w'\theta' \rangle_0\right]^{1/3}$$
$$\theta_* = \frac{\langle w'\theta' \rangle_0}{w_*} \tag{3}$$

The data points coloured in red are additional measurement points taken from the experiment, which is described in (Bange *et al.*, 2007). This experiment was pursuing the same goals, but was carried out in a flat terrain in Northern Germany. It was found that the potential temperature variances are following the ML theory fairly well in the upper half of the scaled boundary layer, and that they complement the measurements by (Bange *et al.*, 2007). No clear trend can be seen in the lower half. One reason could be that the surface heat flux estimation starts to fail here. For horizontal and vertical wind, the graphs of the variances are not comparable to what is expected from the ML theory.

Beyond the analysis with respect to possible ML scalings, some interesting events could be captured during the experiment: On several occasions, it could be seen in the data that the interface between the SCBL and the NIL is far from horizontally homogeneous. In CAP flights of 5 September 2013, approximately 70 m below the inversion that was found in the VP, air masses that had the temperature and water vapour content of the RL were found in parts of the flight leg. On 23 July 2013, a strong discontinuity was found in the development of water vapour profiles. The water vapour content in the SCBL, which continuously increased until 0717 UTC, suddenly drops back to the value above the inversion before starting to increase again. Latent heat flux measurements from the CAP measurements give more insight into what is happening in that instance: just before the water vapour content in the SCBL decreases, strong positive moisture fluxes are measured at 100 m agl, which can be interpreted as dry air entraining into the SCBL from above. After that, positive moisture flux dominates and an ML with higher water vapour content re-establishes itself.

2.4 Wakes Of Wind-Energy Converters

In October 2013, a four-day measurement campaign in the framework of the ‘Lidar Complex’ project was used to take meteorological measurements with the MASC in the close vicinities of large 2.0 – 2.5 MW WECs with rotor diameters of 82 – 110 m. The main objective of the ‘Lidar Complex’ project was validation of lidar instruments

and comparing different instrumentations for wind measurements in wind-energy research – not only in homogeneous and flat terrain but also in complex terrains, i.e. in terrains with large orography and heterogeneous land use. More information is given in Sect. A.4.

The test site in Grevesmühlen, where measurements were done in October 2013, was chosen as a baseline experiment. The area is flat and does conform to the IEC 61400 standard. On site, several instruments were installed: an upward-looking ground-based lidar and a 100 m tower, equipped with sonic anemometers, were located 400 m upstream of one WEC in the main wind direction (South-West). A nacelle-based forward-looking lidar was installed on that same WEC. Hence, measurements with MASC were also centred around this particular WEC. A variety of different experiments with different flight paths was conducted. While in some flights the focus was on upstream measurements to compare with the complementary instruments, other flights were done in the wake of the WEC. Average wind speeds during the measurement flights were up to 15 m s^{-1}.
A major concern about measurement with small RPA in WEC wakes at high wind speeds is that the rapid changes in wind speed and wind direction could force the aircraft into uncontrollable states of flight. Figure 12 confronts the autopilot controlled course, altitude, and airspeed for a flight leg perpendicular to the main wind direction in the wake, with the performance in undisturbed airflow. It shows that the standard deviations of the controlled parameters increase slightly, and the location of the wake can be seen by a drop of the aircraft altitude and a deflection of the aircraft course. However, the disturbance is far from critical and can be corrected by the autopilot within seconds. The example in Fig. 12 shows measurements in an average wind speed of 7 m s^{-1}, but even at higher wind speeds safe operation could be guaranteed with the MASC system.
Knowing that measurements in the wake of the large WEC are possible and safe, more extensive measurements were taken within the wake. Racetracks downstream the WEC, perpendicular to the mean wind at seven altitudes between 75 m and 225 m and three distances to the WEC, were flown to qualify the extension of the wake. In order to visualize the extension of the wake in the y-z-plane (with the x-direction as the main wind direction and z-direction pointing up) at four rotor diameter distances D, an interpolation of the horizontal wind speed measurements between the discrete race-

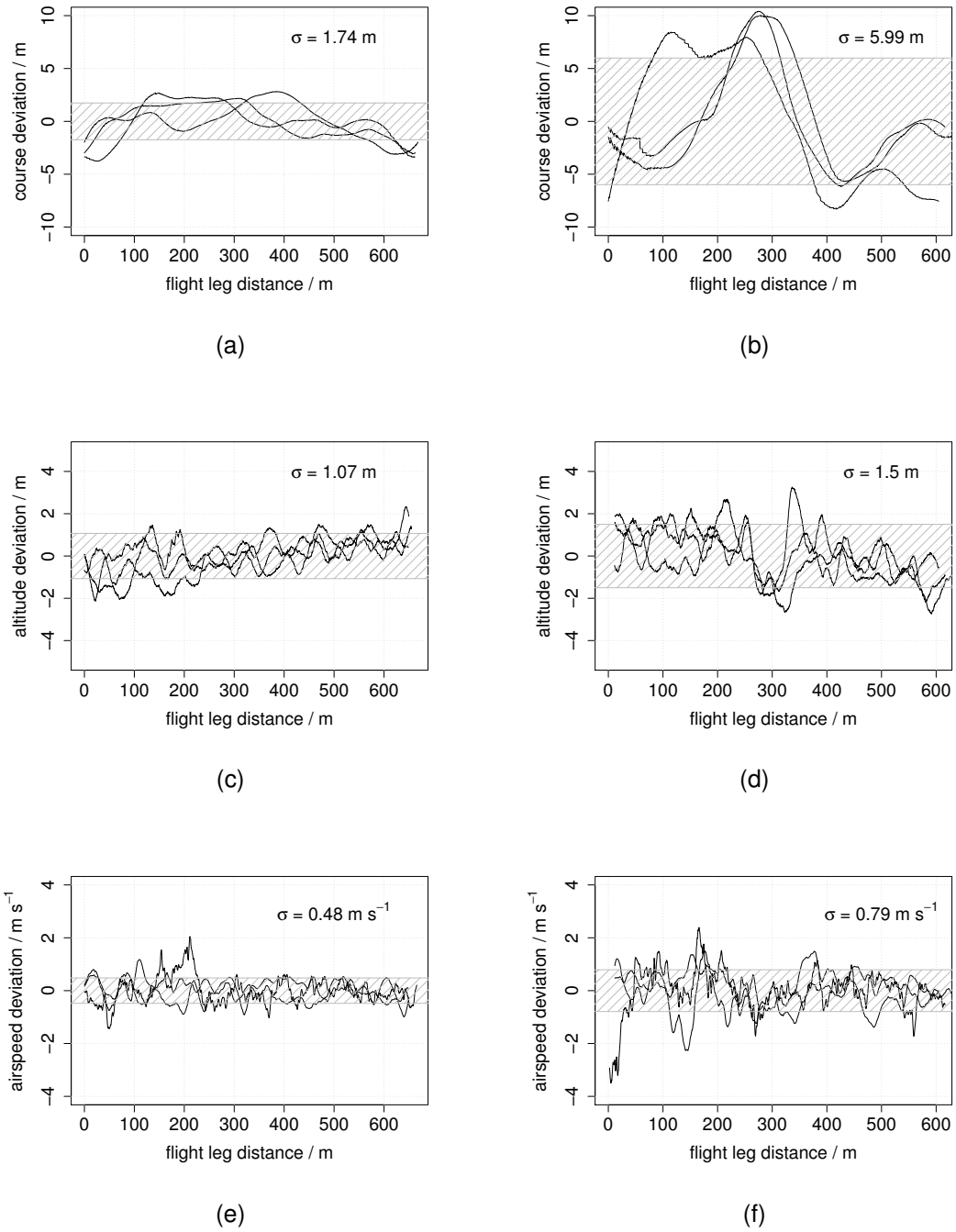

Figure 12: Performance of MASC with ROCS autopilot in undisturbed atmosphere (a),(c),(e) and behind a wind turbine (b),(d),(f). Measurement of data was done during the same flight. The figures show three successive individual flight legs at 100 m altitude (= hub height). An average wind speed of 7 m s^{-1}, perpendicular to the flight path, was present throughout the flight.

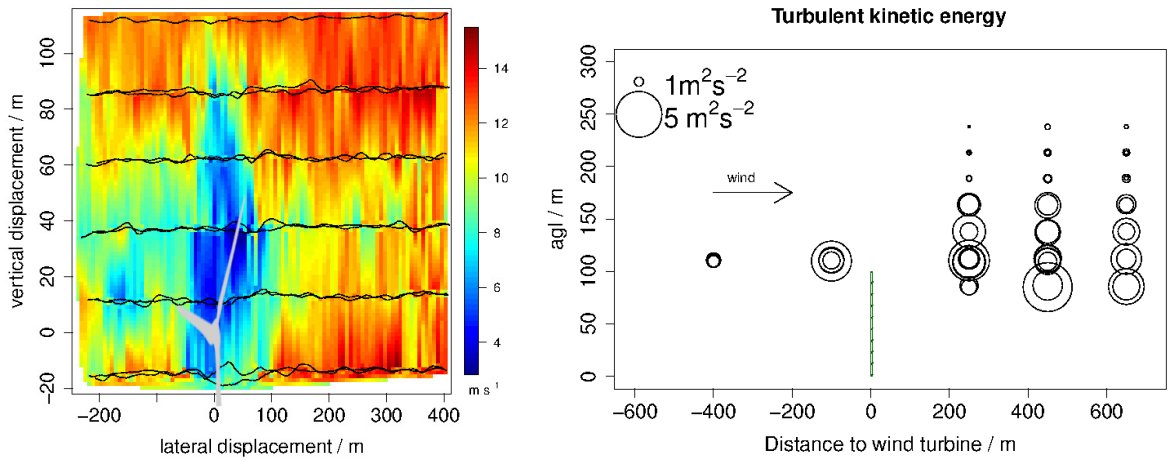

Figure 13: Measurements of MASC in the wake of a large WEC. Left: Interpolation of horizontal wind speed between racetracks in six heights in the y-z-plane, four rotor diameters downstream the WEC. Right: Qualitative TKE measurements in the x-z-plane at seven heights and three distances downstream the WEC.

track heights is shown in Fig. 13 (left). It has to be noted that the picture is somewhat distorted, if single flight legs are used, which do not provide an instantaneous measurement, and therefore cannot account for the meandering of the wake. A solution is to average multiple flight legs at the same altitude in order to obtain an average extension of the wake. For the presented data, two legs at each altitude could be averaged. In future, more legs at the same altitude would be desirable. It shows that the wind speed deficit at the centre of the wake is as high as 70 %. The largest wake effect is found in the rotor plane. To investigate the extension of the wake in the x-z-plane, TKE was calculated for each flight leg and is shown in Fig. 13 (right). TKE over one racetrack length is in this case used as a measure to compare the turbulence in the wake and outside the wake. The values are not comparable with what would be found with a stationary measurement inside the wake, since one racetrack includes parts of the wake and parts of undisturbed airflow. The measurements were taken in a neutrally stratified boundary layer. This shows that under these conditions, the wake has a sharp cut-off just above the rotor plane, which is consistent with LES studies (Abkar and Porté-Agel, 2014). Unfortunately, the test site did not allow flights in further distance behind the

WEC and hence the decay of the wake could not be captured.

3 Discussion

Within this thesis, the application of a small RPA for ABL research has been described. A decade ago, airborne in-situ measurements were only possible in high-budget experiments with large infrastructure. The MASC RPA is yet another proof that technology has advanced to a degree that allows any small research group to do high-quality research with these kind of instruments. A large part of this thesis is dedicated to sensor development, which works towards a measurement system that can compete in data quality and reliability with the already established measurement systems. The goal to achieve 20 Hz frequency resolution of measured signals in flight could be achieved for temperature and airflow. The humidity measurement could be significantly improved, but a reduction of the signal noise is still necessary to capture turbulent signals with 10 Hz or more. Naturally, the application of RPA has to be traded off against remote sensing instruments, towers, or ground-based measurements with regard to the research goals. To classify MASC as a measurement tool for ABL research, a short confrontation of the main benefits and limitations of the system is given in Tab. 3.

It is evident that legal restrictions are the main limitations to the possibilities that are technically available. However, the restrictions are necessary for a seamless integration of RPAS in civil airspace, and experiments have to be designed to meet the requirements of safety and regulation in the first place. Two experiments were presented in this thesis, which demonstrated the capabilities of MASC with its optimized sensor system.

In the field of fundamental research of ABL physics, an experiment was carried out to investigate physical processes in the transition of a NIL to a CBL. The hypothesis that ML scaling can be used to describe the SBL throughout the transition phase cannot hold for all parameters. The variances of horizontal and vertical wind speed did not follow the same laws that are used in the literature for the ML. The variance in temperature, however, was found to be in line with ML theory, at least in the upper half of the scaled boundary layer. It is still open to debate whether the large deviations in the lower part are due to measurement errors in an increasingly convective boundary layer or physical processes that are not accounted for in the Deardorff scaling. Further ex-

+ In-situ measurement with large horizontal and vertical coverage are technically possible. + Airborne in-situ measurements down to a few meters above ground are possible. + Flexible operation in remote areas, requiring only small infrastructure. + Relatively low-cost.
- Legal restrictions in most civilized countries restrict horizontal and vertical coverage to operation in sight. Multiple pilot operation allows to enhance the horizontal coverage, but vertical profiling will be legally impossible above 700 m with the MASC RPA. - Flight operation, at least in Germany, is mostly restricted to the time between sunrise and sunset. - No continuous operation is possible. One measurement flight duration is in the order of 30-60 minutes. The time between landing and the next take-off is approximately 20 minutes.

Table 3: Confrontation of main benefits and limitations of the MASC RPA for ABL research.

periments will be necessary to investigate this in more detail. Possible improvements to the experiment design would be to decrease the height of the CAP flights and see if at an earlier time in the transition phase, the ML theory is also met at lower scaled boundary layer heights. Further improvement, can be done by changing the flight pattern for the VP. A significantly better vertical profile of wind speed and wind direction could be achieved if the RPA does not climb while maneouvering and hence the lengths of the straight legs increase.

Measurements in the wake of large WEC were shown as an example of how MASC can be applied in wind energy research. It was shown that MASC can be operated safely and valuable wind measurements can be taken, which allow quantification of the wind speed deficit in the wake and the extension of the wake. In future experiments it should be sought to take more measurements of the wake in further distance to the WEC to capture the decay of the wake. The measurements need to be repeated in different stability regimes in order to compare the findings of LES simulations and lidar measurements.

4 Outlook

Assuming that RPAS technology will continue to develop quickly, more of these systems will also be applied in atmospheric sciences. It is important for a successful integration of unmanned aircraft in the tool-kit of atmospheric sciences that a close cooperation with local civil aviation authorities (CAAs) is cultivated and safety will always have the highest priority. Only with the help of CAA, experiments that allow further horizontal and vertical extension of measurement flights can be planned. These kind of flights are, however, necessary, regarding the open questions in the field of convective boundary layers. Another possibility to enhance the measurements from RPA is to operate multiple aircraft simultaneously. Two independent MASC, as well as MASC in combination with other RPA, have already been deployed in experiments. A coordinated swarm flight of multiple RPA is the next step, which is technically possible, but still needs to be implemented for the ROCS autopilot. The advantages of such an application are evident: CAP at multiple altitudes allows measurement of instantaneous vertical profiles of fluxes and the observation of the instantaneous extension of a WEC wake. Sensor technology has been advancing continuously, and despite further developments of those sensors that have already been integrated into the MASC measurement system, new sensors can find their way into the application on small RPA. One example is aerosol sensors, that have recently been combined with the MASC measurement system on the larger RPA ALADINA (Altstädter *et al.*, 2015). A different aerosol sensor, which was developed at the University of Leeds (CLASP, see Hill *et al.*, 2008), is currently being integrated to be carried on MASC itself. Even faster sensors are being developed that are possibly able to resolve turbulence up to the dissipation range. The technology that could make this possible is fast response probes, which have a minimum of pneumatic damping and a signal restoration method similar to what is described in Sect. A.2. Further studies are, however, necessary to integrate and qualify these probes for ABL research with small RPA.

References

Abkar, M. and **Porté-Agel, F.**, **2014**: The effect of atmospheric stability on wind-turbine wakes: A large-eddy simulation study. *Journal of Physics: Conference Series*, **524**(1), 012,138.

Altstädter, B., **Platis, A.**, **Wehner, B.**, **Scholtz, A.**, **Wildmann, N.**, **Hermann, M.**, **Käthner, R.**, **Baars, H.**, **Bange, J.** and **Lampert, A.**, **2015**: ALADINA – an unmanned research aircraft for observing vertical and horizontal distributions of ultrafine particles within the atmospheric boundary layer. *Atmospheric Measurement Techniques*, **8**(4), 1627–1639.

Angevine, W. M., **Baltink, H. K.** and **Bosveld, F. C.**, **2001**: Observations of the Morning Transition of the Convective Boundary Layer. *Boundary-Layer Meteorol.*, **101**, 209–227.

Bange, J., **Spieß, T.** and **van den Kroonenberg, A.**, **2007**: Characteristics of the early-morning shallow convective boundary layer from Helipod Flights during STINHO-2. *Theoretical and Applied Climatology*, **90**(1-2), 113–126.

Beare, R., **2008**: The Role of Shear in the Morning Transition Boundary Layer. *Boundary-Layer Meteorology*, **129**(3), 395–410.

Bennett, L. J., **Weckwerth, T. M.**, **Blyth, A. M.**, **Geerts, B.**, **Miao, Q.** and **Richardson, Y. P.**, **2010**: Observations of the Evolution of the Nocturnal and Convective Boundary Layers and the Structure of Open-Celled Convection on 14 June 2002. *Monthly Weather Review*, **138**(7), 2589–2607.

Brötz, B., **Eigenmann, R.**, **Dörnbrack, A.**, **Foken, T.** and **Wirth, V.**, **2014**: Early-Morning Flow Transition in a Valley in Low-Mountain Terrain Under Clear-Sky Conditions. *Boundary-Layer Meteorology*, **152**(1), 45–63.

Deardorff, J. W., **1970**: Convective Velocity and Temperature Scales for the Unstable Planetary Boundary Layer and for Rayleigh Convection. *Journal of the Atmospheric Sciences*, **27**(8), 1211–1213.

Deardorff, J. W., **1974**: Three-Dimensional Numerical Study of the Height and Mean Structure of a Heated Planetary Boundary Layer. *Boundary-Layer Meteorol.*, **7**, 81–106.

Edwards, J., **Basu, S.**, **Bosveld, F.** and **Holtslag, A.**, **2014**: The Impact of Radiation on the GABLS3 Large-Eddy Simulation through the Night and during the Morning Transition. *Boundary-Layer Meteorology*, **152**(2), 189–211.

Eigenmann, R., **Metzger, S.** and **Foken, T.**, **2009**: Generation of free convection due to changes of the local circulation system. *Atmospheric Chemistry and Physics*, **9**(21), 8587–8600.

Emeis, S., **2013**: *Wind energy meteorology*. Springer, Berlin, 198 pp.

Foken, T., **1979**: Temperaturmessung mit dünnen Platindrähten. *Meteorol. Z.*, **5**.

Friehe, C. A. and **Khelif, D.**, **1992**: Fast-response aircraft temperature sensors. **9**, 784–795.

Garratt, J., **1992**: *The Atmospheric Boundary Layer*. University Press, Cambridge, 316 pp.

Harrison, R. and **Pedder, M.**, **2001**: Fine wire thermometer for air temperature measurement. *Review of Scientific Instruments*, **72**(2).

Hill, M. K., **Brooks, B. J.**, **Norris, S. J.**, **Smith, M. H.**, **Brooks, I. M.** and **de Leeuw, G.**, **2008**: A Compact Lightweight Aerosol Spectrometer Probe (CLASP). *Journal of Atmospheric and Oceanic Technology*, **25**(11), 1996–2006.

Holland, G. J., **Webster, P. J.**, **Curry, J. A.**, **Tyrell, G.**, **Gauntlett, D.**, **Brett, G.**, **Becker, J.**, **Hoag, R.** and **Vaglienti, W.**, **2001**: The Aerosonde Robotic Aircraft: A New Paradigm for Environmental Observations. *Bulletin of the American Meteorological Society*, **82**(5), 889 – 901.

Inverarity, G., **2000**: Correcting airborne temperature data for lags introduced by instruments with two-time-constant responses. *J. Atmos. Oceanic Technol.*, **17**, 176–184.

IST AG, **2009**: P14 - Rapid Capacitive Humidity Sensor. Datasheet V4.3-11/2009.

Kaimal, J. C. and **Finnigan, J. J.**, **1994**: *Atmospheric Boundary Layer Flows - Their Structure and Measurement*. Oxford University Press, 289 pp., 289 pp.

Kaimal, J. C., **Wyngaard, J. C.**, **Haugen, D. A.**, **Š, O. R. C.**, **Izumi, Y.**, **Caughey, S. J.** and **Readings, C. J.**, **1976**: Turbulence Structure in the Convective Boundary Layer. *Journal of the Atmospheric Sciences*, **33**(11), 2152 – 2169.

Kolmogorov, A., **1941**: The Local Structure of Turbulence in Incompressible Viscous Fluid for Very Large Reynolds Numbers. *Dokl. Akad. Nauk SSSR*, **30**(4), 299–303, reprint: *Proc. R. Soc. Lond.* A, 1991, **434**, 9–13.

Krogmann, F., **2012**: discussion on the phone, IST AG.

van den Kroonenberg, A., **Martin, S.**, **Beyrich, F.** and **Bange, J.**, **2011**: Spatially-averaged temperature structure parameter over a heterogeneous surface measured by an unmanned aerial vehicle. *Boundary-Layer Meteorol.*, **142**, 55–77.

van den Kroonenberg, A. C., **Martin, T.**, **Buschmann, M.**, **Bange, J.** and **Vörsmann, P.**, **2008**: Measuring the Wind Vector Using the Autonomous Mini Aerial Vehicle $\mathrm{M^2AV}$. *J. Atmos. Oceanic Technol.*, **25**, 1969–1982.

Lapworth, A., **2006**: The Morning Transition of the Nocturnal Boundary Layer. *Boundary-Layer Meteorology*, **119**(3), 501–526.

Lawrence, D. A. and **Balsley, B. B.**, **2013**: High-Resolution Atmospheric Sensing of Multiple Atmospheric Variables Using the DataHawk Small Airborne Measurement System. *Journal of Atmospheric and Oceanic Technology*, **30**(10), 2352–2366.

Leiterer, U., **Dier, H.**, **Nagel, D.**, **Naebert, T.**, **Althausen, D.**, **Franke, K.**, **Kats, A.** and **Wagner, F.**, **2005**: Correction Method for RS80-A Humicap Humidity Profiles and Their Validation by Lidar Backscattering Profiles in Tropical Cirrus Clouds. *J. Atmos. Oceanic Technol.*, **22**, 18–29.

Lenschow, D. H., **1986**: Aircraft Measurements in the Boundary Layer. In: D. H. Lenschow (editor), *Probing the Atmospheric Boundary Layer*, Amer. Meteorol. Soc., Boston, MA, pp. 39–53.

Lenschow, D. H., **Stankov, B. B.** and **Mahrt, L.**, **1979**: The Rapid Morning Boundary-Layer Transition. *J. Atmos. Sci.*, **36**, 2108–2124.

Martin, S. and **Bange, J.**, **2014**: The Influence of Aircraft Speed Variations on Sensible Heat-Flux Measurements by Different Airborne Systems. *Boundary-Layer Meteorology*, **150**(1), 153–166.

Martin, S., **Bange, J.** and **Beyrich, F.**, **2011**: Profiling the lower troposphere using the research UAV 'M2AV Carolo'. *Atmospheric Measurement Techniques*, **4**, 705–716.

Martin, S., **Beyrich, F.** and **Bange, J.**, **2014**: Observing Entrainment Processes Using a Small Unmanned Aerial Vehicle: A Feasibility Study. *Boundary-Layer Meteorology*, **150**(3), 449–467.

Miloshevich, L. M., **Paukkunen, A.**, **Vömel, H.** and **Oltmans, S. J.**, **2004**: Development and Validation of a Time-Lag Correction for Vaisala Radiosonde Humidity Measurements. *J. Atmos. Oceanic Technol.*, **21**(9), 1305–1327.

Pelster, R., **Pieper, R.** and **Hüttl, I.**, **2005**: Thermospannungen – Viel genutzt und fast immer falsch erklärt! *Physik und Didaktik in Schule und Hochschule*, **1**/**4**, 10–22.

Rediniotis, O. and **Pathak, M.**, **1999**: Simple Technique for Frequency-Response Enhancement of Miniature Pressure Probes. *AIAA Journal*, **37**, 897–899.

Reineman, B. D., **Lenain, L.**, **Statom, N. M.** and **Melville, W. K.**, **2013**: Development and Testing of Instrumentation for UAV-Based Flux Measurements within Terrestrial and Marine Atmospheric Boundary Layers. *Boundary-Layer Meteorology*, **30**(7), 1295–1319.

Reuder, J. and **Jonassen, M. O.**, **2012**: First Results of Turbulence Measurements in a Wind Park with the Small Unmanned Meteorological Observer {SUMO}. In: *Selected papers from Deep Sea Offshore Wind Ramp Conference*, Trondheim, NO, vol. 24, pp. 176 – 185.

Reuder, J., **Brisset, P.**, **Jonassen, M.**, **Müller, M.** and **Mayer, S.**, **2009**: The Small Unmanned Meteorological Observer SUMO: A new tool for atmospheric boundary layer research. *Meteorol. Z.*, **18**, 141–147.

SBG Systems, **2014**: Success Story - UAV Flight Analysis for Wind Measurement. Tech. rep., SBG Systems EMEA, http://www.sbg-systems.com/docs/MASC-UAV-Flight-Analysis.pdf [last access: 02.01.2015].

Smalikho, I. N., **Banakh, V. A.**, **Pichugina, Y. L.**, **Brewer, W. A.**, **Banta, R. M.**, **Lundquist, J. K.** and **Kelley, N. D.**, **2013**: Lidar Investigation of Atmosphere Effect on a Wind Turbine Wake. *Journal of Atmospheric and Oceanic Technology*, **30**(11), 2554–2570.

Smith, C. M., **Barthelmie, R.** and **Pryor, S.**, **2013**: In situ observations of the influence of a large onshore wind farm on near-surface temperature, turbulence intensity and wind speed profiles. *Environmental Research Letters*, **8**(3), 034,006.

Sorbjan, Z., **1989**: *Structure of the Atmospheric Boundary Layer*. Prentice Hall advanced reference series: Physical and life sciences, Prentice Hall, 317 pp.

Sorbjan, Z., **1995**: Toward Evaluation of Heat Fluxes in the Convective Boundary Layer. *J. Appl. Meteorol.*, **34**, 1092–1098.

Spieß, T., **Bange, J.**, **Buschmann, M.** and **Vörsmann, P.**, **2007**: First Application of the Meteorological Mini-UAV 'M2AV'. *Meteorol. Z. N. F.*, **16**(2), 159–169.

Stull, R., **1988**: *An Introduction to Boundary Layer Meteorology*. Kluwer Acad., Dordrecht, 666 pp.

Subramanian, B., **Chokani, N.** and **Abhari, R. S.**, **2012**: Full Scale HAWT: Structure of Near Wake Turbulence Measured with Instrumented UAV. In: *EWEA 2012 Conference Proceedings*, Copenhagen, DK.

Sumner, D., **2000**: Calibration Methods for a Seven-Hole Pressure Probe. In: A. Laneville (editor), *Sixth Triennial International Symposium on Fluid Control, Measurement and Visualization (Flucome 2000)*, Sherbrooke, Canada.

Tagawa, M., **Kato, K.** and **Ohta, Y.**, **2005**: Response compensation of fine-wire temperature sensors. *Rev. Sci. Instrum.*, **76**, 094,904, 4 pages.

Teixeira, J., **Stevens, B.**, **Bretherton, C. S.**, **Cederwall, R.**, **Klein, S. A.**, **Lundquist, J. K.**, **Doyle, J. D.**, **Golaz, J. C.**, **Holtslag, A. A. M.**, **Randall, D. A.**, **Siebesma, A. P.** and **Soares, P. M. M.**, **2008**: Parameterization of the Atmospheric Boundary Layer: A View from Just Above the Inversion. *Bulletin of the American Meteorological Society*, **89**(4), 453–458.

Telionis, D., **Yang, Y.** and **Redinioti, O.**, **2009**: Recent developments in multi-hole probe (mhp) technology. In: *20th International Conference of Mechanical Engineering, Gramado, RS, Brazil*, ABCM.

Tetelin, A. and **Pellet, C.**, **2006**: Modeling and optimization of a fast response capacitive humidity sensor. *Sensors Journal, IEEE*, **6**(3), 714–720.

Thomas, R. M., **Lehmann, K.**, **Nguyen, H.**, **Jackson, D. L.**, **Wolfe, D.** and **Ramanathan, V.**, **2012**: Measurement of turbulent water vapor fluxes using a lightweight unmanned aerial vehicle system. *Atmospheric Measurement Techniques*, **5**(1), 243–257.

Treaster, A. L. and **Yocum, A. M.**, **1979**: The calibration and application of five-hole probes. *ISA Trans.*, **18**, 23–34.

Wendisch, M. and **Brenguier, J.**, **2013**: *Airborne Measurements for Environmental Research: Methods and Instruments*. Wiley-VCH, Berlin, 520 pp.

Wildmann, N., **Mauz, M.** and **Bange, J.**, **2013**: Two fast temperature sensors for probing of the atmospheric boundary layer using small remotely piloted aircraft (RPA). *Atmospheric Measurement Techniques*, **6**(8), 2101–2113.

Wildmann, N., **Hofsäß, M.**, **Weimer, F.**, **Joos, A.** and **Bange, J.**, **2014**a: MASC - a small Remotely Piloted Aircraft (RPA) for wind energy research. *Advances in Science and Research*, **11**, 55–61.

Wildmann, N., **Kaufmann, F.** and **Bange, J.**, **2014**b: An inverse-modelling approach for frequency response correction of capacitive humidity sensors in ABL research with small remotely piloted aircraft (RPA). *Atmospheric Measurement Techniques*, **7**(9), 3059–3069.

Wildmann, N., **Ravi, S.** and **Bange, J.**, **2014**c: Towards higher accuracy and better frequency response with standard multi-hole probes in turbulence measurement with remotely piloted aircraft (RPA). *Atmospheric Measurement Techniques*, **7**(4), 1027–1041.

Wu, Y.-T. and **Porté-Agel, F.**, **2011**: Large-Eddy Simulation of Wind-Turbine Wakes: Evaluation of Turbine Parametrisations. *Boundary-Layer Meteorology*, **138**(3), 345–366.

Wu, Y.-T. and **Porté-Agel, F.**, **2012**: Atmospheric Turbulence Effects on Wind-Turbine Wakes: An LES Study. *Energies*, **5**(12), 5340–5362.

Zhou, B. and **Chow, F.**, **2012**: Turbulence Modeling for the Stable Atmospheric Boundary Layer and Implications for Wind Energy. *Flow, Turbulence and Combustion*, **88**(1-2), 255–277.

A Publications

A.1 Two fast temperature sensors for probing of the atmospheric boundary layer using small remotely piloted aircraft (RPA).

The publication is also available at
`http://www.atmos-meas-tech.net/6/2101/2013/`.

Atmos. Meas. Tech., 6, 2101–2113, 2013
www.atmos-meas-tech.net/6/2101/2013/
doi:10.5194/amt-6-2101-2013

Atmospheric Measurement Techniques
Open Access

Two fast temperature sensors for probing of the atmospheric boundary layer using small remotely piloted aircraft (RPA)

N. Wildmann, M. Mauz, and J. Bange

Center for Applied Geoscience, Eberhard-Karls-Universität Tübingen, Tübingen, Germany

Correspondence to: N. Wildmann (norman.wildmann@uni-tuebingen.de)

Received: 15 February 2013 – Published in Atmos. Meas. Tech. Discuss.: 28 March 2013
Revised: 10 July 2013 – Accepted: 17 July 2013 – Published: 22 August 2013

Abstract. Two types of temperature sensors are designed and tested: a thermocouple and a fine wire resistance thermometer. The intention of this study is to figure out which kind of measurement principle is in general more suited for atmospheric boundary layer meteorology with small remotely piloted aircraft (RPA). The sensors are calibrated in a NIST traceable climate chamber and validated in flight against tower measurements, radiosondes and remote sensing. The sensors have a measurement range of at least −10–50 °C, an absolute RMS error of less than ±0.2 K which is stable over the lifetime of the sensors, and a resolution of about 0.01 K. Both devices are tested for typical errors like radiation error and adiabatic heating, as well as for their dynamic response. Spectral resolutions of up to approximately 10 Hz can be obtained with both sensors, which makes them suitable for turbulence measurement. Their low cost of less than 100 EUR in pure hardware is a major advantage for research with small RPA.

1 Introduction

In situ observations in the atmosphere are of highest interest for weather nowcasting, forecasting, avionics and fundamental research. Measuring with aircraft has been a field of research for as long as aircraft exist (Neisser et al., 2002). A good overview of systems and strategies for airborne measurement of wind, temperature, and many other quantities is given in Lenschow (1986) and other specialist literature (Wendisch and Brenguier, 2013; Emeis, 1995). An important aspect for the energy budget of the earth includes the turbulent fluxes and turbulent structures of the atmospheric boundary layer (ABL) (Garratt, 1992). For the sounding of the atmosphere, numerous different methods are available nowadays: ground-based measurements, tower measurements, vertical soundings with radiosondes or tethered balloons, aircraft and helicopter measurements as well as remote sensing with radar[1], lidar[2], sodar[3] and RASS[4], to mention only the most common instruments (Kaimal and Finnigan, 1994). Especially for the measurement of spatial averages of fluxes over heterogeneous terrain, ground-based, tower and radiosonde measurements are not suitable, because they are spot measurements which rely on the assumption of terrain homogeneity to calculate fluxes (Bange et al., 2006). Therefore, aircraft are much better suited instruments for these kinds of measurements. They can cover a wide area and perform in situ measurements that do not rely on model assumptions of the atmosphere like remote sensing instruments do.

In contrast to stationary temperature measurements, sensors in airborne applications are facing specific requirements due to their operation on a moving platform in high stream velocities. While some issues like robustness or electromagnetic compatibility have to be addressed in the design process, other error sources like the heating of the sensor due to the conversion of kinetic energy to heat at the sensor surface have to be considered in the data analysis. The most commonly used temperature sensor for airborne research is the Rosemount total air temperature sensor (Rosemount, 1986). It has been used in many meteorological campaigns with manned aircraft and systematically investigated. For example, Friehe and Khelif (1992) tested the sensor against an

[1] Radio detection and ranging
[2] Light detection and ranging
[3] Sound/sonic detection and ranging
[4] Radio acoustic sounding system

Published by Copernicus Publications on behalf of the European Geosciences Union.

NCAR K sensor and a modified Rosemount probe to find out about time responses, adiabatic heating effects and recovery factors. Inverarity (2000) found methods to correct the dynamic system of the Rosemount probe to measure more precise vertical profiles. Haman et al. (1997) designed a new sensor called "ultra-fast thermometer", which design-wise makes it possible to measure in clouds without contamination of the measurement wire with cloud droplets. It uses a 2.5 µm platinum tungsten wire, which makes it fast enough to make time response corrections obsolete. All these sensors are designed to be installed on manned aircraft, and they are not optimized for small size or light weight.

Smaller sensors for airborne temperature measurement can be found in the context of radiosondes for vertical sounding of the atmosphere up to 30 km. These sondes need to be lightweight to be able to rise and be of low cost, because once released it is not guaranteed that the instrumentation can be recovered. Commercially available sondes work with thermistors or capacitive wire technology for temperature measurement (Nash et al., 2005). Typically, the wires used in these commercial sensors are coated or protected in some way to make them more robust at the cost of response time. Correction algorithms can help to compensate the time response error (Luers, 1997). Radiosondes are not suitable for turbulent flux measurements, because they only rise vertically. At ascent rates below $10\,\mathrm{m\,s^{-1}}$ and time constants ≤ 1 s, the blur in the allocation of the temperature reading to the corresponding altitude has a size of 10 m. For their purpose of vertical soundings up to a few kilometres, this is an acceptable error.

While meteorological measurements with manned aircraft and radiosondes are frequently performed, measurements with small unmanned systems are relatively new and not well established so far. Nevertheless, numerous different systems have been developed within the last decade and have proved to produce valuable data (Martin and Bange, 2013; Martin et al., 2011; Reuder et al., 2009; Spiess et al., 2007; Dias et al., 2012; van den Kroonenberg et al., 2008). In general, the possibilities for meteorological measurements with small remotely piloted aircraft (RPA) are in between manned aircraft measurements and radiosonde soundings. Modern autopilots make it possible to fly predefined paths, even take off and land automatically if desired. Compared to manned aircraft, their cruising speed is typically lower (20–$30\,\mathrm{m\,s^{-1}}$). The security standards are not as high as with manned aircraft, which in general makes them a more flexible tool, but the lack of harmonized rules in aviation authorities can cause additional limitations for flight permissions. Their application off-road makes it more likely that rough landings will damage a sensor. The space and payload capabilities are rather comparable to a radiosonde than a large research aircraft.

This work gives a description of two kinds of temperature sensors for the application on small unmanned aircraft for boundary-layer meteorology. One sensor is based on a thermocouple, while the other one is a fine wire platinum resistance thermometer (FWPRT). Both sensors were calibrated and tested in a laboratory before doing in-flight measurements and comparison of the results with stationary measurements from a 99 m meteorological tower, as well as remote sensing measurements from a sodar and wind profiler. The goal is to allow for measurements of the atmospheric temperature with a reasonable accuracy and sufficient resolution to also resolve turbulent fluctuations with both kind of sensors. By describing the advantages, disadvantages and problems in design and application, a guidance is given towards finding the best suitable sensor for individual RPA applications. It will be shown that these kinds of sensors can be built at low cost and that typical errors for temperature measurement can be avoided or corrected.

2 Sensor design

2.1 Requirements

The temperature sensors described here are designed for the purpose of measuring mean temperature in the ABL, as well as turbulent heat fluxes. As the target value of absolute accuracy in mean measurements, ± 0.1 K is strived for. Although this accuracy is not critical for the evaluation of thermal stratification or turbulent transport, it can still be of relevance if complementary measurements with ground-based, remote sensing or other airborne instruments are performed. A higher absolute accuracy than ± 0.1 K is hardly achieved by commercial instruments, including the reference instrument in the used calibration chamber. Therefore this value is chosen as the target value for the new sensors.

Typical values for temperature fluctuations in different regimes are given for a field experiment in Wangara (Stull, 1988), stating that in a convective regime, fluctuations $\sigma_\theta < 1$ K are to be expected, and in the stable regime the fluctuations are much smaller ($\sigma_\theta < 10^{-2}$ K). From this example alone it can already be seen that it is important to measure temperature with a resolution and precision equal to or better than 0.01 K.

Short response times are important to measure as far as possible into the inertial subrange of turbulence (Kolmogorov, 1941) to minimize the error in flux measurement introduced by neglecting small-scale turbulence. In the boundaries of solid-state temperature sensors that are robust enough for the application on small RPA, a response time smaller than 0.05 s (20 Hz temporal resolution) is considered a target value. Table 1 gives an overview of these requirements.

2.2 Interfaces and data collection

Both sensors that are described here were developed specifically for the application on a small RPA. The measuring system they are connected to is called AMOC (Airborne

Table 1. Summary of requirements for temperature sensors for the determination of turbulent heat fluxes.

Total accuracy	±0.1 K
Precision	0.01 K
Resolution	0.01 K
Time response	< 0.05 s
Measurement range	−10–50 °C

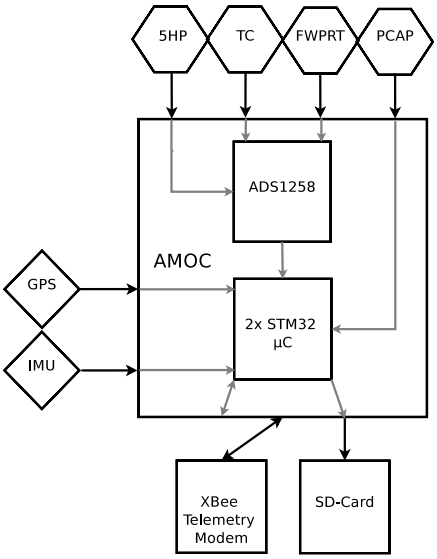

Fig. 1. Block diagram of the meteorological measuring unit for small RPA of type MASC (Multipurpose Airborne Sensor Carrier), developed at the University of Tübingen.

Meteorological Onboard Computer) and was developed in cooperation with the University of Applied Sciences Ostwestfalen-Lippe. The computer is based on two microcontrollers (µC) of type STM32 and interfaces to an inertial measurement unit (IMU) and a GPS receiver. To be able to connect various other sensors, including the two temperature sensors (thermocouple, TC, and FWPRT) described here, a 16-channel analog-to-digital converter (type ADS1258 by Texas Instruments) with 24-bit resolution (15-bit noise-free) and an input range of 0–5 V is integrated. All data are stored on a micro-SD card with a sampling rate of 100 Hz and are also transmitted to a ground station computer for live observation at a rate of 1 Hz. In standard configuration, the whole measuring unit also includes a combined humidity and temperature probe (PCAP) and a five-hole probe (5HP) to measure the true airspeed vector (van den Kroonenberg et al., 2008). A block diagram of the system is given in Fig. 1.

2.3 Thermocouple

Measurements with a thermocouple are in the first place always differential measurements between the measurement

Fig. 2. Thermocouple design with foam coat for thermal insulation of the cold junction.

junction, where the thermocouple wires of unequal alloys are welded together, and the point where the thermoelectric voltage is amplified, or converted to a digital signal. Ideally this point should be in thermal equilibrium with the point where the thermocouple wires are physically connected to the electronics, in order not to measure temperature gradients in the measuring system. The big advantage of this method is the possibility to manufacture thin, long thermocouple wires to make point measurements of temperature in remote locations with a very short response time. To get the true absolute temperature, the differential measurement of the thermocouple always has to be added to a measurement of the cold junction temperature (Michalski et al., 1991). Therefore, a well-defined cold junction of the sensor is essential. A possibility to account implicitly for the cold junction temperature is to generate a voltage at the cold junction that corresponds to the thermoelectric voltage of the chosen thermocouple type for a temperature difference of the actual cold junction temperature. This voltage can then be added to the thermoelectric voltage of the thermocouple itself in an analog circuit, which after amplification and multiplication with the correct calibration coefficients gives an absolute temperature reading. An integrated circuit which takes care of this is the LTK001 by Linear Technology. This chip is used in the design shown in Fig. 2.

For this set-up to work, it is essential that the temperature sensor inside the LTK001 measures the true temperature of the cold junction. If there are gradients between soldering junction of the thermocouple wire and the chip, or if the temperature sensor inside the chip responds too slow to a sudden change in temperature, the temperature reading can be corrupted. To reduce these effects, the whole electronic components including the thermocouple connection were coated in insulating foam (Fig. 2).

Another method to get even more accurate absolute temperature readings from the thermocouple is a complementary filter. This means the thermocouple signal is high-pass

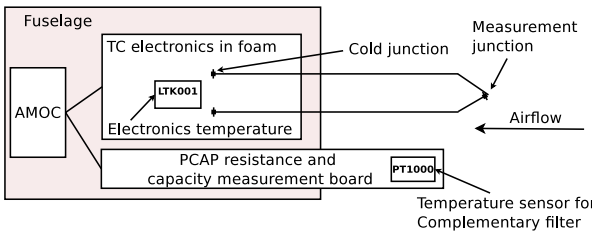

Fig. 3. Schematic drawing of the complete thermocouple measurement strategy.

filtered and added to a signal of a complementary temperature sensor that has a low-pass filter with the same cut-off frequency as applied for the high-pass of the thermocouple. The complementary sensor has to be a more stable and accurate temperature sensor that is also in the flow and responds just fast enough to sense the frequencies that are corrupted by wrong cold junction readings of the thermocouple. For this purpose a PT1000 was installed in close distance to the thermocouple on the RPA. The resistance of the PT1000 is measured with the PCAP01 signal processor by ACAM Messelectronic, which is also responsible for the measurement of a capacitive humidity sensor. This combined sensor is referred to as PCAP in this article. Figure 3 shows a sketch of all the sensors and temperatures involved in the current design. The thermocouple was built and tested with two different wire diameters (25 µm and 13 µm). Like in other meteorological applications (Haman, 1992), the thermocouple type E (CHROMEGA® chromium nickel alloy and Constantan®) was chosen due to its chemical resistance and high sensitivity ($60.9\,\mu V\,K^{-1}$).

For all measurement results of the thermocouple in the following, the complementary filtered signal is used. It showed the more trustworthy results compared to the internal cold-junction compensation of the LTK001. The amplification of the pure thermocouple voltage is chosen to achieve a sensitivity of $20\,mV\,K^{-1}$. Typical noise level for the whole measuring chain is 0.15 mV, so a resolution of 7.5 mK is realistic. The measuring range is adjusted to −10–240 °C. The precision and stability of the operational amplifiers that are used in the design is in the µV range, which is orders of magnitude better than the required precision.

2.4 Fine wire platinum resistance thermometer (FWPRT)

The FWPRT was designed based on Harrison and Pedder (2001). Few adaptations were done in the choice of operational amplifiers, and a printed circuit board was designed to reduce noise and size of the set-up. The basic principle of the circuit is a linearized Wheatstone bridge with current output, which is in the final step amplified and converted to a 0–5 V signal corresponding to approximately −10 to 50 °C measuring range. The measuring range can easily be adapted by

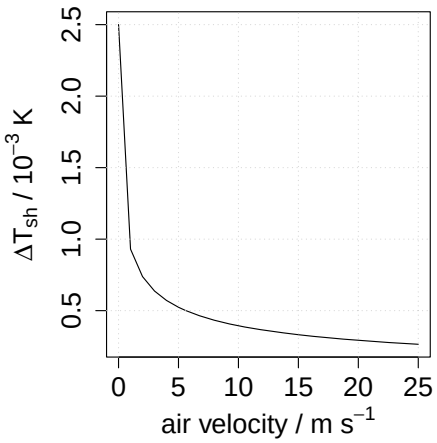

Fig. 4. Theoretically calculated self-heating for a 25 µm platinum wire with the designed measuring circuit.

the choice of the reference resistor in the Wheatstone bridge. One source of error that can already be addressed in the design process is self-heating of the fine wire. The bridge is designed and simulated to have a measuring current through the platinum wire of 0.6 mA. If we take into account that we have forced convection on the wire in flight, we can set up a power budget $P_I = P_c$ which relates the power introduced by the measuring current $P_I = R \cdot I^2$ and the convective heat loss $P_c = \alpha \cdot A\,\Delta T_{sh}$ to calculate the maximum self-heating of the wire:

$$\Delta T_{sh} = \frac{R \cdot I^2}{\alpha \cdot A}, \tag{1}$$

where ΔT_{sh} is the temperature change due to self-heating, $R = 100\Omega$ the resistance of the platinum wire, $I = 0.6 \times 10^{-3}\,A$ the measuring current, α the heat transfer coefficient calculated from the Nusselt number ($0.39 + 0.51 \cdot Re^{0.5}$, with Re = Reynolds number) and the molecular thermal conductivity of the air at a specific airstream velocity, and $A = 3.7 \times 10^{-5}\,m^2$ the curved surface area of the wire (Foken, 1979). Figure 4 shows the theoretical self-heating for these values over a range of airspeeds calculated with Eq. (1). It can be seen that for this measuring current, self-heating effects are two orders of magnitude smaller than the goal for measurement accuracy and thus can be neglected.

The platinum wire of 25 and 13 µm respectively is wrapped around the printed circuit board with minimum contact to the board itself, as can be seen in Fig. 5. It can also be seen that the wires are aligned in flight direction, which will theoretically minimize the effect of adiabatic heating of the wire. The resistance value of 100Ω is a good compromise considering resolution, wire length and self-heating. Reducing wire length to get closer to point measurements will also reduce the resistance. A higher resistance gives better resolution, but the measuring current will necessarily increase,

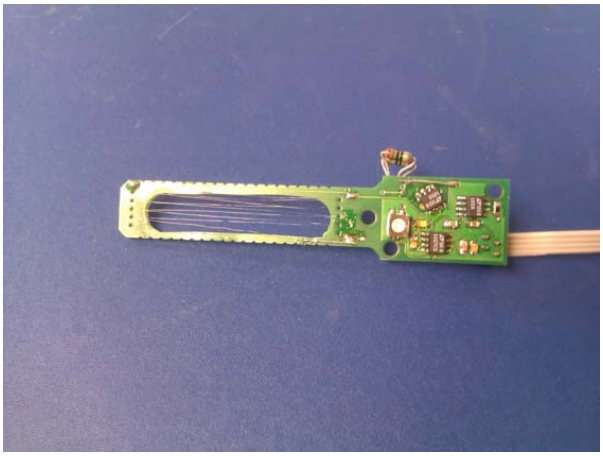

Fig. 5. Fine wire platinum resistance thermometer with 25 µm wire. The flow direction is from the left.

Fig. 6. MASC airframe.

which leads to higher self-heating. The sensor has a sensitivity of 80 mV K^{-1} for a measuring range of −10–50 °C. The noise level is equivalent to the thermocouple circuit, so that a resolution of 1.8 mK is reached. Like in the thermocouple circuit, operational amplifiers were chosen that have a gain stability and precision that outranges the requirements.

3 Validation flights

3.1 The test site

An experiment was performed in September 2012 at a test field of the German Meteorological Service (Deutscher Wetterdienst – DWD) close to Lindenberg, Germany. The site is located at 52.1669° N, 14.1242° E in north-east Germany in a heterogenous but nearly flat terrain. It was used previously in comparative sensor studies for airborne meteorology (Martin et al., 2011). Approximately 200 m from the take-off location for the RPA, a 99 m tower with meteorological instruments at 6 heights, including temperature, humidity, wind speed and wind direction measurements, is installed. The tower is also equipped with sonic anemometers at two levels (50 and 90 m) for turbulence measurements. Besides the tower, there are also various remote sensing instruments installed on the test field. For comparison of temperature measurements, a sodar/RASS and a 482 MHz wind profiler/RASS can be taken into account, which both measure virtual temperature of the atmosphere along with wind speed and wind direction (Engelbart et al., 1999; Engelbart et al., 1996; Engelbart and Bange, 2002). The sodar is installed directly at the test site, while the wind profiler is situated at the observatory in Lindenberg, 5 km north of the site. Additionally, every 6 h, a radiosonde is released in Lindenberg for soundings of temperature, humidity and wind.

3.2 The RPA system MASC

The platforms that are being used at the University of Tübingen to perform meteorological measurements are small RPA named MASC (Multi-purpose Airborne Sensor Carrier), which were developed in-house in cooperation with a local model aircraft builder. The MASC airframe as shown in Fig. 6 is an electrically powered motor glider aircraft of 3.00 m wingspan and a maximum take-off weight of 6 kg. In standard configuration with meteorological payload, the weight does not exceed 5.5 kg. A flight endurance of at least 40 min is possible at this weight with minimum battery load, which corresponds to a travelling distance of more than 50 km at a travelling speed of 22 m s^{-1}. Tests in the wind tunnel showed that the pusher motor does not affect the measurement system at the fuselage tip. Only very little flow disturbance was found due to the fuselage itself at typical airspeeds.

The aircraft are equipped with the autopilot ROCS (Research Onboard Computer System), which was developed at the Institute of Flight Mechanics and Control (IFR) at the University of Stuttgart (Haala et al., 2011). It was originally developed for photogrammetric applications and specifically adapted to the needs of meteorological observations. The autopilot makes it possible to fly pre-defined flight patterns automatically, guaranteeing a constant airspeed of 22–24 m s^{-1} and a level flight with a precision in altitude better than 2 m in straight legs. A bias in altitude can be up to 10 m.

3.3 The experiment

The experiment was carried out in autumn 2012 from 21 to 23 September. Two MASC systems were operated in this period. While on the first and third day of the experiment fair weather allowed a total number of 15 measurement flights with the system, the second day with more gusty winds and light rain was only used for test flights and technical

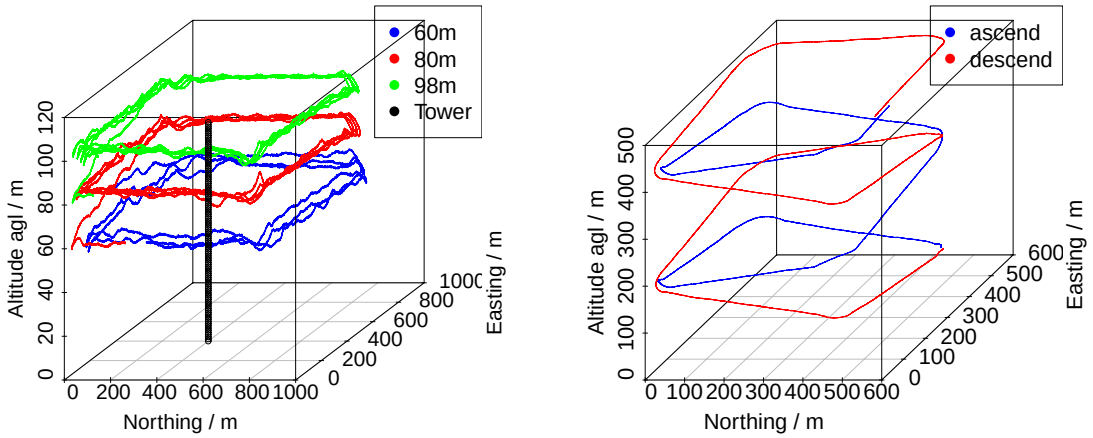

Fig. 7. Flight paths for tower sweep maneuver (left panel) and vertical profiles (right panel). The solid black vertical line represents the measurement tower.

improvements on the system. Several flights were done specifically to validate the temperature measurements of the two sensors described here. Two flights were performed flying squares with a size of 600 m around the tower at three heights where sensors are installed on the tower (60, 80 and 98 m). Another two flights were done at the time when radiosondes were released to measure vertical profiles between 60 and 500 m and compare the results. Figure 7 shows the flight paths for these two maneuvers. For comparison with the tower, the aircraft remained at each altitude for 8 to 10 min to have the same averaging period as the tower data. During straight and level flights, the standard deviation of barometric altitude is below 0.5 m. Including the bends, it is still below 2 m. Lateral deviations from the given track are within ± 2 m. For the vertical profile, a constant climb rate of about 2 m per second was chosen.

All temperature sensors involved were calibrated in a NIST (National Institute of Standards and Technology, USA) traceable climate chamber for a range of 15 °C–50 °C. In the experiment, temperatures slightly below the calibration range were experienced. However, subsequent calibrations of the same type of sensors to lower temperatures showed that the sensor output follows the calibration curve very well down to 10 °C and further, staying well within the desired accuracy of 0.1 K.

3.4 Results

The results of the comparison flights with the tower at three levels can be seen in Fig. 8. All flights show that the FWPRT measures a temperature that is constantly higher than the temperature measured at the tower. The two flights on 21 September were done with exactly the same FWPRT sensor; on 23 September another FWPRT sensor of the same type was used. The sensor used on 23 September has a slightly bigger offset of about 0.6 K, compared to 0.4 K on 21 September. The PCAP sensor that is being used for filtering with the thermocouple systematically shows a lower measurement of about 0.2 K compared to the tower. These constant errors can be interpreted as calibration errors and are easily corrected by subtracting the measured offset. Analysing all 10-minute averages that were possible to extract from airborne measurements throughout the experiment, it was found that a mean error of -0.26 K with a standard deviation of 0.1 K for the PCAP sensor and a mean error of 0.46 K with a standard deviation of 0.09 K for the FWPRT were measured (see Fig. 9). The requirement of 0.1 K hence can be held throughout the experiment, if a calibration offset between the sensors is subtracted once. The random errors include possible errors due to a bias between tower instrument height and controlled aircraft altitude, which can be up to 10 m. An error in altitude of this order at a lapse rate of 0.01 K m^{-1} will result in a temperature error of 0.1 K, which is in the range of the standard deviation. Another possible error source is the fact that the aircraft measurement is a spatial average, while the tower measurement is a point measurement. In laboratory conditions in a climate chamber, the sensors never exceed 0.1 K deviation with a quadratic fit over the whole calibration range. The experiment in Lindenberg could only cover a small range of temperatures. To find out if the errors of the sensors are larger close to the edges of the calibration range or even beyond, more flight tests are needed.

Figures 10 and 11 show the result of the temperature sensors for two sequential vertical profiles at around 11:00 UTC and around 17:00 UTC respectively, in comparison to all other temperature measurements that were done at the test site in Lindenberg. For better comparison with the remote sensing systems, the RPA, radiosonde, and tower measurements are converted to virtual temperature according to the equations in Appendix A. The measurement of relative humidity was done with a capacitive sensor, which was found

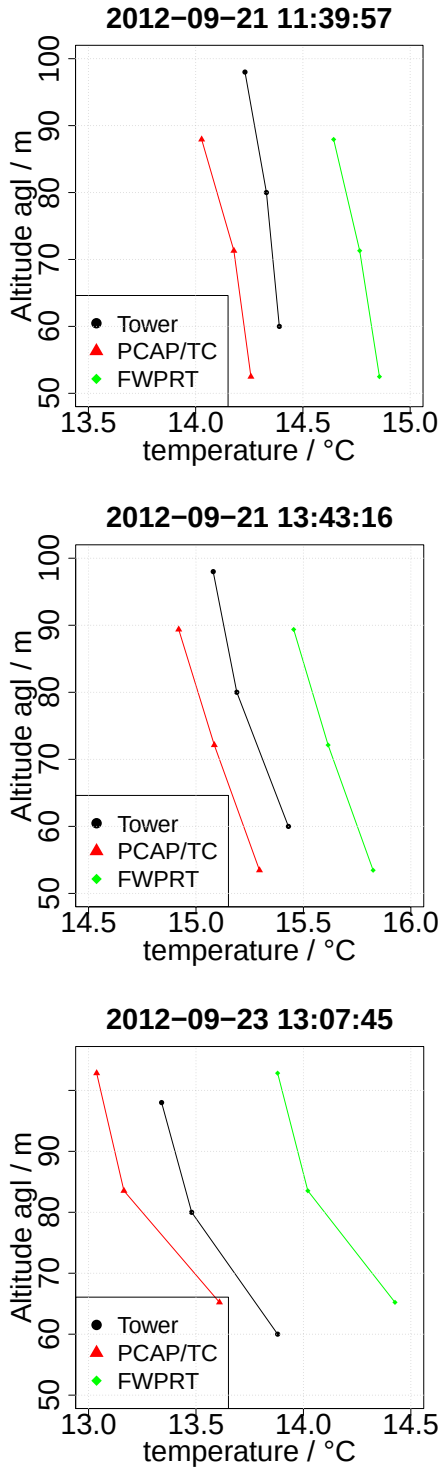

Fig. 8. Comparison of temperature sensors on the RPA with tower data, 10 min averages at three levels and three different flights.

to be in good agreement with the reference instruments in this experiment. Deviations of up to ±5 % RH can be observed, which, according to the conversion to virtual temperature, can cause temperature errors of maximum ±0.05 K for the given situation. Looking at all profiles, it can be seen that, for the vertical profiles as well, the FWPRT has an offset to the tower of about 0.5 K. The offset to the radiosonde and the wind profiler is in the same range. For the FWPRT, the lapse rate of virtual temperature is very well captured by the sensors, and ascents and descents do not show remarkable hysteresis, which shows that the sensor's time response is fast enough for the given climb rate. At around 11:00 UTC, the radiosonde measures a higher lapse rate close to the ground which is captured neither by the tower, nor by the RPA. In the late afternoon measurement, RPA, tower and radiosonde profiles have the same shape down to the ground in consideration of the different ground levels. Most probably a local effect in the area where the radiosonde was released, which is approximately 5 km from the 99 m tower, is the reason for this difference in shape close to the ground between the measurements at around 11:00 UTC. Thermocouple measurements (Fig. 11) show a strong hysteresis, which is due to the PCAP sensor, which is not able to adapt fast enough to temperature changes for the given climb rate, and the thermocouple's reference junction is not stable enough to make it possible to fill the gap to lower frequencies with pure thermocouple measurements.

4 Discussion of measurement errors

Two of the error sources that are most cited when it comes to temperature measurement with aircraft are radiation errors and errors due to adiabatic heating of the sensor element (Breitkopf and Kim, 1980; Foken, 1979; Daniels, 1968; Shannon and Butler, 2003). The measurement campaign in Lindenberg was also used to investigate these errors for the two sensor types described above. Condensation or icing, which both have fatal effects on measurements with fine wires, will not be considered.

4.1 Radiation error

To figure out the effect of radiation on the sensors, square pattern flights were chosen as well. In these flights, the aircraft was flying in all four main geographic directions. The flights were performed in late morning, between 10:00 and 11:00 UTC, with the sun in southern position (azimuth ≈ 174°, elevation ≈ 38°). The sensors are installed on the RPA in a way such that, for flights in north and east direction, sun was shining on the sensors, but in south and west direction, the sensors are shaded by the RPA itself. For FWPRT measurements, no significant offset between different flight directions could be found. For thermocouple measurements, an effect could be observed and is shown in Fig. 12

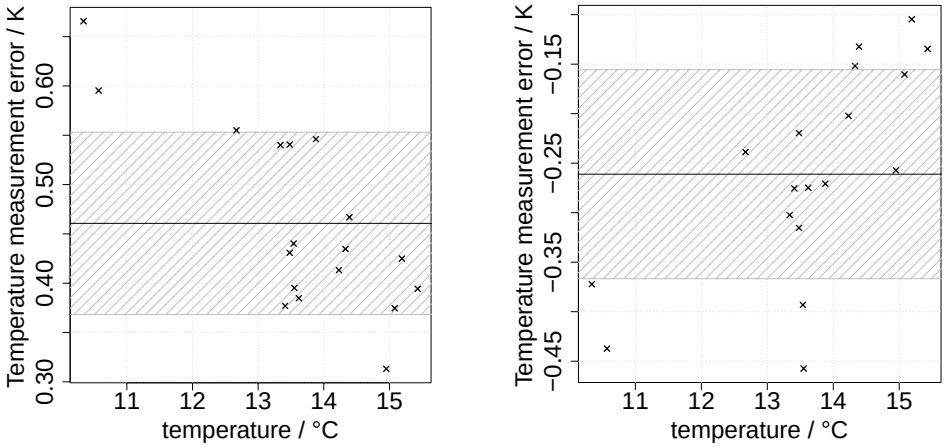

Fig. 9. Errors of FWPRT (left panel) and thermocouple measurements (right panel) compared to tower temperature measurement. Ten-minute averages of RPA and tower measurements at the same altitude and time are used to calculate the error. The solid black line marks the mean error. The shaded area visualizes the standard deviation.

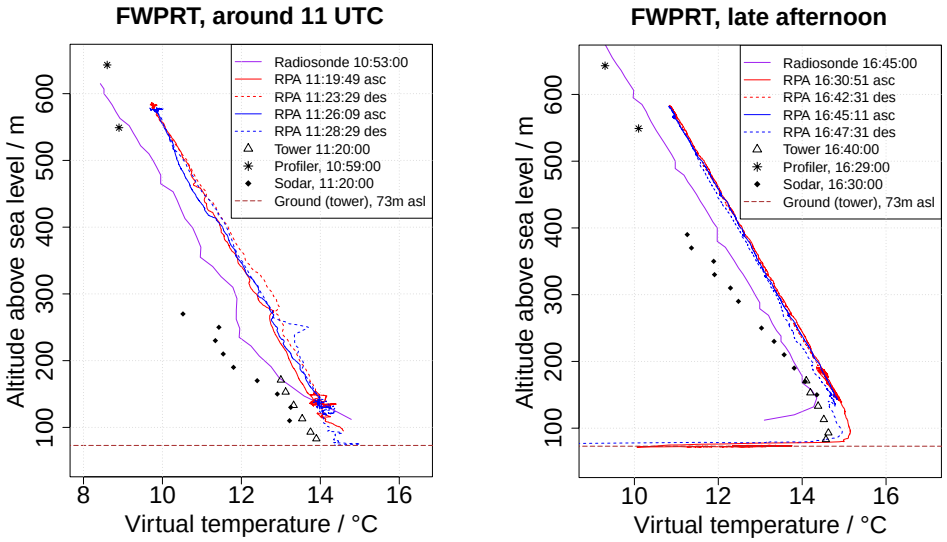

Fig. 10. Comparison of FWPRT on the RPA with remote sensing and tower data for vertical profile flights on Sunday, 23 September 2012.

(left panel). It shows mean values for each leg in the square, coloured according to the flight direction. For each square the temperature rises, but a constant offset between counter-directions of about 0.5 K is observed. The source for this offset is the PT1000 on the PCAP sensor. Repeating the same pattern with a shield around the PCAP sensor gives much better results with no significant offset between all directions (Fig. 12, right panel). The shield is made of a 2 cm diameter carbon tube covered with white adhesive film that completely covers the PCAP electronics. This result agrees with experiments performed in a wind tunnel using a light bulb as radiation source and exposing the sensor system with and without radiation shield. Both fine wire sensors – thermocouple and FWPRT – do not show a significant sensitivity to radiation at the given airspeed of 20 m s^{-1}. This is a good indication that radiation errors can be neglected for this type of sensor. In wind tunnel experiments the radiation input was increased to a much higher level than in the test flights, radiating the sensors with up to 800 W m^{-2}, which corresponds to a hot summer day (see Fig. 13). The times when the radiation was switched on and off can clearly be seen in the PCAP measurements, while the FWPRT reacts with less than 0.2 K deviation from the wind tunnel internal temperature trend.

4.2 Adiabatic heating

Adiabatic heating of a sensor occurs when the air is decelerated at the sensitive element of the measurement instrument.

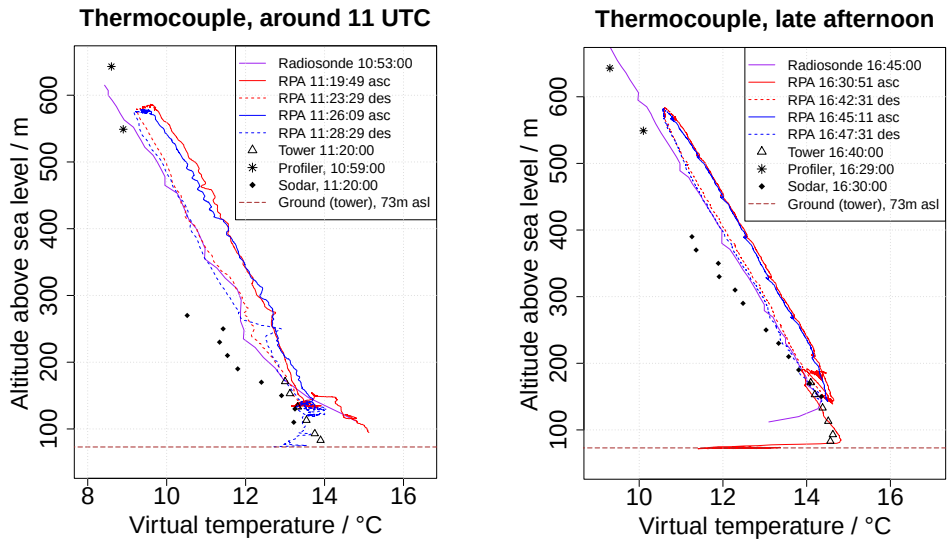

Fig. 11. Comparison of thermocouple on the RPA with remote sensing and tower data for vertical profile flights on Sunday, 23 September 2012.

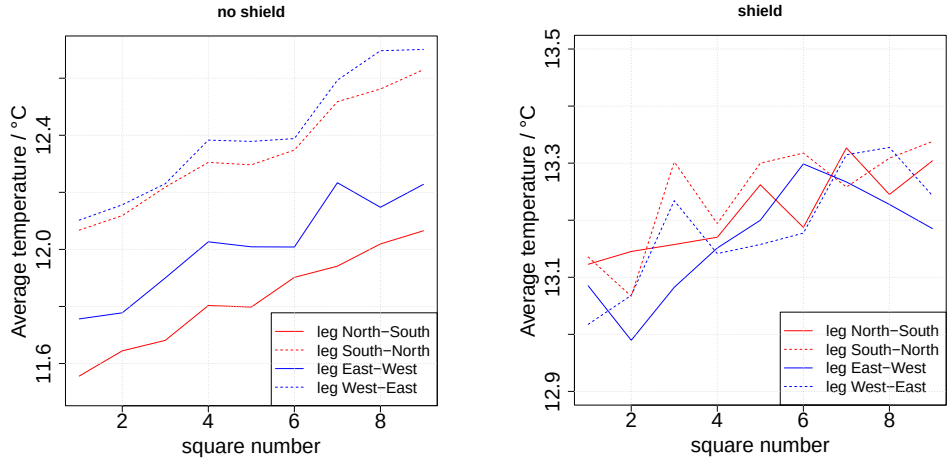

Fig. 12. Averaged thermocouple temperature measurement over legs in all geographic directions with and without radiation shield of the PCAP sensor. Dashed lines are for legs with irradiated sensors; solid lines are for legs with sensors in the shadow of the fuselage.

The kinetic energy of the air is transformed to heat. This heat leads to higher measurements compared to the static temperature. In theory, adiabatic heating can be described with the following adiabatic equation:

$$T_s = r \cdot T_m \left(\frac{P_s}{P_t} \right)^{\kappa}, \quad (2)$$

where T_s is the static temperature of the air, T_m the temperature measured by the sensor, P_s the static pressure, P_t the total pressure including the dynamic pressure at the sensor and $\kappa = R_d/C_p \approx 0.28571$ the Poisson constant (ratio of the gas constant and the specific heat for constant pressure). Using this equation with boundary conditions of 293 K measured temperature, static pressure of 1000 hPa and an airspeed of 25 m s^{-1} leading to a total pressure of 1003.70 hPa, the measured temperature is ≈ 0.3 K higher than the true static temperature. In reality, the air is not only decelerated at the sensitive part of the sensor. The geometry of the sensor plays an important role for the effect of adiabatic heating. This is typically considered by the introduction of a recovery factor r. The value of this recovery factor has to be evaluated in experiments (Breitkopf and Kim, 1980). To see if the adiabatic heating effect plays a role at all for the sensor under investigation, the cross-correlation between temperature measurement and airspeed in a measurement flight at constant altitude can be calculated. Figure 14 shows the results for the

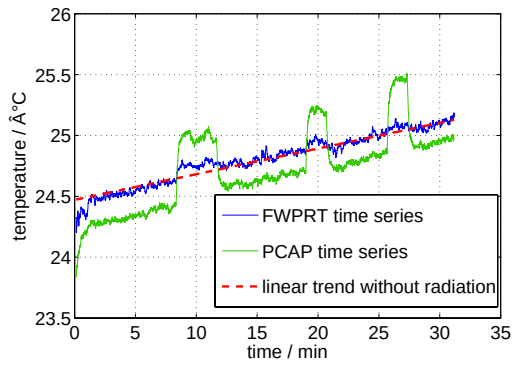

Fig. 13. A time series of a wind tunnel experiment with artificial radiation source.

FWPRT and the thermocouple. Both maximum correlation coefficients are below 0.1. This is considered small enough to neglect errors of adiabatic heating in future experiments.

5 Spectral responses

To measure turbulent fluxes of heat, it is important to resolve eddies as far as possible into the inertial subrange of turbulence. A spectral analysis of the measurements shows how high the temporal resolution of the sensor is, if the result is compared to the Kolmogorov law of locally isotropic turbulence in the inertial subrange (Kolmogorov, 1941). For the spectral analysis, the experiment in Lindenberg was not useable, due to internal noise caused by the telemetry system. This noise could be seen on all analog signals and was especially critical for thermocouple measurements due to the small voltage signal of this sensor. It could be clearly due to the telemetry, because it appeared at the same frequency as the downlink frequency.

Subsequent tests showed that the electronic circuit as it was used in Lindenberg also artificially limited the frequency response for the FWPRT. The current to voltage converter includes an active low-pass filter, which was adjusted to a cut-off frequency of about 5 Hz. A trade-off needed to be found for a higher cut-off frequency while maintaining a reasonable signal-to-noise ratio at the same time.

Figure 17 shows variance spectrum and structure function of a flight with the optimized electronic circuit. In this case, the sensitivity of the sensor is reduced to 40 mV K^{-1}, which still meets the requirements described in Sect. 2. It can be seen that the spectral results of both sensors agree very well, especially in the higher frequency range. The flights were done at 370 m altitude on a summer day in June, just before noon, in southern Germany. At this altitude, a stable stratification was still present as can be seen from a vertical profile taken just before the racetrack pattern flights for the spectral analysis (see Fig. 15). Figure 16 shows the time series of the complete racetrack pattern, including bends. In fact, very similar results have to be expected since the main physical influences to the sensor response are the wire diameter and the forced convection due to airspeed, which in this case are identical for both sensors. Additionally, the same data acquisition system and same operational amplifiers were used, so that these influences are eliminated for the comparison. Remaining differences can mainly be due to imperfect calibration and the error sources that were discussed before. Radiation, adiabatic heating and heat transfer might not contribute significantly to the absolute reading, but can still have some influence on very small scales.

The variance spectrum and structure function do not perfectly follow the Kolmogorov law of locally isotropic turbulence (inertial subrange) in this measurement. There are several possible reasons for this. Due to restrictions in the flight permission, only rather short legs of about 1 km could be performed. Only four legs were used for the averaging of the spectral analysis because of the instationarity of the ABL. Thus, temporal variations of the spectral density can be expected. Also, in the residual layer, turbulence is weak and not necessarily isotropic since the turbulent eddies are compressed vertically.

6 Conclusions

In this study, two temperature sensors for airborne flux measurements in the atmospheric boundary layer were developed and tested extensively. Section 2 introduces the requirements and explains the system design. The resolution and measuring range was designed to be met for both sensor types. Section 3 shows that each of the sensors has the ability to measure temperature within the desired accuracies, if calibration offsets are subtracted. Section 4 discussed the typical errors in airborne temperature measurements like radiation error and adiabatic heating and showed that for the given sensors these are small enough to be within the total accuracy of the sensors. Last, the spectral response of thermocouple and FWPRT were compared in Sect. 5. It showed that both sensors can resolve turbulent fluctuations with little damping up to 10 Hz. The cut-off frequency for both sensors with the given design is at about 20 Hz. Each sensor has certain advantages and disadvantages. While using thermocouple circuits, it is most critical to provide a well-designed cold junction and an appropriate temperature measurement of the cold-junction temperature to achieve good total accuracies. The FWPRT with same diameter needs a longer wire to achieve a good resolution. A longer sensitive part of the sensor also means higher chances for contamination and damage. In future designs of thermocouple circuits, more effort has to be taken into a well-measured cold-junction temperature to make it a stand-alone temperature sensor for both good absolute accuracy and fast response. Alternatively, the result of the thermocouple measurement can also be complementarily filtered with the FWPRT sensor. Future designs of

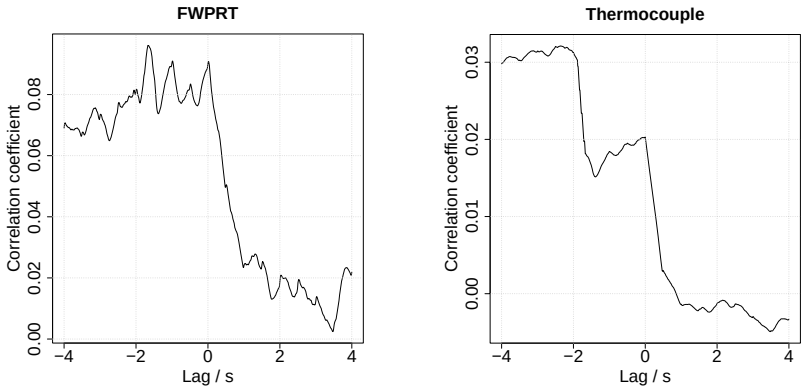

Fig. 14. Correlation function between measurements of two temperature sensors and true airspeed.

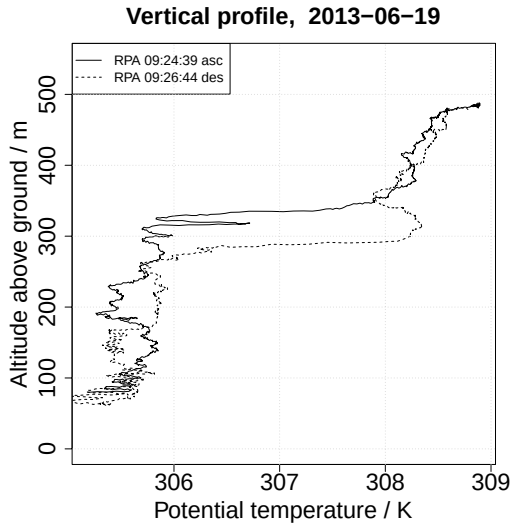

Fig. 15. Vertical profile of potential temperature measured just before the racetrack pattern for the spectral analysis of the sensors.

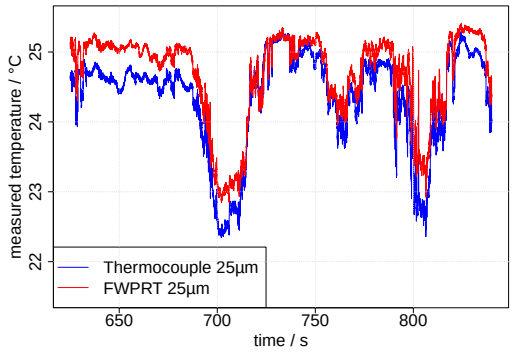

Fig. 16. Time series of thermocouple (blue) and FWPRT (red) in comparison.

the FWPRT sensor could aim for better signal-to-noise ratio with smaller wire length and therefore lower resistance value of the wire. A shorter wire is less susceptible to damage in flight. This would also reduce the contact spots of the wire and thereby heat transfer to the circuit board. Heat transfer did not show to be a problem in the current frequency range, but might affect the sensor at higher frequencies. For both sensors, improvements on the electronic circuits can be done in the future to reduce the time responses as far as possible.

Each of the sensors – as they were tested in this study – have pure hardware and manufacturing costs of less than 100 EUR. Therefore, these types of sensors are the ideal equipment for fast temperature measurements aboard small RPA of type MASC or even smaller.

Appendix A

Virtual temperature

To calculate virtual temperature from each instrument under investigation, the relative humidity and barometric pressure measurements of the respective system are used. First the saturation water vapour E for the measured static temperature T (in °C) is calculated:

$$E = 6.107 \times 10^{\frac{7.45 \cdot T}{235.0+T}} \text{ hPa}. \quad \text{(A1)}$$

The saturation water vapour E is multiplied with the measured relative humidity value φ to get the actual water vapour partial pressure e:

$$e = \frac{\varphi}{100\,\%} \cdot E. \quad \text{(A2)}$$

The mixing ratio m is calculated using the instrument's barometric pressure measurement p_s and water vapour partial pressure e:

$$m = 621.97 \cdot \frac{e}{p_s - e}. \quad \text{(A3)}$$

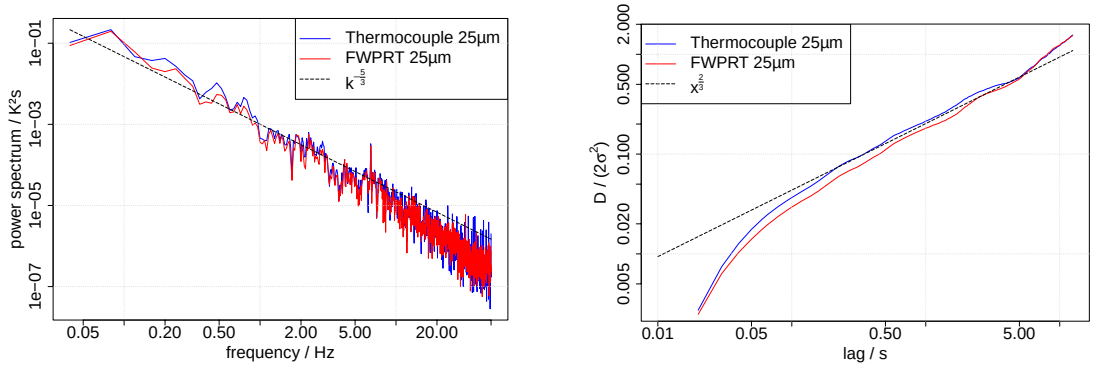

Fig. 17. Variance spectra (left panel) and structure function (right panel) of both sensors, compared to Kolmogorov laws of turbulence: the spectra that are shown are averaged over four single spectra of 25 s time series each. The structure function is normalized by $2\sigma_T^2$.

Finally, the virtual temperature T_v is calculated from measured temperature T and mixing ratio m:

$$T_v = (T + 273.15) \cdot \left(1 + \frac{0.61 \cdot m}{1000}\right). \quad \text{(A4)}$$

The virtual temperature is the temperature at which a dry parcel of air would have the same density as the measured moist parcel of air.

Appendix B

Structure function

The structure function is a statistic measure to show common variation. The eddy-size distribution of a turbulent flow in the inertial subrange, or the local structure of a turbulent flow, was first and foremost quantified using the (auto-)structure function (Kolmogorov, 1941). See also Bange (2009).

$$D_\phi(\tau) = \frac{1}{D-\tau} \int_0^{D-\tau} \mathrm{d}t\,[\phi(t+\tau) - \phi(t)]^2, \quad \text{(B1)}$$

where τ is the lag or shift, ϕ the physical quantity, D the total length of the time series and t the time.

To simplify the interpretation of structure functions, they can be normalized by dividing by twice the variance of the time series:

$$\frac{D_\phi}{2\sigma^2} = \begin{array}{l} 0 : \text{fully correlated} \\ 1 : \text{non-correlated} \\ 2 : \text{fully anti-correlated.} \end{array} \quad \text{(B2)}$$

Acknowledgements. We would like to thank Frank Beyrich and Udo Rummel for the provision of data of all meteorological instruments at the meteorological observatory Lindenberg and their support on-site, Roland Kern for his excellent work on the aircraft, Walter Fichter, Florian Weimer and Alexander Joos at the IFR Stuttgart for their support with the autopilot system and Maximilian Ehrle and Markus Auer for their great job as safety pilots. The measuring equipment would not have been ready to work without the help of Jens Dünnermann and Burkhard Wrenger from the University of Applied Sciences Ostwestfalen-Lippe.

We acknowledge support by Deutsche Forschungsgemeinschaft and Open Access Publishing Fund of Tübingen University.

Edited by: F. X. Meixner

References

Bange, J.: Airborne Measurement of Turbulent Energy Exchange Between the Earth Surface and the Atmosphere, Sierke Verlag, Göttingen, 174 pp., 2009.

Bange, J., Spieß, T., Herold, M., Beyrich, F., and Hennemuth, B.: Turbulent Fluxes from Helipod Flights above Quasi-Homogeneous Patches within the LITFASS Area, Bound.-Lay. Meteorol., 121, 127–151, 2006.

Breitkopf, G. S. W. and Kim, S.: Recovery-Faktor des frontal angeströmten zylindrischen Mantelthermoelementes mit ebener Stirnfläche, Thermo Fluid Dynam, 13, 287–292, 1980.

Daniels, G.: Measurement of gas temperature and the radiation compensating thermocouple, J. Appl. Meteorol., 7, 1026–1035, 1968.

Dias, N., Gonçalves, J., Freire, L., Hasegawa, T., and Malheiros, A.: Obtaining Potential Virtual Temperature Profiles, Entrainment Fluxes, and Spectra from Mini Unmanned Aerial Vehicle Data, Bound.-Lay. Meteorol., 145, 93–111, 2012.

Emeis, S.: Determination of the Surface Sensible Heat Flux From Aircraft Measurements, Betr. Phys. Atmosph., 68, 143–148, 1995.

Engelbart, D., Steinhagen, H., Görsdorf, U., Lippmann, J., and Neisser, J.: A 1290 MHz profiler with RASS for monitoring wind and temperature in the boundary layer, Beitr. Phys. Atmosph., 69, 63–80, 1996.

Engelbart, D., Steinhagen, H., Görsdorf, U., Neisser, J., Kirtzel, H.-J., and Peters, G.: First results of measurements with a newly designed phased-array Sodar with RASS, Meteorol. Atmos. Phys., 71, 71–68, 1999.

Engelbart, D. A. M. and Bange, J.: Determination of Boundary-Layer Parameters using Wind Profiler/RASS and Sodar/RASS in the Frame of the LITFASS-Project, Theor. Appl. Climatol., 73, 53–65, 2002.

Foken, T.: Temperaturmessung mit dünnen Platindrähten, Meteorol. Z., 5, 299–307, 1979.

Friehe, C. A. and Khelif, D.: Fast-response aircraft temperature sensors, 9, 784–795, 1992.

Garratt, J.: The Atmospheric Boundary Layer, University Press, Cambridge, 1992.

Haala, N., Cramer, M., Weimer, F., and Trittler, M.: Performance Test on UAV-Based Photogrammetric Data Collection, vol. 20, in: UAV-g (unmanned aerial vehicle in geomatics) Conference, Zurich, Switzerland, American Meteorological Society, 2011.

Haman, K. E.: A New Thermometric Instrument for Airborne Measurements in Clouds, J. Atmos. Ocean. Tech., 9, 86–90, 1992.

Haman, K. E., Makulski, A., and Malinowski, S. P.: A new ultrafast thermometer for airborne measurements in clouds, J. Atmos. Ocean. Tech., 14, 217–227, 1997.

Harrison, R. and Pedder, M.: Fine wire thermometer for air temperature measurement, Rev. Sci. Instrum., 72, 1539–1541, 2001.

Inverarity, G.: Correcting airborne temperature data for lags introduced by instruments with two-time-constant responses, J. Atmos. Ocean. Tech., 17, 176–184, 2000.

Kaimal, J. C. and Finnigan, J. J.: Atmospheric Boundary Layer Flows – Their Structure and Measurement, Oxford University Press, 289 pp., 1994.

Kolmogorov, A.: The Local Structure of Turbulence in Incompressible Viscous Fluid for Very Large Reynolds Numbers, Dokl. Akad. Nauk SSSR, 30, 299–303, reprint, P. Roy. Soc. Lond. A, 1991, 434, 9–13, 1941.

Lenschow, D.: Probing the Atmospheric Boundary Layer, vol. 1, American Meteorological Society, Boston, MA, USA, 1986.

Luers, J. K.: Temperature Error of the Vaisala RS90 Radiosonde, J. Atmos. Ocean. Tech., 14, 1520–1532, 1997.

Martin, S. and Bange, J.: The Influence of Aircraft Speed Variations on Sensible Heat Flux Measurements by Different Airborne Systems, Bound.-Lay. Meteorol., accepted, 2013.

Martin, S., Bange, J., and Beyrich, F.: Meteorological profiling of the lower troposphere using the research UAV "M2AV Carolo", Atmos. Meas. Tech., 4, 705–716, doi:10.5194/amt-4-705-2011, 2011.

Michalski, L., Eckersdorf, K., and McGhee, J.: Temperature Measurement, John Wiley and Sons Ltd., Chichster, 1991.

Nash, J., Smout, R., Oakley, T., Pathack, B., and Kurnosenko, S.: WMO Intercomparison of High Quality Radiosonde Systems, Tech. rep., WMO Report., available from CIMO, Vacoas, Mauritius, 2–25 February 2005.

Neisser, J., Adam, W., Beyrich, F., Leiterer, U., and Steinhagen, H.: Atmospheric Boundary Layer Monitoring at the Meteorological Observatory Lindenberg as a Part of the 'Lindenberg Column': Facilities and Selected Results, Meteorol. Z. N. F., 11, 241–253, 2002.

Reuder, J., Brisset, P., Jonassen, M., Müller, M., and Mayer, S.: The Small Unmanned Meteorological Observer SUMO: A new tool for atmospheric boundary layer research, Meteorol. Z., 18, 141–147, 2009.

Rosemount: Total Temperature Sensors, Tech. Rep. Bulletin 1012, Rosemount Inc., Burnsville, MN, 1986.

Shannon, K. S. and Butler, B. W.: A review of error associated with thermocouple temperature measurement in fire environments, in: Second international wildland fire ecology an fire management congress and fifth symposium on fire and forest meteorology, 16–20 November 2003, Orlando, FL, American Meteorological Society, Boston, MA, p. 7B.4, 2003.

Spiess, T., Bange, J., Buschmann, M., and Vörsmann, P.: First application of the meteorological Mini-UAV "M2AV", Meteorol. Z., 16, 159–169, 2007.

Stull, R.: An Introduction to Boundary Layer Meteorology, Kluwer Acad., Dordrecht, 1988.

van den Kroonenberg, A. C., Martin, T., Buschmann, M., Bange, J., and Vörsmann, P.: Measuring the Wind Vector Using the Autonomous Mini Aerial Vehicle M^2AV, J. Atmos. Ocean. Tech., 25, 1969–1982, 2008.

Wendisch, M. and Brenguier, J.: Airborne Measurements for Environmental Research – Methods and Instruments, vol. 1, Wiley-VCH, Berlin, 2013.

A.2 Towards higher accuracy and better frequency response with standard multi-hole probes in turbulence measurement with remotely piloted aircraft (RPA).

The publication is also available at
`http://www.atmos-meas-tech.net/7/1027/2014/`.

Atmos. Meas. Tech., 7, 1027–1041, 2014
www.atmos-meas-tech.net/7/1027/2014/
doi:10.5194/amt-7-1027-2014

Atmospheric Measurement Techniques
Open Access

Towards higher accuracy and better frequency response with standard multi-hole probes in turbulence measurement with remotely piloted aircraft (RPA)

N. Wildmann, S. Ravi, and J. Bange

Center for Applied Geoscience, Eberhard-Karls-Universität Tübingen, Tübingen, Germany

Correspondence to: N. Wildmann (norman.wildmann@uni-tuebingen.de)

Received: 8 August 2013 – Published in Atmos. Meas. Tech. Discuss.: 14 November 2013
Revised: 13 February 2014 – Accepted: 26 February 2014 – Published: 22 April 2014

Abstract. This study deals with the problem of turbulence measurement with small remotely piloted aircraft (RPA). It shows how multi-hole probes (MHPs) can be used to measure fluctuating parts of the airflow in flight up to 20 Hz. Accurate measurement of the transient wind in the outdoor environment is needed for the estimation of the 3-D wind vector as well as turbulent fluxes of heat, momentum, water vapour, etc. In comparison to an established MHP system, experiments were done to show how developments of the system setup can improve data quality. The study includes a re-evaluation of the pneumatic tubing setup, the conversion from pressures to airspeed, the pressure transducers, and the data acquisition system. In each of these fields, the steps that were taken lead to significant improvements. A spectral analysis of airspeed data obtained in flight tests shows the capability of the system to measure atmospheric turbulence up to the desired frequency range.

1 Introduction

In many applications multi-hole probes (MHPs) serve the purpose of measuring the flow angle and speed of an airstream. They are commonly used in wind-tunnel and road tests for the automotive industry (Zimmer et al., 2001) as well as in airborne measurements (Crawford and Dobosy, 1992). Many different designs and calibration techniques can be found in literature (Telionis et al., 2009; Sumner, 2000; Pfau et al., 2002; Lemonis et al., 2002). The minimum number of holes that are used for three dimensional flow measurement is four, while probes with five holes are common and seven-hole probes can also be found. With increasing number of holes, the range of the angle of incidence that can still be measured with the probe increases. There are also probes with only one pressure port, which is constantly turned inside the probe (Schlienger et al., 2002). The shape of the probe (conical, hemispherical or faceted) has an effect on the maximum incidence angle as well as on the sensitivity regarding Reynolds number changes (Telionis et al., 2009), due to the different points of flow separation. In airborne meteorology, the MHP made by Goodrich Sensor Systems (Rosemount, 1982) has been the most commonly used probe for measurements in the atmospheric boundary layer. Using flight calibration maneuvers, these MHPs can be used for wind measurement on-board manned aircraft (Friehe et al., 1996; Khelif et al., 1999). The development of the BAT probe (Crawford and Dobosy, 1992) enabled the measurement of the turbulent heat flux by combining fast temperature sensors with the existing system.

Within the last decade, RPASs (remotely piloted air systems) have become more and more affordable and suitable for atmospheric measurements and some have also been equipped with MHPs (Spieß et al., 2007; van den Kroonenberg et al., 2008; Thomas et al., 2012; Martin and Bange, 2014). The big advantage compared to manned aircraft is the decreased disturbance of the airflow by the aircraft, due to the smaller wingspan and wing load, which leads to smaller upwash (Crawford et al., 1996) and the reduced overall size, which decreases the disturbance of turbulence measurements according to Wyngaard et al. (1985). Higher flexibility and lower operating cost are other major advantages with small RPAS. The Meteorological Mini Aerial Vehicle (M^2AV) is

one of such RPAS and the measurement technique that was used in this system will be referred to as a benchmark in this study. New developments made as part of this study will be compared to the M^{2}AV where possible. Since the turbulent wind vector and all turbulent flux measurements are strongly dependent on the measurement of airflow angles and true airspeed, a critical analysis of the systematic errors and sources for noise in the measurement with a MHP will be conducted. This analysis includes the complete measurement chain from the pneumatic setup of the probe and the pressure transducers until the sampling of the data.

The meteorological wind vector $\boldsymbol{v}$ (i.e. the wind vector in the earth's orthonormal, meteorological coordinate system) can be calculated from navigation, flow and attitude measurement aboard a research aircraft using

$$\boldsymbol{v} = \boldsymbol{v}_{\mathrm{gs}} + \mathbf{M}_{\mathrm{mf}} \left(\boldsymbol{v}_{\mathrm{tas}} + \boldsymbol{\Omega} \times \boldsymbol{s}_p \right) \quad (1)$$

(Williams and Marcotte, 2000). The ground-speed vector $\boldsymbol{v}_{\mathrm{gs}}$ describes the movement of the origin of the aircraft-fixed coordinate system (index f) with respect to the earth's surface and is determined using the on-board navigation system. Aboard an RPA the latter is usually a combination of an inertial measurement unit (IMU) and a global navigation satellite system (GNSS). The determination of the ground speed $\boldsymbol{v}_{\mathrm{gs}}$ and the rotation into the earth's coordinate system $\mathbf{M}_{\mathrm{mf}}$ using the Eulerian angles are not subject of the present study, and are described in literature (Haering, 1990; Leise and Masters, 1993; Boiffier, 1998; van den Kroonenberg et al., 2008; Bange, 2009).

The true-airspeed vector $\boldsymbol{v}_{\mathrm{tas}}$ is the flow vector measured by an in situ flow probe, in this study a MHP, preferably mounted at the nose of the RPA. Thus $\boldsymbol{v}_{\mathrm{tas}}$ is defined in the aircraft's coordinate system f. The location of the MHP in relation to the origin of the aircraft-fixed coordinate system f is described by the lever-arm vector $\boldsymbol{s}_p = (x_p, y_p, z_p)$, which points from the origin of the aircraft system f to the location of the MHP. The vector of angular rotation rates $\boldsymbol{\Omega}$ contains the angular velocities of the aircraft system f related to the meteorological system m and is among the primary output data of the IMU.

In the following we focus on the determination of the true-airspeed vector $\boldsymbol{v}_{\mathrm{tas}}$ defined by

$$\boldsymbol{v}_{\mathrm{tas}} = -\frac{|\boldsymbol{v}_{\mathrm{tas}}|}{\sqrt{1+\tan^2\alpha+\tan^2\beta}} \begin{pmatrix} 1 \\ \tan\beta \\ \tan\alpha \end{pmatrix}, \quad (2)$$

(see also Lenschow, 1986; Leise and Masters, 1993; Williams and Marcotte, 2000; van den Kroonenberg et al., 2008; Bange, 2009) with angle of attack α (positive for air flow from below) and sideslip β (positive for flow from starboard). All three variables α, β, and $|\boldsymbol{v}_{\mathrm{tas}}|$ in Eq. (2) can be derived from MHP pressure measurements.

Fig. 1. Research RPA MASC. The position of the MHP approximately 15 cm in front of the fuselage nose tip is depicted with the red ellipse.

Research RPA MASC

At the University of Tübingen the research platform MASC (Multi-purpose Airborne Sensor Carrier) is operated and equipped with a MHP, fast temperature sensors, a barometer and a humidity sensor to enable the measurement of thermodynamic, turbulent scalars as well as the 3-D turbulent wind vector and turbulent fluxes of water vapour, sensible heat and momentum (Fig. 1 and Wildmann et al., 2013). The electrically powered motor-glider airplane with a wingspan between 2.60 and 3.40 m has a total weight of 5–7 kg depending on the battery and payload. Wind-tunnel experiments revealed that the fuselage and running pusher engine did not have a significant influence on the airflow at the location of the MHP. The aircraft is equipped with the autopilot ROCS (Research Onboard Computer System), which has been developed at the Institute for Flight Mechanics and Control (IFR) at the University of Stuttgart (Haala et al., 2011). The autopilot controls a constant airspeed of $24 \pm 1\,\mathrm{m\,s^{-1}}$ and constant altitude with a precision of ± 2 m. Navigation to predefined waypoints is done relative to the take-off position. The flight tests that were performed to validate the results of this study were done with a MASC RPA.

2 The probe

2.1 Mechanical design of the probe

The MHP used at the University of Tübingen has a conical head, nine holes and was designed and manufactured at the Institute for Fluid Dynamics (ISM) of the Technische Universität Braunschweig, Germany. The arrangement of the holes can be seen in Fig. 2. In addition to the five holes on the cone, which are used to measure the flow angles, it has a ring with four holes in a 90° offset pattern in front of it. These holes merge into one pressure port and provide a reference static

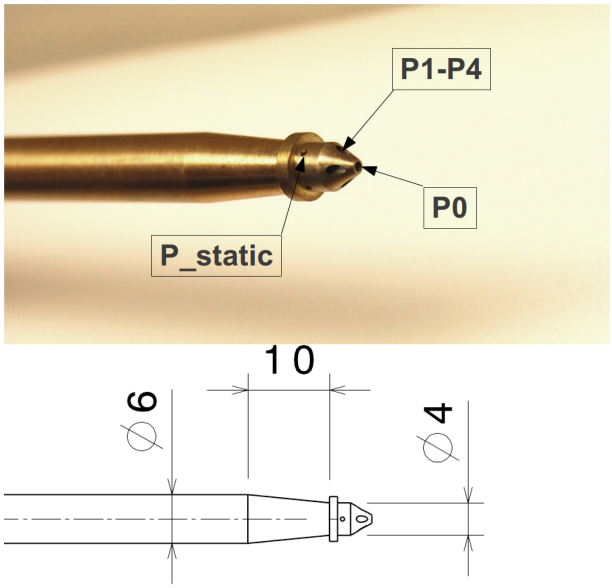

Fig. 2. Probe by ISM Braunschweig, picture and dimensions in millimetres.

pressure, which is less sensitive to the flow angle compared to normal static ports of a Prandtl sonde. This pressure port is then used in the standard calibration described in Sect. 2.2. The same probe was also used in the M^{2}AV. Figure 3 shows a computational fluid dynamic (CFD) simulation of the probe done with OpenFOAM at two different angles of attack.

2.2 Differential pressure to flow angle conversion

The conversion between differential pressures of the six pressure ports of the probe-to-flow angles and true airspeed is usually based on wind-tunnel calibration and can be done in several ways (see Sasangko, 1997; Bohn and Simon, 1975; Treaster and Yocum, 1979). A typical solution is a polynomial fit between normalized pressure differences and airflow angles, true airspeed and static pressure respectively. The ISM probe was intensively used in field campaigns (e.g. Martin et al., 2011; van den Kroonenberg et al., 2011; Spieß et al., 2007) with the M^{2}AV. Table 1 shows how dimensionless coefficients are defined from the pressures at the probe. The definitions on the left are taken from Bohn and Simon (1975), for an English summary see Spieß (2006). They are referred to as the M^{2}AV conversion method in the following. The definition of the pressure ports and differential pressures is described in Figs. 4 and 5. The coefficients k_α and k_β are directly calculated from the pressures at the MHP ports (see Table 1 for different methods to do so). Using a polynomial fit with coefficients that were determined in a wind-tunnel calibration, the angle of sideslip, angle of attack and the coefficients k_q and k_p can be calculated from k_α and k_β. To find dynamic and static pressure, the expressions for k_q and k_p in Table 1 need to be solved for q and p, respectively. A detailed description is given in Appendix A. The true airspeed as used in Eq. (2) has to be calculated using the measured total air temperature T_{tot}, the static pressure p and the dynamic pressure q:

$$|\boldsymbol{v}_{\mathrm{tas}}|^2 = 2c_p T_{\mathrm{tot}} \left[1 - \left(\frac{p}{p+q}\right)^{\kappa}\right] \tag{3}$$

with the Poisson number $\kappa = R/c_p$, where $R = 287\,\mathrm{J\,kg^{-1}\,K^{-1}}$ is the gas constant for dry air and $c_p = 1005\,\mathrm{J\,kg^{-1}\,K^{-1}}$ is the specific heat for dry air.

In the M^{2}AV conversion the ring pressure ports are used to find q and p to get a more angle-independent measurement. However, it was identified that in certain flight conditions the ring can cause problems for turbulence measurement, since the ring port pressure shows an increased noise level, which is induced by the probe itself. Figure 6 shows the result of measurements during the calibration procedure of the MHP in a jet wind tunnel with a turbulence intensity of about 1 %. At a constant airspeed of $22\,\mathrm{m\,s^{-1}}$ and angle of attack of 10° the angle of sideslip β was varied between −20 and 20° in steps of 2°. Each position was held for 10 s and the standard deviation of the ring port pressure was measured. It can be seen that at certain angles of sideslip, the fluctuations of the measured pressure is higher than at other angles. This can be considered to be aerodynamic noise introduced by the probe.

To avoid measuring turbulence that is not primarily related to the atmosphere, a different pressure conversion method (see Table 1, right column) that avoids using the ring port pressure was tested. The method was initially proposed by Treaster and Yocum (1979) and is one of the most basic five-hole probe calibration methods. It only uses one front hole and four side holes.

The calibration results with the occurring nonlinearities are depicted in Figs. 7, 8 and 9. Below 10° the nonlinearities are comparably small, but at higher angles the use of a ninth-order polynomial in calibration becomes necessary to represent the characteristics of the probe. Higher degree polynomials only marginally increase accuracy. The maximum deviation from the resulting polynomial in the calibration procedure is 0.47° for α, 0.59° for β and $0.15\,\mathrm{m\,s^{-1}}$ for airspeed. These values also cover variations of wind-tunnel speed and inaccuracies in the angle settings.

Figure 10 shows the measurement of the airflow angles and true airspeed in one flight leg of 1000 m (including parts of the turns at the beginning and the end). The flight was done at late afternoon on 23 September close to the Lindenberg observatory of the German Meteorological Service. The flight altitude was 100 m above ground in an atmospheric boundary layer with weak stability.

The pressures from the five-hole probe were converted in both ways, with the M^{2}AV method and with the MASC method, avoiding ring-port measurements. While the airflow angles do not show a difference, it can clearly be seen that true airspeed is much less noisy in the latter method.

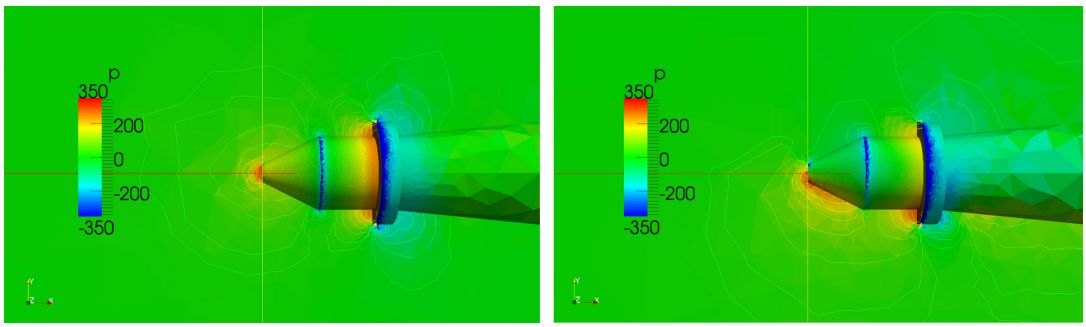

Fig. 3. OpenFOAM flow simulation around the probe tip at 24 m s^{-1} total airspeed at 0° angle of sideslip in both figures, 0° angle of attack in the left figure and 10° angle of attack in the right figure. The colour scale shows differential pressure to the environment in pascals.

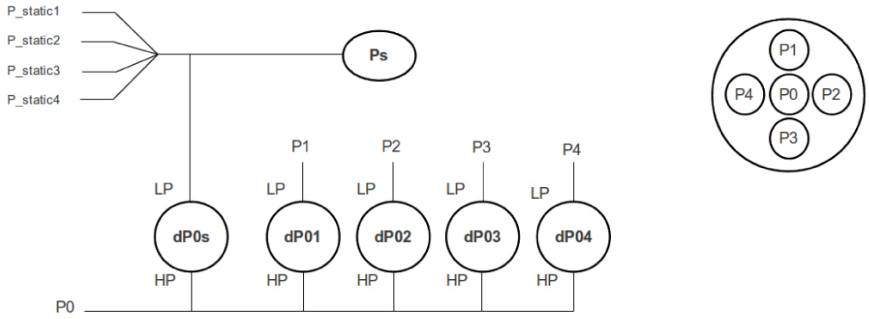

Fig. 4. Tubing system as used by the TU Braunschweig and described in Spieß et al. (2007) for the M^{2}AV. The pressure transducer measurements d$P0i$ are differential pressure readings of the low pressure port (LP) connected to the holes $P1$–$P4$ and the ring portholes P_{static} compared to the high pressure port (HP), which in this case is the common port $P0$. Ps represents a barometric pressure sensor.

The spectra of the velocities estimated through the M^{2}AV (Fig. 11) shows that the noise introduced by the ring-pressure ports manifest as "white-noise" at higher frequencies, while the MASC method shows significantly reduced noise and the presence of the $k^{-\frac{5}{3}}$ slope (Kolmogorov distribution for locally isotropic turbulence in the inertial subrange).

It should be noted that the large difference between the two methods shows up explicitly at certain airflow angles, which were included in the presented time series. However, even though errors are smaller at other angle combinations, they can be completely avoided if the ring port pressure is not used for true airspeed calculation.

3 Tubing response and calibration of the probe

As transient velocities are of particular interest, the pneumatic dynamic response of tubing and transducer needs to be investigated to ensure measurements within a certain error band in the target frequency range. The tubing system within the MHP consists of a combination of a steel tube with an inner diameter of 0.7 mm and another tube of different material (e.g. PVC – polyvinyl chloride) and diameter. The dynamic response of the system depends not only on the length and diameter of the tubing, but also on the air volume inside the pressure transducers. The magnitude and phase response of tubing systems has been well investigated by Bergh and Tijdeman (1965). They derived theoretical estimates of the response of a single tube connected to either a single or multiple transducers connected in series with the variable tubing length, tubing diameter and transducer volume. Further studies by Semaan and Scholz (2012) investigated the validity of the model for short-tubing length and proved it suitable for tubing longer than 150 mm; however, their model does not account for branched tubing systems.

Since differential pressures are required for airflow angle estimation, one strategy would be to connect the holes of a five-hole probe to pressure transducers and calculate the flow angles from the measured differential pressures as described in Spieß et al. (2007) for the M^{2}AV. The schematic of such a setup is shown in Fig. 4. This setup has a strongly branched tubing system at the high pressure port of all transducers (P_0 is branched six times), whereas the low pressure port is in most cases directly connected to one hole of the probe. This setup cannot be simulated by a simple model like the one described by Bergh and Tijdeman (1965).

Alternatively, the holes in the probe can be connected to the transducers in the manner presented in Fig. 5. This

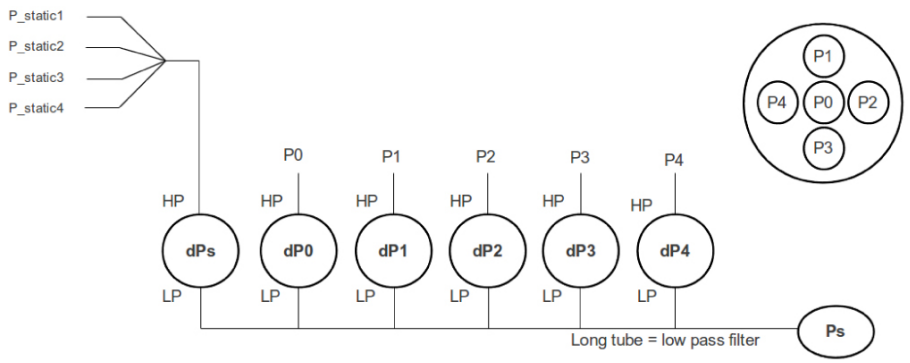

Fig. 5. Alternative tubing setup without branches as used in MASC. The pressure transducer measurements $\mathrm{d}Pi$ are differential readings of all single port pressures of the probe ($P0$–$P4$ and P_{static}, high pressure, HP) compared to one common reference port (low pressure, LP).

Table 1. Comparison of two methods to define dimensionless coefficients for five-hole probe measurements.

	Bohn et al. (1975) (M^2AV)	Treaster and Yocum (1979) (MASC)
ΔP	$\left[\frac{1}{5}\sum_{i=0}^{4}\left(P_i-\frac{1}{5}\sum_{j=0}^{4}P_j\right)^2\right]^{\frac{1}{2}}+\left[P_0-\frac{1}{4}\sum_{i=1}^{4}P_i\right]$	$\frac{(\mathrm{d}P_1+\mathrm{d}P_2+\mathrm{d}P_3+\mathrm{d}P_4)}{4}$
k_α	$\frac{\mathrm{d}P_{01}-\mathrm{d}P_{03}}{\Delta P}$	$\frac{\mathrm{d}P_1-\mathrm{d}P_3}{\mathrm{d}P_0-\Delta P}$
k_β	$\frac{\mathrm{d}P_{02}-\mathrm{d}P_{04}}{\Delta P}$	$\frac{\mathrm{d}P_2-\mathrm{d}P_4}{\mathrm{d}P_0-\Delta P}$
k_q	$\frac{q-\mathrm{d}P_{0s}}{\Delta P}$	$\frac{\mathrm{d}P_0-q}{\mathrm{d}P_0-\Delta P}$
k_p	$\frac{P_\mathrm{s}+\mathrm{d}P_{0s}-p}{\Delta P}$	$\frac{P_\mathrm{s}+\Delta P-p}{\mathrm{d}P_0-\Delta P}$

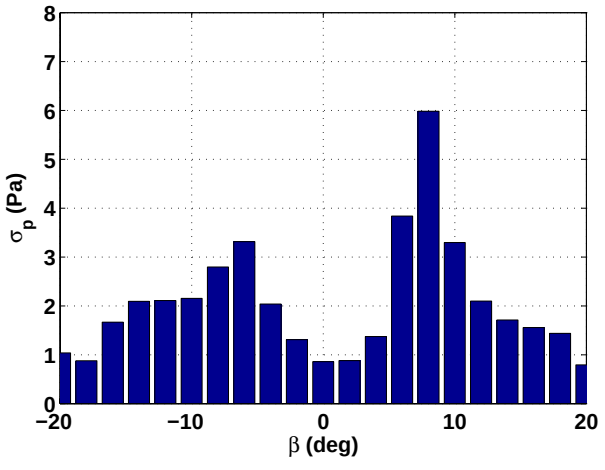

Fig. 6. Standard deviation of the pressure ports P_{static} in front of the ring of the ISM probe during a wind-tunnel calibration. Angle of attack 10°, angle of sideslip shifted from −20 to 20°.

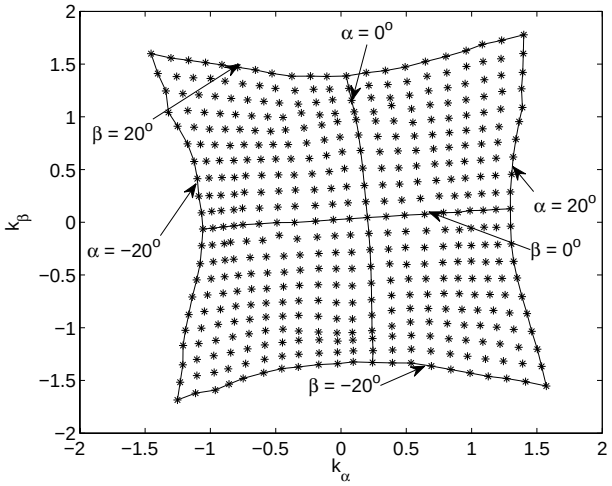

Fig. 7. Two-dimensional plot of k_β over k_α. The figure shows the nonlinearities that are larger for higher airflow angles α and β.

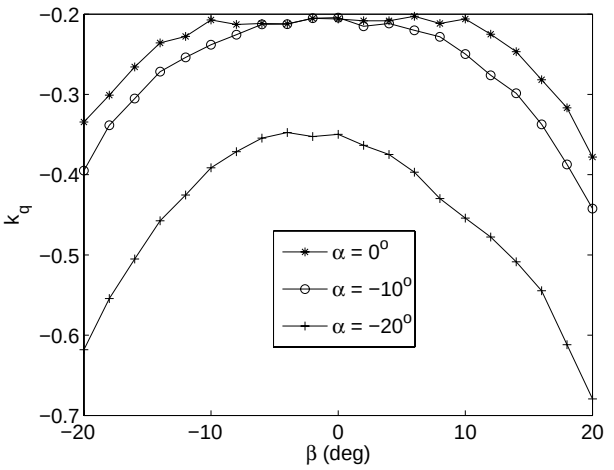

Fig. 8. Calibration coefficient k_q for dynamic pressure against calibration angle β for three attack angles α.

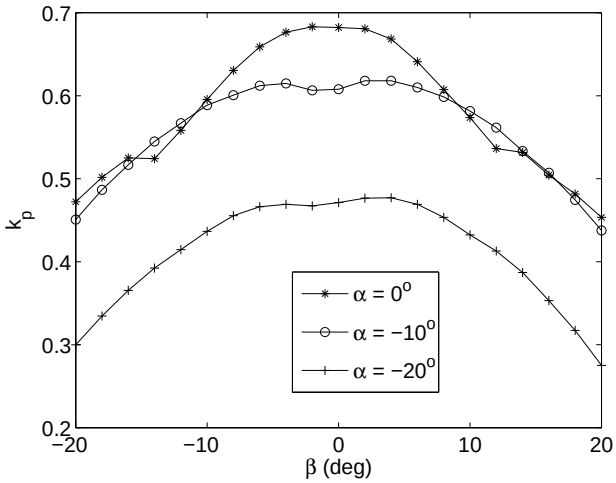

Fig. 9. Calibration coefficient k_p for static pressure against calibration angle β for three attack angles α.

method of tubing connection was used in MASC. The measured pressures can be converted to the same measurement as in the M^{2}AV setup as follows:

$$\mathrm{d}P_{0\mathrm{i}} = \mathrm{d}P_0 - \mathrm{d}P_i \quad \text{with } i = 1, \ldots, 4, s. \tag{4}$$

To compare the M^{2}AV and MASC setups with respect to the tubing system, the model of Bergh and Tijdeman cannot be used because it does not account for branches. Therefore, an experiment was set up to assess the response of the two different tubing strategies (see Fig. 12). What is depicted as "tubing under investigation" in the sketch is in a first experiment replaced with the M^{2}AV's branched tubing system as shown in Fig. 4 between the hole $P0$ and the high pressure port (HP) of transducer d$P0s$. In a second experiment, the tubing is replaced with MASC's single tube, as shown in Fig. 5 between hole $P0$ and the HP port of transducer d$P0$. For all connections, PVC tube of a length similar to the actual setup that would be implemented in MASC (in this case 0.18 m) was used. Instead of the connection to the $P0$ hole of the probe, the free end of the tube is connected to a sealed volume attached to a speaker. A reference measurement was made by placing another transducer directly on the cabin wall without any tubing in between the pressure source and the transducer. The speaker was able to play sine waves with frequencies from 10 to several 100 Hz. The measurement computer was logging the transducer output at a rate of 1 kHz. The maximum investigated frequency was 200 Hz, which is higher than the sampling rate that is used in flight.

Initially, the response of the transducers themselves were tested. The transducers included sensors of the type P4V-Mini by the company AllSensors and sensors of type LBA by the company Sensortechnics. The P4V-Mini sensors work on the principle of a membrane that is displaced by the pressure difference and its deflection is measured by piezoresistivity. The LBA sensors estimate pressure difference through a thermal mass-flow measurement.

To visualize the response of the pressure measurement system, the amplitude and phase response as the two parts of the transfer function H of the system are calculated:

$$H(\omega) = |H(\omega)| e^{i\phi(\omega)}, \tag{5}$$

where ω is the angular frequency and ϕ the phase shift. The amplitude response is presented as the ratio between the standard deviation σ of the tubing system being investigated and the reference:

$$|H(\omega)| = \frac{\sigma_{P0}(\omega)}{\sigma_{P_{\mathrm{ref}}}(\omega)}. \tag{6}$$

To find the phase response of the system, the cross-correlation function $\varrho_{P0,P_{\mathrm{ref}}}$ between the two sensors was calculated for each frequency and the time shift between the two signals needed for maximum correlation was estimated. This time shift was converted to a phase angle in the following manner:

$$\Delta t = t(\max|\varrho_{P0,P_{\mathrm{ref}}}|), \tag{7}$$

$$\phi = \Delta t \cdot \omega \cdot \frac{180}{\pi}. \tag{8}$$

The tests with the P4V-Mini sensors showed considerable variations in the response of each individual transducer. Therefore, the experiment was carried out only with the LBA sensors by Sensortechnics. In Sect. 4 further reasons are given for choosing this type of sensor in future flight measurements. The amplitude and phase response of the two tubing systems are presented in Fig. 13. In the same figure, the theoretical response for the single tube of same length

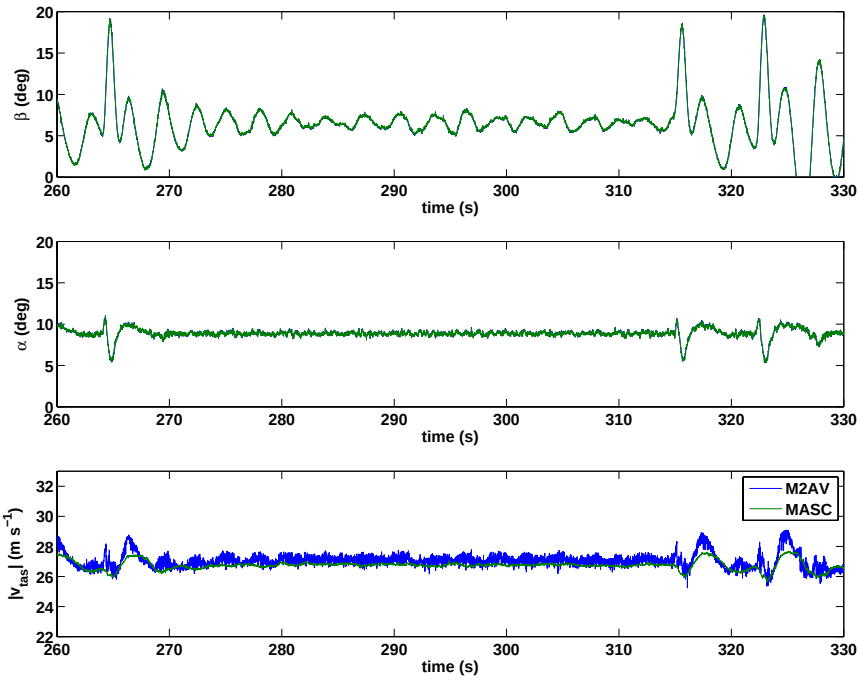

Fig. 10. True airspeed, measured with the five-hole probe and calculated with the M^{2}AV and MASC methods respectively. Angle of attack throughout the leg approximately 10°; angle of sideslip approximately 8°. See text for flight conditions.

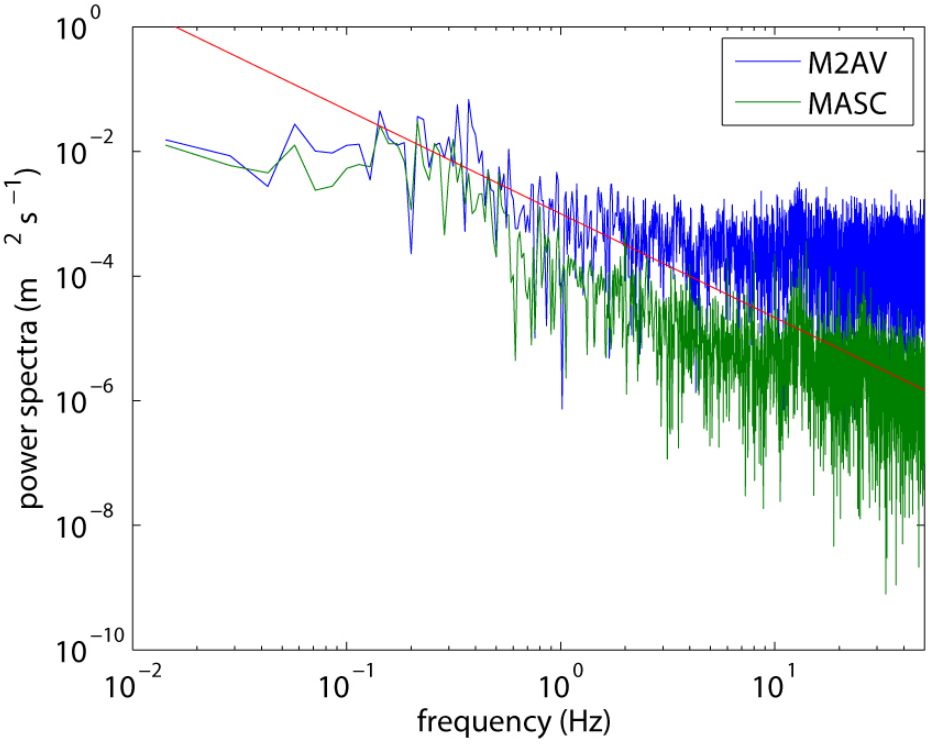

Fig. 11. Spectra of the true airspeed measurement in flight with standard calibration and new method. The red line shows the $k^{-\frac{5}{3}}$ slope.

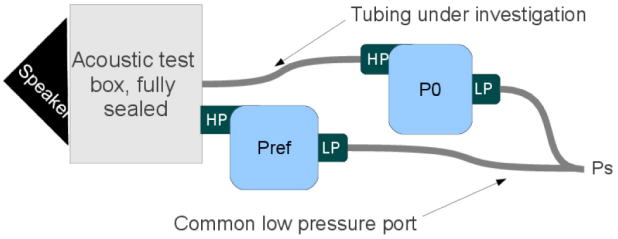

Fig. 12. Schematic drawing of the experiment to measure the tubing response. While the HP port of the reference transducer (Pref) is directly connected to the acoustic box, the HP port of the pressure measurement under investigation ($P0$) is connected with the necessary tubing of the real system. Ps is the common ambient pressure on the LP port of the transducers.

without branches as calculated with the Bergh and Tijdeman model is presented.

It can be seen that both tubing setups resemble oscillatory dynamic systems with at least one resonance frequency. The first resonant frequency of the M^{2}AV system was found to be at around 80 Hz, while it is out of the measurement range for the alternative setup. The damping factor of the M^{2}AV setup is much higher than for the alternative setup, hence the resonance amplitude was much smaller. The phase response attenuates towards $-180°$, which is characteristic for a second-order dynamical system.

It should be recalled that in the M^{2}AV setup, one side of the differential transducers was connected to the side holes of the probe directly, while the other side of the transducers was connected to the front hole with a branch to five other transducers. In light of the acoustic tests performed here, it was identified that the tubing responses on either side of the transducer differ significantly. Though the two tubing systems have a nominally similar amplitude response, a phase shift φ between each other would exist. Therefore an artificial signal S_m would be measured, which can be described as follows:

$$\begin{aligned} S_\mathrm{m} &= \sin\omega t - \sin(\omega t + \varphi), \\ &= \sin\omega t - \sin\omega t \cdot \cos\varphi + \cos\omega t \sin\varphi, \\ &= (1-\cos\varphi)\sin\omega t + \sin\varphi\cos\omega t, \end{aligned}$$

knowing that

$$a\cdot\sin\omega t + b\cdot\cos\omega t = A\cos(\omega t - \alpha)$$

with

$$A = \sqrt{a^2+b^2}, \tag{9}$$

$$\tan\alpha = \frac{b}{a}, \tag{10}$$

the artificial signal is

$$\begin{aligned} S_\mathrm{m} &= \sqrt{(1-\cos\varphi)^2+\sin\varphi^2}\cdot\cos\left[\omega t - \arctan\frac{\sin\varphi}{1-\cos\varphi}\right], \\ &= \sqrt{2(1-\cos\varphi)}\cdot\cos\left[\omega t - \cot^{-1}\frac{\varphi}{2}\right], \\ &= 2\sin\frac{\varphi}{2}\cdot\cos\left[\omega t - \cot^{-1}\frac{\varphi}{2}\right]. \end{aligned} \tag{11}$$

From Fig. 13, at 20 Hz the two tubing connections have a difference in phase shift of about 10°. This implies the transducer would measure a differential signal with an amplitude of $2\sin\frac{10°}{2} = 0.174$ times the original absolute signal, which is added to the measurement and can thereby be defined as an error of almost 20 %.

To see the real behaviour of the two tubing strategies and the artificial signals that are measured due to phase shift effects, a setup equal to that present in the M^{2}AV was tested. That is, both ends of a transducer were connected to the acoustic box whereby one port was connected to the box through a branch with five other transducers connected in parallel and the other port of the transducer was directly connected to the acoustic box via a 18 cm tube. In subsequent tests, both ports of the transducers were connected via 18 cm tubes to the acoustic box, this would resemble the alternate tubing strategy that is now being used on MASC. Ideally, as both ends of the transducers are connected to the same "source" (acoustic box), the pressures in the transducers should nullify one another and no pressures should be logged. The results of a time series measuring a sweep from 10 to 100 Hz (in steps of 10 Hz and a rest time of 10 s at each step) are shown in Fig. 14, left. The increase in amplitude of the pressure signal is not only due to an increasing phase shift, but also due to the increasing power of the speaker at the same gain setting. Figure 14, right, shows a normalized result for the measured frequency range, where the measured signal was divided by the prevailing pressure in the box that was measured with a second transducer. It can be seen that the relative error for 20 Hz is less than theoretically estimated, but it is also obvious that the effect can be observed in real measurements and can be avoided with the point-to-point tubing connections.

4 The pressure transducers

The volume of the pressure transducers adds to the pneumatic transfer function, and variation between different transducers can lead to a significantly different amplitude and phase response of the sensor at higher frequencies. Besides that, most pressure transducers are also sensitive to vibrations. In many MEMS (microelectromechanical system)-based differential pressure transducers, deformation of a membrane exposed to the applied pressure is measured by the means of piezoelectricity (in our study the sensor of type P4V-Mini, as used in the M^{2}AV for example). The piezoelectric voltage

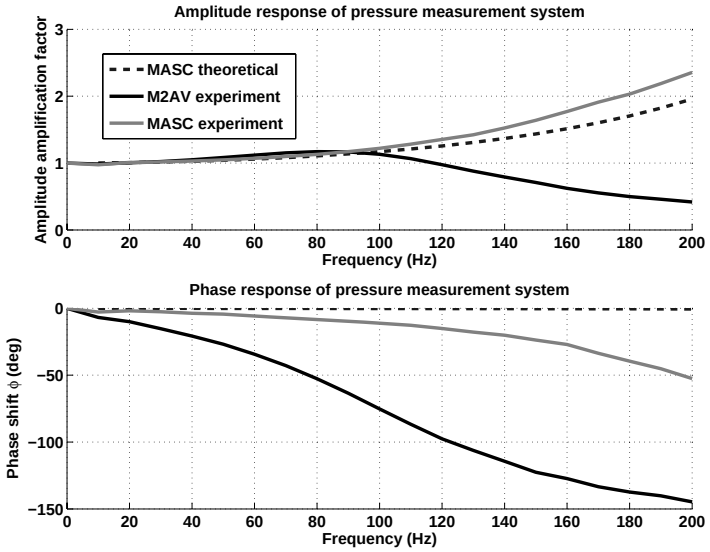

Fig. 13. Amplitude and phase response of the pressure measurement systems, including tubing, branches, transducer, etc. The MASC setup was investigated in an experiment (grey line) and theoretically with the Bergh and Tijdeman model (dashed line). The M^{2}AV setup cannot be calculated with the model and thus is only investigated in an experiment (black line).

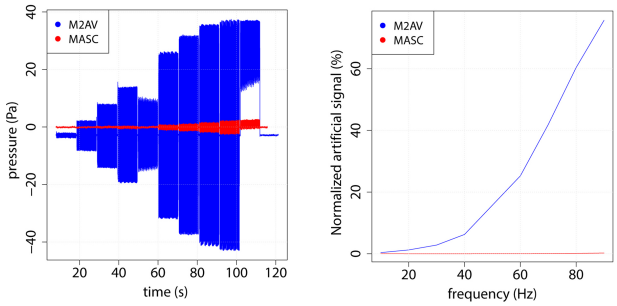

Fig. 14. Acoustic test of the MASC and the M^{2}AV tubing system in comparison. Left: raw measurement of the transducers. Right: percentage of prevailing pressure that is measured as an artefact due to different phase shifts at the high and low pressure ports of the transducer.

is amplified and a voltage linear to the applied pressure is put out by the sensor. However, the membrane can also be deformed by accelerations perpendicular to the membrane surface. Since aircraft are always subject to vibrations and accelerations it is important to consider this effect in the pressure measurements when membrane-based pressure transducers are used. The way to reduce the errors made due to this effect can be to calibrate the sensors for the sensitivity regarding acceleration and measure the given accelerations in flight to subtract the acceleration-induced signal from the transducer output signal. A way to avoid the issue of sensitivity to accelerations completely is to choose a different measuring principle which is not based on a membrane deformation. A suitable alternative are sensors that work on thermal flow measurement (in our study the sensor of type LBA, as used in MASC). Figure 15 shows a comparison between a membrane-based sensor and a thermal flow sensor which were at the same time exposed to accelerations by mounting them on one solid board and applying shock accelerations in three different orientations. It can be seen that the accelerations in the direction perpendicular to the membrane orientation (here the y direction) affect the membrane-based sensor, but not the thermal flow sensor. In the test, accelerations of up to $5\,\mathrm{m\,s^{-2}}$ were applied. Similar accelerations can be found in straight-leg flights with the MASC system. Other aircraft might have less or more vibration depending on the propulsion and flight dynamics. The resulting pressure transducer noise with amplitudes of up to 3 Pa adds to the higher frequency turbulence measurement and causes higher relative errors at lower turbulence intensity.

5 Sampling and anti-aliasing

So far, errors by aerodynamic and mechanical effects that affect the signal that is passed on by the pressure transducer were discussed. The next step in the measuring chain is to convert this analog 0–5 V signal from the pressure transducer to a digital signal and logging the data of all channels synchronously to one file. All data acquiring systems (DAQ) need to address the effect of aliasing in the measured frequency scales. Aliasing is critical in two ways: first, high frequency noise signals can alias into the sampled frequency range, if they are not filtered. Second, the signal

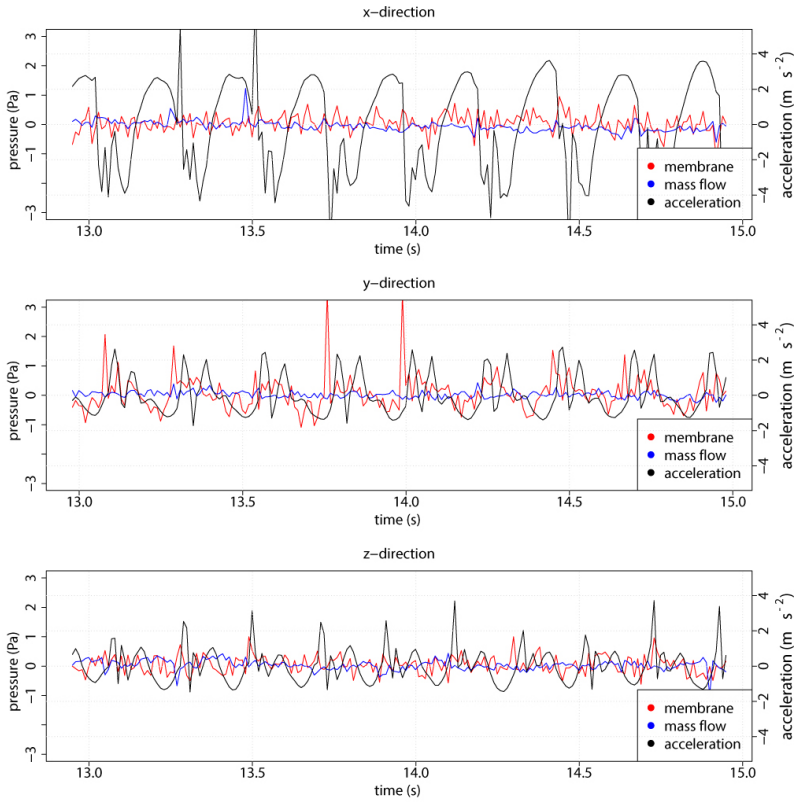

Fig. 15. Vibration/acceleration applied to pressure transducers in distinct directions

of the physical variable to be measured with frequencies slightly higher than half the sampling frequency can fold into the sampled frequency range and then lead to overestimates in the power of the signal at low frequencies. Commercial DAQ are generally unsuitable for RPA because they are either too heavy, too big or need too much power. The University of Tübingen developed the measuring computer AMOC (Airborne Meteorological Onboard Computer) in cooperation with the University of Applied Sciences Ostwestfalen-Lippe. The computer is equipped with two STM32 microcontrollers, a 24 bit, 16 channel analog-to-digital converter, a telemetry interface, a SD (Secure Digital)-card slot for data logging and various other interfaces (see also Wildmann et al., 2013). To obtain reliable turbulence measurements within an error band of 10 %, an anti-aliasing filter was designed and implemented on the measuring computer which contains the following parts.

1. A first order analog filter (RC-low pass) with cut-off frequency at 160 Hz: only 50 % of the original amplitude of signals with 160 Hz passes the filter, and only 10 % of the signal at 500 Hz. The amplitude response of the analog filter can be seen in Fig. 16 as a dashed blue line.

2. Oversampling of the signal at 500 Hz on-board the measuring computer: only signals above 500 Hz appear as aliases in the measured signal on-board the measuring computer. As described above, these signals are already damped to less than 10 % of the original signal.

3. Digital moving average filter with cut-off frequency at 70 Hz in real-time on-board AMOC: the moving average filter is chosen because of its simple implementation, needing only little computing power in real-time processing and giving an optimal noise reduction while keeping sharp step responses (Smith, 1997). The rather poor performance of the filter in frequency separation is still good enough for the given task. From the red dashed line in Fig. 16, it can be seen that the filter still has a quasi-flat response at 10 Hz and still more than 91 % of the signal amplitude is passed at 20 Hz, while at 100 Hz only 25 % passes and, thanks to the complementary analog filter, the response of signals above 150 Hz is always damped to a maximum of 6 % of the original signal.

4. The log onto the SD-card at 100 Hz: logging at 100 Hz is another oversampling step to achieve anti-aliased

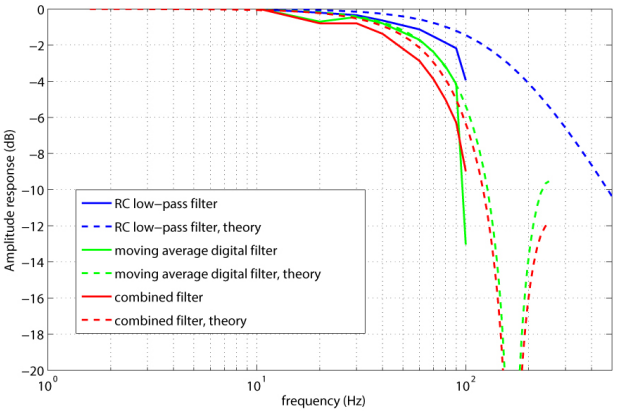

Fig. 16. Amplitude response of the applied filters in the analog channels of the MASC DAQ. The effective filter (red) is a combination of an analog RC low-pass filter (blue) and a digital moving average filter (green). The dashed lines represent the theoretical behaviour of the filters with the applied parameters. The solid lines represent measurements of the real sensor response in an acoustic box experiment.

data of up to at least 20 Hz. Sampling at 100 Hz, signals between 100 and 150 Hz can fold into the frequency range of up to 50 Hz. The previous steps explained how these signals are already damped to less than 25 %. Frequencies above 150 Hz are damped to less than 6 %.

This means that in the frequency range from 0 to 50 Hz a maximum error caused by aliasing of 25 % is theoretically possible. In reality, the measured signal is a turbulent flow, wherein the power of the signal decreases with increasing frequency (power law $k^{-5/3}$ in the inertial subrange of locally isotropic turbulence, Kolmogorov, 1941). This means that the aliases naturally have a lower amplitude compared to the true signal at a specific frequency, which also means that the maximum error that was estimated is overestimated, except for unnatural noise signals. Note that electromagnetic noise typically begins at much higher frequencies that are filtered by the analog filter.

6 Comparison of MASC and M^{2}AV data

In order to demonstrate that the design considerations in the airflow measurement system, as described above, do show the desired improvement in turbulence measurement, an analysis of the frequency response of the system in flight was carried out. Kolmogorov's theory of locally isotropic turbulence in the inertial subrange provides theoretical slopes of variance spectrum and structure function. If measured data is compared to this theory, the quality of turbulence measurement can be evaluated. Figure 17 shows the result of this analysis for true airspeed measurements. To prove that real

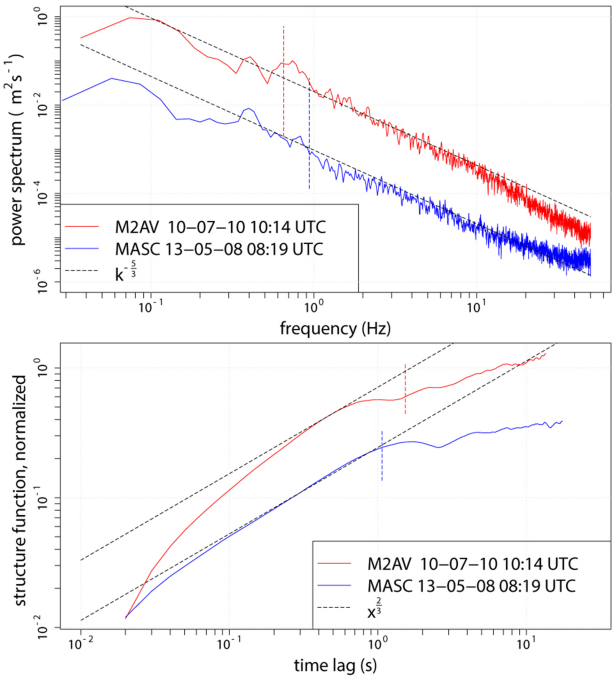

Fig. 17. A variance spectrum and a structure function of true airspeed measured with the MASC RPA in comparison to a measurement with the M^{2}AV RPA. In both plots, the result is an average over 15 legs of 27 s each. The structure function is normalized by $2\sigma^2$ and therefore dimensionless. In both plots, MASC results are shifted towards lower values for better readability. The dashed lines indicate an estimation of the entry point of the inertial subrange. See text for flight conditions.

enhancements compared to established measurement systems like the M^{2}AV were achieved, the result is compared to measurements of the M^{2}AV in very similar meteorological conditions. The M^{2}AV flight was in summer on 10 July 2010. The MASC flight in late spring, 8 May 2013, both in the already mixed layer in the late morning at an altitude of 200 and 100 m respectively. It can be seen that the MASC system follows the theory very well up to 10 Hz. Slight damping according to the theory in Sect. 5 can be observed at higher frequencies. According to the experiments that were done, comparing tubing strategy, pressure transducers and probe calibration, it would be expected that the M^{2}AV system is subject to more noise. The data does not reflect this. Instead, in the structure function, a strong damping is observed in the system starting at a time lag of approximately 0.5 s, which corresponds to turbulent signals with a frequency of 2 Hz. This suggests that the noise was reduced by a low-pass filter in the pressure measurements of the probe. This cannot be ascertained in the absence of more information on the DAQ used in the M^{2}AV. However, it can be stated that the MASC MHP setup meets the desired frequency response better than the M^{2}AV system. Analysis of seven more flights of

the M^2AV in campaigns between 2007 and 2011 were analysed and supported the findings.

7 Conclusions

It was shown in this study how a standard MHP can be optimized for turbulence measurements by following a few, easy steps. It is of high importance to know the frequency response of each piece in the measuring chain, starting with the pneumatic response of the MHP itself, the tubing and the pressure transducers. The common error of vibration sensitivity in membrane-based pressure transducers was discussed, and to avoid this effect we suggest to use thermal flow sensors instead. It was also shown how the data acquisition has to be optimized for nondisturbed turbulence measurement in the desired frequency range. The effect of antialiasing can be minimized by an appropriate filter design. Considering these points, precise measurements of mean flow and turbulent fluctuation of up to 20 Hz can be achieved with the given MHP and DAQ system. To use the MHP in RPA applications for wind and flux measurement, it has to be embedded into a measurement system consisting of the aircraft itself, inertial measurements and an autopilot in best case. Issues such as flow distortion by the fuselage and wings have to be discussed for each individual aircraft type (Crawford et al., 1996; Wyngaard et al., 1985). The fusion of airflow data with inertial measurements to calculate wind is already described by van den Kroonenberg et al. (2008).

Acknowledgements. The authors would like to thank the anonymous reviewers for their valuable comments and suggestions to improve the quality of the paper. We would furthermore like to thank Maximilian Ehrle and Markus Auer for their great job as safety pilots and Bernd Peters and the IAG Stuttgart for the support and time with the jet wind tunnel. The measuring equipment would not have been ready to work without the help of Jens Dünnermann and Burkhard Wrenger from the University of Applied Sciences Ostwestfalen-Lippe. We acknowledge the support from Dr. Ing. Peter Scholz at the University of Braunschweig for questions regarding the MHP design.

We acknowledge support by Deutsche Forschungsgemeinschaft and Open Access Publishing Fund of Tübingen University.

Edited by: S. Malinowski

References

Bange, J.: Airborne Measurement of Turbulent Energy Exchange Between the Earth Surface and the Atmosphere, Sierke Verlag, Göttingen, Germany, 174 pp., ISBN 978-3-86844-221-2, 2009.

Bergh, H. and Tijdeman, H.: Theoretical and Experimental Results for the Dynamic Response of Pressure Measuring Systems, vol. 238, National Luchten Ruimtevaartlaboratorium, Amsterdam, NL, 1965.

Bohn, D. and Simon, H.: Mehrparametrige Approximation der Eichräume und Eichflächen von Unterschall- bzw. Überschall-5-Loch-Sonden, Archiv für technisches Messen + messtechnische Praxis, 42, 31–37, 1975.

Boiffier, J.-L.: The Dynamics of Flight – the Equations, Wiley, Chichester, UK, 1998.

Crawford, T. L. and Dobosy, R. J.: A Sensitive Fast-Response Probe to Measure Turbulence and Heat Flux from any Airplane, Bound.-Lay. Meteorol., 59, 257–278, 1992.

Crawford, T. L., Dobosy, R. J., and Dumas, E. J.: Aircraft Wind Measurement Considering Lift-Induced Upwash, Bound.-Lay. Meteorol., 80, 79–94, 1996.

Friehe, C. A., Burns, S. P., Khelif, D., and Song, X.: Meteorological and Flux Measurements from the NOAA WP3D Aircraft in TOGA COARE, in: 8th Conference on Air-Sea Interaction, J42–J45, AMS, Atlanta, GA, 1996.

Haala, N., Cramer, M., Weimer, F., and Trittler, M.: Performance Test on UAV-Based Photogrammetric Data Collection, in: UAV-g (unmanned aerial vehicle in geomatics) Conference, Zurich, Switzerland, vol. 16–20, American Meteorological Society, 2011.

Haering, E. A.: Airdata Calibration of a High-Performance Aircraft for Measuring Atmospheric Wind Profiles, Tech. Mem. 101714, NASA, Edwards, CA, 24 pp, 1990.

Khelif, D., Burns, S. P., and Friehe, C. A.: Improved Wind Measurements on Research Aircraft, J. Atmos. Oceanic Technol., 16, 860–875, 1999.

Kolmogorov, A.: The Local Structure of Turbulence in Incompressible Viscous Fluid for Very Large Reynolds Numbers, Dokl. Akad. Nauk SSSR, 30, 299–303, reprint: Proc. R. Soc. Lond. A, 1991, 434, 9–13, 1941.

Leise, J. A. and Masters, J. M.: Wind Measurements from Aircraft, US Department of Commerce, National Oceanic and Atmospheric Administration, Aircraft Operation Center, Miami, Florida, USA, 1993.

Lemonis, G., Schmücker, M., and Struck, H.: A Fast Response Probe System for In-Flight Measurements of Atmospheric Turbulence, Aerospace Sci. Tech., 6, 233–243, 2002.

Lenschow, D. H.: Aircraft Measurements in the Boundary Layer, in: Probing the Atmospheric Boundary Layer, edited by Lenschow, D. H., 39–53, Amer. Meteorol. Soc., Boston, MA, 1986.

Martin, S. and Bange, J.: The Influence of Aircraft Speed Variations on Sensible Heat-Flux Measurements by Different Airborne Systems, Bound.-Lay. Meteorol., 150, 153–166, doi:10.1007/s10546-013-9853-7, 2014.

Martin, S., Bange, J., and Beyrich, F.: Meteorological profiling of the lower troposphere using the research UAV "M2AV Carolo", Atmos. Meas. Tech., 4, 705–716, doi:10.5194/amt-4-705-2011, 2011

Pfau, A., Schlienger, J., Kalfas, A. I., and Abhari, R. S.: Virtual Four Sensor Fast Response Aerodynamic Probe (FRAP), in: 16th Symposium on Measuring Techniques in Transonic and Supersonic Flow in Cascades and Turbomachines, Cambridge, UK, 2002.

Rosemount: Model 858 Flow Angle Sensors, Rosemount Inc., Minneapolis, MN, bulletin 1014, 1982.

Sasangko, H.: Rand- und Spaltströmungen in stark gestaffelten Verdichtergittern aus schwach gewölbten Profilen, Technische Universität Braunschweig, ZLR-Forschungsbericht, 01, 1997.

Schlienger, J., Pfau, A., Kalfas, A. I., and Abhari, R. S.: Single Pressure Transducer Probe for 3D Flow Measurements, in: 16th Symposium on Measuring Techniques in Transonic and Supersonic Flow in Cascades and Turbomachines, Cambridge, UK, 2002.

Semaan, R. and Scholz, P.: Pressure correction schemes and the use of the Wiener deconvolution method in pneumatic systems with short tubes, Experiments in Fluids, 53, 829–837, 2012.

Smith, S. W.: The scientist and engineer's guide to digital signal processing, California Technical Publishing, San Diego, CA, USA, 1997.

Spieß, T.: A Contribution to Turbulence Measurements with Autonomous Micro Aerial Vehicles, Ph.D. thesis, Institute for Aerospace Systems, Techn. Univ. Braunschweig, Germany, 137 pp., 2006.

Spieß, T., Bange, J., Buschmann, M., and Vörsmann, P.: First Application of the Meteorological Mini-UAV "M2AV", Meteorol. Z. N. F., 16, 159–169, 2007.

Sumner, D.: Calibration Methods for a Seven-Hole Pressure Probe, in: Sixth Triennial International Symposium on Fluid Control, Measurement and Visualization (Flucome 2000), edited by: Laneville, A., Sherbrooke, Canada, 2000.

Telionis, D., Yang, Y., and Redinioti, O.: Recent developments in multi-hole probe (mhp) technology, in: 20th International Conference of Mechanical Engineering, Gramado, RS, Brazil, ABCM, 2009.

Thomas, R. M., Lehmann, K., Nguyen, H., Jackson, D. L., Wolfe, D., and Ramanathan, V.: Measurement of turbulent water vapor fluxes using a lightweight unmanned aerial vehicle system, Atmos. Meas. Tech., 5, 243–257, doi:10.5194/amt-5-243-2012, 2012.

Treaster, A. L. and Yocum, A. M.: The calibration and application of five-hole probes, ISA Trans., 18, 23–34, 1979.

van den Kroonenberg, A. C., Martin, T., Buschmann, M., Bange, J., and Vörsmann, P.: Measuring the Wind Vector Using the Autonomous Mini Aerial Vehicle M^2AV, J. Atmos. Oceanic Technol., 25, 1969–1982, 2008.

van den Kroonenberg, A. C., Martin, S., Beyrich, F., and Bange, J.: Spatially-averaged temperature structure parameter over a heterogeneous surface measured by an unmanned aerial vehicle, Bound.-Lay. Meteorol., 142, 55–77, 2011.

Wildmann, N., Mauz, M., and Bange, J.: Two fast temperature sensors for probing of the atmospheric boundary layer using small remotely piloted aircraft (RPA), Atmos. Meas. Tech., 6, 2101–2113, doi:10.5194/amt-6-2101-2013, 2013.

Williams, A. and Marcotte, D.: Wind Measurements on a Maneuvering Twin-Engine Turboprop Aircraft Accounting for Flow Distortion, J. Atmos. Oceanic Technol., 17, 795–810, 2000.

Wyngaard, J. C., Rockwell, L., and Friehe, C. A.: Errors in the Measurement of Turbulence Upstream of an Axisymmetric Body, J. Atmos. Oceanic Technol., 2, 605–614, 1985.

Zimmer, G., Alam, F., Watkins, S., and Peric, C.: Comparison of a High Blockage Wind Tunnel, an Open Jet Wind Tunnel and On-road Testing with Respect to External Surface Pressures, in: SAE 2001 World Congress Detroit, MI, Technical Papers, 2001–01–1087, 2001.

Appendix A

Five-hole probe pressures to airflow vector conversion

For a better understanding, a detailed step by step description of the measurement with a five-hole probe will be given here. The description needs to be divided into the wind-tunnel calibration procedure and the actual instantaneous measurement of the airspeed vector.

A1 Wind-tunnel calibration

A wind-tunnel calibration is essential for the measurement with a multi-hole probe. The goal of the wind-tunnel calibration is to find a relationship between the measured pressures $\mathrm{d}P_i$ and the airflow angles α and β. Besides this, the probe needs to be calibrated to measure the correct dynamic and static pressure at any airflow angle (within the calibration range). In order to make this fit robust against changes in airspeed (i.e. changes in Reynolds number), a polynomial fit is not directly applied to the raw pressure readings, but dimensionless coefficients are defined (see Table 1).

The presetting of the wind tunnel is a certain dynamic pressure q and static pressure p, which should be continuously measured with an independent measuring system during the calibration routine. k_α and k_β serve as the variables of the polynomial functions for α, β, and k_p, and k_q. k_p and k_q can be understood as correction values for dynamic pressure and static pressure with regards to the airflow angle at the probe.

$$\begin{aligned} \alpha &= f_\alpha(k_\alpha, k_\beta) \\ \beta &= f_\beta(k_\alpha, k_\beta) \\ k_p &= f_s(k_\alpha, k_\beta) \\ k_q &= f_q(k_\alpha, k_\beta) \end{aligned} \tag{A1}$$

The functions $f_x(k_\alpha, k_\beta)$ are arranged as a polynomial of order m and the two variables:

$$f_x(k_\alpha, k_\beta) = \sum_{i=0}^{m} (k_\alpha)^i \left[\sum_{j=0}^{m} X_{ij} (k_\beta)^j \right], \tag{A2}$$

with X_{ij} the coefficients $c_{\alpha,ij}$, $c_{\beta,ij}$, $c_{s,ij}$ and $c_{q,ij}$, for the estimation of α, β, k_p and k_q respectively. To achieve a good accuracy with the polynomial fit, calibration with angle steps of 2° is recommended. The calibration range for the MHP under investigation is suggested to be not larger than 20° in all directions. A sufficiently large number of calibration settings yields four overestimated systems of linear equations, which can be presented in matrix notation:

$$\begin{aligned}
&\begin{bmatrix} 1\, k_{\beta 0}\, k_{\beta 0}^2 \,\dots\, k_{\alpha 0}\, k_{\alpha 0}k_{\beta 0}\, k_{\alpha 0}k_{\beta 0}^2 \,\dots\, k_{\alpha 0}^n k_{\beta 0}^n \\ 1\, k_{\beta 1}\, k_{\beta 1}^2 \,\dots\, k_{\alpha 1}\, k_{\alpha 1}k_{\beta 1}\, k_{\alpha 1}k_{\beta 1}^2 \,\dots\, k_{\alpha 1}^n k_{\beta 1}^n \\ \vdots \\ 1\, k_{\beta n}\, k_{\beta n}^2 \,\dots\, k_{\alpha n}\, k_{\alpha n}k_{\beta n}\, k_{\alpha n}k_{\beta n}^2 \,\dots\, k_{\alpha n}^n k_{\beta n}^n \end{bmatrix} \begin{bmatrix} c_{\alpha,0} \\ c_{\alpha,1} \\ \vdots \\ c_{\alpha,n} \end{bmatrix} \\
&\begin{bmatrix} 1\, k_{\beta 0}\, k_{\beta 0}^2 \,\dots\, k_{\alpha 0}\, k_{\alpha 0}k_{\beta 0}\, k_{\alpha 0}k_{\beta 0}^2 \,\dots\, k_{\alpha 0}^n k_{\beta 0}^n \\ 1\, k_{\beta 1}\, k_{\beta 1}^2 \,\dots\, k_{\alpha 1}\, k_{\alpha 1}k_{\beta 1}\, k_{\alpha 1}k_{\beta 1}^2 \,\dots\, k_{\alpha 1}^n k_{\beta 1}^n \\ \vdots \\ 1\, k_{\beta n}\, k_{\beta n}^2 \,\dots\, k_{\alpha n}\, k_{\alpha n}k_{\beta n}\, k_{\alpha n}k_{\beta n}^2 \,\dots\, k_{\alpha n}^n k_{\beta n}^n \end{bmatrix} \begin{bmatrix} c_{\beta,0} \\ c_{\beta,1} \\ \vdots \\ c_{\beta,n} \end{bmatrix} \\
&\begin{bmatrix} 1\, k_{\beta 0}\, k_{\beta 0}^2 \,\dots\, k_{\alpha 0}\, k_{\alpha 0}k_{\beta 0}\, k_{\alpha 0}k_{\beta 0}^2 \,\dots\, k_{\alpha 0}^n k_{\beta 0}^n \\ 1\, k_{\beta 1}\, k_{\beta 1}^2 \,\dots\, k_{\alpha 1}\, k_{\alpha 1}k_{\beta 1}\, k_{\alpha 1}k_{\beta 1}^2 \,\dots\, k_{\alpha 1}^n k_{\beta 1}^n \\ \vdots \\ 1\, k_{\beta n}\, k_{\beta n}^2 \,\dots\, k_{\alpha n}\, k_{\alpha n}k_{\beta n}\, k_{\alpha n}k_{\beta n}^2 \,\dots\, k_{\alpha n}^n k_{\beta n}^n \end{bmatrix} \begin{bmatrix} c_{s,0} \\ c_{s,1} \\ \vdots \\ c_{s,n} \end{bmatrix} \\
&\begin{bmatrix} 1\, k_{\beta 0}\, k_{\beta 0}^2 \,\dots\, k_{\alpha 0}\, k_{\alpha 0}k_{\beta 0}\, k_{\alpha 0}k_{\beta 0}^2 \,\dots\, k_{\alpha 0}^n k_{\beta 0}^n \\ 1\, k_{\beta 1}\, k_{\beta 1}^2 \,\dots\, k_{\alpha 1}\, k_{\alpha 1}k_{\beta 1}\, k_{\alpha 1}k_{\beta 1}^2 \,\dots\, k_{\alpha 1}^n k_{\beta 1}^n \\ \vdots \\ 1\, k_{\beta n}\, k_{\beta n}^2 \,\dots\, k_{\alpha n}\, k_{\alpha n}k_{\beta n}\, k_{\alpha n}k_{\beta n}^2 \,\dots\, k_{\alpha n}^n k_{\beta n}^n \end{bmatrix} \begin{bmatrix} c_{q,0} \\ c_{q,1} \\ \vdots \\ c_{q,n} \end{bmatrix}.
\end{aligned} \tag{A3}$$

A solution for the coefficients c can be found with a least squares method. For the coefficients $c_{\alpha,i}$ this would, for example, yield

$$\begin{aligned} \boldsymbol{\alpha} &= \mathbf{K} \cdot \boldsymbol{c}_\alpha, \\ S(\boldsymbol{c}_\alpha) &= \sum_{i=1}^{m} \left| \alpha_i - \sum_{j=1}^{n} K_{ij} c_{\alpha,j} \right|^2 = \left\| \boldsymbol{\alpha} - \mathbf{K} \cdot \boldsymbol{c}_\alpha \right\|^2, \\ \hat{\boldsymbol{c}}_\alpha &= \arg\min_{\boldsymbol{c}_\alpha} S(\boldsymbol{c}_\alpha), \end{aligned} \tag{A4}$$

where S is the minimization criterion and $\hat{c}_\alpha$ is the best fit for the given calibration. For linear independent columns, a unique solution can be found by solving the normal equation:

$$\begin{aligned} \mathbf{K}^T K \cdot \hat{\boldsymbol{c}}_\alpha &= \mathbf{K}^T \boldsymbol{\alpha}, \\ \hat{\boldsymbol{c}}_\alpha &= (\mathbf{K}^T K)^{-1} \cdot \mathbf{K}^T \boldsymbol{\alpha}. \end{aligned} \tag{A5}$$

Thus, the output of the wind-tunnel calibration are the coefficients $\boldsymbol{c}_\alpha$, $\boldsymbol{c}_\beta$, $\boldsymbol{c}_\mathrm{s}$ and $\boldsymbol{c}_q$.

A2 Measurement with the multi-hole probe

Once the probe has been calibrated, velocity and flow angles in arbitrary flows may be estimated as follows.

– The instantaneous pressures across each hole of the probe are converted to instantaneous $\Delta P, k_\alpha$, and k_β according to Table 1.

– Subsequently, $\boldsymbol{k}_p$, $\boldsymbol{k}_q$, $\boldsymbol{\alpha}$ and $\boldsymbol{\beta}$ are estimated:

$$\begin{aligned} \boldsymbol{\alpha} &= \mathbf{K} \cdot \boldsymbol{c}_\alpha, \\ \boldsymbol{\beta} &= \mathbf{K} \cdot \boldsymbol{c}_\beta, \\ \boldsymbol{k}_p &= \mathbf{K} \cdot \boldsymbol{c}_\mathrm{s}, \\ \boldsymbol{k}_q &= \mathbf{K} \cdot \boldsymbol{c}_q. \end{aligned} \tag{A6}$$

– Finally, the static pressure and the dynamic pressure are calculated solving the equations in Table 1 for p and q, respectively.

Table A1. Calculation of static and dynamic pressure from five-hole probe measurements with two different methods.

	Bohn et al. (1975)	Treaster and Yocum (1979)
p	$P_\mathrm{s} + \mathrm{d}P_{0\mathrm{s}} - k_p \cdot \Delta P$	$P_\mathrm{s} + \Delta P - k_p \cdot (\mathrm{d}P_0 - \Delta P)$
q	$\mathrm{d}P_{0\mathrm{s}} + k_q \cdot \Delta P$	$\mathrm{d}P_0 - k_q \cdot (\mathrm{d}P_0 - \Delta P)$

A.3 An inverse-modelling approach for frequency response correction of capacitive humidity sensors in ABL research with small remotely piloted aircraft (RPA).

The publication is also available at
`http://www.atmos-meas-tech.net/7/3059/2014/`.

Atmos. Meas. Tech., 7, 3059–3069, 2014
www.atmos-meas-tech.net/7/3059/2014/
doi:10.5194/amt-7-3059-2014

Atmospheric Measurement Techniques
Open Access

An inverse-modelling approach for frequency response correction of capacitive humidity sensors in ABL research with small remotely piloted aircraft (RPA)

N. Wildmann, F. Kaufmann, and J. Bange

Center for Applied Geoscience, Eberhard Karls Universität Tübingen, Tübingen, Germany

Correspondence to: N. Wildmann (norman.wildmann@uni-tuebingen.de)

Received: 29 January 2014 – Published in Atmos. Meas. Tech. Discuss.: 5 May 2014
Revised: 16 August 2014 – Accepted: 21 August 2014 – Published: 22 September 2014

Abstract. The measurement of water vapour concentration in the atmosphere is an ongoing challenge in environmental research. Satisfactory solutions exist for ground-based meteorological stations and measurements of mean values. However, carrying out advanced research of thermodynamic processes aloft as well, above the surface layer and especially in the atmospheric boundary layer (ABL), requires the resolution of small-scale turbulence. Sophisticated optical instruments are used in airborne meteorology with manned aircraft to achieve the necessary fast-response measurements of the order of 10 Hz (e.g. LiCor 7500). Since these instruments are too large and heavy for the application on small remotely piloted aircraft (RPA), a method is presented in this study that enhances small capacitive humidity sensors to be able to resolve turbulent eddies of the order of 10 m. The sensor examined here is a polymer-based sensor of the type P14-Rapid, by the Swiss company Innovative Sensor Technologies (IST) AG, with a surface area of less than 10 mm^2 and a negligible weight. A physical and dynamical model of this sensor is described and then inverted in order to restore original water vapour fluctuations from sensor measurements. Examples of flight measurements show how the method can be used to correct vertical profiles and resolve turbulence spectra up to about 3 Hz. At an airspeed of 25 $m\,s^{-1}$ this corresponds to a spatial resolution of less than 10 m.

1 Introduction

1.1 Water vapour in atmospheric research

The atmospheric boundary layer (ABL) is in direct contact with the Earth surface and subject to water exchange with the soil, rivers, lakes and oceans. Although it is decoupled by a temperature inversion from the free atmosphere, entrainment processes lead to an exchange of water vapour through the inversion (Stull, 1988). This exchange of water, enforced by turbulent transport in the ABL, leads to a high temporal, horizontal and vertical variability of water vapour. Water vapour concentration is not only important for cloud formation, rainfall and fog; it also plays an important role in the energy balance of the Earth surface and for thermodynamic processes in the atmosphere. Recent large-eddy simulations (LES) showed how the structure parameter of humidity is much less understood than the structure parameter of temperature. The structure parameter, or structure function parameter (Stull, 1988), is a characteristic parameter of a turbulent signal in the locally isotropic subrange and can also be used to estimate fluxes of the corresponding quantities (Wyngaard and Clifford, 1978). The ABL structure is typically described by means of similarity theories and parametrizations (Garratt, 1992) in order to compare results in different regimes. While for example the Monin–Obukhov similarity theory is found to be valid in all regimes for temperature, the same theory does not apply to humidity, especially if entrainment into the mixed layer is present (Maronga, 2013). A more detailed description of entrainment processes is needed, which will need precise measurements of water vapour fluxes to validate the models. Recently, first

measurements of entrainment processes with small remotely piloted aircraft (RPA) were reported (Martin et al., 2013), but only temperature and wind could be analysed, due to a lack of fast-response humidity measurements. Essential for the measurement of turbulent fluctuations is a high sampling rate and a short time response throughout the measurement chain, high measurement resolution and high accuracy. One goal of this study is to provide a method to enhance present sensors on small RPA in order to make the required measurements in the ABL.

1.2 Water vapour measurement in airborne systems

In situ measurement of atmospheric processes above the surface layer requires airborne sensor carriers in the form of fixed-wing aircraft, helicopters, balloons or similar. There are research aircraft for upper-troposphere and lower-stratosphere measurements, but also for measurements in the ABL, which are the focus of this study. Examples of research aircraft for boundary-layer research are the Dornier 128 (Bange et al., 2002; Corsmeier et al., 2001) and the MetAir Dimona (Neininger et al., 2001). A slightly different type of airborne system that was used for ABL research is the helicopter probe Helipod (Bange and Roth, 1999). All of them carry at least one instrument to investigate water vapour and its fluxes in the ABL. An overview of the state of the art of instrumentation for airborne measurements is given in Bange et al. (2013), and a short summary is presented in Sect. 2.1 of this article. It should be noted that manned research aircraft are subject to high operating costs and thus are only used in short, dedicated field experiments. Within the last decade, technical progress has made it possible to use small RPA, equipped with autopilots and waypoint navigation, for research purposes in many fields (Martin et al., 2011, 2013; Martin and Bange, 2013; van den Kroonenberg et al., 2011, 2008; Spieß et al., 2007; Jonassen, 2008; Chao et al., 2008; Jensen and Chen, 2013). Their flexibility and low operating cost enables researchers to come up with new, innovative ideas to probe the atmosphere in a way that was not possible before. Along with these possibilities come the challenges of making instrumentation even smaller and more lightweight in order for it to be carried on these aircraft while still competing with the quality of ground-based sensors. The smallest of these unmanned aerial vehicles (UAVs), as they are also called, weigh up to 5 kg and carry capacitive humidity sensors of different kinds (Reuder et al., 2009; Martin et al., 2011). Larger RPA, up to 50 kg, can carry more sophisticated sensors that are too large for the smaller RPA, such as krypton hygrometers (Thomas et al., 2012). Small RPA have several advantages: it is comparatively easy to obtain flight permission for them in central Europe. They do not require special ground facilities, such as a catapult or a runway, and they are low-cost. Furthermore, small RPA do not disturb the turbulent flow they have to measure, which increases accuracy, while, at the same time, the sensors allow a fast-response measurement of the variable of interest. This shows that an improved response time for capacitive humidity sensors can be of great benefit for atmospheric research and especially for turbulence measurements. The University of Tübingen operates the RPA MASC (Multi-purpose Airborne Sensor Carrier), which is equipped with fast temperature sensors (Wildmann et al., 2013), a flow probe (Wildmann et al., 2014) and a capacitive humidity sensor. All flight measurements that are presented in this article were carried out with the MASC RPA.

1.3 Control theory and signal restoration

In this study, methods of control theory will be applied to achieve better results in the measurement of humidity with capacitive sensors. In control theory, mathematical models are derived from physical systems and put into standard forms to describe the dynamics of the system and to eventually design controllers to influence the system's behaviour. Instead of designing controllers for the system, the mathematical description of the dynamic behaviour of the system can also be used to restore the original signal from a measurement if the dynamics of the sensor are well described. Similar work has been done in the field of airspeed measurement with flow probes (Rediniotis and Pathak, 1999) to correct for time delays in the pneumatic setup of these sensors. Another example are thermocouples in combustion engines where fast response of the sensors in harsh conditions is desired (Tagawa et al., 2005). It is shown in this report how similar techniques can be applied for capacitive humidity sensors in ABL research. Compared to simple time delay corrections that were reported to be applied to capacitive humidity sensors in radiosondes (Leiterer et al., 2005; Miloshevich et al., 2004), the approach using control theory methods makes it possible to better understand the dynamics that are found for this type of sensor.

2 Water vapour measurement

2.1 State of the art

A variety of sensors is used to measure water vapour concentration in the atmosphere. Polymer-based absorption hygrometers are used for observations of relative humidity in most modern weather stations, where a fast response time is not an issue (Kuisma et al., 1985). Some of the most common and most modern radiosondes are the Vaisala RS92, GRAW DFM-09 and Modem M10. All of them carry capacitive, polymer-based humidity sensors and claim fast response times. However, radiosondes are designed to provide accurate vertical profiles but only limited information about turbulence. Their sampling rate is usually of the order of 1 Hz, the resolvable frequencies much lower. The most widely used instrument for ground-based flux measurements is the LI-7500A gas analyser by the company Li-Cor® (Eckles, 2001).

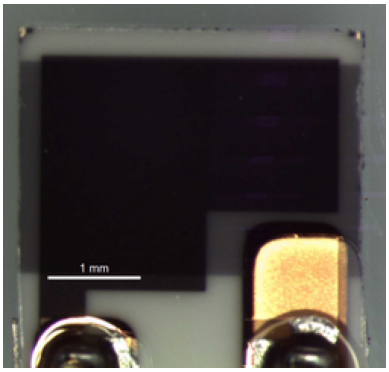

Figure 1. Sensitive element of a capacitive humidity sensor. The black polygon is the polymer between two gold electrodes.

Table 1. Overview of P14 Rapid characteristics.

Size	approx. 3×2 mm
Active element area	6×10^{-6} m^2
Thickness	1 µm
Material	unknown polymer
Specified response time	< 1.5 s

In airborne measurements, a wide variety of customized instruments is being used, including, e.g., Lyman-α absorption hygrometers (e.g. Buck, 1976; Bange et al., 2002), tunable diode laser absorption spectroscopy hygrometers (TDLAS, e.g. May, 1998; Zondlo et al., 2010; Paige, 2005), infrared absorption hygrometers (e.g. LI-7500A), chilled-mirror dew point instruments (DPM, Neininger et al., 2001), krypton hygrometers (Campbell et al., 1985; Thomas et al., 2012) or polymer-based thin-film capacitive absorption hygrometers (see Spieß et al., 2007; Reuder et al., 2009). Only the optical instruments are usually used for turbulence analysis.

Additional sensor types that have not previously been mentioned and are found in ground-based meteorology are psychrometers and resistive or inductive hygrometers.

2.2 Capacitive humidity sensors

None of the instruments that are used on manned aircraft can easily be carried by small RPA, where compact size and light weight are essential. A trade-off has to be made regarding accuracy, response time and long-term stability of the sensors. Considering all the sensor types mentioned in Sect. 2.1, only the capacitive humidity sensor can be easily integrated into a small RPA with current state of the art technology. The size of these elements is typically less than 1 cm^2, and, in non-severe conditions, accuracy and stability of the elements is adequate.

Table 2. List of tested polymer-based humidity sensors

Model	Company
P14 Rapid	IST AG
G-US.171R2	U.P.S.I.
HIH4030	Honeywell
HYT-241	Hygrosens
SHT75	Sensirion
HMP50	Vaisala
DigiPicco	IST AG
HTM-B71	Tronsens

Capacitive humidity sensors are in most cases based on thin-film polymers (Tetelin and Pellet, 2006; Sen and Darabi, 2008; Shibata et al., 1996). The materials adsorb water at the sensor surface from where it diffuses into the material and changes the relative permittivity and therefore the capacitance of the sensor (see Sect. 2.3). With decreasing thickness of the polymer, the time constant also decreases. One of the fastest of this kind on the market is the P14 Rapid by Innovative Sensor Technology (IST) AG (Fig. 1, Table 1), which has a time response of < 1.5 s falling edge, according to the specification (IST AG, 2009). Other sensors that are commercially available and were tested, both in a climate chamber and in flight, are listed in Table 2. The sensors HYT-241, HTM-B71, SHT75 and DigiPicco have a digital output that only allows low sampling rates. HIH4030 and HMP50 are analogue sensors. All of these sensors showed a slower time response than the P14 Rapid. The G-US.171R20 did show a very fast response to humidity changes but was extremely sensitive to temperature changes as well. The calibration of this sensor was not found to be stable in the long term.

Polymer sensors can be subject to hysteresis, as adsorption and desorption do not necessarily take place at the same rate. They also might show a certain temperature sensitivity. A quantification of these effects needs to be done for each sensor type, since the effects can differ a lot depending on the dielectric material and the design of the element. The P14 Rapid sensor was found to be the fastest sensor available and showed little hysteresis and temperature sensitivity. All experiments were carried out using this particular sensor. The polymer type is a trade secret, thus parts of the model derived in Sect. 2.3 rely on experimental parameter estimation. The polymer thickness of 1 µm was obtained from IST (F. Krogmann, personal communication, 2012). In the setup that was used for this study, the sensor is connected to the PCAP01 capacitance converter chip on a custom-made printed circuit board (PCB, see Fig. 2). The converter measures the charge and discharge time of the capacitor in comparison to a known reference capacitance and provides the ratio of the two on a digital output. The digital signal is then processed by the AMOC (Airborne Meteorological Onboard Computer), which was developed at the University of

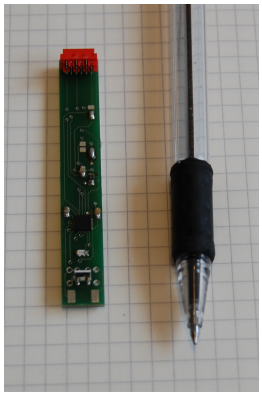

Figure 2. Humidity sensor on printed circuit board with the capacitance measurement chip PCAP01.

Applied Sciences Ostwestfalen-Lippe and the University of Tübingen. The computer stores the data at 100 Hz onto an SD card. At the same time, the sensor signal can be monitored in real time on a remote computer.

In order to better understand the measurements that are done with the P14 Rapid, Sect. 2.3 introduces a model which relates the measured capacitance to the water concentration in the polymer. In a steady state, the water concentration in the polymer equals the water concentration at the sensor surface. Section 2.4 introduces a calibration to get the relative humidity from the surface water concentration. Finally, Sect. 3 describes how the diffusion process of water from the sensor surface into the polymer can be modelled and how, by inversion of this model, the surface concentration of the sensor – and thus the ambient relative humidity – can be estimated throughout a measurement flight.

2.3 Physical model

In Sect. 3, a dynamical model will be presented, which describes the change of water concentration in the polymer with time. In order to work with this model, it is necessary to translate the measurement variable capacitance C to the corresponding average water concentration in the polymer c. In this section, a physical model is presented, which describes this relation. In a parallel-plate capacitor, the charge per voltage is defined as the capacitance. It can also be expressed as a function of the area A of the parallel plate, the distance d between the plates, the relative permittivity ε_r of the material between the plates and the vacuum permittivity ε_0:

$$C = \frac{Q}{U} = \varepsilon_0 \varepsilon_\mathrm{r} \frac{A}{d} = (\varepsilon_\mathrm{r} - 1)\varepsilon_0 \frac{A}{d} + \varepsilon_0 \frac{A}{d}. \tag{1}$$

For the following investigation, it helps to decompose the capacity of the humidity sensor into partial capacities (Eq. 2), in particular the capacitance of the vacuum between the plates C_0, the capacitance of the polymer alone C_Poly and the capacitance of absorbed water in the polymer $C_{\mathrm{H_2O}}$. C_Poly and C_0 are constant and provide an offset capacitance for zero water concentration, while $C_{\mathrm{H_2O}}$ accounts for the sensitivity of the capacitance to changes in water concentration in the polymer.

$$\begin{aligned} C &= \varepsilon_0 (\varepsilon_\mathrm{r}^{\mathrm{H_2O}} + \varepsilon_\mathrm{r}^{\mathrm{Poly}}) \frac{A}{d} \\ &= \underbrace{\varepsilon_0 \varepsilon_\mathrm{r}^{\mathrm{Poly}} \frac{A}{d}}_{:=C_\mathrm{Poly}} + \underbrace{(\varepsilon_\mathrm{r}^{\mathrm{H_2O}} - 1)\varepsilon_0 \frac{A}{d}}_{:=C_{\mathrm{H_2O}}} + \underbrace{\varepsilon_0 \frac{A}{d}}_{:=C_0}. \end{aligned} \tag{2}$$

The Debye equation for molar polarisation P_m connects the microscopic characteristics, which are the electrical dipole moment μ and the polarizability α, to the relative permittivity ε_r of a material (Debye, 1929).

$$P_\mathrm{m} = \frac{\varepsilon_\mathrm{r}^{\mathrm{H_2O}} - 1}{\varepsilon_\mathrm{r}^{\mathrm{H_2O}} + 2} = \frac{Z}{3\varepsilon_0} \cdot \left(\alpha + \frac{\mu^2}{k_B T} \right), \tag{3}$$

with particle density $\mathrm{Z} = \frac{\varrho}{\mathrm{M}} \mathrm{N_A}$ and ϱ being the density, M the molecular mass, N_A the Avogadro constant, k_B the Boltzmann constant and T the temperature. $\varepsilon_\mathrm{r}^{\mathrm{H_2O}}$ can be derived from Eq. (2) to yield

$$\varepsilon_\mathrm{r}^{\mathrm{H_2O}} = \frac{(C - C_\mathrm{Poly})}{C_0}. \tag{4}$$

The particle density Z can also be expressed as the integral of water concentration c in the volume

$$Z(t) = \frac{\int_z \int_y \int_x c(x, y, z, t)\, \mathrm{d}x\, \mathrm{d}y\, \mathrm{d}z \cdot N_A}{V}. \tag{5}$$

For spatially constant concentration ($\nabla c = 0$)

$$Z = \frac{c \cdot V \cdot N_A}{V} = c \cdot N_A \quad . \tag{6}$$

With the help of Eqs. (2), (3) and (6), water concentration can be found as a function of capacitance and temperature:

$$c = \frac{\frac{(C - C_\mathrm{Poly})}{C_0} - 1}{\frac{(C - C_\mathrm{Poly})}{C_0} + 2} \cdot \frac{3\varepsilon_0}{\alpha + \frac{\mu^2}{k_B T}} \cdot \frac{1}{N_A} \frac{\frac{C - C_\mathrm{Poly}}{C_0} - 1}{2 + \frac{C - C_\mathrm{Poly}}{C_0}} \cdot \frac{1}{Q N_A} \quad . \tag{7}$$

While C is the capacitance actually measured and C_0 is defined as $\varepsilon_0 \frac{A}{d}$, C_poly is unknown before calibration. It is estimated by extrapolation of the calibration regression to zero relative humidity. The calibration procedure is described in Sect. 2.4.

2.4 Calibration

Calibration is used to connect the water concentration at the sensor surface c_s to relative humidity in the environment. Diffusion into the polymer will lead to a balance of water concentration c throughout the whole polymer after a finite

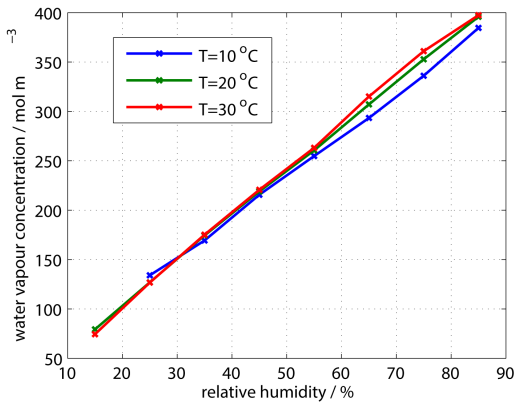

Figure 3. Calibration of a P14 Rapid humidity sensor. Calibration was done at three different temperatures.

time. The dynamics of this process are modelled in Sect. 3. For the calibration, humidity is held at a constant level for at least 30 min to assure equilibrium of the water concentration. It is not necessarily the case that polymer-based capacitive humidity sensors show a linear relationship between measured capacitance and relative humidity (Shibata et al., 1996). Figure 3 shows the result of three calibrations at three different temperatures. On the y axis of the graph, the measured capacitance was directly translated into water vapour concentration, according to Eq. (7). Before doing this, C_{poly} must be set, so that an extrapolation of the curve in Fig. 3 will yield zero water concentration in the polymer at zero ambient relative humidity. A practical way to get a good estimation for C_{poly} is to find the zero-crossing of a regression curve between measured capacitance and relative humidity, which is $(C_{\text{poly}} + C_0)$. Since C_0 is a known sensor property, C_{poly} can be calculated and was found to be approximately 60 pF for the sensor examined here. The temperature in the calibration chamber is kept constant and relative humidity is increased stepwise from 15 to 85 % during the calibration. A dew point mirror in conjunction with a PT100 temperature sensor inside the calibration chamber is used as reference instrument to control relative humidity and temperature. While sensor physics depends on both temperature and water vapour partial pressure, the P14 Rapid follows a linear relationship with relative humidity within the calibrated temperature range. The calibration chamber used was calibrated against a secondary standard with an accuracy of 0.4 % RH. A root mean square error of less than 1 % RH between the calibration curve and the measured values is found for the capacitive humidity sensor calibration in the chamber at 10 °C or more. The facilities that were available to the authors did not allow calibration at lower temperatures.

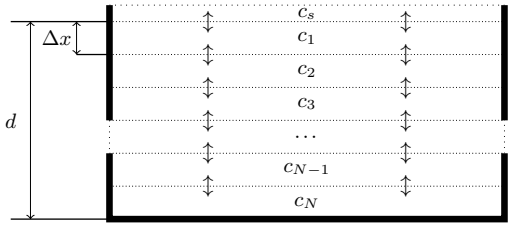

Figure 4. Sketch of the sensor model.

3 Dynamic signal restoration

3.1 Dynamic model

A dynamic model describes the behaviour of a system over time. This behaviour is typically described mathematically by a set of differential equations. In the case of a capacitive humidity sensor, the dynamics are mainly influenced by the diffusion of water vapour from the sensor surface into the polymer. While the water concentration c in the polymer was constant in space in the stationary model described in Sect. 2.3, the following section will describe how the concentration changes in time and space. The diffusion flux $\mathbf{J}$ is described by Fick's law as shown in Eq. (8). It is assumed that a model with a spatially constant diffusion coefficient D describes the behaviour of the sensor well enough. Figure 4 shows a sketch of the model of finite volumes in the sensor polymer.

$$\mathbf{J} = -D \cdot \nabla c \tag{8}$$

Combined with the continuity equation of mass conservation (Eq. 9), Fick's second law can be derived (Eq. 10).

$$\frac{\partial c}{\partial t} = -\nabla \cdot \mathbf{J} \tag{9}$$

$$= D\,\nabla^2 c \tag{10}$$

Since these equations yield a differential equation of second order, a simplification is needed to find a manageable solution. A common solution to these kinds of problems is a numerical approach, such as the finite-volume method (LeVeque, 2002). According to this method, the mass conservation Eq. (9) is integrated over a finite-volume element V_n.

$$\iiint_{V_n} \frac{\partial c}{\partial t}\,\mathrm{d}V = -\iiint_{V_n} (\nabla \cdot \mathbf{J})\,\mathrm{d}V \tag{11}$$

The divergence theorem (or the combination of the continuity equation with the Gauss theorem) allows one to write the right-hand side of the equation as a surface integral. The left-hand side can be solved to obtain the product of spatially averaged concentration change in a volume element and its volume.

$$\frac{\partial \overline{c_n}}{\partial t} V_n = -\oiint_{\mathrm{s}} \mathbf{J}\,\mathrm{d}S \tag{12}$$

In the following, concentrations with an index always represent spatial averages over a finite volume, and the overbar notation to indicate the averaging, as in $\overline{c_n}$, will be omitted. Concentration gradients in horizontal directions are considered to be 0, as the sensor is small enough that a constant humidity above the whole sensor surface can be assumed. Therefore, there will be no horizontal fluxes of water and the volume elements V_n can be simplified to layers as shown in Fig. 4. The surface integral can be simplified to the sum of diffusion from the layer above $(n-1)$ and the layer below $(n+1)$ for each layer n in the polymer and therefore yields

$$\frac{\partial c_n}{\partial t} = \frac{-D \cdot \frac{c_n - c_{n-1}}{\Delta x} \cdot A_{n,n-1}}{V_n} + \frac{-D \cdot \frac{c_n - c_{n+1}}{\Delta x} \cdot A_{n,n+1}}{V_n}, \quad (13)$$

where $A_{n,n-1}$ and $A_{n,n+1}$ are the top and bottom surface area of the polymer layers respectively and Δx is the layer thickness. A matrix representation of the simplified diffusion model with $\mathbf{Y} = \frac{D \cdot A}{\Delta x \cdot V_n}$ is given in Eq. (14).

$$\begin{pmatrix} \frac{\partial c_1}{\partial t} \\ \frac{\partial c_2}{\partial t} \\ \frac{\partial c_3}{\partial t} \\ \frac{\partial c_4}{\partial t} \\ \vdots \\ \vdots \\ \vdots \\ \frac{\partial c_{N-1}}{\partial t} \\ \frac{\partial c_N}{\partial t} \end{pmatrix} = \begin{pmatrix} -2Y & Y & 0 & 0 & 0 & 0 & \cdots & 0 \\ Y & -2Y & Y & 0 & 0 & 0 & \cdots & 0 \\ 0 & Y & -2Y & Y & 0 & 0 & \cdots & 0 \\ 0 & 0 & Y & -2Y & Y & 0 & \cdots & 0 \\ \vdots & & & & \ddots & & & \vdots \\ \vdots & & & & & \ddots & & \vdots \\ 0 & 0 & 0 & 0 & \cdots & Y & -2Y & -Y \\ 0 & 0 & 0 & 0 & \cdots & 0 & Y & -Y \end{pmatrix}$$
$$\cdot \begin{pmatrix} c_1 \\ c_2 \\ c_3 \\ c_4 \\ \vdots \\ \vdots \\ \vdots \\ c_{N-1} \\ c_N \end{pmatrix} + \begin{pmatrix} Y \\ 0 \\ 0 \\ 0 \\ \vdots \\ \vdots \\ \vdots \\ 0 \\ 0 \end{pmatrix} \cdot c_\mathrm{s}$$
$$c_\mathrm{m} = (1\ 1\ 1\ \cdots\ 1) \begin{pmatrix} \frac{c_1}{N} \\ \frac{c_2}{N} \\ \frac{c_3}{N} \\ \vdots \\ \frac{c_N}{N} \end{pmatrix} \quad (14)$$

Boundary conditions exist for the layer at the surface of the sensor and the bottommost layer. At the surface layer the concentration that is adsorbed from ambient water vapour diffuses into the layer. At the bottom, no diffusion is possible from below.

Equation (14), translated to vector notation, conforms with the standard layout of a single-input–single-output (SISO) state–space model as used in control theory (Lutz and Wendt, 2007):

$$\frac{\partial}{\partial t}\boldsymbol{c} = \mathbf{Y}\boldsymbol{c} + (Y\ 0\ 0\ \cdots\ 0)^T\, c_\mathrm{s}$$
$$c_\mathrm{m} = \left(\frac{1}{N}\ \frac{1}{N}\ \frac{1}{N}\ \cdots\ \frac{1}{N}\right)\boldsymbol{c}. \quad (15)$$

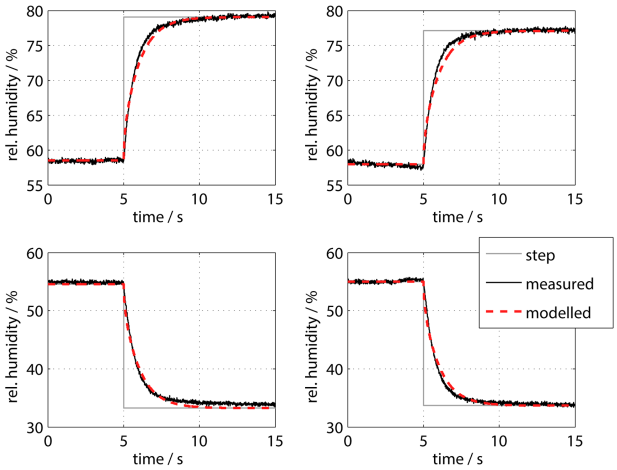

Figure 5. Result of a step response experiment with rising-edge (upper figures) and falling-edge (lower figures) humidity in comparison to model results. The model was run with 40 layers and a diffusion coefficient $D = 0.38\ \mu\mathrm{m}^2\ \mathrm{s}^{-1}$ in all cases.

The vector $\boldsymbol{c}$ of water concentrations in each layer of the model is the state vector. The diffusion matrix $\mathbf{Y}$ is the system (or state) matrix, which describes how the current concentrations $\boldsymbol{c}$ in each layer affect the change in concentrations $\frac{\partial}{\partial t}\boldsymbol{c}$. The input (or control) vector $(Y\ 0\ 0\ \cdots\ 0)^T$ determines how the system input affects the states $\boldsymbol{c}$. It is modelled to describe the diffusion of water vapour into the topmost layer of the sensor. The single-input variable of the whole system is the surface concentration c_s and the single output variable is the averaged water concentration in the polymer c_m that is presented as a function of the measured capacitance in Eq.(7). The so-called output vector $\left(\frac{1}{N}\ \frac{1}{N}\ \frac{1}{N}\ \cdots\ \frac{1}{N}\right)$ maps the states $\boldsymbol{c}$ to the output variable c_m, which, in the case of the sensor model, is a simple averaging of the concentrations in all layers.

3.1.1 Model validation

To show that this model does agree with reality, step response experiments with rising and falling edge steps of humidity were performed. The results in Fig. 5 show that the model agrees well with reality if the correct diffusion coefficient is applied. Of course, it has to be noted that the diffusion coefficient, since it is the one unknown parameter in the model, also serves as a correction factor for other model inaccuracies and therefore is most likely not the true physical diffusion coefficient. Remaining deviations between model and measurement can also result from a nonperfect step input. For the experiment, a humidity sensor was placed in a very small chamber ($< 2\ \mathrm{cm}^3$) at ambient humidity. At time 0 the constant airflow into the chamber is switched to an airflow of well-defined humidity from the dew point generator, which is also used for calibration. It is assumed that the humidity around

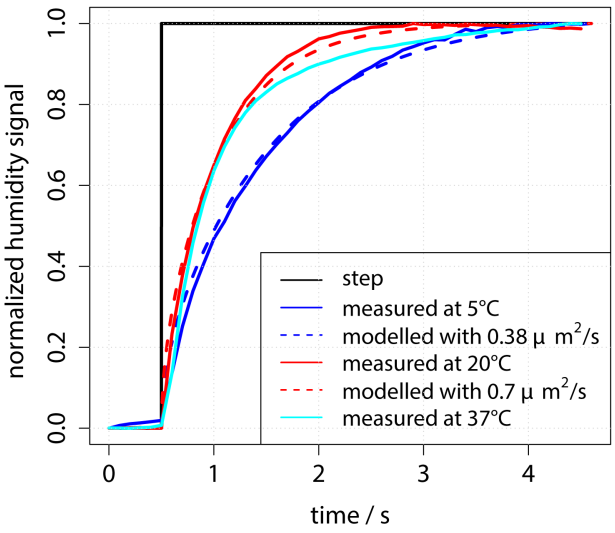

Figure 6. Step responses of the same sensor at different temperatures. The y axis is normalized to 0 for humidity before the step and 1 for humidity after the step. This is legitimate since the dynamics does not depend on the step amplitude.

the sensor changes completely in less than 100 ms, based on the outlet flow of the generator and the size of the chamber. Comparing the rising and falling edge steps, it becomes evident that no difference in time response can be observed for both cases, and the model works with the same diffusion coefficient without hysteresis. This implies that diffusion is the dominant factor in comparison to adsorption and desorption regarding the dynamics of the sensor, and the model is suitable for describing the dynamic behaviour of the sensor.

To investigate the sensitivity of the diffusion coefficient to ambient temperature, tests were done at three different temperatures (5, 20 and 37 °C). The result in Fig. 6 shows that the diffusion coefficient at 5 °C is lower compared to the other two temperatures, which agree quite well. This means that it is not possible to apply a universal diffusion coefficient for one sensor, but the diffusion coefficient needs to be adapted to the given ambient temperature, especially in low-temperature environments. However, small deviations as they appear in the ABL will not be critical for the model.

3.2 Inverse model for signal restoration

Having found a model that reasonably describes the dynamic behaviour of the sensor, it is now possible to use this model to restore the original signal of relative humidity in the atmosphere from measured data. For this purpose it is necessary to invert the model, which is equivalent to solving the system equations for the surface water vapour concentration c_s.

Since the state–space model cannot easily be inverted, the first step is to transform Eq. (15) to a transfer function in the Laplace domain. This can be done as presented in Eq. (16) according to Lutz and Wendt (2007).

$$c_m(s) = \left(\frac{1}{N}\ \frac{1}{N}\ \cdots\ \frac{1}{N}\right)(s\mathbf{E}-\mathbf{Y})^{-1}(Y\ 0\ \cdots\ 0)^T \cdot\ c_s(s)$$
$$= G(s) \cdot\ c_s(s) \tag{16}$$

E is a unity matrix of the same dimensions as the system matrix **Y**. The variable s is a result of the Laplace transformation. $G(s)$ is the transfer function in the Laplace domain. A transfer function of a linear dynamic system can be expressed as a fraction with a numerator and a denominator polynomial of the parameter s in the Laplace domain (Astrom and Murray, 2009, chapter 8). This fraction can simply be inverted to solve Eq. (16) for the original signal:

$$c_s(s) = G(s)^{-1} \cdot\ c_m(s). \tag{17}$$

A drawback of this method is that it only works well if the measured signal and the applied model fit well. Noise that is not modelled will be amplified more with increasing polynomial order in the transfer function. On the other hand, the model will be more accurate with a higher number of modelled layers in the polymer, which leads to a high polynomial order in the transfer function. A way of dealing with this problem is oversampling and careful filtering of the measured signal in order to achieve a good signal-to-noise ratio.

Figure 7 shows a signal flow block diagram (see, e.g., Astrom and Murray, 2009, pp. 55–59) of the signal restoration. It includes input and output filters that were applied to achieve a restored signal that is not disturbed by amplified noise of the inverse modelling. For the input, a sharp low-pass filter of 20th order at a cutoff frequency of 10 Hz is chosen to eliminate the white noise of the capacitance measurement, which dominates above this frequency. In the output filter, a first-order low pass is good enough to filter out the remaining noise after the signal restoration. The block diagram was generated with Matlab Simulink®, which was also used in a first approach to carry out the convolution of the measured signal with the transfer function.

4 Results

4.1 Vertical profiles

For vertical profiles, slow dynamics of sensors lead to blurred measurements with either overestimated or underestimated water vapour concentration at each altitude, depending on the lapse rate. The effect shows clearly whether RPA flights are used with consecutive ascents and descents. The sensor dynamics result in a hysteresis between ascent and descent measurement of relative humidity. In the past it was common practice to take the average of ascent and descent flights, which gives a good approximation for the true value, or to apply some time delay correction of first order as described in Jonassen (2008) for RPA and in Leiterer et al. (2005) and Miloshevich et al. (2004) for radiosondes.

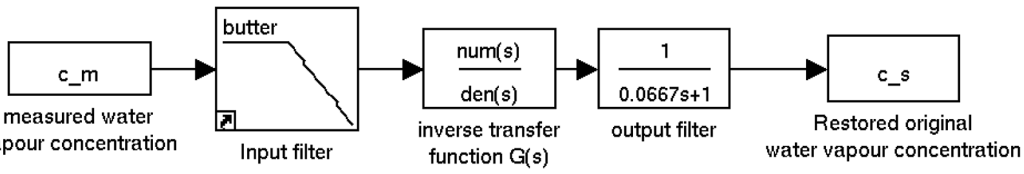

Figure 7. Block diagram of signal restoration. The input signal of the humidity sensor is filtered with a Butterworth filter of order 20 at a cutoff frequency of 10 Hz. After the inverse transformation, the signal is filtered again with a simple first-order delay low pass with cutoff frequency at 15 Hz.

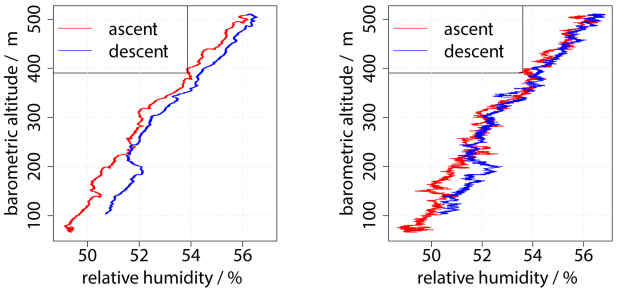

Figure 8. Vertical profile of relative humidity before and after correction.

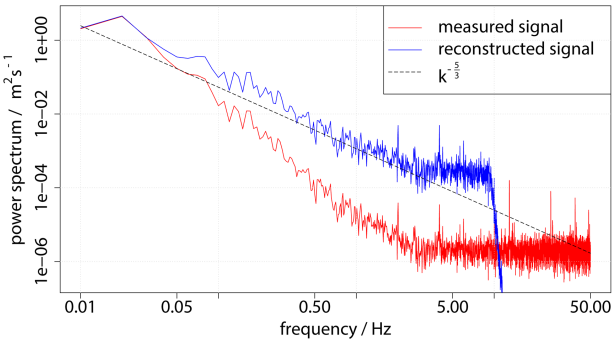

Figure 9. Power spectrum of relative humidity before and after correction. The number of layers in the sensor model is set to $N = 40$. From the vertical profile, the diffusion constant was found to be $D = 0.1\,\mu m^2\,s^{-1}$. The spectrum is averaged over five flight legs.

In Fig. 8, a vertical profile is shown with raw measurements and with a restored signal for relative humidity, applying the method described in Sect. 3. It clearly shows how an offset present between ascent and descent of the flight is eliminated in almost every detail, except for a few altitudes, where obviously local events of water vapour disturb the continuity of the profile, as can be seen between 150 and 200 m or at 350 m barometric altitude. The parameter that is critical to tune in the sensor model is the diffusion coefficient as described above. Within the minute or two that are needed for an ascent and a descent of a vertical profile with the RPA, in a nonconvective boundary layer, the mean relative humidity will not shift into one direction or the other, so that the parameter can be tuned to show a minimum offset between ascent and descent. Once the diffusion coefficient is found from a vertical profile, it is possible to use this parameter for the signal restoration of the complete flight with a duration of 30–60 min. It is, however, recommended to redo the vertical profile diffusion coefficient estimation for each flight since contamination and small damage invisible to the human eye were found to significantly change the sensor dynamics. Different sensors of the same batch can even show slightly different characteristics. Of course, this way of determining the diffusion coefficient only works if gradients of water vapour concentration do exist at least in parts of the vertical profile.

4.2 Spectral response

A MASC RPA at the University of Tübingen is equipped with fast sensors for temperature and wind measurement in order to measure turbulence. The goal of this study is to make turbulence studies for water vapour possible with capacitive humidity sensors. To quantify the improvements that were achieved in working towards this goal, it is useful to investigate the spectral response of the sensor before and after the signal restoration. Figure 9 shows the power spectral density of the relative-humidity signal over the frequency for both cases. The original signal is strongly effected by the slow sensor dynamics for frequencies above 0.05 Hz (red curve). At about 3 Hz the signal vanishes in noise entirely (spectral power is almost constant for higher frequencies). The restored signal almost perfectly follows the expected $-5/3$ slope for locally isotropic turbulence in the inertial subrange according to Kolmogorov (1941), until about 3 Hz (blue curve). For higher frequencies, noise is dominant and thus is the limiting factor of the signal restoration.

Another method to show the distribution of turbulent energy on different scales is the structure function according to Kolmogorov (1941). Deviations of the measured values from the theoretical slope for locally isotropic turbulence in the inertial subrange, which in the case of the double-logarithmically plotted structure function is $2/3$, are a strong

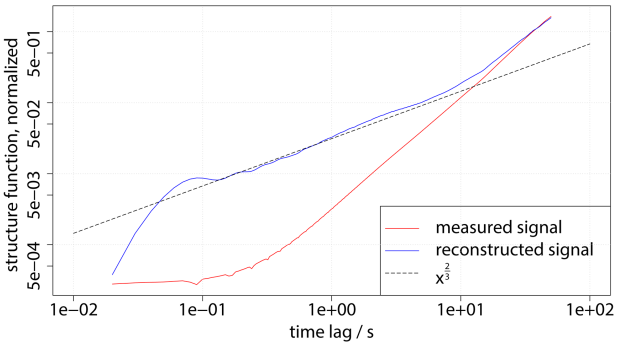

Figure 10. Structure function before and after correction.The number of layers in the sensor model is set to $N = 40$. The diffusion constant was found to be $D = 0.1\,\mu m^2\,s^{-1}$ from the vertical profile. The structure function is normalized by $2\sigma^2$ and averaged over five flight legs.

indication of sensor dynamics or other errors in the measurement; this is the case even more clearly than for the power spectral densities. Figure 10 shows how close the structure function of the restored signal is to the theory until a time lag of about 0.3 s (corresponding to 3 Hz), especially compared to the original signal.

5 Conclusions

This report addressed the problem of water vapour measurement for turbulence analysis with small RPA. It was established that capacitive humidity sensors are currently the only feasible solution for these measurements onboard an RPA of 5 kg, as operated in Tübingen, or smaller. A method is introduced to enhance the quality of such measurements with the help of control theory methods in post-processing. The dynamic diffusion model derived in Sect. 3 is therefore inverted to find the water concentration on the sensor surface from measured average water concentration in the polymer. Since the measurement variable of the sensor is, in the first place, the capacitance, the physics of how to translate the measured capacitance into water concentration was introduced in Sect. 2.3. A calibration approach was used to connect sensor surface water concentration to ambient relative humidity (Sect. 2.4). To summarize, the model can be applied in five steps:

1. calculation of average water concentration in the polymer c_m for a time series of capacitance of the sensor according to Sect. 2.3;
2. setup of the state–space model according to Sect. 3.1;
3. conversion of the state–space model into a transfer function according to Sect. 3.2, Eq. (16);
4. deconvolution of the measured average water concentration signal c_m in the polymer with the transfer function in order to find the water concentration at the surface of the polymer c_s (Eq. 17);
5. recovery of the relative humidity from the surface water concentration c_s through the calibration described in Sect. 2.4.

It is shown in Sect. 4 how vertical profiles can be corrected using the presented method. We propose using a minimization of error between ascent and descent of a vertical profile flight with an RPA to find the correct diffusion coefficient for the given temperature and sensor. This is necessary, since the exact relation between diffusion coefficient and temperature could not be determined in a laboratory experiment and information about the polymer type is not available. The benefit of determining the diffusion coefficient empirically for each measurement flight is that this parameter is the only unknown in the dynamic model and therefore can also be used to correct for other inaccuracies in the model. A spectral analysis of flight legs in the atmospheric boundary layer with a diffusion coefficient determined from a vertical profile during the same flight showed promising results for turbulence analysis. It can be stated that the enhancement of the sensor makes it possible to resolve turbulent fluctuations up to 3 Hz, which corresponds to a 10 m eddy size at $25\,m\,s^{-1}$ airspeed. Compared to temperature and wind measurement on a MASC RPA (up to 20 Hz), this is still fairly low and will need to be improved in future work. The main constraints for the given setup are the signal-to-noise ratio and the sensitivity of the capacitance measurement. Improvements of the measurement circuit with several parallel sensors can possibly solve this problem. Measurements of turbulent fluctuations up to 10 Hz seem possible. The systematic approach of the signal restoration is open to further extensions of the sensor model, e.g. physical descriptions of water adsorption on the sensor surface or temperature dependence of diffusion into the polymer. These extensions can lead to significantly higher complexity, which cannot be described by a linear time-invariant system any more. For measurements in the summer convective boundary layer in central Europe, the described simplifications are appropriate and provide promising results. To apply the method in very cold temperatures or in radiosonde applications, where strong temperature differences are experienced in a single ascent, further studies that are beyond of the scope of this paper are required.

Acknowledgements. We are grateful to one anonymous referee and the Associated Editor Murray Hamilton for their fruitful comments, which helped to improve the quality of this paper.

We would like to thank Maximilian Ehrle and Markus Auer for their great job as safety pilot in the test flights. The measuring equipment would not have been ready to work without the help of Jens Dünnermann and Burkhard Wrenger from the University of Applied Sciences Ostwestfalen-Lippe.

We acknowledge support by the Deutsche Forschungsgemeinschaft and the Open Access Publishing Fund of Tübingen University.

Edited by: M. Hamilton

References

Astrom, K. and Murray, R.: Feedback Systems: An Introduction for Scientists and Engineers, Princeton University Press, 2009.

Bange, J. and Roth, R.: Helicopter-Borne Flux Measurements in the Nocturnal Boundary Layer Over Land – a Case Study, Bound.-Lay. Meteorol., 92, 295–325, 1999.

Bange, J., Beyrich, F., and Engelbart, D. A. M.: Airborne Measurements of Turbulent Fluxes during LITFASS-98: A Case Study about Method and Significance, Theor. Appl. Climatol., 73, 35–51, 2002.

Bange, J., Esposito, M., and Lenschow, D. H.: Airborne Measurements for Environmental Research – Methods and Instruments, chap. 2: Measurement of Aircraft State, Thermodynamic and Dynamic Variables, 641 pp., Wiley, 2013.

Buck, A. L.: The Variable-Path Lyman-Alpha Hygrometer and Its Operating Characteristics, Bull. Am. Meteorol. Soc., 57, 1113–1118, 1976.

Campbell, G., Tanner, B., and Gauthier, R.: Krypton hygrometer, available at: http://www.google.com/patents/US4526034 (last access: 17 September 2014), uS Patent 4,526,034, 1985.

Chao, H., Baumann, M., Jensen, A., Chen, Y., Cao, Y., Ren, W., and McKee, M.: Band-reconfigurable multi-UAV-based cooperative remote sensing for real-time water management and distributed irrigation control, IFAC World Congress, Seoul, Korea, 2008.

Corsmeier, U., Hankers, R., and Wieser, A.: Airborne Turbulence Measurements in the Lower Troposphere Onboard the Research Aircraft Dornier 128-6, D-IBUF, Meteorol. Z., 4, 315–329, 2001.

Debye, P.: Polare Molekeln, S. Hirzel, Leipzig, 200 pp., 1929.

Eckles, R.: Gas analyzer, available at: http://www.google.com/patents/US6317212 (last access: 17 September 2014), uS Patent 6,317,212, 2001.

Garratt, J.: The Atmospheric Boundary Layer, University Press, Cambridge, 1992.

IST AG: P14 – Rapid Capacitive Humidity Sensor, datasheet V4.3-11/2009, 2009.

Jensen, A. and Chen, Y.: Tracking tagged fish with swarming unmanned aerial vehicles using fractional order potential fields and Kalman filtering, in: 2013 International Conference on Unmanned Aircraft Systems (ICUAS), 1144–1149, IEEE, 2013.

Jonassen, M. O.: The Small Unmanned Meteorological Observer (SUMO), Master's thesis, University of Bergen – Geophysical Institute, 2008.

Kolmogorov, A.: The Local Structure of Turbulence in Incompressible Viscous Fluid for Very Large Reynolds Numbers, Dokl. Akad. Nauk SSSR, 30, 299–303, reprint: Proc. R. Soc. Lond. A, 1991, 434, 9–13, 1941.

Kuisma, H., Lehto, A., and Jalava, J.: Capacitive humidity sensor and method for the manufacture of same, available at: http://www.google.com/patents/US4500940 (last access: 17 September 2014), uS Patent 4,500,940, 1985.

Leiterer, U., Dier, H., Nagel, D., Naebert, T., Althausen, D., Franke, K., Kats, A., and Wagner, F.: Correction Method for RS80-A Humicap Humidity Profiles and Their Validation by Lidar Backscattering Profiles in Tropical Cirrus Clouds, J. Atmos. Oceanic Technol., 22, 18–29, 2005.

LeVeque, R. J.: Finite Volume Methods for Hyperbolic Problems, Cambridge University Press, doi:10.1017/CBO9780511791253, 2002.

Lutz, H. and Wendt, W.: Taschenbuch der Regelungstechnik: mit MATLAB und Simulink, Harri Deutsch, Frankfurt am Main, Germany, 2007.

Maronga, B.: Monin-Obukhov similarity functions for the structure parameters of temperature and humidity in the unstable surface layer: results from high-resolution large-eddy simulations, J. Atmos. Sci., 71, 716–733, doi:10.1175/JAS-D-13-0135.1, 2013.

Martin, S. and Bange, J.: The Influence of Aircraft Speed Variations on Sensible Heat Flux Measurements by Different Airborne Systems, Bound.-Lay. Meteorol., 150, 153–166, doi:10.1007/s10546-013-9853-7, 2013.

Martin, S., Bange, J., and Beyrich, F.: Meteorological profiling of the lower troposphere using the research UAV "M2AV Carolo", Atmos. Meas. Tech., 4, 705–716, doi:10.5194/amt-4-705-2011, 2011.

Martin, S., Beyrich, F., and Bange, J.: Observing Entrainment Processes Using a Small Unmanned Aerial Vehicle: A Feasibility Study, Bound.-Lay. Meteorol., 150, 449–467, doi:10.1007/s10546-013-9880-4, 2013.

May, R. D.: Open-path, near-infrared tunable diode laser spectrometer for atmospheric measurements of H_2O, J. Geophys. Res.-Atmos., 103, 19161–19172, doi:10.1029/98JD01678, 1998.

Miloshevich, L. M., Paukkunen, A., Vömel, H., and Oltmans, S. J.: Development and Validation of a Time-Lag Correction for Vaisala Radiosonde Humidity Measurements, J. Atmos. Oceanic Technol., 21, 1305–1327, doi:10.1175/jtech1770.1, 2004.

Neininger, B., Fuchs, W., Baeumle, M., Volz-Thomas, A., Prévôt, A. S. H., and Dommen, J.: A Small Aircraft for More Than Just Ozone: MetAir's 'Dimona' After Ten Years of Evolving Development, in: 11th Symp. on Meteorological Observations and Instrumentation, Albuquerque, NM, Amer. Meteor. Soc., 123–128, 2001.

Paige, M. E.: Compact and Low-Power Diode Laser Hygrometer for Weather Balloons, J. Atmos. Oceanic Technol., 22, 1219–1224, doi:10.1175/jtech1770.1, 2005.

Rediniotis, O. and Pathak, M.: Simple Technique for Frequency-Response Enhancement of Miniature Pressure Probes, AIAA Journal, 37, 897–899, 1999.

Reuder, J., Brisset, P., Jonassen, M., Müller, M., and Mayer, S.: The Small Unmanned Meteorological Observer SUMO: A new tool for atmospheric boundary layer research, Meteorol. Z., 18, 141–147, 2009.

Sen, A. and Darabi, J.: Modeling and Optimization of a Microscale Capacitive Humidity Sensor for HVAC Applications, Sensors Journal, IEEE, 8, 333–340, 2008.

Shibata, H., Ito, M., Asakursa, M., and Watanabe, K.: A digital hygrometer using a polyimide film relative humidity sensor, IEEE Trans. Instr. Measure., 45, 564–569, 1996.

Spieß, T., Bange, J., Buschmann, M., and Vörsmann, P.: First Application of the Meteorological Mini-UAV "M2AV", Meteorol. Z. N. F., 16, 159–169, 2007.

Stull, R.: An Introduction to Boundary Layer Meteorology, Kluwer Acad., Dordrecht, 1988.

Tagawa, M., Kato, K., and Ohta, Y.: Response compensation of fine-wire temperature sensors, Rev. Sci. Instrum., 76, 094904, 4 pp., 2005.

Tetelin, A. and Pellet, C.: Modeling and optimization of a fast response capacitive humidity sensor, Sensors Journal, IEEE, 6, 714–720, 2006.

Thomas, R. M., Lehmann, K., Nguyen, H., Jackson, D. L., Wolfe, D., and Ramanathan, V.: Measurement of turbulent water vapor fluxes using a lightweight unmanned aerial vehicle system, Atmos. Meas. Tech., 5, 243–257, doi:10.5194/amt-5-243-2012, 2012.

van den Kroonenberg, A., Martin, S., Beyrich, F., and Bange, J.: Spatially-averaged temperature structure parameter over a heterogeneous surface measured by an unmanned aerial vehicle, Bound.-Lay. Meteorol., 142, 55–77, 2011.

van den Kroonenberg, A. C., Martin, T., Buschmann, M., Bange, J., and Vörsmann, P.: Measuring the Wind Vector Using the Autonomous Mini Aerial Vehicle M^2AV, J. Atmos. Oceanic Technol., 25, 1969–1982, 2008.

Wildmann, N., Mauz, M., and Bange, J.: Two fast temperature sensors for probing of the atmospheric boundary layer using small remotely piloted aircraft (RPA), Atmos. Meas. Tech., 6, 2101–2113, doi:10.5194/amt-6-2101-2013, 2013.

Wildmann, N., Ravi, S., and Bange, J.: Towards higher accuracy and better frequency response with standard multi-hole probes in turbulence measurement with remotely piloted aircraft (RPA), Atmos. Meas. Tech., 7, 1027–1041, doi:10.5194/amt-7-1027-2014, 2014.

Wyngaard, J. C. and Clifford, S. F.: Estimating Momentum, Heat, and Moisture Fluxes from Structure Parameters, J. Atmos. Sci., 35, 1204–1211, 1978.

Zondlo, M. A., Paige, M. E., Massick, S. M., and Silver, J. A.: Vertical cavity laser hygrometer for the National Science Foundation Gulfstream-V aircraft, J. Geophys. Res., 115, D20309, doi:10.1029/2010JD014445, 2010.

A.4 MASC - a small Remotely Piloted Aircraft (RPA) for wind energy research.

The publication is also available at
http://www.adv-sci-res.net/11/55/2014/.

Adv. Sci. Res., 11, 55–61, 2014
www.adv-sci-res.net/11/55/2014/
doi:10.5194/asr-11-55-2014

Advances in Science & Research
Open Access Proceedings

MASC – a small Remotely Piloted Aircraft (RPA) for wind energy research

N. Wildmann[1], M. Hofsäß[2], F. Weimer[3], A. Joos[3], and J. Bange[1]

[1]Center for Applied Geosciences, Eberhard-Karls-University Tübingen, Tübingen, Germany
[2]Stuttgart Wind Energy (SWE) at the Institute for Aircraft Design (IFB), University of Stuttgart, Stuttgart, Germany
[3]Institute of Flight Mechanics and Control, University of Stuttgart, Stuttgart, Germany

Correspondence to: N. Wildmann (norman.wildmann@uni-tuebingen.de)

Received: 14 January 2014 – Revised: 29 March 2014 – Accepted: 9 May 2014 – Published: 27 May 2014

Abstract. Originally designed for atmospheric boundary layer research, the MASC (Multipurpose Airborne Sensor Carrier) RPA (Remotely Piloted Aircraft, also known as Unmanned Aerial Vehicle, UAV) is capable of making in-situ measurements of temperature, humidity and wind in high resolution and precision. The autopilot system ROCS (Research Onboard Computer System) enables the aircraft to fly pre-defined routes between waypoints at constant altitude and airspeed. The system manages to operate in wind speeds up to 15 m s^{-1} safely. It is shown that a MASC can fly as close as one rotor diameter upstream and downstream of running wind turbines at these wind speeds and take valuable data of incoming flow and wake. The flexible operation of an RPA at the size of a MASC can be a major advantage of the system compared to tower measurements and remote sensing in wind energy research. In the project "Lidar Complex" comparisons of RPA measurements with lidar systems and tower measurements are carried out at two different test sites. First results, including turbulence and wake measurements, from a campaign in autumn 2013 are presented.

1 Introduction

Small Remotely Piloted Aircraft (RPA, also known as Unmanned Aerial Vehicle, UAV) have been increasingly used in atmospheric sciences throughout the last decade. In atmospheric boundary layer (ABL) research, systems like SUMO (Reuder et al., 2009) for vertical sounding of the atmosphere, or the M^{2}AV (Spieß et al., 2007; Martin et al., 2011), which is additionally capable of measuring turbulent fluxes of sensible heat (Martin and Bange, 2014) and individual turbulent outbursts like entrainment (Martin et al., 2014), have become valuable instruments for data collection. Also outside Europe similar systems are operated, as presented in Thomas et al. (2012) and Bonin et al. (2013). Boundary-layer research has become increasingly interesting for the wind-energy community, since efficiency of wind turbines is directly related to the effects in the boundary layer. Therefore the same (Reuder and Jonassen, 2012) or similar (Subramanian et al., 2012) RPA that have been used for fundamental boundary-layer research have recently been applied in wind-energy research. The thermal stratification of the atmosphere, which can be investigated with vertical profiles collected by RPA, has effects on wind shear and turbulence. Both of these effects have large impact on the efficiency and fatigue of wind turbines. Simple analysis of wind sites assuming the wind profiles of thermally neutral stratification neglect these effects and can lead to a wrong estimation of the risks associated with the deployment of a wind energy converter (WEC). While large-eddy-simulation (LES) is used to study the effects of turbulence in detail (e.g. Zhou and Chow, 2012; Wu and Porté-Agel, 2012, 2011), measurements are necessary to validate and initialize these studies. Small RPA as a flexible and cost-effective tool can serve this purpose. It is shown in this paper how the small RPA MASC (Multi-purpose Airborne Sensor Carrier), which was developed at the University of Tübingen, based on the experiences with the M^{2}AV, is now used in the project "Lidar Complex" for wind energy research (see Fig. 1).

Figure 1. Research RPA MASC in front of a Kenersys K110 WEC (picture taken by Joe Smith, University of Tübingen).

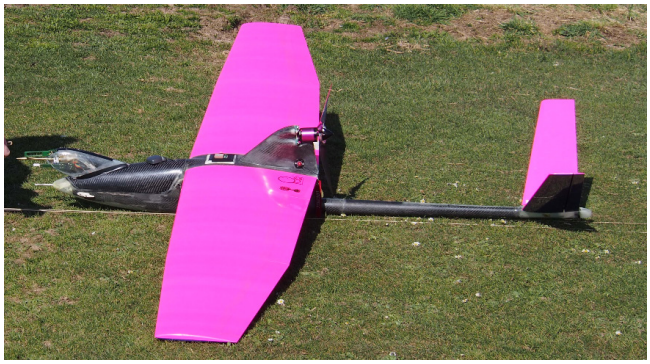

Figure 2. Research RPA MASC.

2 System description

MASC is a small fixed wing RPA with one electrical pusher engine (see Fig. 2). Three different wing sizes exist for the aircraft ranging from 2.60 to 3.40 m. With minimum battery and payload the total weight of the MASC is less than 5 kg. Flight time in this configuration is limited to approximately 15 min. The endurance can be increased up to one hour by adding more batteries. The total weight of the system will than exceed 7.5 kg. For take-off, a bungee launch procedure is performed at the University of Tübingen. The alternative of a landing gear limits take-off and landing spots to flat runways and would also increase total weight of the aircraft. For slow and safe landings the MASC is equipped with flaps to decelerate before touch down. Table 1 summarizes the characteristics of the MASC aircraft.

Table 1. Characteristics of the MASC RPA.

wing span	2.60 m, 3.00 m or 3.40 m
rudder configuration	ailerons, flaps, v-tail
weight	5–7.5 kg, depending on battery load
payload	max. 1.5 kg
endurance	15–60 min, depending on battery load
cruising speed	24 m s^{-1}
propulsion	electrical pusher motor
take-off	bungee launch

Table 2. Typical ROCS autopilot performance.

tracking accuracy	±5 m
altitude precision	±2 m
airspeed precision	±1 m s^{-1}

2.1 Autopilot

The ROCS (Research Onboard Computer System), developed at the Institute of Flight Mechanics and Control (iFR) at the University of Stuttgart, is a autopilot system with waypoint navigation capabilities. Its embedded linux system, enhanced with an FPGA (Field Programmable Gate Array) chip, provides computing power for complex navigation tasks. In the field of meteorological measurements, only a fraction of the possibilities are used so far.

The basic sensor suite of the ROCS autopilot consists of a single-channel GPS receiver, a micro-electro-mechanical-system (MEMS) inertial measurement unit (IMU) as well as barometric and differential MEMS pressure transducers. From this, position, velocity, and attitude of the UAV are estimated using a extended Kalman Filter (EKF). The estimates are then used in the guidance process to keep the UAV on the desired flight track. An overview of performance characteristics is given in Table 2.

2.2 Meteorological measurement system

The meteorological measurement system consists of sensors for all thermodynamic scalars. It is designed to be able to measure turbulent fluxes and structures, providing good measurements up to a cut-off frequency of 10–20 Hz for wind and temperature measurements and 1 Hz for humidity. A central data logging unit called AMOC (Airborne Meteorological Onboard Computer) stores raw sensor data at a sampling rate of 100 Hz onto a SD-card. A 1 Hz telemetry downlink

Table 3. MASC measurement equipment characteristics.

variable	sensor type	accuracy
temperature	PT100 and thermocouple	±0.5 K
humidity	capacitive sensor P14-Rapid	±3 % RH
pressure	barometer HCA-BARO	±0.5 hPa
wind	five hole probe, plus GPS/INS	±0.5 m s^{-1}

for live observation on a groundstation laptop is provided by the system.

There are two temperature sensors installed in parallel – a thermocouple and a resistance thermometer - both in a fine wire design. A detailed description of these sensors can be found in Wildmann et al. (2013). Detailed information on the flow probe setup is presented in Wildmann et al. (2014). In both papers the data logger AMOC is also described in more detail. The complementary measurement of ground speed and orientation of the aircraft with the commercial Inertial Navigation System (INS) IG-500N by SBG systems enables in-situ wind measurement. The commercial capacitive humidity sensor P14 Rapid by Innovative Sensor Technology (IST) with custom electronics and a MEMS barometer (HCA-BARO by Sensortechnics) complete the thermodynamic measurement.

3 Project “Lidar Complex”

The project “Lidar Complex” was initiated by the research network “WindForS” (www.windfors.de), based in Southern Germany. The goal of the project is to establish lidar technology for wind energy plant site evaluation in complex terrain. Additional goals are the comparison of different measurement techniques and the validation of wind field models in terrain that does not conform to IEC61400. It is planned to design a turbulent wind field generator, fed by real measurement data, which can be used to analyse WEC behaviour. An experiment was carried out in October 2013 in flat terrain in Northern Germany to establish a baseline for the comparison of all instruments. In spring 2014, experiments at the test site in complex terrain in the Swabian Alb will be extended.

3.1 Test site Grevesmühlen/Baltic Sea

The test site in Grevesmühlen, located approximately 15 km upcountry of the coast of the Baltic Sea in Germany, was included in the project “Lidar Complex” as a reference site for measurements in a terrain with a low complexity level. Although there are several small areas of sparse woods and different crop types, the orography is flat and the terrain conforms with IEC standards. The site has three WECs (Kenersys K110 2.4 MW, K100 2.5 MW and K82 2.0 MW) placed in a triangle with 1.2–1.5 km distance to each other. In main wind direction, which is from the south-west, a measurement tower is placed in front of one of the WECs. The tower is equipped with a sonic anemometer at hub height, three cup anemometers, three wind vanes, a rain sensor, a temperature sensor at hub height, a barometric pressure sensor and a humidity sensor. Besides a measurement tower there are also two lidar systems installed in the vicinity of this particular WEC. One of them, a Leosphere “Windcube v2” pulsed lidar, is situated close to the measurement tower, looking upwards and the other one is a forward looking, nacelle-based lidar that was provided by SWE (Rettenmeier et al., 2010; Peña et al., 2013). Figure 3 shows several different flight paths that were performed at this site in a four day campaign from 21 to 24 October 2013.

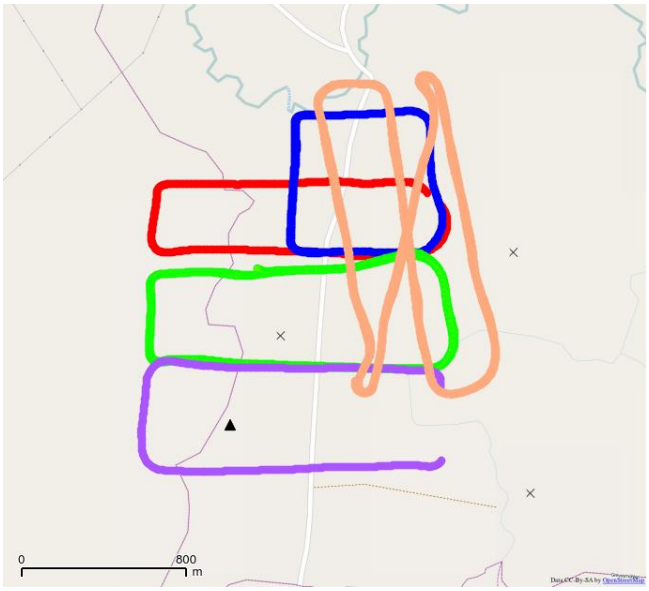

Figure 3. Extracts of recorded flight tracks at test site Grevesmuehlen. Vertical profiles up to 500 m are measured with a square pattern (blue). Rectangular “racetrack” patterns at constant altitude serve to measure turbulence parameters upstream (purple), downstream (red) and between the wind turbines (green, orange). The position of the WECs is depicted as crosses in the map, the measurement tower as a black triangle.

3.2 Test site Schnittlingen/Swabian Alb

One of the biggest accumulations of WECs in the state of Baden-Württemberg, Germany, can be found on a plateau in the Swabian Alb, close to the town Schnittlingen. It consists of nine converters in total, seven of them in a one kilometer square that was chosen as the core site for first flight tests with MASC in May 2013. These seven converters have hub heights between 70 and 105 m and nominal power of 850 kW to 2.7 MW. A 100 m meteorological meaurement tower is installed on site and will be re-equipped with meteorological instruments in 2014. The terrain at this test site has a much higher complexity level compared to Grevesmühlen.

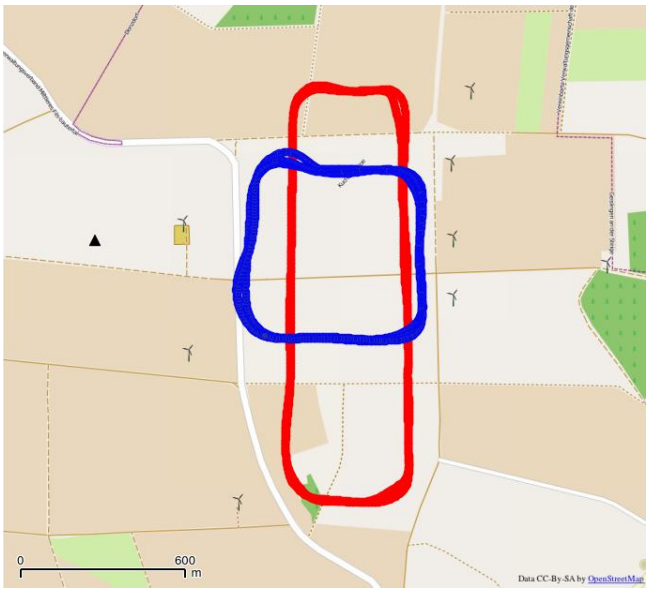

Figure 4. Extracts of recorded flight tracks at test site Schnittlingen. Vertical profiles up to 500 m were measured with a square pattern (blue). Rectangular "racetrack" patterns at constant altitude serve to measure turbulence parameters (red). The position of the WECs can be seen from the OpenStreetMap layer, the measurement tower is depicted as a black triangle.

The wind field is highly influenced by the so-called "Albtrauf", which is an approximately 100 m steep escarpment about 2 km upstream in the main wind direction of the test site. One research goal of the project is to investigate the impact of the escarpment on the wind field.

4 Results

4.1 Flight performance in high wind speeds and in the wake of wind turbines

A short test experiment in late spring 2013 at the test site in the Swabian Alb was used as a proof of concept. Experience was gained about optimal flight strategies and quality of sensor data in the immediate vicinity of WECs.

MASC showed good performance throughout the experiment. The maximum wind speeds that were found during these days were 12 m s^{-1}. More flights were conducted in October 2013 at the site in Grevesmühlen. Again, MASC was able to take data up- and downstream of a wind turbine in wind speeds up to 15 m s^{-1}. Figure 5 shows the precision of the autopilot controlled flight in the wake of a WEC in comparison to flight legs in the undisturbed boundary layer. While in all three depicted variables (course, altitude and airspeed) the presence of the wake can be observed at around 300 m flight leg distance, the aircraft never entered a critical state. The largest deviations from the demand values can be found in the course with up to 10 m deflection. This behaviour is intended, since course deviations are least critical for meteorological measurements and the autopilot controller was tuned accordingly.

4.2 Comparative measurements upstream

In the experiment in Grevesmühlen, a wide variety of measurement equipment was present as described in Sect. 3. A first analysis of the data was carried out to show if systematic errors between the different sensors could be obseserved. The best agreement of all measurements can be found between ground-based lidar and tower-based sonic anemometer measurements. The reason is, that these measurements have the least spatial offset and thus measure the same air mass at the same time. The time series of sonic measurements in the observed period has a standard deviation of approx. 1 m s^{-1}. Deviations among the measurement systems are within this range, so that a good agreement can be assumed. Figure 6 shows data from sonic anemometer measurements on the tower, data from the nacelle-based lidar, the ground-based lidar and RPA measurements. Since RPA measurements are not point measurements, the sections of straight and level flight (legs) that were approximately 800 m long were extracted and averaged for the comparison. The error bars show the standard deviation of the measurements within these legs. It is evident that a perfect agreement between the sensors is not possible, because spatial and temporal biases can have large effects on the instantaneous wind measurement in the turbulent boundary layer. Given these conditions, the agreement is a good basis for further investigations on the wind field at the site in Grevesmühlen and for the next experiments in complex terrain. The good accuracy of wind-vector measurements from RPA has also been shown in other studies (Martin et al., 2011; van den Kroonenberg et al., 2008).

4.3 Measurements in the wake of a wind turbine

As shown in Fig. 5, MASC is able to fly safely in the wake of a 2.4 MW WEC. At the test site in Grevesmühlen, measurement flights were performed in the wake with flight legs in six distinct heights from just below the hub of the turbine at 75 m, up to 225 m. The flight legs are oriented perpendicular to the main wind direction. The resulting wind measurements presented in Fig. 7 show a picture of the shape and intensity of the wake in a distance of four rotor diameters behind the WEC. For better visualization, the linear interpolation technique after Akima (1978) was applied between the measurements of the single flight legs at different altitudes, while the original flight leg paths are still depicted with black lines. Since the flight legs are not performed in parallel at the same time, the shape of the wake is somewhat distorted. Two flight legs at each altitude are used to average the results. The wind speed drops from about 12 m s^{-1} in the free stream to about 5–6 m s^{-1} in the wake of the turbine. This is a wind speed deficit of about 50–60 % in a four rotor diameter distance to

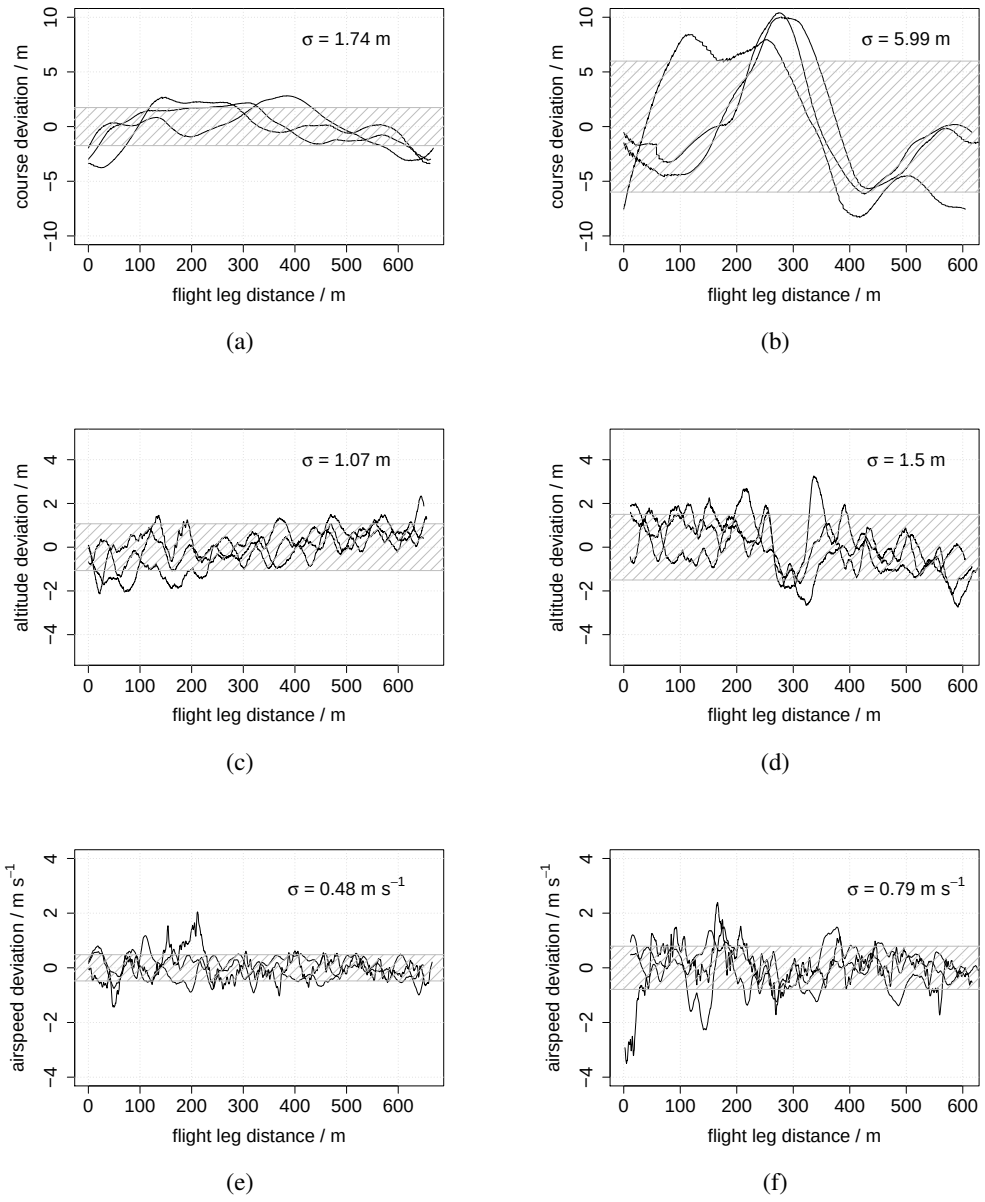

Figure 5. Performance of MASC with ROCS autopilot in undisturbed atmosphere **(a)**, **(c)**, **(e)** and behind a wind turbine **(b)**, **(d)**, **(f)**. All data were measured during the same flight (see green track in Fig. 3). The figures show three successive, individual flight legs at 100 m altitude (= hub height). Offsets between demanded values for course, altitude and airspeed were subtracted and can be higher than the standard deviations σ. An average wind speed of 7 m s^{-1} perpendicular to the flight path was present throughout the flight.

the turbine. These values are in agreement with lidar measurements performed by Iungo et al. (2013) or Käsler et al. (2009) for similar sized turbines and wind speeds.

4.4 Turbulence characteristics in a wind park

Turbulence has a high impact on efficiency of a wind turbine and also on the fatigue of rotors. However, a quantitative description of the effects of turbulence is difficult and not yet available. MASC with its instrumentation for small scale turbulence measurement can deliver valuable data for studies towards a deeper insight into the effects of turbulence on the turbines. Figure 8 shows measurements of turbulent kinetic energy (TKE) upstream and downstream a wind turbine calculated from wind measurements of MASC according to:

$$\mathrm{TKE} = \frac{1}{2}\left(\sigma_u^2 + \sigma_v^2 + \sigma_w^2\right) \quad (1)$$

with standard deviations σ of the wind-vector components u, v and w for 700 m long flight legs. As expected, an increased level of turbulence is found in the wake of the turbine, which slowly starts to decay in a distance between 400 and 600 m.

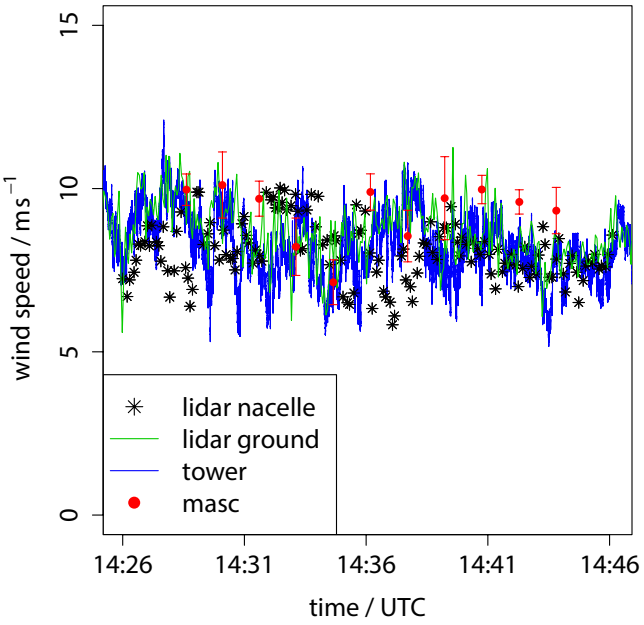

Figure 6. Comparison of horizontal wind speed in the main wind direction measured by tower wind sonic, nacelle-based lidar, ground-based lidar and MASC on 22 October 2013. For the nacelle based lidar, a measuring point 80 m in front of the nacelle was chosen, for the ground based lidar a measurement point at hub height close to the tower was selected.

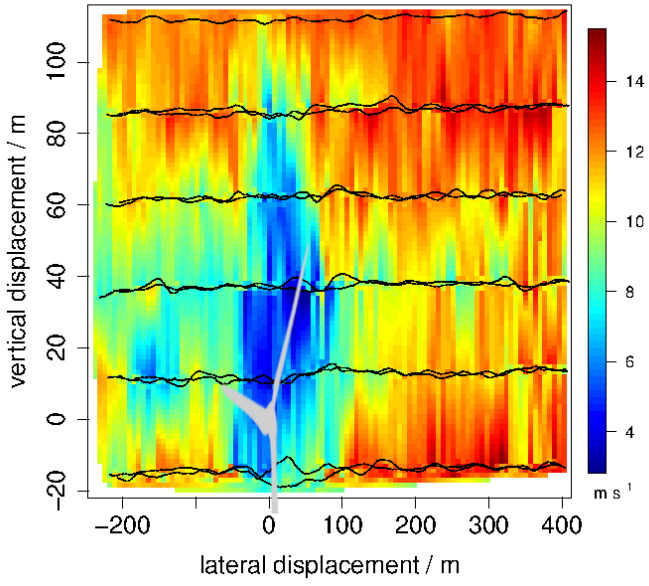

Figure 7. Wind speed measurement from RPA MASC in the wake of a K110 WEC. Flight legs (black lines) are performed perpendicular to the main wind direction, four rotor diameters downstream of the WEC, in six distinct altitudes. Linear interpolation was applied between the wind speed measurement of the single legs and visualized with a colour scale. The position of the WEC is illustrated by the gray shade.

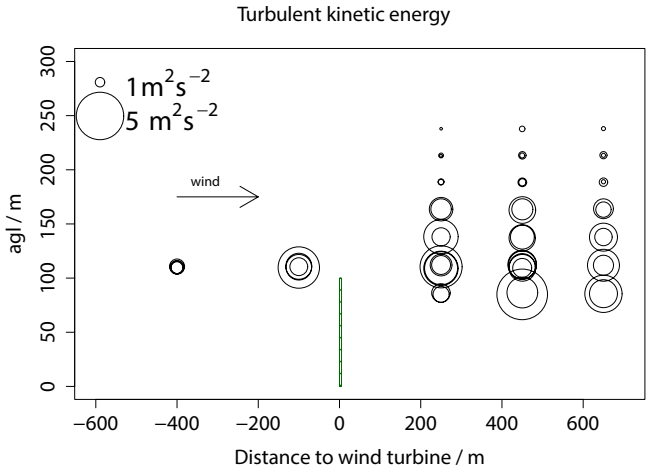

Figure 8. Turbulent kinetic energy measured in flight legs behind a WEC (green line) in different distances and in comparison to upstream turbulence. Each circle represents one single flight leg.

In this case it also appears that a higher degree of turbulence is present upstream, very close to the wind turbine.

5 Conclusions

Remotely Piloted Aircraft of type MASC with an instrumentation that allows vertical soundings of the atmosphere as well as in-situ turbulence measurement are not only a valuable tool for fundamental boundary layer research, but can be directly applied for wind energy research. Even in high wind speeds, the RPA MASC is able to operate safely, also in the wake of large WEC. Its flexible operation in almost any location and low operating cost makes it superior to stationary measurement equipment like towers and lidars for short, focussed experiments. It is shown how the data collected by MASC can provide information about inflow conditions, the wake structure of a WEC and the turbulence of the inflow and wake of the turbine. In the project “Lidar Complex”, MASC is first used extensively in wind energy research.

Acknowledgements. We are much obliged to the referees for their detailed review of this paper. The Project “Lidar complex” is funded by the German Federal Ministry for the Environment, Nature Conservation and Nuclear Safety (BMU) on the basis of a resolution of the German Bundestag. The MASC airframe was build by “ROKE-Modelle”. We like to thank our safety pilots Maximilian Ehrle and Markus Auer for the perfect job in the measurement campaigns. We acknowledge support by Deutsche Forschungsgemeinschaft and Open Access Publishing Fund of Tuebingen University.

Edited by: S.-E. Gryning
Reviewed by: P. B. Chilson and one anonymous referee

References

Akima, H.: A Method of Bivariate Interpolation and Smooth Surface Fitting for Irregularly Distributed Data Points, ACM Trans. Math. Softw., 4, 148–159, doi:10.1145/355780.355786, 1978.

Bonin, T., Chilson, P., Zielke, B., and Fedorovich, E.: Observations of the Early Evening Boundary-Layer Transition Using a Small Unmanned Aerial System, Bound.-Layer Meteorol., 146, 119–132, doi:10.1007/s10546-012-9760-3, 2013.

Iungo, G. V., Wu, Y.-T., and Porté-Agel, F.: Field Measurements of Wind Turbine Wakes with Lidars, J. Atmos. Oceanic Technol., 30, 274–287, doi:10.1175/JTECH-D-12-00051.1, 2013.

Käsler, Y., Rahm, S., Simmet, R., and Trujillo, J. J.: Wake measurements of a multi-MW wind turbine with long range lidar, in: Euromech Colloquium 508 on wind turbine wakes, European Mechanics Society, Madrid, Spain, 2009.

Martin, S. and Bange, J.: The Influence of Aircraft Speed Variations on Sensible Heat-Flux Measurements by Different Airborne Systems, Bound.-Layer Meteorol., 150, 153–166, doi:10.1007/s10546-013-9853-7, 2014.

Martin, S., Bange, J., and Beyrich, F.: Meteorological profiling of the lower troposphere using the research UAV "M^2AV Carolo", Atmos. Meas. Tech., 4, 705–716, doi:10.5194/amt-4-705-2011, 2011.

Martin, S., Beyrich, F., and Bange, J.: Observing Entrainment Processes Using a Small Unmanned Aerial Vehicle: A Feasibility Study, Bound.-Layer Meteorol., 150, 449–467, doi:10.1007/s10546-013-9880-4, 2014.

Peña, A., Hasager, C., Lange, J., Anger, J., Badger, M., Bingöl, F., Bischoff, O., Cariou, J.-P., Dunne, F., Emeis, S., Harris, M., Hofsäss, M., Karagali, I., Laks, J., Larsen, S., Mann, J., Mikkelsen, T., Pao, L., Pitter, M., Rettenmeier, A., Sathe, A., Scanzani, F., Schlipf, D., Simley, E., Slinger, C., Wagner, R., and Würth, I.: Remote Sensing for Wind Energy, DTU Wind Energy E, DTU Wind Energy, 2013.

Rettenmeier, A., Hofsäß, M., Schlipf, D., Trujillo, J. J., Siegmeier, B., and Kühn, M.: Wind field analyses using a nacelle – based LIDAR system, in: European Wind Energy Conference, Warsaw, Poland, 2010.

Reuder, J. and Jonassen, M. O.: First Results of Turbulence Measurements in a Wind Park with the Small Unmanned Meteorological Observer {SUMO}, in: Selected papers from Deep Sea Offshore Wind Ramp Conference, Vol. 24, 176–185, Trondheim, NO, doi:10.1016/j.egypro.2012.06.099, 2012.

Reuder, J., Brisset, P., Jonassen, M., Müller, M., and Mayer, S.: The Small Unmanned Meteorological Observer SUMO: A new tool for atmospheric boundary layer research, Meteorol. Z., 18, 141–147, 2009.

Spieß, T., Bange, J., Buschmann, M., and Vörsmann, P.: First Application of the Meteorological Mini-UAV "M^2AV", Meteorol. Z. N. F., 16, 159–169, 2007.

Subramanian, B., Chokani, N., and Abhari, R. S.: Full Scale HAWT: Structure of Near Wake Turbulence Measured with Instrumented UAV, in: EWEA 2012 Conference Proceedings, Copenhagen, DK, 2012.

Thomas, R. M., Lehmann, K., Nguyen, H., Jackson, D. L., Wolfe, D., and Ramanathan, V.: Measurement of turbulent water vapor fluxes using a lightweight unmanned aerial vehicle system, Atmos. Meas. Tech., 5, 243–257, doi:10.5194/amt-5-243-2012, 2012.

van den Kroonenberg, A. C., Martin, T., Buschmann, M., Bange, J., and Vörsmann, P.: Measuring the Wind Vector Using the Autonomous Mini Aerial Vehicle M^2AV, J. Atmos. Oceanic Technol., 25, 1969–1982, 2008.

Wildmann, N., Mauz, M., and Bange, J.: Two fast temperature sensors for probing of the atmospheric boundary layer using small remotely piloted aircraft (RPA), Atmos. Meas. Tech., 6, 2101–2113, doi:10.5194/amt-6-2101-2013, 2013.

Wildmann, N., Ravi, S., and Bange, J.: Towards higher accuracy and better frequency response with standard multi-hole probes in turbulence measurement with remotely piloted aircraft (RPA), Atmos. Meas. Tech., 7, 1027–1041, doi:10.5194/amt-7-1027-2014, 2014.

Wu, Y.-T. and Porté-Agel, F.: Large-Eddy Simulation of Wind-Turbine Wakes: Evaluation of Turbine Parametrisations, Bound.-Layer Meteorol., 138, 345–366, doi:10.1007/s10546-010-9569-x, 2011.

Wu, Y.-T. and Porté-Agel, F.: Atmospheric Turbulence Effects on Wind-Turbine Wakes: An LES Study, Energies, 5, 5340–5362, doi:10.3390/en5125340, 2012.

Zhou, B. and Chow, F.: Turbulence Modeling for the Stable Atmospheric Boundary Layer and Implications for Wind Energy, Flow, Turbul. Combust., 88, 255–277, doi:10.1007/s10494-011-9359-7, 2012.

A.5 Observations of the Early Morning Boundary-Layer Transition with Small Remotely-Piloted Aircraft.

The final publication is available at
http://link.springer.com/article/10.1007/s10546-015-0059-z.

Boundary-Layer Meteorol
DOI 10.1007/s10546-015-0059-z

ARTICLE

Observations of the Early Morning Boundary-Layer Transition with Small Remotely-Piloted Aircraft

Norman Wildmann[1] · **Gerrit Anke Rau**[1] · **Jens Bange**[1]

Received: 23 November 2014 / Accepted: 25 June 2015

Abstract A remotely-piloted aircraft (RPA), equipped with a high resolution thermodynamic sensor package, was used to investigate physical processes during the morning transition of the atmospheric boundary layer over land. Experiments were conducted at a test site in heterogeneous terrain in south-west Germany on 5 days from June to September 2013 in an evolving shallow convective boundary layer, which then developed into a well-mixed layer later in the day. A combination of vertical profiling and constant-altitude profiling (CAP) at 100 m height above ground level was chosen as the measuring strategy throughout the experiment. The combination of flight strategies allows the application of mixed-layer scaling using the boundary-layer height z_i, convective velocity scale w_* and convective temperature scale θ_*. The hypothesis that mixed-layer theory is valid during the whole transition was not confirmed for all parameters. A good agreement is found for temperature variances, especially in the upper half of the boundary layer, and the normalized heat-flux profile. The results were compared to a previous study with the helicopter-borne turbulence probe Helipod, and it was found that similar data quality can be achieved with the RPA. On all days, the CAP flight level was within the entrainment zone for a short time, and the horizontal variability of temperature and water vapour along the flight path is presented as an example of the inhomogeneity of layer interfaces in the boundary layer. The study serves as a case study of the possibilities and limitations with state-of-the-art RPA technology in micrometeorology.

Keywords Convective boundary layer · Entrainment · Morning transition · Remotely-piloted aircraft · Unmanned aerial vehicle

1 Introduction

The morning transition of the atmospheric boundary layer (ABL) has been defined and investigated previously. Lapworth (2006) defines the morning transition as the time at which

✉ Norman Wildmann
norman.wildmann@uni-tuebingen.de

1 Center for Applied Geosciences, Eberhard Karls University Tübingen, Tübingen, Germany

Published online: 30 August 2015

the near-surface heat flux changes sign. Angevine et al. (2001) define a morning transition phase that extends from sunrise until convection reaches a level of 200 m above the ground. This height was chosen because measurements were limited to that height, but estimations of the height of the nighttime inversion layer (NIL) through experiments often support this value. Stull (1988) has a broader definition of the morning transition, including the whole period, until the convective boundary layer (CBL) is fully developed. According to this definition, the transition is divided into two parts: in the first part, warming of the Earth's surface enables the development of a shallow convective boundary layer (CBL) below the remaining nighttime inversion layer. The growth of this shallow CBL, fed by entrainment from aloft and a positive heat flux from the ground, is also called the burning off of the nighttime inversion layer (Stull 1988). The second phase of the morning transition starts when the top of the shallow CBL reaches the bottom of the residual layer of the previous day. In this phase, thermals rise through the whole ABL and reach the inversion layer, forming the fully developed mixed layer. The definition in Angevine et al. (2001) equals the first phase of the definition of Stull (1988). In the presented research, the focus is on this first phase of the transition, but data extend into the second phase as well.

The general processes associated with the morning transition are well understood and described. However, detailed descriptions are rare and are an ongoing field of research. During the morning transition, the vertical and horizontal extents of the CBL are small. Thus, it is easier to study their characteristics, without disturbing effects like clouds (Bange et al. 2007). Legal restrictions often do not allow a large horizontal extent of the flight pattern with small remotely-piloted aircraft (RPA). In the shallow CBL during the morning transition, these short flight legs are however sufficient for turbulence measurement, since eddies are still small.

Concerning the experimental validation of morning transition processes, Lenschow et al. (1979) showed how complex orography can influence the transition. In the valley sites that were observed in their study, rapid changes in temperature and wind speed occur. Cold-air pools that formed in the valley at night disperse when an already mixed layer is advected into the valley from warmer upstream slopes and plateaus. All recent studies, whether experimental (Angevine et al. 2001; Lapworth 2006; Bange et al. 2007; Bennett et al. 2010) or numerical (Sorbjan 2007; Beare 2008), agree that surface heating is the driving factor for the start of the transition, but also emphasize that entrainment plays a major role in the heating of the ABL once the surface heat flux changes sign. A main influence for the speed of the transition was found to be wind shear (Angevine et al. 2001). The weaker the wind shear, the longer it takes for the convection to pick up. Beare (2008) agrees with the effect of shear on the morning transition and presents large-eddy simulations (LES) to show how the mixed shallow convective and stable boundary layer is shear-driven. Bennett et al. (2010) put a focus on the humidity variability in the early morning and were able to observe that the humidity field of thermals—i.e. the area in a CBL where water vapour content differs significantly from its surroundings—is broader than for temperature and momentum. They also found a transition from horizontal convective rolls towards open cell convection. Edwards et al. (2014) found that including radiative effects in LES models of the morning transition improves the agreement between simulation and experiments. Especially the long-wave radiative cooling of the residual layer before sunrise enhances the growth of the mixed layer in the transition period, because it smooths the transition between the strongly stable nighttime inversion and the residual layer. Brötz et al. (2014) use morning-transition measurements in a low-mountain terrain to show how coherent turbulent structures affect the measurement of fluxes with the eddy covariance method. For the same experimental data, Eigenmann et al. (2009) showed

how free convective conditions are given during the morning transition, when valley winds become weak and change in direction.

Given that the same physical processes that drive the mixed layer growth are also responsible for the growth of the shallow CBL, it seems likely that the same scaling methods can be applied. Bange et al. (2007) performed airborne measurements to identify systematic behaviour that can help to describe the shallow CBL. Therefore, mixed-layer scaling of the daytime CBL was applied to the transition phase. It showed that the same scaling parameters cannot easily be used for the transition period. Sorbjan (2007) showed with LES that the dimensionless variance profiles of horizontal and vertical wind speed, which were also calculated by Bange et al. (2007), evolve during the transition and therefore cannot be described by mixed-layer scaling. For temperature, he found that in the mixed layer, the profiles of dimensionless variances coincide.

Current research is often driven by LES models that are used to improve the understanding of processes in the ABL and investigate the influence of different parameters (humidity, radiation, shear) in detail. These detailed investigations require a much larger database of experimental data for different atmospheric conditions, in order to validate the findings of the models and evaluate their applicability to real-world scenarios. A series of measurements with a small RPA is presented in this study, which delivers not only vertical soundings of temperature, humidity and wind vector, but also area-averaged turbulence measurements. These in situ data can help to validate theory and simulation. The analysis is split into two main parts. In Sect. 5.1, mixed-layer scaling is applied, following the example of Bange et al. (2007) and compared to their results, in order to evaluate the quality of such a scaling approach for two different experiments. In Sect. 5.2, distinct features of horizontal variability in the interface between shallow CBL and residual layer, as well as in the shallow CBL itself are discussed.

2 Experiment Description

2.1 Overview

In 2013, small research RPA were used to carry out a series of morning transition experiments in southern Germany. It was the goal of the project to collect valuable data about this transition period with a single instrument and in an area that has been poorly observed by other meteorological instruments. The test site in the Neckar valley, which was available for the experiment, is close to the cities of Tübingen and Reutlingen in south-west Germany, featuring an area with heterogeneous land use and some considerable orography as described below. In the framework of the Water and Earth System Science competence cluster (WESS, http://www.wess.info), which focusses on the water cycle and associated solute fluxes at the catchment scale, the demand for high resolution atmospheric measurements has increased in the area. Table 1 gives a list of all flight experiments that were conducted during the experiment, including information about the number of flights per day, flight time, time of first take-off and last landing, and the sunrise time of each day. Details on the flight strategies are given in Sect. 3.

In densely populated areas, as are common in central Europe, the extent of the flight area is limited by adjacent roads and villages, which the RPA is not allowed to fly over according to the general rules for RPA operation. The usable flight area roughly extends to 1.5 km in the east–west direction and 500 m in the north–south direction. The area is characterised by

Table 1 List of flight experiments with number of flights (NoF), total time in the air (tta), start and end time of the experiment, sunrise time and maximum height above ground level (a.g.l.) on each day

Date	NoF #	tta (min)	Start (UTC)	End (UTC)	Sunrise (UTC)	Max. height (a.g.l. m)
6 June	5	60	0540	0732	0319	300
5 July	8	99	0505	0840	0325	450
23 July	8	85	0505	0850	0344	450
14 Aug.	7	99	0605	0935	0414	500
5 Sept.	8	98	0605	0930	0445	500

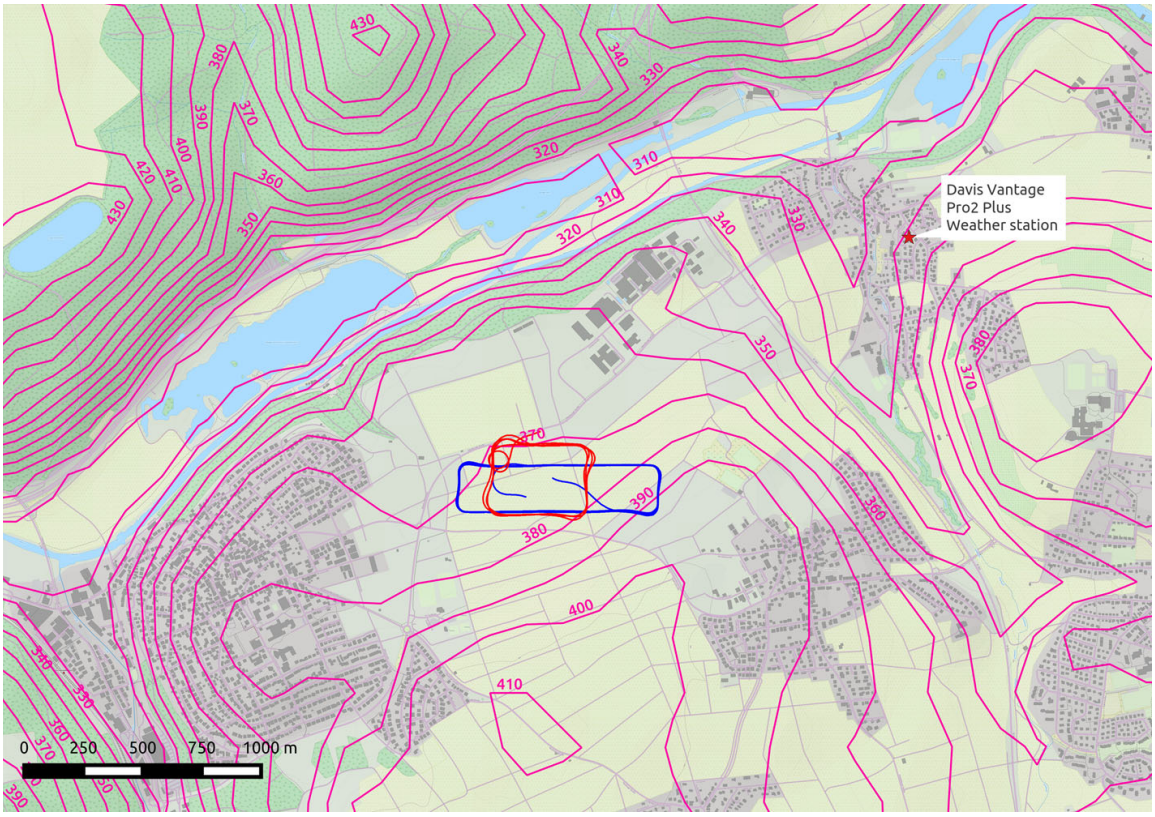

Fig. 1 Map of the experiment site in the Neckar valley, with flight path for vertical profiles (*red*) and constant-altitude profiling (*blue*). Background map layer: Data CC-by-SA by OpenStreetMap

a 100-m high hill in the north–west, a lake and a river in the valley at the foot of the hill, different patches of farmland and small villages in the surrounding area (see Fig. 1). The five selected experiment days are all days with high incoming radiation and a potentially evolving CBL. A local weather station which is also depicted in Fig. 1, provided measurements of global radiation input. On all days the global radiation increased almost linearly from 200 to 600 W m^{-2} in the time frame of the experiment (2–5 h after sunrise). However, each day has some specific characteristics, which are explained in Sect. 4.

2.2 Instrumentation

2.2.1 Multi-purpose Airborne Sensor Carrier

To collect in situ measurements in the atmosphere, the group of Environmental Physics at the University of Tübingen operates the Multi-purpose Airborne Sensor Carrier (MASC, see

Fig. 2 MASC RPA at take-off in the Neckar valley (*left*) and sonic anemometer Young Model 81000 installed on site (*right*)

Table 2 List of the sensors/sensor systems that are used, and their absolute accuracy

Sensor	Measured parameter	Total accuracy
FWPRT	Temperature	±0.5 K
TC	Temperature	±0.5 K
IST AG P14 rapid	Rel. humidity	±5 % RH
HCA	Barom. pressure	±3 hPa
5HP + GPS/IMU	Wind	±1 m s^{-1}

Fig. 2), which is a small RPA with a total weight of 5–8 kg, depending on the battery- and payload. It is powered by an electrical pusher engine and can fly up to one hour at a typical cruising speed of 25 m s^{-1}. Using the research onboard computer system (ROCS) autopilot, developed at the Institute for Flight Mechanics and Control (IFR) Stuttgart, the aircraft is flying pre-defined flight paths at controlled altitude and airspeed. The performance of the system for wind energy research purposes is described in Wildmann et al. (2014a). To perform measurements of thermodynamic scalars and turbulence, the system is equipped with a five-hole probe system (Wildmann et al. 2014c), a fine-wire platinum resistance thermometer and a thermocouple for fast response temperature measurements (both Wildmann et al. 2013), a capacitive humidity sensor, a barometric pressure transducer, and an inertial measurement unit with GPS receiver. The method to calculate the three-dimensional wind vector from the airflow vector and the inertial measurements of the RPA is presented in Kroonenberg et al. (2008). The wind and temperature measurements achieve a frequency resolution of 10–20 Hz. Humidity measurements after post-processing are able to resolve turbulence up to 3 Hz (Wildmann et al. 2014b). The total accuracy of the instruments is presented in Table 2. These accuracies include possible biases, which are not critical for flux measurements and lapse rates. For more detailed information about the precision, time responses and common errors, we refer to the given references. The altitude of the aircraft is determined through barometric measurements in comparison to the initial pressure at ground level, supported by GPS information to correct for long-term drifts. The altitude relative to the take-off position is referred to as the height above ground level (a.g.l.) herein, although the actual ground level below the flight pattern can deviate up to 15 m from the take-off position due to orography. The calculated height is typically maintained with a precision of ±2 m by the autopilot (see also Wildmann et al. 2014a). At the test site for this experiment, the weight of the aircraft was limited by the flight permission to 5 kg, which only allows a single battery and thus reduces the flight time to 15 min.

2.2.2 Sonic Anemometer

In order to be able to scale measurements obtained in flight with e.g. surface flux, a sonic anemometer of type Young Model 81000 was installed on-site on 14 August and 5 September 2013 (see Fig. 2). Vertical turbulent fluxes of sensible heat were calculated using the eddy-covariance method (Foken and Nappo 2008). Since the area covered by the aircraft is not homogeneous, but consists of patches with different crop types, the measured surface flux is not necessarily representative for the whole area. This problem is well known, and cannot be resolved with a single sonic anemometer. Ground truth of at least one instrument at one site was still considered valuable for scaling approaches, and comparison to area-average estimates of fluxes. The authors are aware of typical errors of $\approx 10-15$ % in vertical velocity and heat-flux measurements with orthogonal sonic anemometers as used in this study (Kochendorfer et al. 2012; Frank et al. 2013).

3 Methods

In this section the measurement strategy and methods of analysis of the data are introduced.

3.1 Vertical Profiles

To measure the stratification of the atmosphere, vertical profile flights were carried out. The vertical profile flight path was a combination of consecutive ascent and descent with a constant vertical velocity, performed in a 400 m horizontal square (see also Fig. 1). The pattern was designed as a compromise between the desire to measure a vertical column with as little horizontal variability of the atmosphere as possible and flying straight legs for precise airflow measurement with a five-hole probe during the ascent and descent. The vertical velocity was set to approximately 5 m s^{-1}, so that, at a sampling rate of 100 Hz, the vertical distance between each measurement point is in the range of 0.05 m. These flights provide quasi-instantaneous vertical profiles of temperature, humidity, and wind vector. Especially for the wind vector in a CBL, these profiles can differ from a time-averaged profile. This method has the advantage that small-scale features can be observed, but especially wind speed and wind direction show large fluctuation in an increasingly convective environment, as discussed in Sect. 4. The vertical profiles of potential temperature θ characterize the evolution of the boundary layer and are of highest interest in the estimation of the height of the shallow CBL, which corresponds to the base of the thermal inversion h_i. In general, in this study, virtual potential temperature θ_v is used for the vertical profiles in order to easily compare to temperatures measured by the sonic anemometer. θ_v is calculated as

$$\theta_v = (1 + 0.608\, q)\, \theta \tag{1}$$

with specific humidity q. The vertical profiles are slant profiles over an inhomogeneous terrain as can be seen in Fig. 1. In the lower parts, the profiles could be affected by these inhomogeneities. Using the vertical profiles of θ_v, h_i was estimated at the cross-section of the potential temperature gradients of the nighttime inversion layer and the shallow CBL (see Fig. 3a). Proper scaling according to Deardorff (1974) uses the height of minimum heat flux as the scaling height z_i. Since the method to calculate fluxes from RPA requires horizontal averaging (eddy covariance method), a vertical profile of fluxes could not be measured using instantaneous profiles. Instead, following the example of Bange et al. (2007), it is assumed that $z_i \approx h_i$. In cases where h_i is not as clearly found from the proposed method as in Fig. 3a,

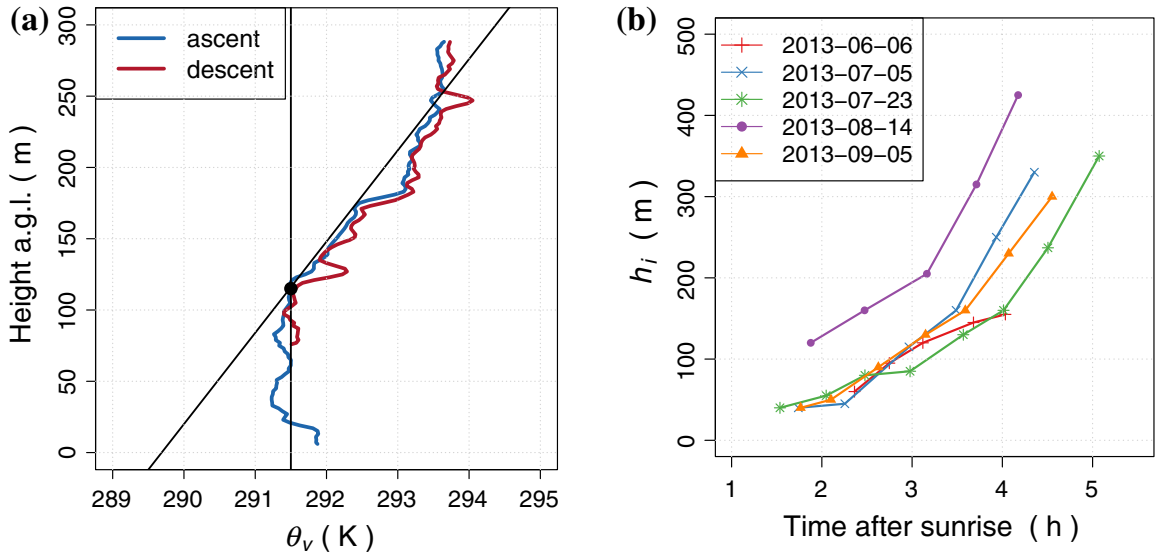

Fig. 3 **a** Sketch of the method to derive the boundary-layer height z_i from the vertical profile of virtual potential temperature θ_v. The *black lines* represent the lapse rates of the atmosphere in the shallow CBL and the nighttime inversion layer or residual layer respectively. The height where they intersect—marked by a *black dot*—is used as the boundary-layer height z_i; **b** evolution of boundary-layer height for all measurement days

relative humidity and wind profiles were consulted as well to make the best possible estimate. Some profiles do not allow an estimation of h_i at all, because the CBL had outgrown the measurement height. These cases are not considered for further analysis.

3.2 Constant-Altitude Profiling

In a single measurement flight, the vertical profile path that was described above, is followed by long straight and level paths, so-called flight legs, at a constant altitude. The height above ground level for these legs was chosen to be 100 m persistently throughout the experiment. The height was chosen for comparability with Bange et al. (2007) and because it is a safe operating height for the RPA. In the monitored time of the transition, the boundary layer grows through the measurement height and the development of area-averaged scalar variables and fluxes is measured at this particular height. This method was introduced by Bange et al. (2007) and is called constant-altitude profiling (CAP).

The flight path for CAP was set to be a rectangle, also called a 'racetrack' that extends about 850 m in the east–west direction and 200 m in the north–south direction (see also Fig. 1, blue line). Since turns have to be cut from the flight path for the data analysis, the usable flight leg length is about 800 m. In one flight, up to seven complete racetracks are flown. Mean values of scalars are calculated as the average of all single legs and variances are calculated over the concatenated and detrended time series of all single legs, in order to capture variances of length scales bigger than the flight leg length. Fluxes were calculated using the eddy covariance method:

$$H = \rho c_\mathrm{p} \langle w'\theta' \rangle, \tag{2}$$

$$LE = \rho L_\mathrm{v} \langle w'q' \rangle, \tag{3}$$

where H is the sensible heat flux, LE is the latent heat flux, w is the vertical wind component, q is the specific humidity, ρ is the air density, c_p is the specific heat of the air at constant pressure, and L_v is the latent heat of vaporization at 20 °C, all averaged along single

flight legs. Recent studies about heat flux measurements with RPA have been presented by Reineman et al. (2013), Bonin et al. (2013), Martin and Bange (2014), Knuth and Cassano (2014). Fluxes are calculated over each single leg and then averaged for one complete flight. Fig. 4a shows the calculated fluxes H and LE over time during the morning transition of 14 August 2013. The error bars show the standard deviation of all single leg flux calculations in one flight. It shows that errors get larger later in the day, since the integral length scale will increase and the largest eddies are possibly not sufficiently sampled any more with a flight leg of the given length. It also shows that latent heat fluxes have larger errors. A theoretical way to calculate potential errors of flux measurements from airborne measurements was introduced by Lenschow and Stankov (1986). It suggested to distinguish between systematic statistical flux errors, which occur due to flight legs of insufficient length, and random statistical flux errors. Field campaigns with the helicopter sonde 'Helipod' and the manned research aircraft 'Do 128', both operated by the University of Braunschweig, demonstrated that in a typical mid-European summer afternoon (a moderately convective boundary layer over heterogeneous terrain), flight legs of 10 km length are sufficient to neglect the systematic statistical flux error (Bange et al. 2002). It is evident that in a weak shallow CBL, the required length will be significantly smaller. Regarding the random statistical flux error, Lenschow and Stankov (1986) suggested that a measurement length of 10–100 times the boundary-layer height is required to measure variances to 10 % accuracy within the convective boundary layer (this condition is extended to 10^2–10^4 times the boundary-layer height for scalar fluxes and to 10^3–10^5 for stress fluxes). However, Bange et al. (2002) show that the difference between 'Helipod' and 'Do 128' measurements was much smaller than the estimated statistical uncertainties, suggesting that the statistical errors of the flight measurements are over-estimated in general. Therefore, the statistical deviation of single flight legs, as shown in Fig. 4a, is a more appropriate measure for the random statistical error of the measurement.

CAP can also serve to detect and measure horizontal variability of thermodynamic variables. Since the entrainment layer also grows through the CAP measurement height, thermals and entrainment effects could be observed on some occasions.

3.3 Estimation of Surface Fluxes

In order to compare the development of the morning transition on all experiment days and find common behaviour, scaling parameters will need to be defined. Section 3.1 already showed how the scaling height z_i can be estimated from the RPA measurements. Further scaling parameters for the CBL are the convection velocity scale w_* and the convective temperature scale θ_*. Both of these parameters use the surface kinematic heat flux $\langle w'\theta' \rangle_0$,

$$w_* = \left[\frac{g}{\overline{\theta}} z_i \langle w'\theta' \rangle_0 \right]^{1/3}, \tag{4}$$

$$\theta_* = \frac{\langle w'\theta' \rangle_0}{w_*}, \tag{5}$$

where g is the acceleration due to gravity. On 14 August and 5 September, data from the sonic anemometer could be used to calculate $\langle w'\theta' \rangle_0$ with an averaging length equivalent to the length of one CAP flight. However, in order to be able to also scale the 3 days when no sonic anemometer was available, assumptions can be made to estimate the surface fluxes. Bange et al. (2007) proposed that in a quasi-stationary situation, with constant heating rate $\dot{\theta}$ viz. $\partial\theta/\partial t$—as is found in the morning transition phase—the heat flux at height z can be approximated by

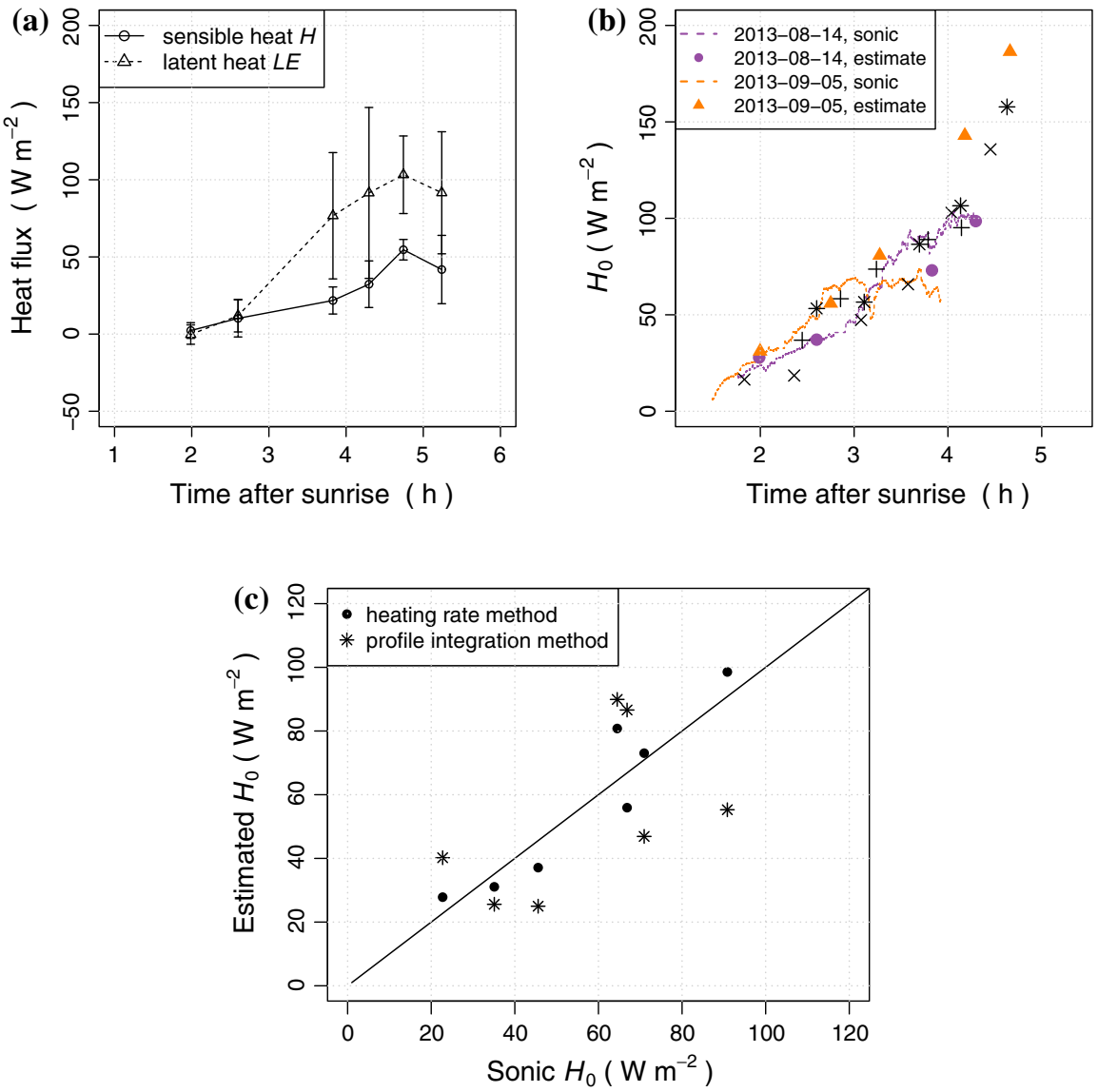

Fig. 4 **a** Measurement of heat fluxes on 14 August 2013 with the MASC RPA at 100 m a.g.l. *Error bars* are the standard deviation of the single leg fluxes in one flight. **b** Surface flux measurements by sonic anemometer compared to the estimated surface fluxes. In *black*, the estimated values for the 3 days without sonic anemometer are given. **c** Evaluation of methods to estimate the surface heat flux in comparison to the sonic anemometer. The *solid line* represents the line of identity. All available data points of 14 August and 5 September are included

$$H(z) = \rho c_\mathrm{p} \, (h_0 - z) \, \dot{\theta}. \tag{6}$$

The heating rate in the shallow CBL can easily be found from measurements from the RPA. The height h_0 is the height at which the heat flux crosses zero. The factor B is introduced as the ratio between h_0 and the inversion base height h_i. Following the hypothesis that the shallow CBL can be described with a common scaling on the 5 days of the experiment, we assume that B is constant.

$$B = \frac{h_0}{h_i} = \text{const.} \tag{7}$$

The surface heat flux $H(z = 0)$ can then by calculated as

$$H(z = 0) = B z_i \rho c_\mathrm{p} \dot{\theta}. \tag{8}$$

Sorbjan (1995) found B to be close to 0.75 from LES results in the mixed layer. The results from Bange et al. (2007) however suggested a value $B \approx 0.55$. Beare (2008) also found in an LES study that B in the morning is generally smaller than 0.75, and showed that it is also dependent on the mean wind speed. In order to find the best value for B for the presented experiment, an iterative method was applied that adjusted B in the calculation of surface fluxes to the value of B found from the heat flux profile of all flights (Fig. 11a). Equation 8 was first calculated with $B = 0.75$. In the third iteration, the method has already converged to a value $B \approx 0.68$. The surface fluxes calculated according to Eq. 8 are shown in comparison to the sonic anemometer flux measurement for 14 August and 5 September in Fig. 4b. It shows that the estimation fits very well on 14 August, but is much higher, especially later than 4 h after sunrise on 5 September. One reason could be that the assumption of a constant heating rate $\dot{\theta}$ in the shallow CBL is not always valid in the later part of the transition. The vertical profiles of this day also suggest that warm air advection was present in the latest two flights which will definitely introduce an error to the surface heat flux estimation. For all other cases, the surface heat flux estimation that is presented here provides a reasonable estimate with an uncertainty in the range of 20 %. Appendix gives an example of the error propagation into the surface heat flux estimation for given uncertainties of B, z_i and $\dot{\theta}$. The uncertainty seems relatively high, but is not uncommon for heat-flux measurements in heterogeneous terrain (Beyrich et al. 2006).

A different way to determine heat-flux profiles from successive vertical profiles of potential temperature has been presented by Deardorff et al. (1980) and has been applied to RPA measurements by Bonin et al. (2013). Derived from the prognostic equation for mean potential temperature, the turbulent heat flux at all heights can be calculated, assuming advection, radiation, molecular diffusion and other body sources of heat are neglected, from

$$\overline{w'\theta'}(z) = \int_{z}^{z_i} \dot{\theta} \mathrm{d}z. \tag{9}$$

For evaluation of the method that was presented before, the surface heat flux was also calculated with Eq. 9. Figure 4c shows an error plot which confronts the ground based sonic anemometer flux measurements of 14 August and 5 September with the methods derived from Bange et al. (2007) and Bonin et al. (2013) respectively. It shows that for the presented experiment, the surface flux estimation through boundary-layer height and heating rate shows a better agreement over the whole measurement range and will thus be used for the following analysis. The observed deviations from the sonic anemometer measurements are within the range of the predicted uncertainty.

4 Results

Here, an overview of the measured vertical profiles of temperature, humidity and wind is given, followed by a presentation of the evolution of boundary-layer height and heat fluxes. The individual characteristics of each single measurement day are summarized thereafter.

4.1 Vertical Profiles

In Figs. 5 and 6 (left), the virtual potential temperature θ_v profiles are plotted. Each plot contains the consecutive profiles that were measured on one measurement day; times (UTC) of the flights are given in the legend. Removing small-scale turbulent fluctuations increases

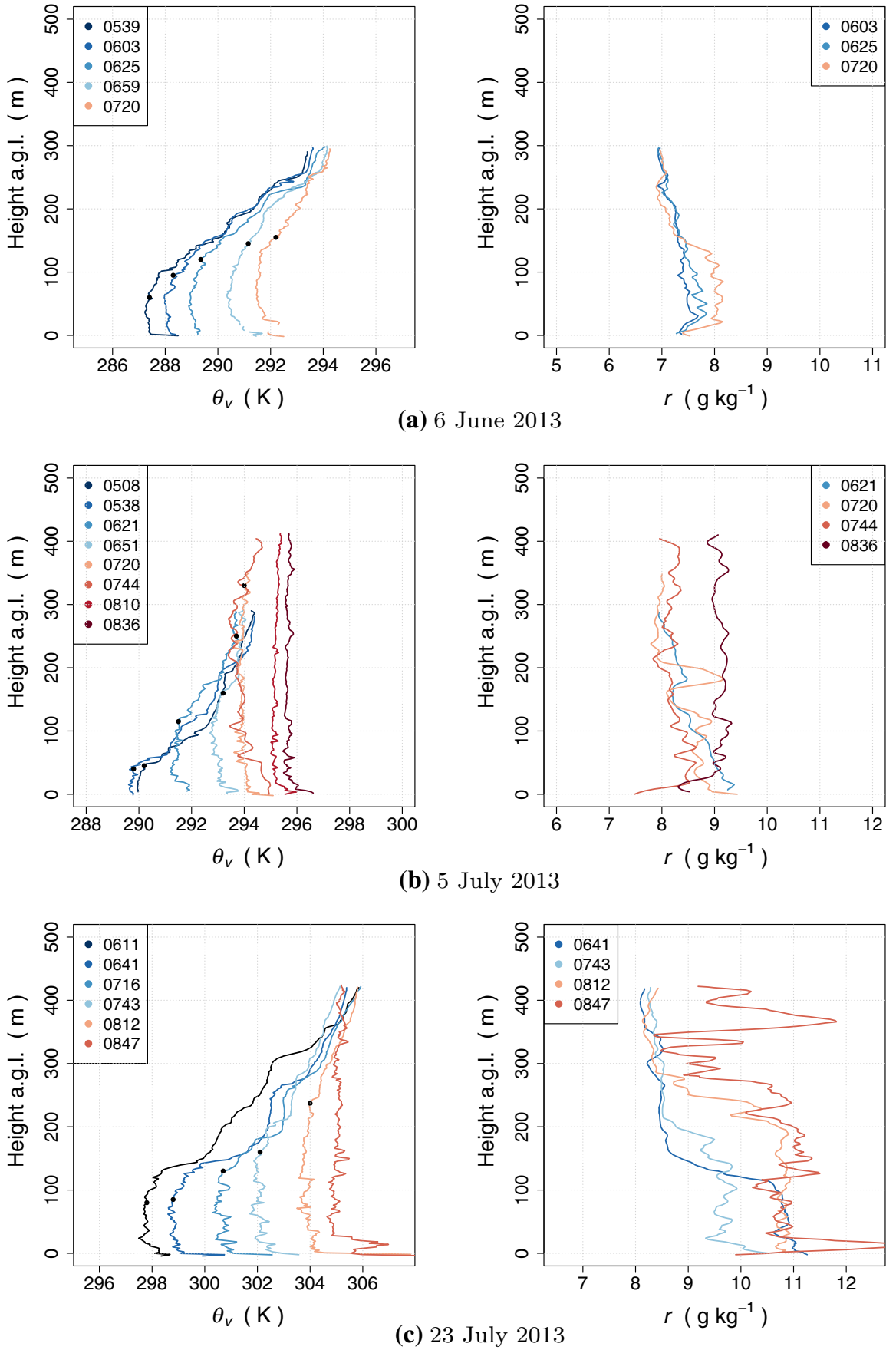

Fig. 5 Vertical profiles of virtual potential temperature θ_v (*left*) and mixing ratio r (*right*) for 6 June, 5 July and 23 July. For better readability, a few profiles of mixing ratio are omitted from the plot. The x-axes of the plots are uniformly scaled to a range of 12 K for temperature and 6 g kg^{-1} for mixing ratio. Estimated boundary-layer heights are marked with *black dots*

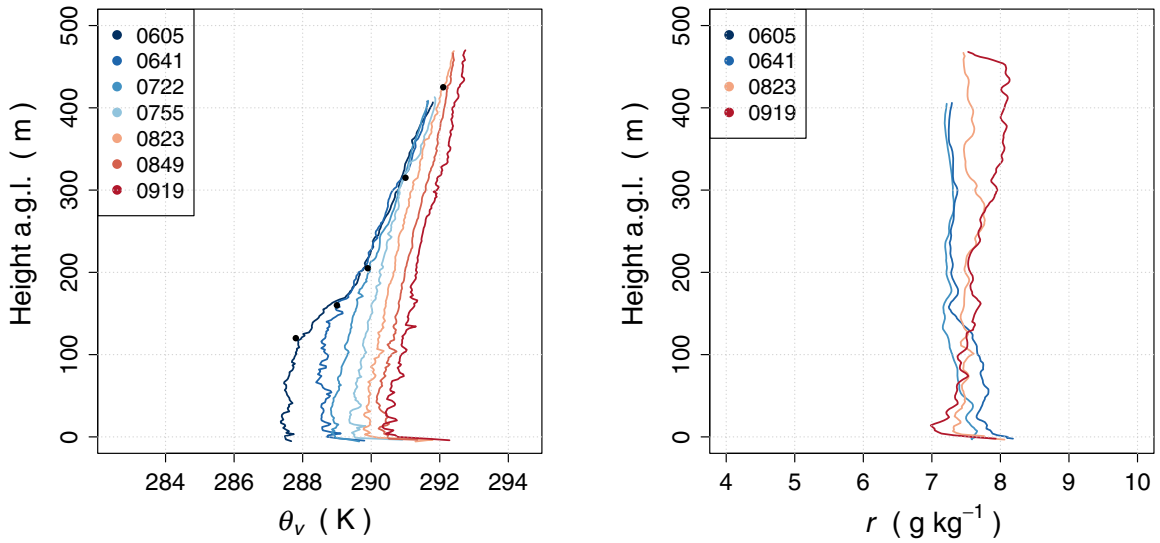

(a) 14 August 2013

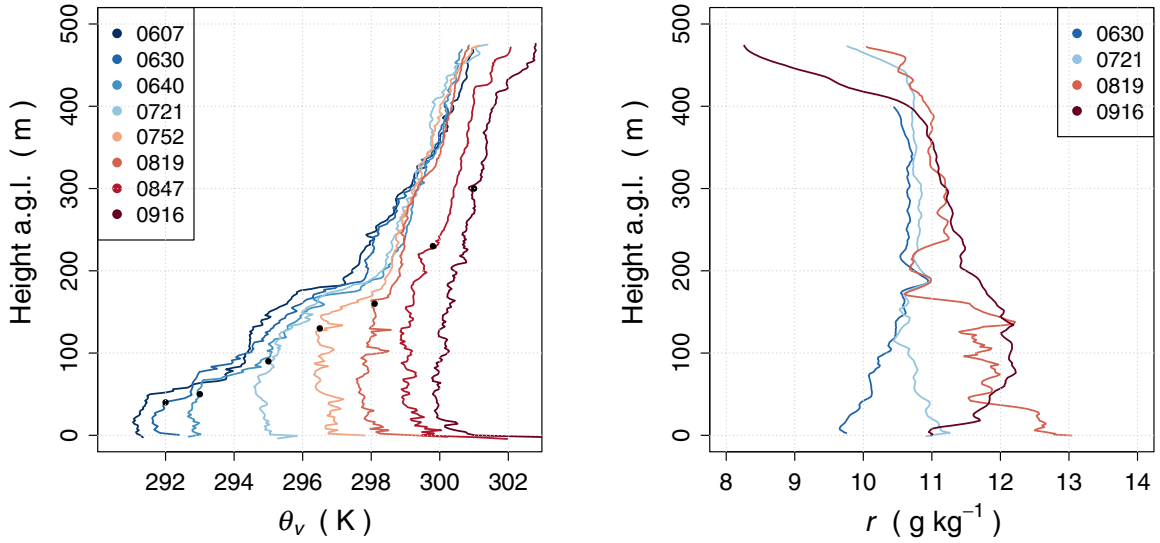

(b) 5 September 2013

Fig. 6 Vertical profiles of virtual potential temperature θ_v (*left*) and mixing ratio r (*right*) for 14 August and 5 September. For better readability, a few profiles of mixing ratio are omitted from the plot. The x-axes of the plots are uniformly scaled to a range of 12 K for temperature and 6 g kg^{-1} for mixing ratio. Estimated boundary layer heights are marked with *black dots*

the readability of the vertical profiles, hence the data were spatially averaged in height blocks of 2 m.

On all days, a shallow CBL developed and outgrew the nighttime inversion in the observed time frame. Differences are found in the heating rate of the shallow CBL, the nighttime inversion depths and its temperature gradient.

Selected profiles of the mixing ratio of water vapour r for each measurement day are plotted next to the corresponding vertical profiles of potential temperature in Figs. 5 and 6 (right). As for the temperature profiles, a 2-m block average is applied. Additionally, a 10-m-wide moving average is applied, and some profiles are omitted from the plot to further increase the readability, since the profiles overlap on large parts of the figure. The depicted profiles were chosen because they well document the development of the boundary layer. The colours help to relate a certain profile to the corresponding temperature profile of the same

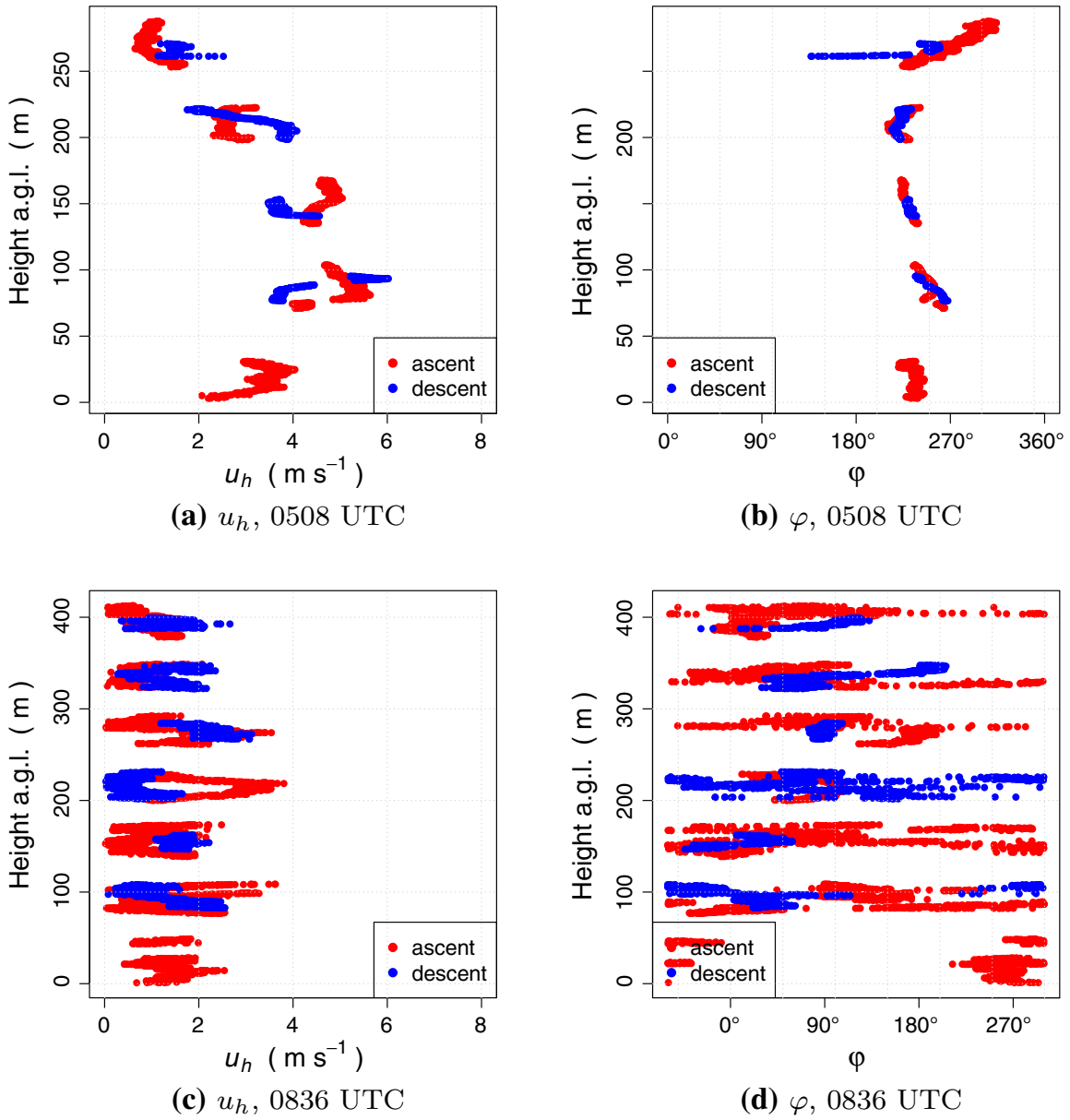

Fig. 7 Vertical profiles of horizontal wind speed u_h and wind direction φ at two different times of day on 5 July 2013

day. On all days, it can be observed that water vapour is transported from the surface into the shallow CBL during the morning transition. The profiles differ significantly as a result of the initial stratification of humidity in the nighttime boundary layer and the boundary-layer development during the transition.

Instantaneous wind profiles measured by RPA with the proposed flight path can be hard to interpret in convective regimes with small mean wind speed. A comparison between raw wind speed and wind direction measurements of an early morning flight, and measurements in an already well-developed CBL—where convective winds prevail—is given in Fig. 7 for 5 July 2013. For both cases, the parts of the flight with large roll angle of the aircraft ($\Phi > 17°$) have been removed. Kroonenberg et al. (2008) showed how orientation angle errors are propagated into the wind calculation and can lead to significant errors. In dynamic manoeuvres, as in the turns of the MASC, the inertial measurement system shows relatively weak performance for correct angle estimation, and therefore these parts of the flight are not used for wind

measurement. While in the early flight (Fig. 7a, b), winds are non-turbulent and a smooth profile can directly be seen in the vertical profile, the flight in the convective regime (Fig. 7c, d) shows much larger variance, which, especially for the wind direction, does not provide a clear picture of the airflow in the boundary layer. Despite this, reasonable profiles can be condensed from the averaged ascent and descent, with a vertical block average of 20-m height and a moving average over five blocks, as can be seen in Figs. 8 and 9. Manual measurements of wind speed and wind direction with a hand-held cup anemometer at 2 m above ground are added to the graphs in Fig. 8. Figure 9 contains measurements of the sonic anemometer for the ground-level measurement. A gap remains between the ground measurements and the lowest altitude of automatic flight of the RPA. Wind speeds at the 2-m level are below $2\,\mathrm{m\,s^{-1}}$ for all days. On some days, a nocturnal jet is still measured during the morning transition. A turn from westerly to easterly winds in the shallow CBL is found on 4–5 days. The westerly winds in the nights are likely caused by mesoscale effects. On the synoptic scale, winds with an easterly component prevail, as is also found in the dataset for these days in the later morning.

4.2 Boundary-Layer Height

The shallow CBL growth is presented as the development of the inversion-bottom height h_i over time in Fig. 3b. The values were estimated using the method described in Sect. 3 and Fig. 3a. The time axis is normalized to hours after sunrise for better comparability. The development of the boundary-layer height in the early phase shows almost linear growth until about 3.5 h after sunrise. The growth rate differs between the single days from $25\,\mathrm{m\,h^{-1}}$ on 23 July to $60\,\mathrm{m\,h^{-1}}$ on 5 July and 5 September.

4.3 Constant-Altitude Profiling

Another way to obtain information about the development of wind from the conducted experiment is to use the average wind measurement of the CAP parts of the flights. The development of horizontal wind speed u_h and wind direction φ at 100 m is shown in Fig. 10a, b. The common pattern of westerly winds turning counter-clockwise towards easterly winds during the morning transition is confirmed by the measurements at 100 m. The wind speeds are generally calm and decrease from 2–5 to $1–3\,\mathrm{m\,s^{-1}}$ as the direction turns. At 100 m, the change of wind direction and drop of wind speed are delayed and damped compared with the ground measurements of the sonic anemometer. The wind speed and wind direction measurements from the vertical profiles at 100 m are within the variance of the wind measurements during the CAP parts of the flights.

From CAP, fluxes were derived according to Sect. 3.2 and their development is presented for all days collectively in Fig. 10c, d. This figure also contains the surface flux measurements by the sonic anemometer on 14 August and 5 September. At the flight altitude of 100 m, the sensible heat flux crosses zero with a significant delay compared with the surface heat flux. Small positive fluxes can first be found two hours after sunrise at 100 m, whereas a significant increase was not observed until four hours after sunrise. The latent heat flux also shows an increase, which starts earlier and is steeper than for the sensible heat flux. The variation is much larger, which can partly be due to measurement errors, which are larger for the humidity sensor and the latent heat flux (see Fig. 4a). However, this unsteadiness also fits with the strong variations in the vertical profiles of mixing ratio. A sudden drop of latent heat flux is observed on two of the days at four hours after sunrise, which is investigated in more detail in Sect. 5.2.

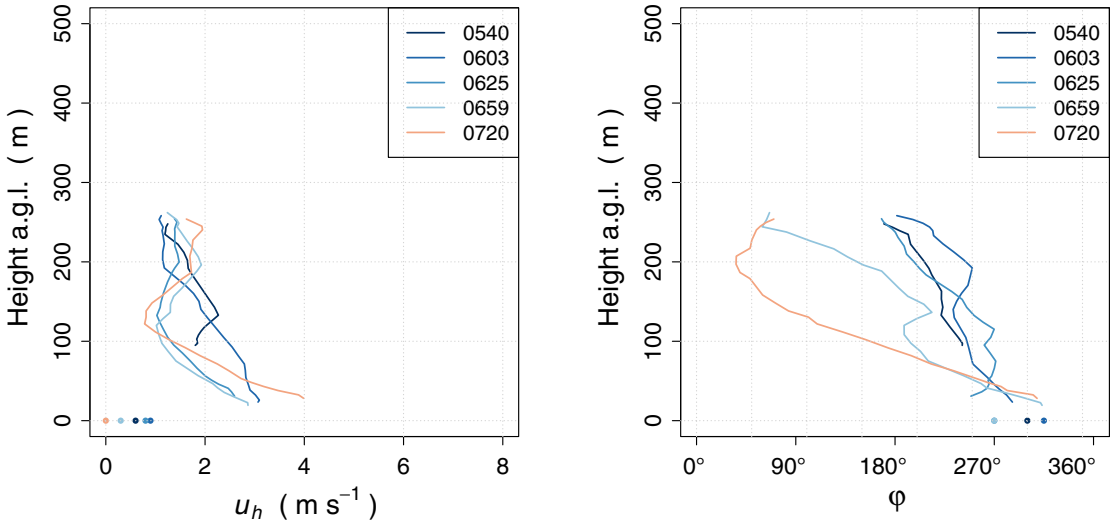

(a) 6 June 2013

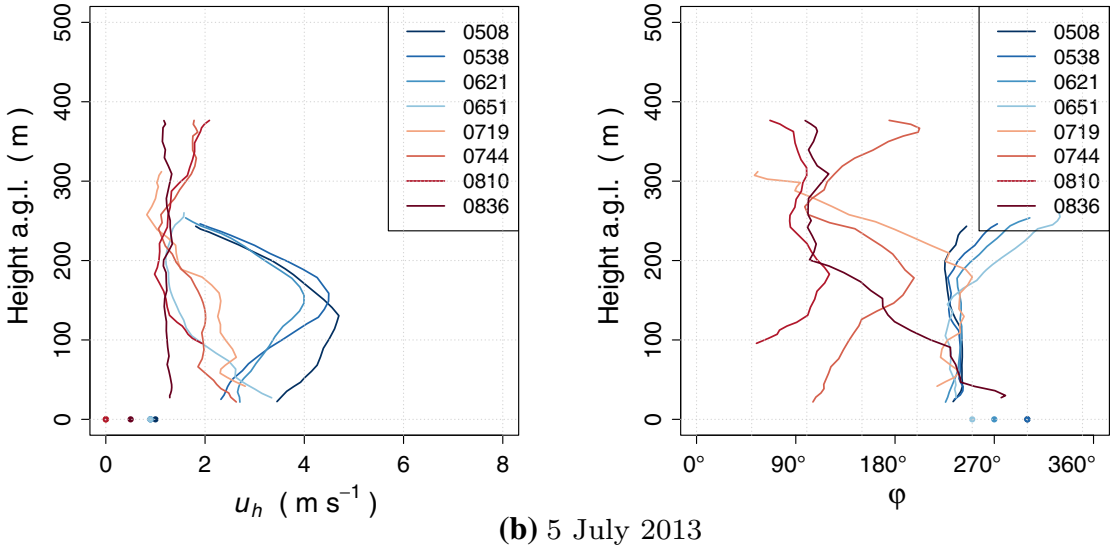

(b) 5 July 2013

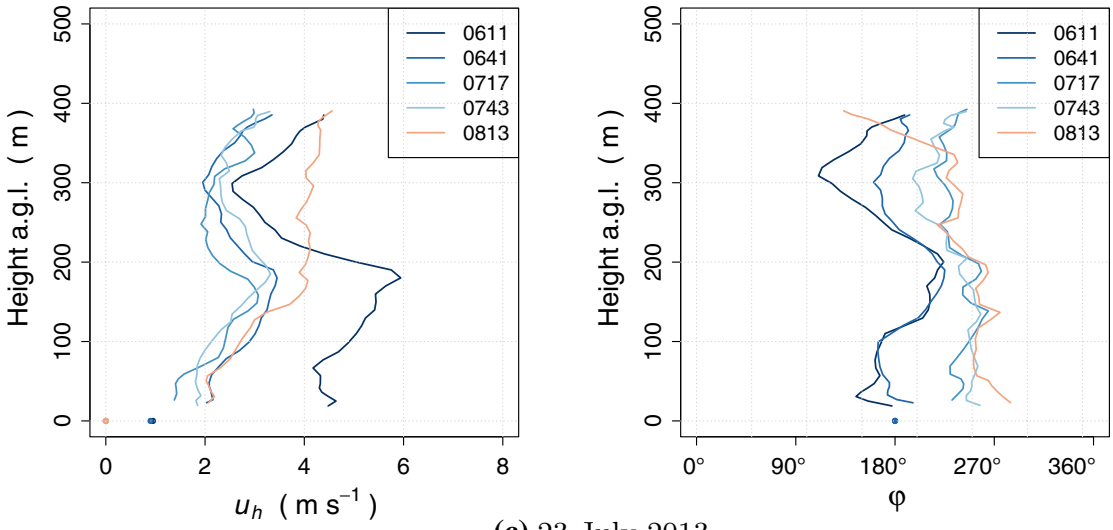

(c) 23 July 2013

Fig. 8 Vertical profiles of wind speed u_h (*left*) and direction φ (*right*) for 6 June, 5 July and 23 July. The x-axes of the plot are uniformly scaled to a range of 10 m s^{-1} and 360°. The lowest measurement point is taken from observations from the ground crew with hand-held meteorological sensors at 2 m. Points are missing where too low wind speed did not allow proper estimation of wind direction at the 2-m level

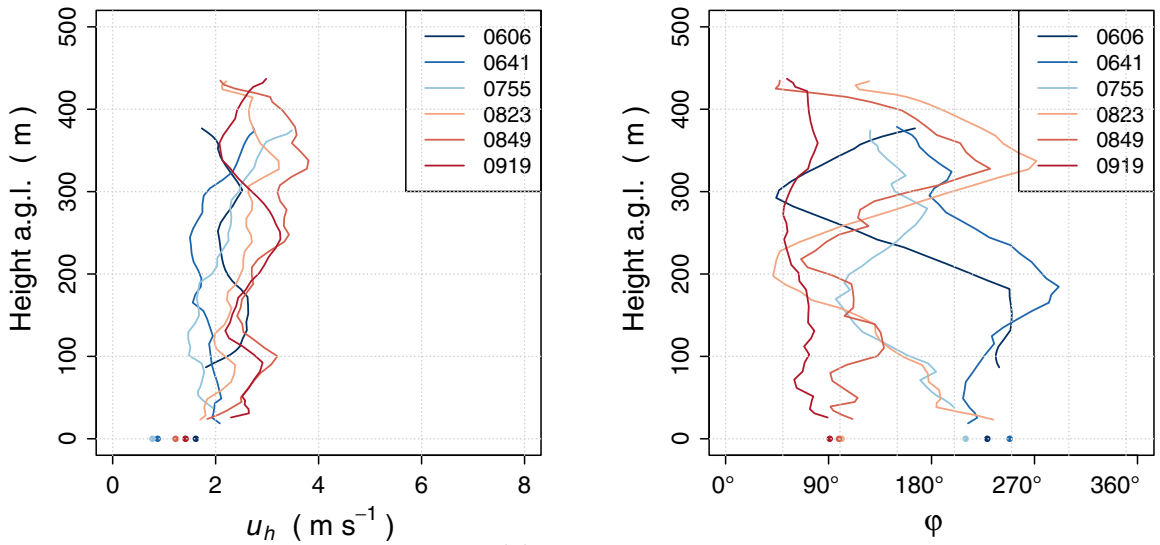

(a) 14 August 2013

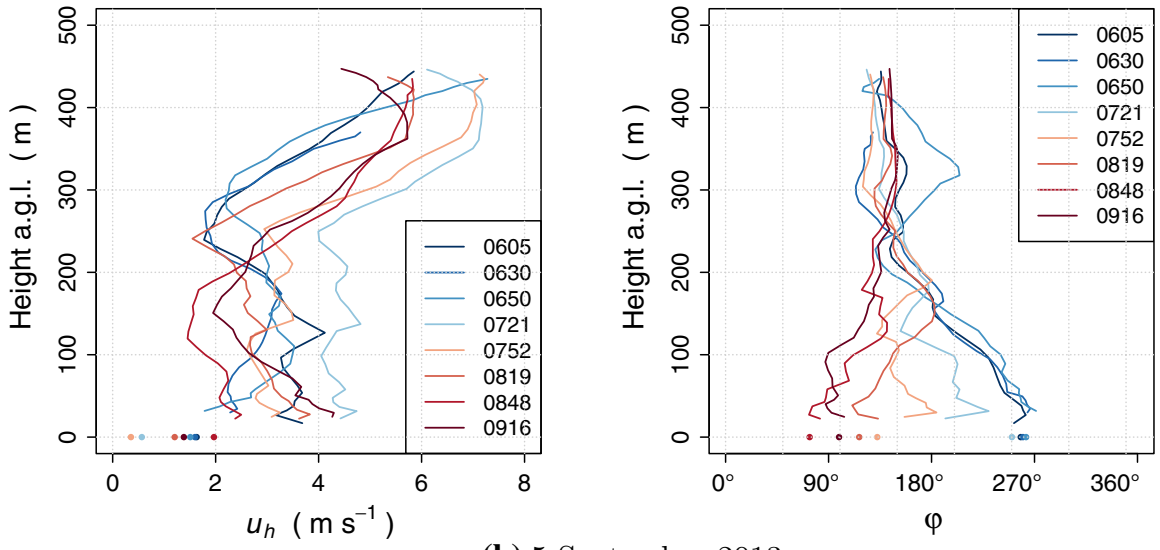

(b) 5 September 2013

Fig. 9 Vertical profiles of wind speed u_h (*left*) and direction φ (*right*) for 14 August and 5 September. The x-axes of the plot are uniformly scaled to a range of 10 m s^{-1} and 360°. The lowest measurement point is taken from the sonic anemometer at 2 m

4.4 Differences Between Measurement Days

In light of the results presented so far, an elaboration of the differences between the single measurement days is possible. Table 3 presents a list of important boundary conditions for the individual morning transitions. The minimum temperature of the night before T_min and the maximum temperature of the day T_max, as well as the average wind speed for the day $\overline{u}$, were found from a Davis Vantage Pro2 measurement station close by (see also Fig. 1). The hourly values were compared with the data obtained at the test site and were in good agreement. This also applies to the mean mixing ratio $\overline{r}$, calculated over the time of the experiment, and the mean sea level pressure (MSLP), calculated from the RPA measurements using the international barometric height formula assuming a standard atmosphere according to United States Committee (1976). The heating rate of the shallow CBL $\dot{\theta}$ and the nighttime inversion layer height z_NIL were estimated from potential temperature vertical profiles. It is not always

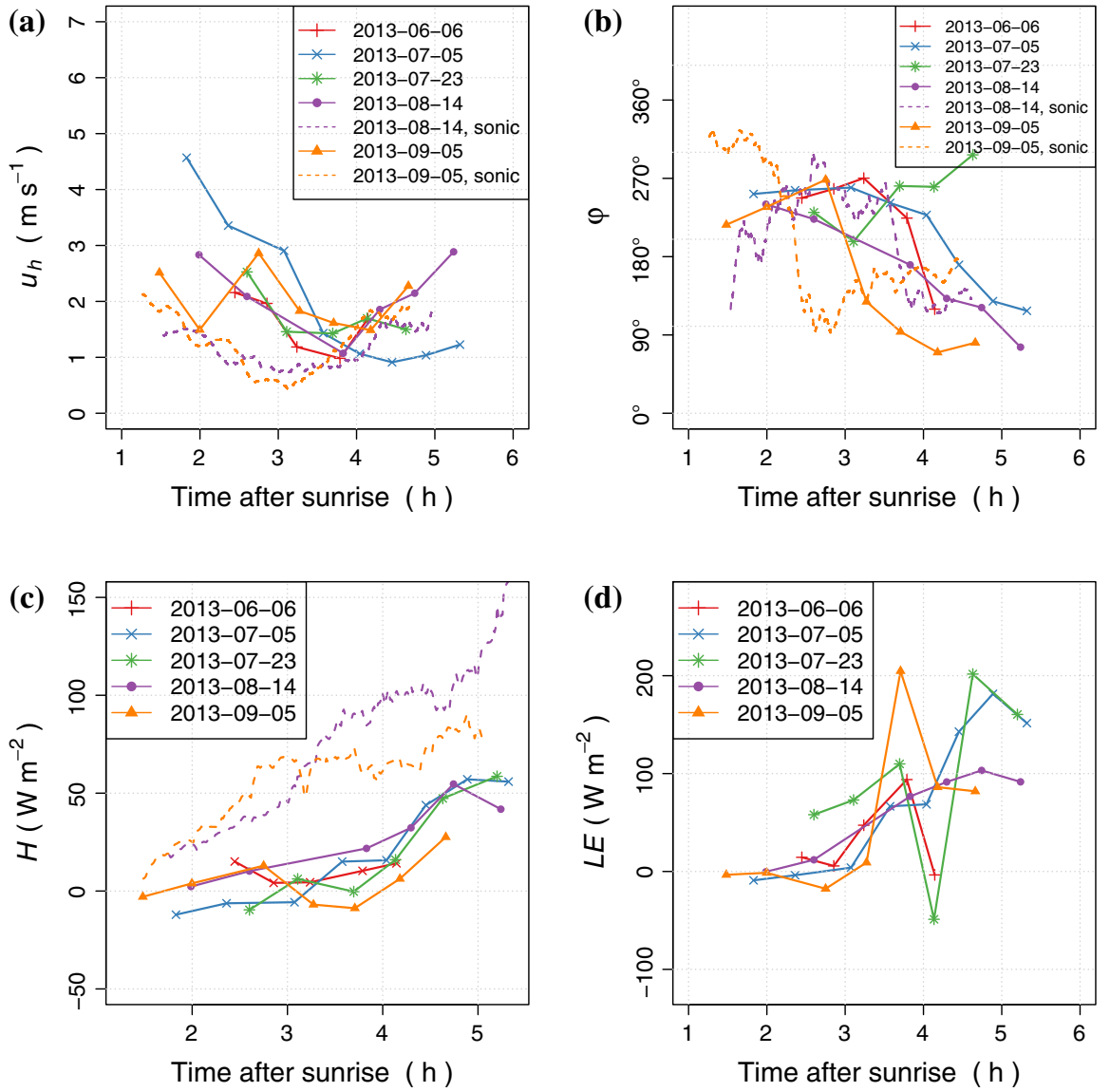

Fig. 10 Evolution of wind speed u_h (**a**), wind direction φ (**b**), sensible heat flux H (**c**) and latent heat flux LE (**d**) during the morning transition. The *solid lines* show the development at a height of 100 m measured with CAP; *dashed lines* are sonic anemometer measurements

obvious where the inversion layer ends and the residual layer starts, since numerous sublayers are found on almost every day. The given heights are the best assessment by the authors. The residual layer above the inversion should have near-neutral static stability. On all measurement days, a layer at the top level of the first vertical profile is found with significantly lower static stability than the layers below. It is the bottom height of this layer that is considered z_{NIL}. Cloud type and cloud cover are observations by the ground crew. In the following, a short description of the special characteristics of each measurement day is given:

4.4.1 6 June 2013

The cloudless sky on 6 June allows a strong heating rate of the developing CBL. Within the inversion layer, which is estimated to be about 250 m high, various sublayers of varying stability prevail, being burned off stepwise during the morning transition. A relatively dry boundary layer is found with only little evaporation from the ground. Weak westerly winds

Table 3 Meteorological boundary conditions of the experiment days

Date	T_{min} (°C)	T_{max} (°C)	$\overline{r}$ ($g\,kg^{-1}$)	$\overline{u}$ ($m\,s^{-1}$)	MSLP (hPa)	$\dot{\theta}$ ($K\,h^{-1}$)	z_{NIL} (m)	Clouds
6 June	8.2	25.7	7.5	1.5	1017	2.7	250	0
5 July	13.9	25.8	8.8	1.8	1026	1.8	100	1/8 → 5/8 Cu
13 July	15.6	33.1	10	1.9	1013.5	3	320	0
14 Aug.	9.3	21.2	7.5	1.5	1022	1	170	1/8 Ci → 3/8 Cu
5 Sept.	12.3	30.4	11	1.5	1016	2.8	190	0

Surface data for T_{min}, T_{max} and $\overline{u}$ were obtained from the local Davis weather station, while $\overline{r}$, mean sea-level pressure (MSLP) $\dot{\theta}$ and z_{NIL} were derived from RPA data. Cloud cover and type are observations by the ground crew

throughout the boundary layer in the early morning turn towards easterly winds between three and four hours after sunrise, with a minimum of wind speed at 3.5 h after sunrise. During and after the last flight, convective, fair-weather cumulus clouds start to form.

4.4.2 5 July 2013

The low heating rate of the CBL on 5 July correlates with the partially cloudy conditions, especially in the early phase of the transition. The shallow, only 100-m-deep inversion is burned off in the first 3.5 h after sunrise. A considerable amount of water vapour appears to be evaporated from the ground into the CBL, especially after the nighttime inversion layer has been burned off. A nocturnal jet centred at 200 m a.g.l. is observed very clearly until 3.5 h after sunrise. After this time, the wind direction changes from westerly to easterly, and wind speed is significantly lower. While the cloud cover decreases during the transition until 4.5 h after sunrise, cumulus clouds start to form increasingly from this time on.

4.4.3 23 July 2013

In the experiment, 23 July 2013 is the day with the highest maximum temperature. A strong heating rate of the CBL is given. No clouds are observed during the whole morning. Interestingly, the growth of the boundary layer is the slowest of all days, which is due to the pronounced and deep nighttime inversion layer. As already observed on 6 June, sublayers within the nighttime inversion layer are gradually burned off. Significant water vapour mixing into the CBL is documented by the vertical profiles. One event with a sudden drop of mixing ratio of water vapour in the CBL stands out and is discussed in more detail in Sect. 5.2. In contrast to all other days, no wind direction change from westerly to easterly during the transition is observed; instead, the wind direction even slightly turns from south to west. In the first flight, a jet-like increase of wind speed at 200 m is found, similar to what was observed in the early flights on 5 July.

4.4.4 14 August 2013

Of all flight days, 14 August is the day with the lowest heating rate of the CBL and therefore also the lowest maximum temperature during the day. High cirrus clouds just after sunrise prevented strong radiation. However, because the temperature gradient of the inversion is supposed to have been small, the inversion layer is burned off quickly. Characteristic for the day is also the remaining weak stability in the mixed layer, after the inversion layer has been burned off. This is also the reason for a low water vapour variability and mixing in the boundary layer. The typical wind direction change from west to east is found in the lowest 300 m. Wind speed is homogeneous and weak throughout the boundary layer.

4.4.5 5 September 2013

On 5 September a high heating rate of the shallow CBL is found, combined with a deep nighttime inversion layer. The water vapour content throughout the whole observed part of the atmosphere is higher than on all other days. Since the concentration is also high above the surface inversion, no large change of humidity occurs, except for the latest flights, where dry air is entraining from above 400 m. Profiles to higher altitudes would have been necessary to capture this event in more detail. Wind speeds are comparatively high on this day, especially

above 300 m, where a distinct increase of wind speed is present during the whole transition period. The change of wind direction from west to east is found below 300 m and is sharper than for all other days. The additional measurements by sonic anemometer reveal how this change of wind direction is delayed for the 100-m level compared with the 2-m level (see Fig. 10b).

5 Discussion

5.1 Scaling of the Morning Transition

In Sect. 4 an overview of the development of the boundary layer during the morning transition on five single days was presented. Even though the days were chosen because similar conditions were expected with low wind speeds, nearly cloudless sky and high radiation input, it was found that the single days showed quite different behaviour in detail. One goal of the experiments is to evaluate the applicability of mixed-layer scaling in the growing shallow CBL for a variety of measurement days. In Sect. 3 the convective velocity scale w_* and the convective temperature scale θ_*, as well as the scaling height z_i were introduced, and methods to estimate these values from the dataset were presented. Figure 11a shows the normalized sensible heat flux derived for all flights that were performed during the experiment against the scaled flight height $\zeta = z/z_i$ (with $z_i \approx h_i$, see Sect. 3). Despite the scatter, the measurements agree with mixed-layer theory (Stull 1988). Entrainment from above the inversion leads to a negative heat flux at the top of the boundary layer. Below the point where it crosses zero, the scaled heat flux increases linearly towards the ground. The fact that the linear regression does not cross the normalized flux axis at 1, but at about 0.85, is a hint that surface fluxes are overestimated by the proposed method.

With the help of the convective scaling parameters, the measurements of scalar variances at CAP flight level can be compared for all flight days. In Fig. 11 the dimensionless variances of potential temperature, horizontal and vertical wind are plotted against ζ. The CBL scalings derived by Sorbjan (1989) are depicted in the figures by solid lines,

$$\sigma_\theta^2/\theta_*^2 = 2(1-\zeta)^{4/3}\zeta^{-2/3} + 0.94\zeta^{4/3}(1-\zeta)^{-2/3}, \tag{10}$$

$$\sigma_u^2/w_*^2 = 0.36, \tag{11}$$

$$\sigma_w^2/w_*^2 = 1.08\zeta^{1/3}(1-\zeta)^{1/3}. \tag{12}$$

This figure shows that only in the upper half of the boundary layer are similar values of $\sigma_\theta^2/\theta_*^2$ compared with CBL theory found. While the scaled variances increase towards the boundary-layer top, they appear to be too small in the middle of the boundary layer. The chosen altitude of 100 m for the CAP was too high and the top of the vertical profile too low to collect measurement points below $\zeta = 0.2$. The variances of the horizontal wind component also increase towards the boundary-layer top, which is in contradiction to that found in literature (Garratt 1992). The vertical wind-component variances are close to the predicted profile for the mixed layer. To rule out errors that could possibly be introduced by the assumptions that were made regarding surface heat flux in Sect. 3, the dimensionless variances were also calculated using the sonic anemometer flux measurements for 14 August and 5 September and added in red colour to the figure. This shows that, on 5 September, where a significant overestimation of surface fluxes derived from the heating rate was found compared with the sonic anemometer due to warm-air advection, the values calculated from

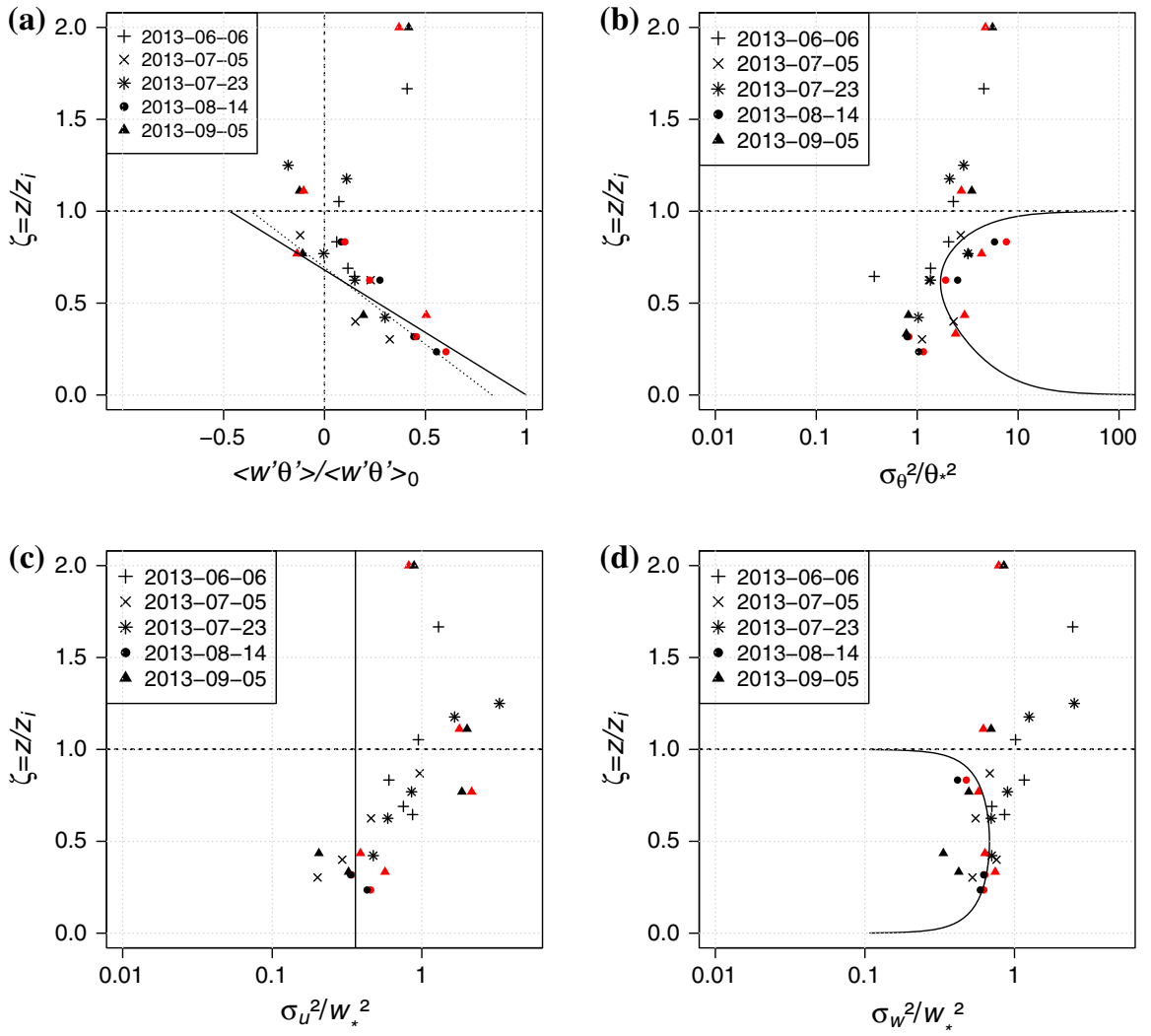

Fig. 11 Normalized sensible heat flux (**a**) and dimensionless variances of potential temperature (**b**), horizontal wind-speed component (**c**) and vertical wind-speed component (**d**). The *dashed line* shows the boundary-layer top ($\zeta = 1$). The *dotted line* in **a** gives the linear regression of all measurement points below $\zeta = B$. The *solid lines* are theoretical profiles that are found in literature for the mixed layer (e.g. Sorbjan 1989; Garratt 1992, see Eqs. 10–12). The values in *red* are scaled with the convective scales as calculated with measured data from the sonic anemometer for 14 August and 5 September

the sonic anemometer surface flux actually fit the theory better. The values are in good agreement for all other measurement points.

Boundary-layer scaling is only valuable if it can be applied in different locations, at different times and for data collected with different measurement systems. Bange et al. (2007) used the same methods as described in this study at a different test site, with the Helipod measurement system. The data of Bange et al. (2007) and of this study are shown in a collective plot in Fig. 12. For the upper half of the boundary layer, the measurements of dimensionless variances of potential temperature are in fairly good agreement. Since comparatively few data points were collected with the Helipod in that range, the data of the current study fill this gap nicely. In the lower half, the measured points from this study show smaller values in comparison. The collective plot shows that the increase in variances of u_h is found in both independent experiments. A possible explanation is that shear effects are not negligible for both experiments and are particularly strong at the boundary-layer top.

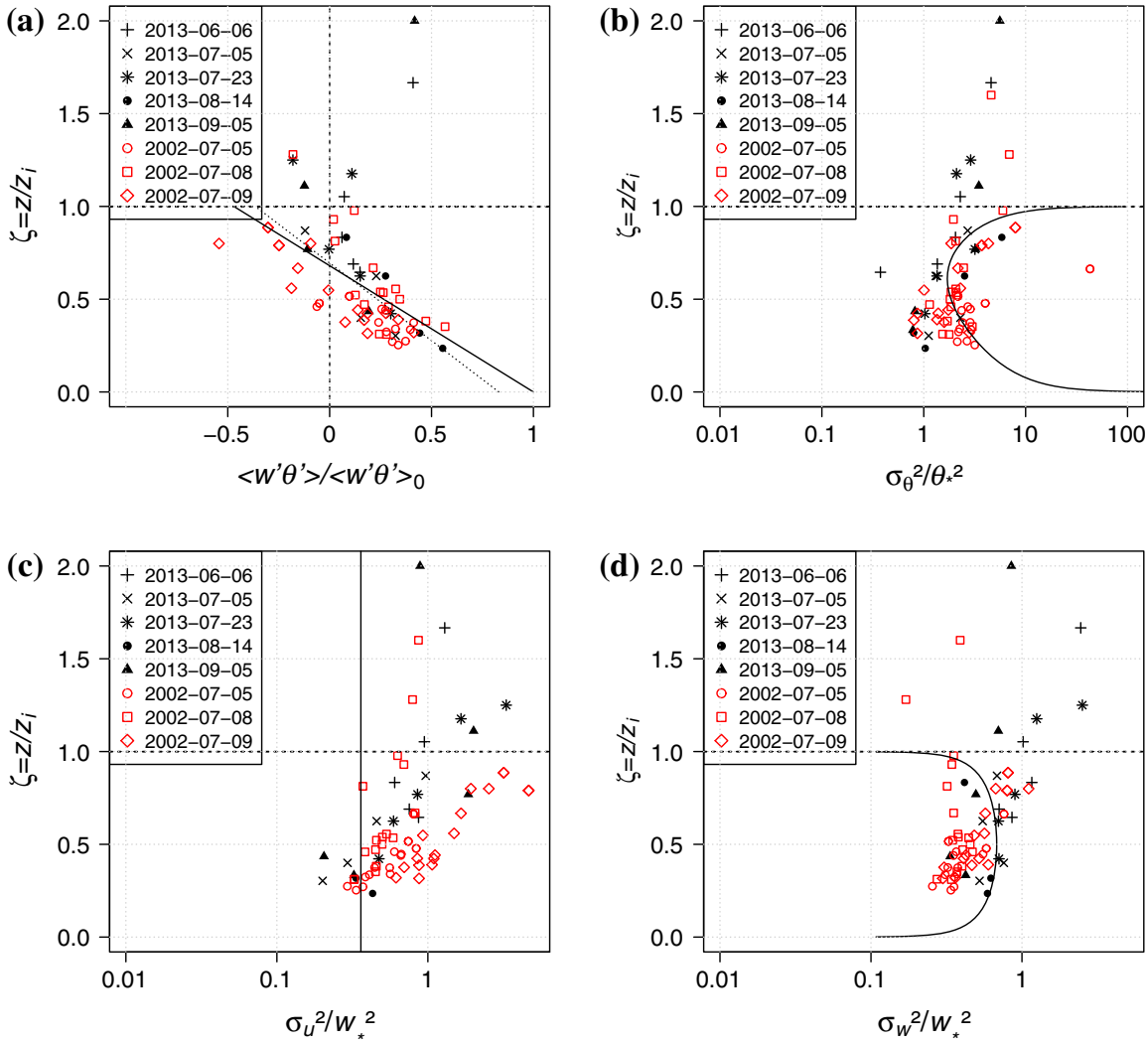

Fig. 12 Same as Fig. 11, but including data from Bange et al. (2007)

Further scaling approaches, including friction velocity u_* to account for shear-driven turbulence in the shallow CBL, could be applied to the measurement days with the additional sonic anemometer. However, the results are not consistent and are therefore not shown here.

5.2 Measurement of Small-Scale Features in the Shallow CBL

As seen above, universal scaling of the morning transition is extremely difficult and the large scatter is a hint that not all processes are described sufficiently. In this section, two examples of small-scale features that were captured during the experiment are described in more detail to gain a better understanding of the boundary-layer development.

5.2.1 5 September 2013

Since the RPA covers a wide area during its flights, the measurements can give information about horizontal variability of the measured scalars at a constant altitude. During a CAP flight, the altitude of the unmanned aircraft is maintained with a precision of ±1 m using GPS-supported barometric pressure measurements. Especially at the interface between different layers, this method can reveal how sharp and homogeneous the crossover between two layers

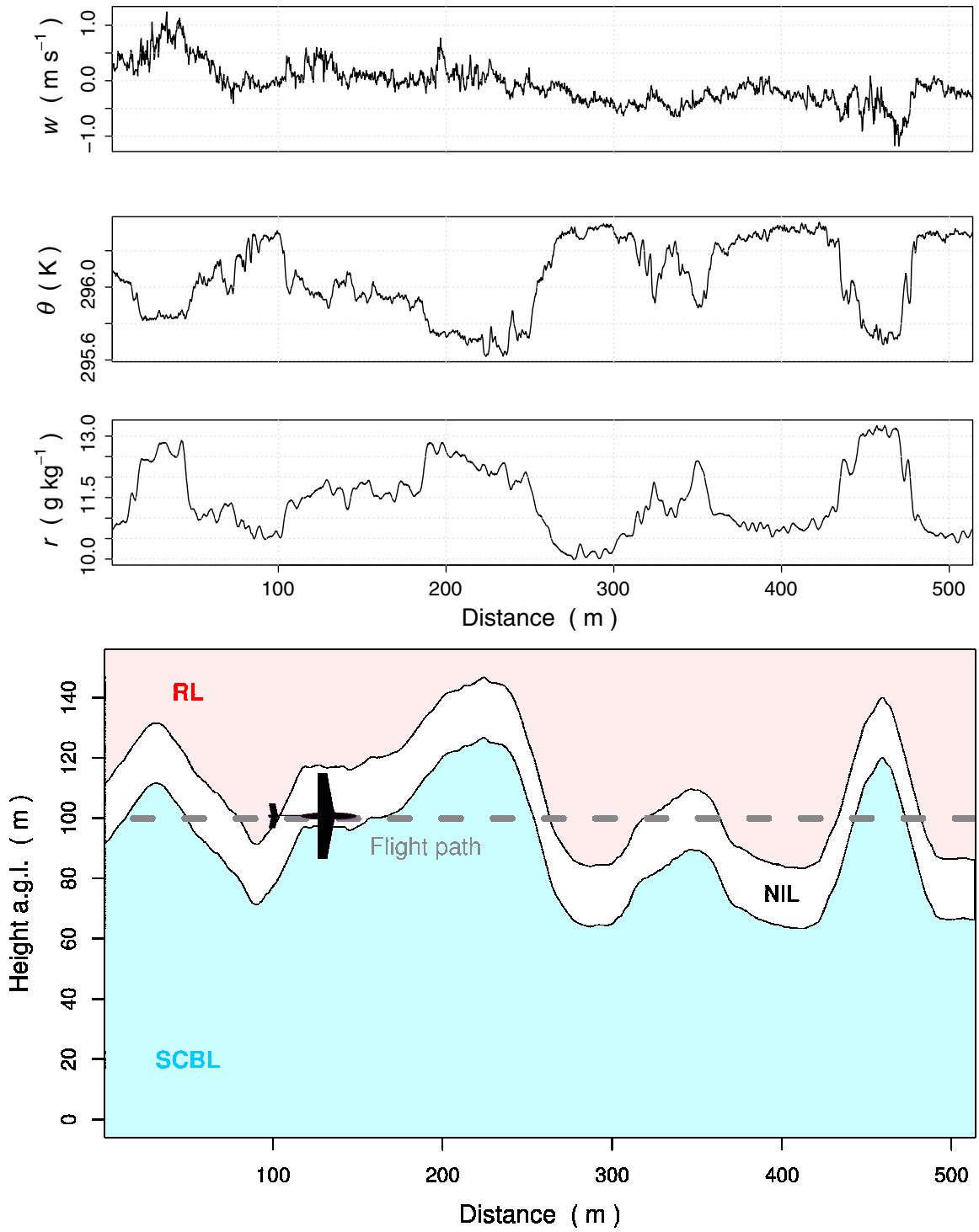

Fig. 13 Observation of horizontal variability of temperature, mixing ratio and vertical wind component on 5 September 2013, 0825 UTC. At the *bottom*, a sketch of the proposed flight through the interface between residual layer and shallow CBL on 5 September 2013 is given

appears. Considering that, during the morning transition, air is entraining the shallow CBL at the bottom of the inversion, it is very likely that large horizontal inhomogeneities are found in this layer. Figure 13 shows measurements of a flight leg at 0825 UTC on 5 September 2013. According to the corresponding vertical profile of potential temperature, the flight altitude was approximately 70 m below the bottom of the remaining inversion layer. Still, a large horizontal inhomogeneity can be found with alternating masses of dry, warm air

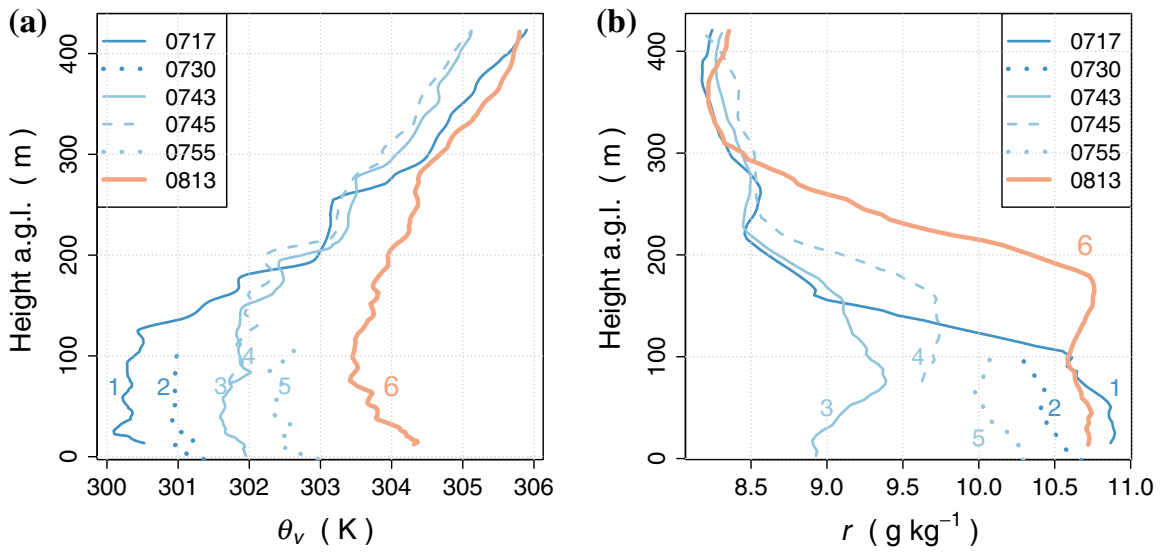

Fig. 14 Vertical profiles of potential temperature θ and mixing ratio r, including landing approach descents on 23 July 2013

from above the inversion and moist, cold air from within the shallow CBL. The steps of potential temperature along one leg are as large as 0.6 K, and the mixing ratio steps up to 3 g kg^{-1}, which coincides with the differences between the current shallow CBL and the residual layer. Thus, it can be assumed that the depths of the shallow CBL—also due to distinct entrainment events in parts of the boundary layer—are far from homogeneous in this phase of the morning transition. At the bottom of Fig. 13, a sketch of the assumed boundary layer structure at 0825 UTC on 5 September 2013 is given.

5.2.2 23 July 2013

In the fourth flight at 0743 UTC on 23 July 2013, approximately four hours after sunrise, a very strong downward latent heat flux was measured (see Fig. 10d). The vertical profile of this flight shows a decrease of moisture in the shallow CBL just before. A more detailed look at the development of the vertical profiles of humidity and temperature is given in Fig. 14. The graph also includes measurements from the descents to the landing approach of the RPA after the CAP measurements. The profiles are consecutively numbered for better allocation. While the shallow CBL temperature monotonically increases, a decrease of humidity in the shallow CBL starts just before 0730 UTC. At 0743 UTC, humidity is at its lowest, almost reaching the values of the layer above the inversion. After this, the humidity increases again, showing similar values in the shallow CBL at 0813 UTC as found at 0717 UTC. Examination of the single CAP racetracks of the two flights starting at 0717 UTC and 0743 UTC, respectively, gives more insight into the boundary-layer processes: At 0726 UTC, CAP at 100 m is in the entrainment zone, and strong horizontal variability of the water vapour mixing ratio is found along the flight legs, analogous to what was found on 5 September at 0825 UTC (see Fig. 15, black lines). Local kinematic fluxes of heat and moisture ($\langle w'\theta' \rangle$ and $\langle w'r' \rangle$) were calculated with a 50-m moving window, and show large bursts of positive fluxes of moisture, which appear as dry air being entrained into the shallow CBL. Martin et al. (2014) showed how entrainment can be measured with unmanned aircraft in the CBL by showing evident downward intrusion of warm air into the CBL. The presented data also show how, at the same time, dry air is mixed into the shallow CBL of the morning transition. In the later flight, at 0748 UTC, the 100-m level is approximately in the middle of the shallow CBL, and distinct

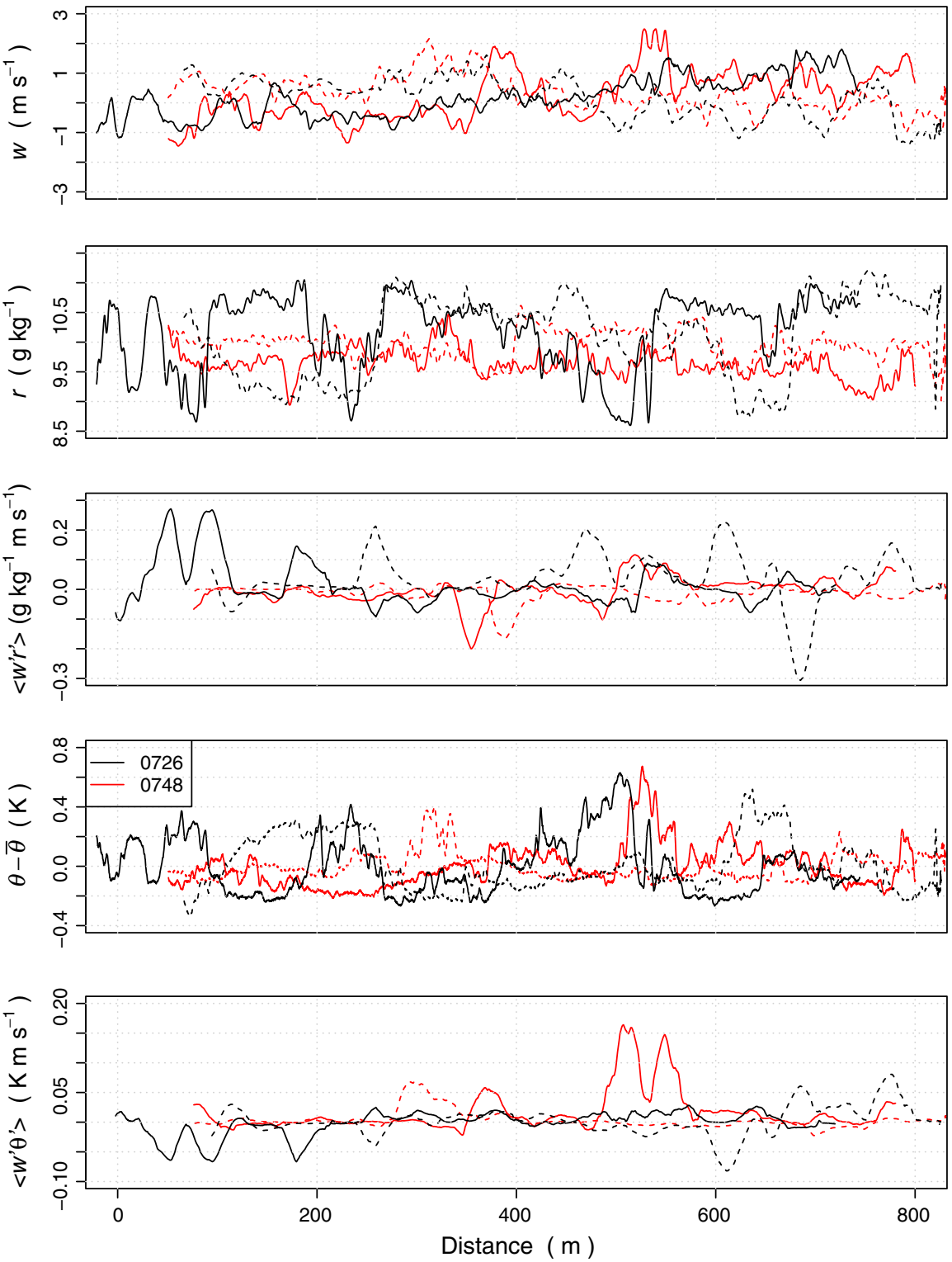

Fig. 15 w,r,$\langle w'r' \rangle$,θ and $\langle w'\theta' \rangle$ for several CAP racetracks on 23 July 2013. At 0726 UTC the RPA is still in the entrainment zone, whereas at 0748 UTC, the CAP level is in the centre of the shallow CBL. *Solid lines* are east–west legs; *dashed lines* are west–east legs

warm-air updrafts, i.e. thermals, are measured (Fig. 15, red lines). These rising thermals manifest in a peak in sensible heat flux. The moisture in these convective cells does not show an obvious pattern. In the west–east leg, drier air seems to be present in the updraft, while in the east–west leg, no significant difference compared with the surrounding air is measured. In both flight directions, a distinct peak of negative kinematic moisture flux is found at a similar

location (i.e. ≈350 m flight distance). For all single racetracks of this flight, a negative latent heat flux is calculated, but the demonstrated peaks in Fig. 15 are the main contributor to the strong negative peak in Fig. 10d. The averaged latent heat flux of the east–west racetrack at 0748 UTC alone is $-154\,\mathrm{W\,m^{-2}}$.

6 Conclusions

The morning transition from a nighttime inversion layer to a mixed layer on various days with little cloud cover above a hilly terrain with heterogeneous land use has been investigated. A single RPA was used to measure all thermodynamic variables with high resolution throughout the transition phase from approximately 2 to 5 h after sunrise. Vertical profiles of temperature, humidity and wind were measured to observe the development of thermal stratification of the atmosphere. Constant-altitude profiling at 100 m delivered area-averaged flux measurements of sensible and latent heat. The following conclusions can be drawn from the experiment:

- Although only convective days were chosen for the experiment, the results presented in Sect. 4 reveal that each day had very specific, individual properties.
- Fluxes calculated based on RPA measurements are reasonable and fit with the development of the boundary layer as it is observed in the vertical profiles. The gradients of sensible heat flux compare well with surface measurements from a sonic anemometer after the zero-crossing.
- In Sect. 3 it was shown how the boundary-layer height can be estimated from potential temperature profiles. A way to estimate surface heat fluxes from the heating rate in the shallow CBL was introduced in Sect. 3.3. Using this information, mixed-layer scaling was applied to the dataset (see Sect. 5.1). As also found by Sorbjan (2007), dimensionless variances of wind speed are difficult to describe in a common scaling approach for the transition phase, but temperature variances coincide with mixed-layer theory. In the given dataset, this is true only for the upper half of the boundary layer, while variances believed to be too low are found below 0.5ζ.
- The variances of horizontal wind speed surprisingly increase towards the top of the scaled boundary layer. Variances of vertical wind speed are close to what is found in literature, but are subject to large scatter.
- The results were compared with Bange et al. (2007), who used comparable methods for their analysis but measured with the helicopter-borne probe Helipod over flat and heterogeneous terrain. The results are remarkably similar, both showing slightly lower values for temperature variances in the lower half of the boundary layer and an increase of horizontal wind variances towards the boundary-layer top. The scarce data in the upper third of the boundary layer in Bange et al. (2007) could be complemented with data from the presented study.
- Many of the assumptions made for analysis of the data become invalid in the later phase of the transition, i.e. after the nighttime inversion layer has been burned off: the prerequisite of stationarity is not fulfilled anymore; advection cannot be neglected anymore; the increase of temperature in the shallow CBL cannot be approximated linearly any longer; and the integral length scales of turbulence will outgrow the averaging length. It also becomes more difficult to estimate the boundary-layer depth with the proposed method. It is thus not surprising that the measurements in the lower scaled boundary layer—which in the CAP experiment strategy are those measurements that are taken later in the morning—are subject to larger error and significant scatter.

– The overall scatter of the data is comparably large and can be related to uncertainties in the methodology, especially the estimation of the boundary-layer height z_i and the ratio between the inversion bottom and flux zero-crossing B, which is needed for the surface-flux estimation.
– A strong argument in favour of measurements with small RPA is that small-scale features can be measured in situ with high resolution. An example is given in Sect. 5.2, which showed the horizontal variability of the interface between the shallow CBL and the residual layer, as well as entrainment events, and single thermals in the CBL.
– The advantage of RPA campaigns compared with systems such as helicopter-borne probes or manned research aircraft is that experiments to obtain a larger database can be performed more cost-efficiently and in almost any location, with low infrastructure requirements.

Naturally, if embedded in larger field experiments with complementary instruments (e.g. surface flux measurements by a scintillometer or a network of sonic anemometers), the analysis of RPA measurements can be significantly enhanced. Another possibility to improve the measurements is to fly several aircraft simultaneously, at several altitudes, to obtain instantaneous vertical profiles of fluxes for each stage of the morning transition and prove if the assumption of stationarity, which is presupposed for this study, is correct. With longer flight legs (i.e. less statistical uncertainty) on a square-shaped flight pattern, an inverse modelling approach according to Bange et al. (2006) could be applied to find surface heat fluxes more accurately. Another way to improve the results would be to reduce the altitude of the CAP flights, in order to achieve improved measurements in the lower half of the scaled boundary layer.

Acknowledgments We thank all those who helped during the experiments by supporting the ground crew in the field or with fruitful discussions to improve the quality of the data evaluation. Special thanks go to Roland Dörsam, who provided measurements from his weather station close to the measurement site.

Appendix: Uncertainty Estimation of Surface Heat Fluxes

The uncertainty of the estimated surface heat flux H_0 can be evaluated theoretically. We consider the uncertainties $\sigma_B = 0.1$, $\sigma_{z_i} = 20\,\mathrm{m}$, $\sigma_{\dot{\theta}} = 1 \times 10^{-4}\,\mathrm{K\,s^{-1}}$, and apply Gaussian error propagation to Eq. 8,

$$\sigma_H = \sqrt{\left(\frac{\partial H}{\partial B}\sigma_B\right)^2 + \left(\frac{\partial H}{\partial z_i}\sigma_{z_i}\right)^2 + \left(\frac{\partial H}{\partial \dot{\theta}}\sigma_{\dot{\theta}}\right)^2} \tag{13}$$

with the boundary conditions $B = 0.68$, $z_i = 200\,\mathrm{m}$, $\dot{\theta} = 1 \times 10^{-3}\,\mathrm{K\,s^{-1}}$, $\rho = 1.18\,\mathrm{kg\,m^{-3}}$ and $c_\mathrm{p} = 1006\,\mathrm{J\,kg^{-1}\,K^{-1}}$. The result is an uncertainty of $\sigma_H = 33\,\mathrm{W\,m^{-2}}$ for a surface heat flux of $161\,\mathrm{W\,m^{-2}}$, which is approximately 20 %.

References

Angevine WM, Baltink HK, Bosveld FC (2001) Observations of the morning transition of the convective boundary layer. Boundary-Layer Meteorol 101:209–227

Bange J, Zittel P, Spieß T, Uhlenbrock J, Beyrich F (2006) A new method for the determination of area-averaged turbulent surface fluxes from low-level flights using inverse models. Boundary-Layer Meteorol 119:527–561

Bange J, Spieß T, van den Kroonenberg A (2007) Characteristics of the early-morning shallow convective boundary layer from Helipod flights during STINHO-2. Theor Appl Climatol 90(1–2):113–126. doi:10.1007/s00704-006-0272-2

Bange J, Beyrich F, Engelbart DAM (2002) Airborne measurements of turbulent fluxes over heterogeneous terrain with Helipod and Do 128—error analysis and comparison with ground-based systems. In: 15th Conference on boundary layer and turbulence, American Meteorological Society, Wageningen, The Netherlands, pp 378–381

Beare R (2008) The role of shear in the morning transition boundary layer. Boundary-Layer Meteorol 129(3):395–410. doi:10.1007/s10546-008-9324-8

Bennett LJ, Weckwerth TM, Blyth AM, Geerts B, Miao Q, Richardson YP (2010) Observations of the evolution of the nocturnal and convective boundary layers and the structure of open-celled convection on 14 June 2002. Mon Weather Rev 138(7):2589–2607. doi:10.1175/2010MWR3200.1

Beyrich F, Leps JP, Mauder M, Bange J, Foken T, Huneke S, Lohse H, Lüdi A, Meijninger W, Mironov D, Weisensee U, Zittel P (2006) Area-averaged surface fluxes over the LITFASS region based on eddy-covariance measurements. Boundary-Layer Meteorol 121(1):33–65. doi:10.1007/s10546-006-9052-x

Bonin T, Chilson P, Zielke B, Fedorovich E (2013) Observations of the early evening boundary-layer transition using a small unmanned aerial system. Boundary-Layer Meteorol 146(1):119–132. doi:10.1007/s10546-012-9760-3

Brötz B, Eigenmann R, Dörnbrack A, Foken T, Wirth V (2014) Early-morning flow transition in a valley in low-mountain terrain under clear-sky conditions. Boundary-Layer Meteorol 152(1):45–63. doi:10.1007/s10546-014-9921-7

Deardorff JW (1974) Three-dimensional numerical study of the height and mean structure of a heated planetary boundary layer. Boundary-Layer Meteorol 7:81–106

Deardorff JW, Willis GE, Stockton BH (1980) Laboratory studies of the entrainment zone of a convectively mixed layer. J Fluid Mech 100:41–64. doi:10.1017/S0022112080001000

Edwards J, Basu S, Bosveld F, Holtslag A (2014) The impact of radiation on the GABLS3 large-eddy simulation through the night and during the morning transition. Boundary-Layer Meteorol 152(2):189–211. doi:10.1007/s10546-013-9895-x

Eigenmann R, Metzger S, Foken T (2009) Generation of free convection due to changes of the local circulation system. Atmos Chem Phys 9(21):8587–8600. doi:10.5194/acp-9-8587-2009

Foken T, Nappo C (2008) Micrometeorology, 1st edn. Springer, Berlin

Frank JM, Massman WJ, Ewers BE (2013) Underestimates of sensible heat flux due to vertical velocity measurement errors in non-orthogonal sonic anemometers. Agric For Meteorol 171–172:72–81. doi:10.1016/j.agrformet.2012.11.005

Garratt JR (1992) The atmospheric boundary layer. Cambridge University Press, UK, 316 pp

Knuth SL, Cassano JJ (2014) Estimating sensible and latent heat fluxes using the integral method from in situ aircraft measurements. J Atmos Ocean Technol 31:1964–1981. doi:10.1175/JTECH-D-14-00008.1

Kochendorfer J, Meyers T, Frank J, Massman W, Heuer M (2012) How well can we measure the vertical wind speed? Implications for fluxes of energy and mass. Boundary-Layer Meteorol 145(2):383–398. doi:10.1007/s10546-012-9738-1

Lapworth A (2006) The morning transition of the nocturnal boundary layer. Boundary-Layer Meteorol 119(3):501–526. doi:10.1007/s10546-005-9046-0

Lenschow DH, Stankov BB, Mahrt L (1979) The rapid morning boundary-layer transition. J Atmos Sci 36:2108–2124

Lenschow DH, Stankov BB (1986) Length scales in the convective boundary layer. J Atmos Sci 43:1198–1209

Martin S, Beyrich F, Bange J (2014) Observing entrainment processes using a small unmanned aerial vehicle: a feasibility study. Boundary-Layer Meteorol 150(3):449–467. doi:10.1007/s10546-013-9880-4

Martin S, Bange J (2014) The influence of aircraft speed variations on sensible heat-flux measurements by different airborne systems. Boundary-Layer Meteorol 150(1):153–166. doi:10.1007/s10546-013-9853-7

Reineman BD, Lenain L, Statom NM, Melville WK (2013) Development and testing of instrumentation for UAV-based flux measurements within terrestrial and marine atmospheric boundary layers. J Atmos Ocean Technol 30(7):1295–1319. doi:10.1175/JTECH-D-12-00176.1

Sorbjan Z (1989) Structure of the atmospheric boundary layer. Prentice Hall Advanced Reference Series: Physical and Life Sciences. Prentice Hall, New Jersey, 317 pp

Sorbjan Z (1995) Toward evaluation of heat fluxes in the convective boundary layer. J Appl Meteorol 34:1092–1098

Sorbjan Z (2007) A numerical study of daily transitions in the convective boundary layer. Boundary-Layer Meteorol 123(3):365–383. doi:10.1007/s10546-006-9147-4

Stull R (1988) An introduction to boundary layer meteorology. Kluwer Academic, Dordrecht, 666 pp

United States Committee (1976) U.S. standard atmosphere, 1976. National Oceanic and Atmospheric Administration, Washington, DC

van den Kroonenberg AC, Martin T, Buschmann M, Bange J, Vörsmann P (2008) Measuring the wind vector using the autonomous mini aerial vehicle M^2AV. J Atmos Ocean Technol 25:1969–1982

Wildmann N, Mauz M, Bange J (2013) Two fast temperature sensors for probing of the atmospheric boundary layer using small remotely piloted aircraft (RPA). Atmos Meas Tech 6(8):2101–2113. doi:10.5194/amt-6-2101-2013

Wildmann N, Hofsäß M, Weimer F, Joos A, Bange J (2014) MASC—a small remotely piloted aircraft (RPA) for wind energy research. Adv Sci Res 11:55–61. doi:10.5194/asr-11-55-2014

Wildmann N, Kaufmann F, Bange J (2014) An inverse-modelling approach for frequency response correction of capacitive humidity sensors in ABL research with small remotely piloted aircraft (RPA). Atmos Meas Tech 7(9):3059–3069. doi:10.5194/amt-7-3059-2014

Wildmann N, Ravi S, Bange J (2014) Towards higher accuracy and better frequency response with standard multi-hole probes in turbulence measurement with remotely piloted aircraft (RPA). Atmos Meas Tech 7(4):1027–1041. doi:10.5194/amt-7-1027-2014